

Quantum chemical studies of reactive species in water

THÈSE N° 7347 (2016)

PRÉSENTÉE LE 13 DÉCEMBRE 2016

À LA FACULTÉ DE L'ENVIRONNEMENT NATUREL, ARCHITECTURAL ET CONSTRUIT
LABORATOIRE DE MODÉLISATION DE LA CHIMIE ENVIRONNEMENTALE
PROGRAMME DOCTORAL EN CHIMIE ET GÉNIE CHIMIQUE

ÉCOLE POLYTECHNIQUE FÉDÉRALE DE LAUSANNE

POUR L'OBTENTION DU GRADE DE DOCTEUR ÈS SCIENCES

PAR

Daniela TROGOLO

acceptée sur proposition du jury:

Dr R. Hovius, président du jury
Prof. J. S. Arey, Prof. U. von Gunten, directeurs de thèse
Prof. K. McNeill, rapporteur
Prof. L. Winkel, rapporteuse
Prof. M. Ceriotti, rapporteur



ÉCOLE POLYTECHNIQUE
FÉDÉRALE DE LAUSANNE

Suisse
2016

Hoc etiam magis haec animum te advertere par est
corpora quae in solis radiis turbare videntur,
quod tales turbae motus quoque materiali
significant clandestinos caecosque subesse.
multa videbis enim plagis ibi percita caecis
commutare viam retroque repulsa reverti
nunc huc nunc illuc in cunctas undique partis.
scilicet hic a principiis est omnibus error.

— Lucrezio, *De Rerum Natura*, II, 125-132.

An empty node is a sad node.

— DT

Acknowledgments

I want to thank everyone who supported me during this looong and sometimes never-ending PhD.

First of all, I want to thank Sam. He gave me this opportunity 4 years ago. He guided me through science and he taught me what performing scientific research really means. I would not be here writing these acknowledgments if it weren't for him.

Then, I want to thank my family (la mia mamma, il mio papà, i miei zii, and Philipp). They were my support when I felt lonely and tired. They dispensed advices and help when I asked.

I want to thank my friends. In a random order: Elena, Chiara, Esra, Serena, Giorgia, Andrea, Giulia, Riccardo. All equally important and essential to me. However, a special acknowledgment goes to Elena who checked my Italian translation of the abstract. Se l'abstract in italiano contiene degli errori, é colpa sua. Non mia, eh! :-)

Finally, I want to thank my colleagues Jonas and Saer. Jonas taught me to play *Jass* and I taught him *Scopa*, when Sam was not around. :-) I want also to thank Karine (the best secretary a lab can ever have) and Jenn (the best office mate I ever had). Both of them enjoyed my Italian coffee and were always available to share their time with me!

Office GR C2 535, August 30th, 2016

Abstract

In this thesis, quantum chemical methods have been applied to elucidate the thermodynamics and the kinetics of reactions involving reactive species in water. Due to their high reactivity in water, many transient species are difficult to study by experimental means only. Here, quantum chemical models are used to provide a deeper insight into the chemical nature and aqueous behaviors of such species.

In the first chapter, I investigate the gas phase electronic structure and the thermodynamics of inorganic chloramines, bromamines, and bromochloramines, collectively termed halamines. The halamines are halogen oxidants that arise from reactions between ammonia and hypohalous acids during water disinfection processes, and these reactive species are implicated in the formation of disinfection byproducts that are harmful to human health. Despite their relevance in both drinking water chemistry and in biochemistry, the stabilities and speciation of these molecules are difficult to investigate by experimental means. To accurately predict the electronic structures and gas phase thermodynamic properties of halamines, I design a computational protocol, TA14, based on the high-quality Weizmann and Feller-Peterson-Dixon composite methods. TA14 combines a systematic sequence of wave function theory calculations, including the evaluations of dynamical and static electron correlation (CCSDTQ), core/valence electron correlation contributions, scalar and spin-orbit relativistic contributions, and VPT2 anharmonic vibrations. Using TA14, I successfully assess the gas phase total atomization energies, free enthalpies of formation, $\Delta_f H_{gas}^o$, and Gibbs free energies of formation, $\Delta_f G_{gas}^o$, of halamines within uncertainty bounds of 1-3 kJ mol⁻¹. Analysis of the energy components contributing to total atomization energies of halamines reveals that N-Cl and N-Br bonds are held together mostly or entirely by electron correlation forces, with small or even negative Hartree Fock contributions. For example, the Hartree Fock component of the total atomization energy, TAE_{HF}, is negative for both NBr₃ and NBr₂Cl, implying that these molecules would be predicted as unstable without accounting for dynamical electron correlation. Reported thermochemical data enable the determination of equilibrium constants for reactions involving halamines, opening possibilities for more quantitative studies of the chemistry of these poorly understood compounds.

In the second chapter, I evaluate the aqueous equilibria and speciation of halamines. I combine theoretical benchmark-quality gas phase Gibbs free energies of formation (chapter 2) with the computed Gibbs free energies of solvation, ΔG_{solv}^* , thereby obtaining aqueous phase Gibbs free energies of formation, $\Delta_f G_{aq}^o$, for halamines. The 'half-and-half' solvation approach, based on averaging the estimates of SMD implicit solvent model and the cluster-

continuum solvent model, produces an average error of 3.3 kJ mol^{-1} in ΔG_{solv}^* for a set of structurally related molecules containing H, N, O, and Cl. Taking into consideration the combined uncertainties of the computed $\Delta_f G_{gas}^o$ values and the computed ΔG_{solv}^* values, we assign an uncertainty of $6\text{-}7 \text{ kJ mol}^{-1}$ to the theoretical standard Gibbs free energies of formation in aqueous phase, $\Delta_f G_{aq}^*$, of halamines. $\Delta_f G_{aq}^*$ values are key thermodynamic properties for investigating chemical processes involving halamines during drinking water treatment. The newly reported thermodynamic data can be used to determine the stabilities (reaction equilibria) of halamines in water. Based on our estimated uncertainties of $6\text{-}7 \text{ kJ mol}^{-1}$ in the computed $\Delta_f G_{aq}^*$ values of halamines, we expect roughly 1 order-of-magnitude uncertainty in the aqueous equilibrium constants for the reactions leading to the production of halamines in water. I also estimate acid dissociation constant values, pK_a , of both the protonated and neutral halamines and methylated amines, based on quantum chemical computations. These results bring new insights into the electronic nature and stabilities of these reactive species in water, enabled by quantitative computational investigations of properties that are not possible to determine experimentally.

In the third chapter, I evaluate a previously proposed molecular pathway that leads from *N,N*-dimethylsulfamide to *N,N*-nitrosodimethylamine (NDMA), a US Environmental Protection Agency regulated carcinogen, during ozonation of bromide-containing natural water. The molecular modeling involves several challenges, including electronic structures having multireference character, intermediates and transition state structures that are aqueously solvated, and intermolecular migration reactions. To describe this transformation, I take advantage the M05 and B2PLYPD density functional theory methods that were previously developed and tested for investigating multireference electronic structures and reaction barrier heights. The multi-step molecular mechanism involves the reactions of *N,N*-dimethylsulfamide with hypobromous acid, produced by the ozonation of naturally-occurring bromide, and with ozone. This leads to an anionic intermediate that resembles a fragile complex between an electrophilic nitrosyl bromide (BrNO) molecule and an electron-rich dimethylaminosulfinate ($(\text{SO}_2)\text{N}(\text{CH}_3)_2(-)$) fragment. This loosely bound intermediate decomposes by two branches: an exothermic channel that produces NDMA, and an entropy-driven channel giving non-NDMA products.

In the last chapter, I computationally investigate the molecular pathways that lead from biogenic sulfur-containing compounds (thiols, polysulfides, and thioethers) to carbonyl sulfide (OCS) in the ocean. OCS ventilates from the oceans to the atmosphere, where it is directly implicated in the cloud condensation nuclei and in the formation of the stratospheric sulfate layer. However, the predominant molecular sources of OCS in the oceans are unknown, and previously reported experimental results suggested that thiyl/sulfhydryl radicals could play a key role in both the photochemical and non-photochemical production pathways of OCS. Quantum chemical modeling and reaction kinetics simulations are applied to study the complex molecular reactions leading to OCS in water. Hypothesized reaction mechanisms involving thiyl/sulfhydryl radicals and CO are assessed with density functional theory electronic structure methods. These results show that thiyl radicals, which can be produced from the oxidation of thiolates or possible from the bond cleavage of dimethylsulfide,

are key precursors of OCS in seawater. Hydrogen sulfide and polysulfide species such as HS^- , S^{2-} , S_2^{2-} , and S_2^{2-} are likely involved in the formation of OCS in ocean surface as well. APEX photochemical models reveal that the transient species, Br_2^- , plays a main role in the phototransformation of dimethylsulfide, methionine, cysteine, and glutathione, whereas CO_3^- could play a significant role in the photodegradation of cysteine and glutathione at low concentrations of DOC. The results of the study have implications for our understanding of the role of OCS in ocean biogeochemistry and climate.

Keywords: quantum chemical methods, DFT, thermochemistry, coupled cluster methods, solvation, disinfection byproducts, NDMA, chloramines, bromamines, carbonyl sulfide.

Riassunto

In questa tesi sono state studiate con metodi quantomeccanici la termodinamica e la cinetica di reazioni che coinvolgono specie reattive in fase acquosa. A causa dell'elevata reattività, infatti, molte specie molecolari transienti sono difficili da analizzare in laboratorio. Per contro, l'applicazione di metodi computazionali permette di studiare la natura chimica e la reattività di queste molecole in acqua.

Il primo capitolo concerne la struttura elettronica e la termodinamica in fase gas di clorammine, bromammine e bromoclorammine. Queste ammine inorganiche sono potenti ossidanti che vengono generati dalle reazioni dell'ammoniaca con l'acido ipocloroso e l'acido ipobromoso, durante processi di disinfezione delle acque. Le clorammine, le bromammine e le bromoclorammine sono specie assai reattive e partecipano in reazioni che portano alla formazione di prodotti di disinfezione tossici per l'uomo. Nonostante la loro rilevanza in ambito della chimica di disinfezione e nella biochimica, la stabilità e la distribuzione di queste ammine in acqua non possono essere studiate estensivamente in laboratorio. Per questo ho sviluppato un protocollo computazionale, chiamato TA14, che si basa su metodi compositi, quali i metodi Weizmann e la procedura Feller-Peterson-Dixon. Il protocollo TA14 prevede l'applicazione di una sequenza sistematica di metodi coupled cluster fino al livello CCSDTQ al fine di valutare i contributi statici e dinamici dell'energia elettronica di correlazione. Nel protocollo sono anche inclusi i seguenti contributi all'energia elettronica totale: contributi di energia di correlazione di valenza, contributi relativistici scalari e di accoppiamenti spin-orbita e, infine, le vibrazioni anarmoniche calcolate con il metodo VPT2. Grazie al metodo TA14, ho potuto calcolare le energie di atomizzazione in fase gas, le entalpie di formazione e le energie libere di formazione delle clorammine, delle bromammine e delle bromoclorammine con accuratezza di 1-3 kJ mol⁻¹. Un'attenta analisi delle componenti dell'energia di atomizzazione delle ammine ha rivelato che i legami N-Cl e N-Br sono costituiti per lo più da forze di correlazione elettronica, come è mostrato dai contributi energetici Hartree-Fock prossimi allo zero o addirittura negativi. Per esempio, la componente Hartree-Fock dell'energia di atomizzazione, TAE_{HF} , risulta essere negativa per le molecole NBr_3 e NBr_2Cl . Ciò implica che queste molecole non si sarebbero formate se non grazie alla presenza di queste forze di energia di correlazione. Queste clorammine, bromammine e bromoclorammine sono infatti potenti nucleofili che possono decomporsi piuttosto facilmente per produrre specie radicaliche in acqua.

Nel secondo capitolo ho simulato gli equilibri in acqua delle clorammine, bromammine e bromoclorammine. Ho pertanto combinato i risultati dei calcoli in fase gassosa del secondo

capitolo con nuove energie libere di solvatazione di queste specie qui calcolate. Le energie di solvatazione sono state calcolate utilizzando sia il modello di solvatazione implicita SMD, sia il modello di solvatazione continua sviluppato da Bryantsev et al. recentemente. La media dei valori prodotti da due approcci computazionali è affetta da un'incertezza di 3.3 kJ mol^{-1} nella ΔG_{solv}^* per un set di molecole strutturalmente simili alle ammine e contenenti H, N, O e Cl. Prendendo in considerazione sia le incertezze relative alle energie in fase gassosa sia le incertezze delle energie di solvatazione, le energie libere di formazione delle clorammine, bromammine e bromoclorammine da me calcolate hanno un'accuratezza totale di $6\text{-}7 \text{ kJ mol}^{-1}$. Le energie libere di formazione sono proprietà termodinamiche chiave per investigare processi di reazione che coinvolgono queste ammine durante la disinfezione delle acque potabili. Ho quindi utilizzato questi nuovi dati per determinare le costanti di equilibrio delle reazioni di formazione delle clorammine, bromammine e bromoclorammine in acqua. Le costanti di equilibrio di queste reazioni sono ora disponibili e potranno essere incluse in modelli cinetici che simulano i processi di disinfezione i quali, quindi, risulteranno più accurati.

Nel terzo capitolo ho studiato in dettaglio il meccanismo di reazione che dalla *N,N*-dimetilsulfammide porta alla *N,N*-nitrosodimetilammina (NDMA), un noto agente carginogeno, in seguito all'ozonizzazione di acque potabili contenenti tracce di bromuro. Lo studio di tale meccanismo di reazione comporta multiple sfide, in quanto prevede l'analisi di strutture elettroniche aventi carattere multireferenziale, include lo studio di intermedi e di strutture corrispondenti a stati di transizione che sono ampiamente solvatati, e richiede lo studio di una reazione di migrazione intermolecolare. Per descrivere questo complesso meccanismo di reazione, sono stati condotti degli esperimenti stopped-flow in combinazione con simulazioni di meccanica quantistica. I funzionali della densità che ho adottato per studiare la struttura elettronica delle molecole aventi carattere multireferenziale, come ozono, addotti contenenti ozono e stati di transizione sono M05 e B2PLYPD. I primi passi della reazione sono costituiti dagli attacchi dell'acido ipobromoso (prodotto dell'ozonizzazione di bromuri presenti nell'acqua potabile) e dell'ozono sulla *N,N*-dimetilsulfammide; da questi primi passi, si forma un addotto anionico simile ad un complesso molecolare contenente un frammento elettrofilico BrNO e un frammento $((\text{SO}_2)\text{N}(\text{CH}_3)_2(-))$ elettron-ricco. Dai risultati delle simulazioni questo complesso risulta assai fragile, tant'è che si decompone velocemente seguendo due cammini preferenziali: un cammino esotermico che produce la NDMA e un cammino favorito entropicamente che conduce a prodotti diversi dalla NDMA.

Nel quarto ed ultimo capitolo ho analizzato i meccanismi di reazione che portano alla formazione del solfuro di carbonile negli oceani a partire da molecole contenenti zolfo, quali tioli, polisolfuri e tioeteri. Il solfuro di carbonile è estremamente reattivo in acqua (con un tempo di emivita di 2 giorni), ma persiste in troposfera per un tempo di emivita di circa 8 mesi. Dagli oceani, infatti, si trasferisce nella troposfera e da qui viene trasportato nella stratosfera, dove si decompone contribuendo alla formazione dello strato di particelle di solfato stratosferico. Nonostante gli oceani contribuiscano sostanzialmente alla concentrazione atmosferica di solfuro di carbonio, i meccanismi di formazione di questo composto negli oceani non sono del tutto noti. Le uniche informazioni a disposizione derivano da precedenti

studi sperimentali hanno ipotizzato che radicali derivanti da tioli o polisolfuri possano avere un ruolo chiave nella produzione fotochimica e non-fotochimica del solfuro di carbonile. Ho quindi modellizzato la termodinamica e la cinetica di reazioni di formazione del solfuro di carbonile che coinvolgono radicali sulfurici e il monossido di carbonio. Ho infine dimostrato che radicali allo zolfo, derivanti dalla decomposizione fotochimica di tioli, polisolfuri e tioeteri, sono precursori del solfuro di carbonile negli oceani. Inoltre, grazie ai risultati dello studio fotochimico basato sul software APEX, ho dimostrato radicali anioni quali Br_2^- e CO_3^- sono coinvolti nei processi di decomposizione fotochimica del dimetil solfuro, metionina, cisteina e glutathione, e che quindi possono partecipare alla formazione del solfuro di carbonile negli oceani. I risultati di questo studio computazionale contribuiscono sostanzialmente alla comprensione del ruolo del solfuro di carbonile nella biogeochimica oceanica.

Parole chiave: metodi quantomeccanici, teoria del funzionale della densità, termochimica, coupled cluster, solvatazione, prodotti di disinfezione, NDMA, clorammine, bromammine, solfuro di carbonile.

Contents

Acknowledgments	i
Abstract (English/Italian)	iii
1 Introduction	1
1.1 Introduction	1
1.1.1 Quantum chemical modeling approaches for reactive molecules arising in aquatic systems	2
1.1.2 Quantum chemistry modeling applied to reactive species arising in water disinfection chemistry	3
1.1.3 Molecular modeling of carbonyl sulfide, a natural marine compound that links ocean photochemistry with climate	4
2 Benchmark Thermochemistry of Chloramines, Bromamines, and Bromochloramines: Halogen Oxidants Stabilized by Electron Correlation	7
2.1 Abstract	8
2.2 Introduction	8
2.3 Methods	12
2.3.1 Selected Molecules of Study and Reference Data	12
2.3.2 Model Chemistries and Basis Sets	12
2.3.3 Geometries and frequencies	13
2.3.4 Electronic energies	13
2.3.5 Thermochemical Properties	17
2.3.6 Diagnostics for Nondynamical Correlation Effects	19
2.4 Results and Discussion	20
2.4.1 Total Atomization Energies	20
2.4.2 Importance of Nondynamical Correlation for Halamines	23
2.4.3 Comparison of Computed TAE_{0K} Values with Previous Experimental and Theoretical Data	23
2.4.4 Gas Phase Enthalpies of Formation at 0 K and at 298 K	26
2.4.5 Gibbs Free Energies of Formation at 298 K	29
2.5 Implications for Aqueous Chemistry of Chloramines and Bromamines	30
2.6 Acknowledgments	32

3	Equilibria and Speciation of Chloramines, Bromamines, and Bromochloramines in Water	33
3.1	Abstract	34
3.2	Introduction	34
3.3	Methods	36
3.3.1	Computational Estimates of Free Energies of Solvation	36
3.3.2	Implicit Solvent Models: Methods and Basis Sets	36
3.3.3	Cluster-continuum Solvent Models: Methods and Basis Sets	37
3.3.4	Computational Estimates of Aqueous pK_a	38
3.4	Results and Discussion	39
3.4.1	Evaluation of Solvent Models for Halogen Species and Amines.	39
3.4.2	Estimated Aqueous Standard Free Energies of Formation for Chloramines, Bromamines, and Bromochloramines	41
3.4.3	Aqueous Equilibrium Constants of Reactions that Produce to Chloramines, Bromamines, and Bromochloramines	43
3.5	Implications for Reaction Rate Constants	46
3.5.1	pK_a Values for Chloramines, Bromamines, and Bromochloramines: Theoretical Estimates	48
3.6	Acknowledgment	50
4	Molecular Mechanism of NDMA Formation from <i>N,N</i>-Dimethylsulfamide During Ozonation: Quantum Chemical Insights into a Bromide-Catalyzed Pathway	51
4.1	Abstract	52
4.2	Introduction	52
4.3	Materials and Methods	54
4.3.1	Selection of Model Chemistries	54
4.3.2	Computation of the Aqueous Free Energy of Reaction for Elementary Reaction Steps	55
4.3.3	Computation of Aqueous Reaction Gibbs Free Energies of Activation and Estimation of Reaction Rate Constants	57
4.3.4	Computational Estimates of Aqueous pK_a Values	58
4.3.5	Natural Population Analysis (NPA)	59
4.3.6	Experimental Determination of the Rate Constant for the Reaction of <i>HOBr</i> with <i>N,N</i> -Dimethylsulfamide	59
4.4	Results and Discussion	59
4.4.1	Quantum Chemical LFER for Estimation of pK_a Values of <i>DMS</i> , <i>Cl</i> – <i>DMS</i> , and <i>Br</i> – <i>DMS</i>	59
4.4.2	Reaction Steps <i>a</i> , <i>b</i> , <i>c</i> , and <i>d</i> in the Presence of Ozone and Bromide. Bromination of <i>DMS</i> versus <i>DMS</i> [−] , and Speciation Equilibria of <i>DMS</i> / <i>DMS</i> [−] and <i>BrDMS</i> / <i>BrDMS</i> [−]	60
4.4.3	Quantum Chemical Modeling of the rate constant of reaction step <i>b</i> . . .	63
4.4.4	Reaction Steps <i>e</i> and <i>f</i> . Oxidation of <i>DMS</i> and <i>DMS</i> [−] by Ozone	64

4.4.5	Reaction Step <i>g</i> . Can <i>Br</i> – <i>DMS</i> Undergo SO_2 Extrusion to Form <i>Br</i> – <i>UDMH</i> ?	64
4.4.6	Reaction Steps <i>h</i> , <i>i</i> , and <i>j</i> . Ozone Reaction with <i>Br</i> – <i>DMS</i> [–] (or <i>Cl</i> – <i>DMS</i> [–])	65
4.4.7	Cluster-Continuum Modeling of the Fragile Intermediate B and Subsequent Reaction Intermediates	66
4.4.8	Reactions of the Brominated Intermediate B: a Branching in the Pathway	66
4.4.9	Overall Interpretation of the Pathway	68
4.5	Implications for Other <i>NDMA</i> Pathways	70
4.6	Acknowledgments	71
5	Mechanisms of OCS Formation in Seawater from DMS, Biogenic Thiols, and Polysulfides	73
5.1	Abstract	74
5.2	Introduction	74
5.3	Methods	84
5.3.1	Model Chemistries and Basis Sets	84
5.3.2	Computational Estimates of Aqueous Phase Gibbs Free Energies of Reaction	84
5.3.3	Computational Estimates of Aqueous Phase Gibbs Free Energies of Activation	85
5.3.4	Aqueous Equilibrium Constants of Reactions Leading to OCS Formation	86
5.3.5	Aqueous Rate Constants of Reactions Leading to OCS Formation	87
5.3.6	Description of the Profile of the Reaction Potential Energy Surface (Relaxed Scan)	87
5.3.7	Natural Population Analysis to Estimate Atomic Charge Distribution	87
5.3.8	NPA spin density analyses to locate the unpaired electron in open shell systems	88
5.3.9	Photochemical Modeling with the Aqueous Photochemistry of Environmentally-occurring Xenobiotics (APEX) Software	88
5.4	Results and Discussion	92
5.4.1	Assignment of Error Bounds for the Theoretical Aqueous Thermochemical Properties	92
5.4.2	First Step of the OCS Formation: Formation of Thiyl/Sulfhydryl Radicals and Anions	96
5.4.3	The relative importance of different possible natural oxidants for marine sulfur species: APEX photochemical model results	103
5.4.4	Second Step of the OCS Formation: Reactions of Reactive Sulfur-containing Species with CO to produce OCS	109
5.5	Implications	115
5.6	Acknowledgments	117

Contents

6	Conclusions	119
6.1	Main Results	119
6.2	Main Challenges	119
6.3	Future Developments and Improvements	120
A	Appendix A	123
A.1	Supporting Information	123
A.1.1	Benchmark Thermochemistry of Chloramines, Bromamines, and Bromochloramines: Halogen Oxidants Stabilized by Electron Correlation - SUPPORTING INFORMATION	123
A.1.2	Equilibria and Speciation of Chloramines, Bromamines, and Bromochloramines in Water - SUPPORTING INFORMATION	128
A.1.3	Molecular Mechanism of <i>NDMA</i> Formation from <i>N,N</i> -Dimethylsulfamide During Ozonation: Quantum Chemical Insights into a Bromide-Catalyzed Pathway - SUPPORTING INFORMATION	136
A.1.4	Mechanisms of OCS Formation in Seawater from DMS, Biogenic Thiols, and Polysulfides - SUPPORTING INFORMATION	153
	Bibliography	193
	Curriculum Vitae	195

1 Introduction

1.1 Introduction

Aqueous short-lived reactive species play a crucial role in many domains, from water disinfection chemistry to the phototransformations of organic compounds in the ocean. For example, photochemical formation and decomposition of sulfur-containing species, including DMS, OCS, and H₂S, take place near the ocean surface and are mostly driven by short-lived reactive species. Reactive species that are used for water disinfection treatments contribute to the unintended production of toxic byproducts. For example, during ozonation of drinking water, bromide reacts rapidly with ozone, generating bromate,[1, 2, 3] a well-known carcinogenic species. Bromide can also become oxidized by ozone to generate hypobromous acid, which reacts with organic micropollutants, such as phenols and amines, as well as inorganic compounds, like ammonia.[4] However, the aqueous behavior and the speciation of these reactive species remain often difficult to study by experimental means due to their extremely high reactivity in water.

Quantum chemical modeling offers an alternative to explore reaction mechanisms involving reactive species in water. By taking advantage of quantum chemistry, aqueous equilibrium constants and kinetic constants can be predicted, molecular mechanisms involving short-lived reactive species can be explored, and linear free energy relationships between known experimental values and newly computed properties can be established. However, quantum chemistry has its own set of limitations. For example, halogen- and oxygen-containing reactive species, exhibit sometimes complex multireference electronic structures that can be difficult to treat computationally. Quantum chemical models are thus complementary to experiment; we can take advantage of available experimental values and combine them together with computed properties, enabling us to gain information and insights that are difficult to obtain by experimental means only.

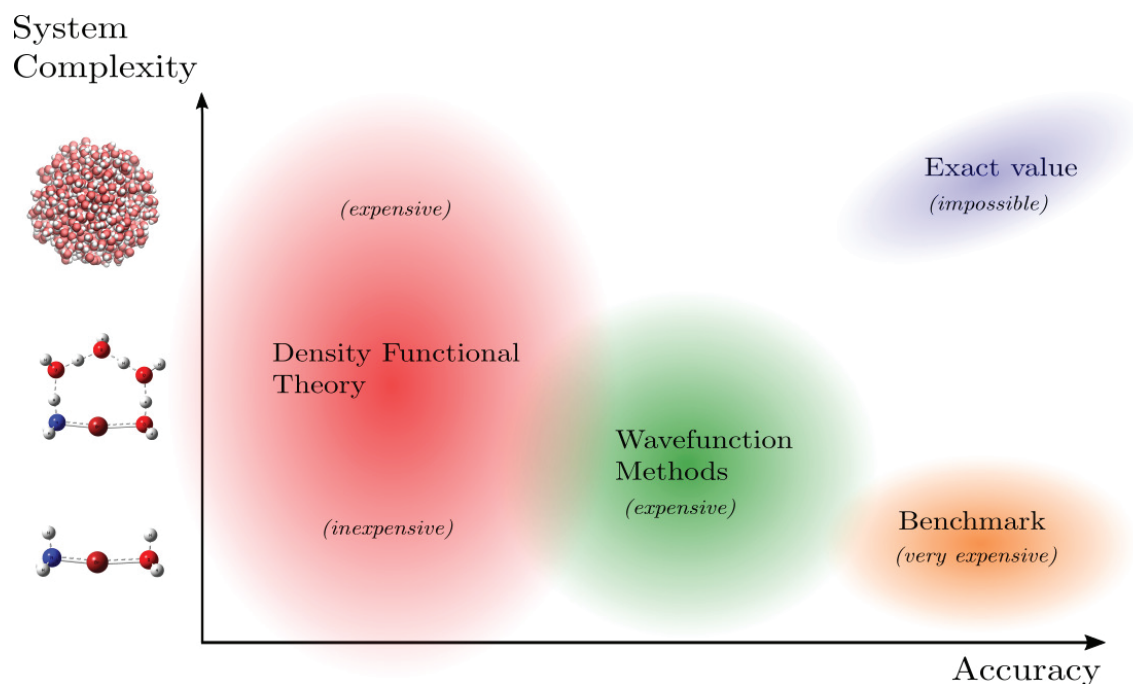


Fig. 1.1 Qualitative scheme of the applicability of the quantum chemical methods employed in this thesis.

1.1.1 Quantum chemical modeling approaches for reactive molecules arising in aquatic systems

I have applied density functional theory (DFT) methods and wave function methods to describe the behaviors of reactive molecules in aqueous solution. The choice of the proper methods to compute aqueous equilibrium constants and rate constants of reactions involving short-lived reactive species depends on the size of the system, the electronic structure of the molecular system investigated, and the uncertainty that can be accepted in the prediction of the thermodynamic and kinetic properties (Figure 1.1). The electronic structures of aqueous reactive species, such as halogen oxidants, ozone, or radical species, often exhibit multireference character.[5, 6] This means that the reference configuration (defined as the Hartree-Fock wavefunction) that describes the electron configuration of such systems is affected by quasidegeneracy and is not well-described by a single predominating configuration.[7] A well-known example is the multireference electronic structure of ozone that is formally a closed-shell singlet with the diradical character of about 33%.[8] For these cases, high-level wavefunction methods, which can take into account the non-dynamic electronic correlation energies of multireference electronic structures, are more appropriate than DFT approaches that are single-reference methods.[5] However, the size (number of electrons being modeled) of these reactive systems make the wavefunction simulations quite expensive in terms of computational cost. Based on the considerations above, I have employed DFT methods to predict the geometries, thermodynamic properties, and kinetics of molecular systems with more than 4 atoms of the second row of the periodic table. In this thesis,

expensive wavefunction methods have been applied to study molecules up to 4 atoms and 112 electrons that exhibit multireference character.

In this thesis, quantum chemical methods have been selected on a case by case basis. DFT methods have been employed to investigate the molecular pathway that leads from *N,N*-dimethylsulfamide to *N,N*-nitrodimethylamine during oxidative water treatment and the reaction mechanisms of carbonyl sulfide formation from sulfur-containing anions, radicals, and radical anions in the ocean. The size of the molecules involved in the mechanisms was the key factor in making the choice of the DFT method. Total atomization energies and gas phase free energies of formation of chloramines, bromamines, and bromochloramines were assessed with 1-3 kJ mol⁻¹ accuracy. A composite wavefunction method was employed in this case since the molecules investigated were small (up to 4 atoms, and up to 112 electrons). Each case study presents unique challenges and quantum chemical methods have been selected accordingly.

1.1.2 Quantum chemistry modeling applied to reactive species arising in water disinfection chemistry

Disinfection is essential to maintain hygienic conditions and guarantee chemical water quality in drinking water and swimming pool waters. Even though disinfectants target the microbial pathogens that can cause waterborne diseases, they produce potentially toxic disinfection byproducts (DBPs), only some of which have been identified and regulated. Each of the most common disinfectants (chlorine, ozone, chlorine dioxide, and chloramines) can result in the production of different types of DBPs by reacting with natural organic matter and other micropollutants.[9] For example, trihalomethanes (THMs) include regulated carcinogenic and/or mutagenic DBPs that have been detected in chlorinated, chloraminated, and ozonated drinking waters.[9] Halogenated acetic acids (HAAs) are formed by disinfection of natural waters with chlorine, chlorine dioxide, ozone, and chloramines.[9] HAAs can be mutagenic and irritate the skin, eyes, and mucose membranes.[10] Trichloramine is a DBP formed in presence of both chlorine and nitrogen-containing compounds, and is directly involved with the swimming-pool-associated asthma. Chloramination of drinking water promotes the formation of nitrosamine, including the EPA regulated *N*-nitrosodimethylamine (NDMA). Ozonation has been proposed as an alternative to chlorine-containing disinfectants, since ozone reduces the amount of THMs and HAAs; however, in presence of bromide, ozonation leads to formation of bromate, which has been identified as a carcinogenic in laboratory animals,[11, 12] as well as other potentially dangerous organo-brominated compounds.[13]

Despite the compelling health issues caused by DBPs in drinking water, the molecular pathways leading to the formation of the DBPs are often undetermined. Extremely reactive and short-lived intermediates are involved in the formation of DBPs and are often difficult to detect and investigate by experimental means only, precluding a complete understanding of the chemical pathways leading to DBPs in drinking water and swimming pool water. Quantum

chemical models can be applied to elucidate the reaction mechanisms of formation of these potentially toxic DBPs. By taking advantage of computational tools, aqueous thermodynamic properties, rate constants, and intermediate structures of molecular mechanisms of reactions leading to the formation of dangerous DBPs can be assessed in order to more fully understand the chemistry that takes place during water disinfection.

I have employed quantum chemical modeling tools to investigate the molecular mechanisms, the thermodynamics, and the kinetics of aqueous reactions leading to DBPs. In the second and third chapters, I have employed different computational techniques to investigate the speciation and the behavior of halamines, halogen oxidants that are implicated in the formation of DBPs in water facilities. In the fourth chapter, I apply density functional theory methods to elucidate each step of the molecular mechanism that leads from *N,N*-dimethylsulfamide to NDMA during ozonation of bromide-containing drinking water.

1.1.3 Molecular modeling of carbonyl sulfide, a natural marine compound that links ocean photochemistry with climate

Carbonyl sulfide links oceanic and atmospheric sulfur chemistry with climate change

Carbonyl sulfide (OCS) is a volatile gas that links ocean biology, ocean photochemistry, and climate, creating the potential for feedbacks in the ongoing changes of the ocean and climate systems. Oceanic OCS is produced by photochemical and non-photochemical pathways most likely involving sulfur-containing organic species, generated by phytoplankton activity.[14, 15, 16, 17, 18, 19, 20, 21, 22] Oceanic OCS ventilates into the atmosphere where it is oxidized to sulfate and contributes to cloud condensation nuclei formation.[21, 23] Sulfur chemistry in the ocean and atmosphere are tied to climate in the so-called CLAW hypothesis,[24, 25] in which ocean phytoplankton activity and cloud formation are connected via the air-sea gas exchange fluxes of sulfur-containing compounds. According to the CLAW hypothesis,[24, 25] changes in oceanic OCS production may therefore influence cloud cover, which in turn would affect phytoplankton growth and OCS production. It thus represents a potential feedback between ocean biogeochemistry and the climate system.

Carbonyl sulfide contributes to the Junge aerosol layer

In 1961, Junge et al. discovered a stratospheric aerosol layer mainly composed of sulfate particles.[26] Crutzen and coworkers[27, 28] showed that OCS is the major source of the sulfate that composes the Junge aerosol layer (Figure 1.2). Since OCS is relatively inert in the troposphere, having an half-life time of more than 8 months, it can be transported to the stratosphere where it undergoes photodissociation through the absorption of ultraviolet sunlight.[27] The photodecomposition of OCS to CO and atomic S is the rate determining step of the mechanism of OCS loss and takes place at $\lambda \leq 289.5$ nm.[29] Therefore, the light

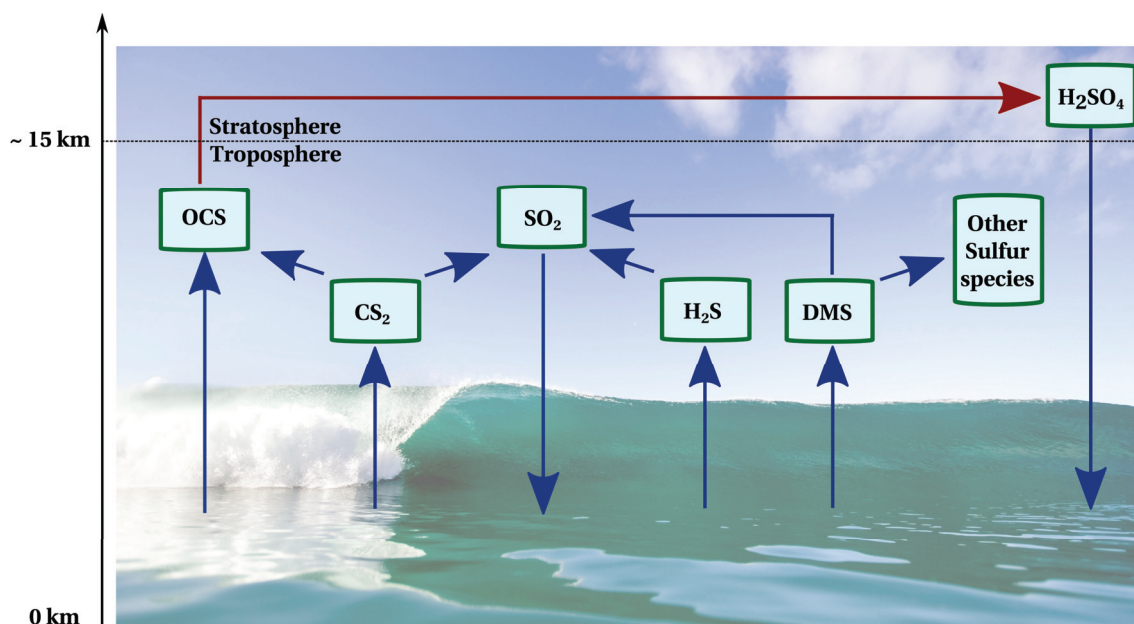


Fig. 1.2 Qualitative scheme of the important atmospheric pathways for reduced sulfur species originating in the ocean. Tropospheric OCS ventilates into the stratosphere, where its oxidation leads to the sulfuric acid, contributing to acid precipitation and cloud condensation nuclei.

absorption of OCS in the troposphere is quite weak, whereas in the stratosphere OCS quickly photodissociates.

Oceans and tropospheric CS₂ are natural sources of OCS in the atmosphere

The reaction of atmospheric CS₂ with OH radicals leads to the formation of OCS in the atmosphere.[30, 31, 29] Additionally, sunlight-driven transformations of sulfur precursor compounds produced by phytoplankton take place in the surface ocean water column, leading to OCS. Oceanic OCS production from organosulfur compounds is enhanced under the influence of light,[18] and this behavior might be explained by a molecular pathway involving radicals in the formation of OCS.[17, 18, 32, 33] However, the molecular mechanisms that lead to OCS in the ocean remains unclear. Without an understanding of the precursors, species, and mechanisms involved in oceanic OCS formation, it is difficult to make projections about how OCS production may change in the future, and it is difficult to fully assess how OCS production is coupled with changes in the ocean system.

In the fifth chapter, I focus on modeling the reaction mechanisms that produce OCS from sulfur-containing precursors such as biogenic thiols, DMS, and polysulfides. I have considered radical and anionic pathways involving sulfur-containing compounds and CO. By analyzing the thermodynamic properties and the kinetics of hypothesized reactions, I have identified several feasible pathways that might lead to OCS in the ocean.

2 Benchmark Thermochemistry of Chloramines, Bromamines, and Bromochloramines: Halogen Oxidants Stabilized by Electron Correlation

Daniela Trogolo^a and J. Samuel Arey^{*a,b}

Adapted from:

Phys. Chem. Chem. Phys., 2015,**17**, 3584-3598

DOI:10.1039/C4CP03987D

Contributions:

I am the main author of this chapter. I carried out all quantum chemical simulations. Sam Arey provided guidance in the computational methods and interpretation of results, and he substantially contributed to the manuscript writing and editing.

^a Environmental Chemistry Modeling Laboratory, École Polytechnique Fédérale de Lausanne (EPFL), Station 2, 1015 Lausanne, Switzerland.

^b EAWAG, Swiss Federal Institute of Aquatic Science and Technology, Dübendorf, Switzerland.

2.1 Abstract

Chloramines, bromamines, and bromochloramines are halogen-containing oxidants that arise from the reaction of hypohalous acids with ammonia in water. Although relevant to both water disinfection chemistry and biochemistry, these molecules are difficult to study in the laboratory, and their thermochemical properties remain poorly established. We developed a benchmark level *ab initio* calculation protocol, termed TA14, adapted from the Weizmann theory and Feller-Peterson-Dixon approaches to determine the molecular structures and thermochemical properties of these compounds. We find that the halamine molecules are bound largely, and in some cases entirely, by electron correlation forces. This presumably explains their high reactivity as electrophilic oxidants. We provide computed heats of formation at 0 K ($\Delta_f H_{0K}^0$) and at 298 K ($\Delta_f H_{298K}^0$) and Gibbs free energies of formation at 298 K ($\Delta_f G_{298K}^0$) for the 9 inorganic chloramines, bromamines, bromochloramines in gas phase. Based on comparisons to previous theoretical and experimental data for a set of 11 small molecules containing N, O, H, Cl, and Br, we propose uncertainties ranging from 1 to 3 kJ mol⁻¹ for computed thermodynamic properties of the halamines. Reported thermochemical data enable the determination of equilibrium constants for reactions involving halamines, opening possibilities for more quantitative studies of the chemistry of these poorly understood compounds.

2.2 Introduction

Halogen-containing oxidants have long received attention, due to their role in processes affecting human health and environmental hygiene.[34, 35] Chlorination and chloramination are the predominant methods of drinking water disinfection in the United States.[36, 37, 38] Chlorine is commonly applied either as gaseous Cl₂, which dissolves in water at room temperature, or as a salt of hypochlorite, OCl⁻:



Cl₂ and hypochlorite both lead to the formation of hypochlorous acid, HOCl (pK_a=7.5 [39]). In ammonia-containing water, HOCl undergoes substitution reactions with ammonia, following a well-known process that leads to the formation of chloramines:[40, 41, 42, 43, 44]





Monochloramine can be directly added to water during drinking water disinfection treatment.[38, 36, 37, 45] Operationally, these reactions are controlled by the ratio of chlorine to ammonia nitrogen, pH, temperature, and the presence of natural acid catalysts as phosphate, sulfate, and carbonate.[44, 46]

Bromamines and bromochloramines may arise as well, in bromine-containing waters.[47, 48, 49, 50, 51, 52, 53, 54, 55] During disinfection treatment, bromide can become oxidized to hypobromous acid/hypobromite, contributing to the formation of bromamines and bromochloramines in water.[4] The role of bromide in monochloramine decay was considered in the kinetic model provided by Vikesland et al.[46] Lei et al. reported on the formation kinetics of bromamines,[56] and Luh and Mariñas recently investigated the formation kinetics of bromochloramines, providing more information on their aqueous chemistry.[57]

Chloramines and bromamines are implicated in the formation of potentially toxic disinfection byproducts (DBPs) during water treatment.[58, 36, 37, 59, 60] Chloramines can undergo substitution and oxidation reactions involving natural organic matter.[61] Snyder and Margerum[62] and then Isaac and Morris[63, 64] showed that monochloramine could transfer chlorine to organic nitrogen compounds by general acid catalysis. During water disinfection, monochloramine can play a direct role in the formation of halonitriles, halonitroalkanes, and nitrosamines.[65] Monochloramine reactions with dissolved organic matter can also lead to production of haloacetic acids.[66] The reaction between dichloramines and organic nitrogen precursors such as dimethylamine can explain the observed production of *N*-nitrosodimethylamine (NDMA) and other nitrosamines,[67, 68] which are probable human carcinogens according to the US Environmental Protection Agency. Fewer data are available concerning the role of bromamines and bromochloramines in reactions that lead to DBP formation. Le Roux et al. reported an enhancement of the formation of NDMA from reactions between bromine-containing oxidant species and tertiary amines or dimethylamine, suggesting a direct role of bromamines.[59] Monobromamine and dibromamine were also found to react with cyanide ion (CN^-) leading to the formation of CNBr , a volatile DBP.[60] According to Valentine,[69] the bromine atom of bromochloramine is highly reactive. Despite their considerable roles in disinfection byproduct formation, the speciation of chloramines, bromamines, and bromochloramines is not fully known, and this impedes mechanistic studies of DBP formation, which can involve many potential reaction pathways.

Due to the volatility of chloramines,[70, 71] these molecules also have implications in the poor air quality in indoor swimming pools. According to Richardson et al., [72] NH_2Cl , NHCl_2 , NCl_3

can escape into the atmosphere of swimming pool environments. They largely contribute to the typical smell and irritant properties of the air of these facilities.[73]

Chloramines and bromamines are also released extracellularly by activated mammalian eosinophils and neutrophils (white blood cells).[74, 75] The haem enzymes eosinophil peroxidase and myeloperoxidase catalyse the production of HOBr and HOCl that can react with extracellular matrix, including proteins, proteoglycans, and other nitrogen organic compounds, generating substituted bromamines and chloramines.[76, 75, 77, 78, 79] The N-bromination reactions promoted by HOBr, which exhibits higher rate constants than the corresponding reactions by HOCl, may damage tissue, affecting cellular and tissue function, in inflammatory diseases such as asthma.[77] Moreover, the so-generated halamines can undergo one-electron reduction processes that cleave the N-X (where X = Cl or Br) bond.[80, 81] Indeed, redox-active metal ions and superoxide radicals can reduce N-halogenated species, leading to the formation of N-centered radicals and radical bromine atoms.[81]

Despite these concerns, halamine speciation is not fully understood and thus the reactivities of halamines with components of natural waters and biological fluids are difficult to study. Halamines are unstable at neutral pH and autodecompose by a complex set of reactions only partially known.[44, 61, 46] As a consequence, kinetic experiments on chloramine formation cannot be always successfully conducted under realistic water conditions found in water treatment facilities.[44] Additionally, sampling and analysis of the chloramines in the atmosphere is difficult, requiring specific sampling devices and analytical methods.[73] Due to these challenges, fundamental thermochemical properties of halamines have not been extensively determined with experiments either in gas phase or in aqueous phase.

Quantum computational methods could offer more tractable estimates of the thermochemistry of chloramines, bromamines, and bromochloramines. However existing work is limited. In 1997, Milburn et al. [82] reported theoretical enthalpy of formation values for inorganic chloramines at MP4[83, 84, 85, 86] and QCISD(T)[87] levels of theory. More recently, Rayne and Forest[88] estimated gas phase standard state enthalpies of formation at 298 K ($\Delta_f H_{298K}^0$) for 398 species that contained the elements hydrogen through bromine at the G4[89] level, including NH_2Cl , NHCl_2 , NCl_3 , NH_2Br , and NHBBr_2 . This approach produced a MAD (mean absolute deviation) of $2.68 \text{ kcal mol}^{-1}$ with respect to experimental $\Delta_f H_{298K}^0$ values for 144 compounds. More recently, Rayne and Forest[90] assessed new $\Delta_f H_{298K}^0$ values for NH_2Cl , NHCl_2 , and NCl_3 using G4MP2.[91] These estimates likely have about 2-3 kcal mol^{-1} uncertainties. In 2011, monochloramine was included in the W4-11 dataset:[92] this is the only halamine whose total atomization energy was determined with benchmark accuracy. Finally, thermochemistry estimates remain absent for NBr_3 and for the bromochloramines.

Calculations of energies for compounds containing halogens are not without their difficulties. Therefore chloramines, bromamines, and bromochloramines require a carefully constructed *ab initio* computational recipe, with attention to several fine quantum mechanical effects, in order to obtain accurate thermochemistry data. Since these inorganic molecules contain

the heavy elements chlorine and bromine, fine quantum mechanical effects must be evaluated properly if sub-kcal mol⁻¹ or sub-kJ mol⁻¹ energies are sought. Indeed, the "gold standard of quantum chemistry", or CCSD(T) with complete basis-set limit extrapolation, has to be combined with core valence correlation energy calculations and relativistic effects in order to predict accurate thermochemistry for chlorine- and bromine-containing molecules.[93, 94, 95, 96] For molecules with elements from the first and second rows, relativistic and core-correlation contributions to bond energies are relatively small,[93, 97, 95] but these components increase with the size of the atoms involved. For example, Feller et al. reported scalar relativistic contributions of -0.14 kcal mol⁻¹ and -0.54 kcal mol⁻¹ to the total atomization energies (TAE) of Cl₂ and Br₂, respectively.[95] Core-valence correlation components of the TAEs of these molecules were -0.13 kcal mol⁻¹ and 0.29 kcal mol⁻¹, respectively.[95] Post-CCSD(T) energy contributions may also be important. The magnitude of post-CCSD(T) effects is small for systems that are reasonably described by a single reference configuration.[93] However, for species affected by severe nondynamical correlation, post-CCSD(T) contributions to the TAE may exceed 1 kcal mol⁻¹. [98, 95] Halogen-containing molecules often exhibit severe nondynamical correlation effects; examples include F₂, FO₂, F₂O₂, FO, F₂O, OClO, and ClOO.[97] Hence, for chloramines and bromamines, we suspected that an extension of the correlation treatment beyond CCSD(T) may be needed.

Specialized methods, such as the HEAT (High-accurate extrapolated *ab initio* thermochemistry), [99, 100, 101] Weizmann-*n*, [102, 103, 93] and Feller-Peterson-Dixon (FPD) [95, 96, 104] protocols have been designed to estimate accurate thermochemistry even for difficult cases as those described above. W4 provided thermochemical data up to chlorine-containing molecules with a 'benchmark accuracy' of 1 kJ mol⁻¹ (0.24 kcal mol⁻¹). [93] The HEAT target accuracy was sub-kJ mol⁻¹ for first-row systems, whereas the FPD approach suggested an accuracy of 0.2 to 0.4 kcal mol⁻¹ for small molecules up to the third row. The FPD protocol is more flexible, being developed molecule-by-molecule, and has been applied up to bromine-containing species, including BrO, Br₂, HBr, BrF, and BrCl.[95] These computational methods (Weizmann-*n*, FPD) are commonly recognized as benchmarks for small molecules. Although we were inspired by these established methods, we did not apply any of these protocols in their prescribed formulation. The W3 method does not include second order spin-orbit corrections, and W3 treats core-valence correlation energy with only the MTSmall basis set. These choices would not be appropriate for benchmark thermochemistry of molecules containing bromine. On the other hand, the more rigorous W4 and FPD procedures were intractably expensive for the not-so-small halamine species, with available algorithms and hardware. Hence the halamines warranted the development of a tailored computational recipe for the determination of high-accuracy thermochemistry.

In the present study, we calculated high-quality benchmark gas-phase thermochemical data, including total atomization energies, heats of formation at 0 K and at 298 K, and Gibbs free energies of formation at 298 K for chloramines, bromamines, bromochloramines, and other related small halogenated molecules. For this purpose, we developed a computational protocol, termed as TA14 in the remainder of the manuscript, which is adapted from the high-

quality HEAT, Weizmann-*n*, and Feller-Peterson-Dixon (FDP) procedures. TA14 combines a systematic sequence of coupled cluster methods up to CCSDTQ with large correlation consistent basis sets and includes relativistic effects, core-valence electron correlation, and diagonal Born-Oppenheimer correction, aiming for kJ mol^{-1} accuracy with affordable computing time. A test set of small compounds containing chlorine and bromine was chosen to briefly evaluate the performance of the protocol, and comparisons with high-quality experimental values and previously published computational benchmarks are made. This leads to the first published set of high accuracy thermochemistry data for chloramines, bromamines, and bromochloramines.

2.3 Methods

2.3.1 Selected Molecules of Study and Reference Data

Our chemical set comprised 20 neutral inorganic molecules, divided by chemical composition into non-halamines (set A) and halamines (set B). Set A includes H_2 , N_2 , O_2 , Cl_2 , Br_2 , HCl , HBr , HOCl , HOBr , H_2O , and NH_3 . Set B contains NH_2Cl , NHCl_2 , NCl_3 , NH_2Br , NHBr_2 , NBr_3 , NHBrCl , NBrCl_2 , and NBr_2Cl .

Experimental enthalpies of formation and experimental total atomization energies were available in the literature for the entire set A. Experimental total atomization energies at 0 K, TAE_{0K}^{Expt} , and heats of formation at 0 K, $\Delta_f H_{0K}^{0,Expt}$, and at 298 K, $\Delta_f H_{298K}^{0,Expt}$, are taken from several sources: CODATA,[105] the Active ThermoChemical Tables,[106, 107] JANAF thermochemical database,[108] and NIST Computational Chemistry Comparison and Benchmark DataBase (CCCBDB).[109] In cases where several experimental values were available for the same molecule, the value with the lowest listed uncertainty was selected.

2.3.2 Model Chemistries and Basis Sets

Hartree-Fock, CCSD,[110] and CCSD(T)[110, 111, 112] calculations were carried out using the program CFOUR.[113] CCSDT,[114, 115, 116] CCSDT(Q),[117] and CCSDTQ[118, 119, 120] calculations were conducted with the MRCC package[121] interfaced to the CFOUR program suite. Scalar relativistic calculations and B2PLYPD[122, 123] frequency analysis were conducted using Gaussian09.[124] Second-order molecular spin-orbit components were computed with NWchem.[125]

The basis sets employed in all calculations belong to the correlation consistent family of Dunning and co-workers [126, 127, 128, 129, 130] and are abbreviated PVXZ, AVXZ, and AWCVXZ for cc-pVXZ, aug-cc-pVXZ, and aug-cc-pWCVXZ basis set types, respectively, throughout the remainder of the article. The aug-cc-pV(X+d)Z basis sets employed by *Wn* methods were not available for bromine. Complete basis-set limit results were achieved using different extrapolation formulae, as explained below.

2.3.3 Geometries and frequencies

With three exceptions, all reference geometries were obtained at the all-electron (AE)-CCSD(T)/AVQZ level. For NBrCl₂, NBr₂Cl, and NBr₃, geometries were optimized at the all-electron (AE)-CCSD(T)/AVTZ level. For open-shell species, single-point energy calculations were based on UHF reference wave functions, whereas the default restricted Hartree-Fock reference was employed for the closed-shell molecules. Due to high spin contamination using an unrestricted reference, O₂ was treated as a restricted open-shell species. The Watts-Gauss-Bartlett [131] (e.g., CFOUR/ACESII) definition of restricted open-shell CCSD(T) was applied. These reference geometries were used for electronic energy calculations, and they are given in Table A.1 of the Appendix for all molecules.

Harmonic and anharmonic zero-point vibrational energies were computed at 298 K using analytic second derivatives for the B2PLYPD/AVQZ model chemistry. The VPT2[132, 133] approach was applied to compute the anharmonic corrections as implemented in Gaussian09. Anharmonic frequencies are reported in Table A.2 of the Appendix for all the halamines and the hypohalous acids. Since Gaussian09 does not allow the calculations of anharmonic frequency contributions for linear molecules, we employed B2PLYPD/AVQZ for harmonic frequency calculations and combined these with experimental anharmonic contributions for diatomic molecules.[134, 135, 136] Molecular rotations were determined assuming rigid geometries, thus rotations were assumed uncoupled to vibrations. Based on these frequency data and corresponding B2PLYPD/AVQZ geometries, zero-point vibrational energies and thermal contributions to the gas phase enthalpy and gas phase Gibbs free energy were computed at 298 K in the NVT ensemble for all studied molecules.[137]

2.3.4 Electronic energies

Our methodology for computing the electronic energy was adapted from the recently developed W3, W4, and FPD protocols,[103, 93, 95] and it is aimed to being an appropriate compromise between computing cost and basis set convergence. By including all terms that can contribute to the energy at the sub-kJ mol⁻¹ level, the TA14 protocol allows the determination of high quality electronic energies and thermodynamic properties of halogenated compounds. The protocol applied to compute the electronic energy is purely *ab initio*: no fitted parameters or empirical terms are included.

Table 2.1 Comparison of the TA14 Computational Protocol with Other Benchmark Thermochemistry Protocols

Component	FPD _[95] ^d	W3 _[103]	W4 _[93]	TA14
Reference geometry	FC-CCSD(T) / AV6Z	FC-CCSD(T) / pV(Q+d)Z	FC-CCSD(T) / pV(Q+d)Z	AE-CCSD(T) / AVQZ
Anharmonic ZPVE	Expt data	CCSD(T) /VTZ+1 ^a	CCSD(T) /VTZ+1 ^a	B2PLYPD /AVQZ ^b
Electronic Energy				
HF extrapolation	AV6Z	AV(Q,5)+dZ	AV(5,6)+dZ	AV(Q,5)Z
Valence CCSD extrapolation	AV6Z	AV(Q,5)+dZ	AV(5,6)+dZ	AV(Q,5)Z
Valence (T) extrapolation	AV6Z	AV(T,Q)+dZ	AV(Q,5)+dZ	AV(T,Q)Z
Valence T-(T) extrapolation	PVQZ	PV(D,T)Z	PV(D,T)Z	PV(T,Q)Z
Valence (Q)		1.25 PVDZ	1.10 PVTZ	PVTZ
Valence Q-(Q)		1.25 PVDZ	1.10 PVDZ	PVDZ
Valence Q	PVTZ		PVDZ	
Valence 5	PVDZ		PVDZ	
Valence 6				
CCSD(T) Core shell	PWCV5Z	MTSmall	AWCV(T,Q)Z	AWCV(T,Q)Z
T-(T) Core shell			PWCVTZ ^c	
CCSDTQ Core shell	PWCVDZ			
Scalar Relativistic CCSD(T)	DK-PVTZ	MTSmall	DK-AV(Q+d)Z	DK-AVQZ
First-order atomic spin-orbit correction	expt data	expt data	expt data	expt data
Second-order molecular spin-orbit correction	CAS-CI/AVTZ-PP			SO-B3LYP/ECP
DBOC	HF/AVTZ		HF/AVTZ	HF/AVQZ, CCSD/AVDZ

^aSee W2[102], W3[103] and W4[93] protocols. ^bThe VPT2 approach was used. ^cW4.2 also includes this higher core shell contribution. ^dThis Feller-Peterson-Dixon procedure was defined for Br₂ [95].

An overview of the TA14 protocol, together with other highly accurate thermochemistry composite methods, is shown in Table 2.1. Within the Born-Oppenheimer approximation, the total energy of a compound may be separated into electronic and vibrational contributions. The ground state electronic energy is expressed by the following additivity scheme:

$$\begin{aligned}
 E_e^{TA14} = & E_{HF,Extrap} + \Delta E_{CCSD,Extrap} \\
 & + \Delta E_{(T),Extrap} + \Delta E_{T-(T),Extrap} \\
 & + \Delta E_{(Q)} + \Delta E_{Q-(Q)} + \Delta E_{CORE} \\
 & + \Delta E_{REL} + \Delta E_{1^{st}SO} + \Delta E_{2^{nd}SO} \\
 & + \Delta E_{DBOC}
 \end{aligned} \tag{2.6}$$

In Eq 2.6, the term $E_{HF,Extrap}$ is the Hartree-Fock energy, and $\Delta E_{CCSD,Extrap}$, $\Delta E_{(T),Extrap}$ and $\Delta E_{T-(T),Extrap}$ are the valence correlation energies, where the label "Extrap" indicates extrapolation to the complete basis-set limit, explained further below. $\Delta E_{CCSD,Extrap}$ is given by the CCSD energy contribution, and $\Delta E_{(T),Extrap}$ describes the energy contribution from the perturbative treatment of triple excitations. $\Delta E_{T-(T),Extrap}$ describes the energy difference between full triples and the perturbative triples approximation. $\Delta E_{(Q)}$ and $\Delta E_{Q-(Q)}$ are the perturbative quadruples contribution and the full quadruples contribution, respectively. The resulting frozen core FC-CCSDTQ energy is very close to the frozen-core non-relativistic FullCI limit.[138] ΔE_{CORE} is the last nonrelativistic component of the total energy and describes core-valence correlation effects. The term ΔE_{REL} represents scalar relativistic effects. First-order and second-order spin-orbit corrections are given as $\Delta E_{1^{st}SO}$ and $\Delta E_{2^{nd}SO}$, and ΔE_{DBOC} is the diagonal Born-Oppenheimer correction. Each of these terms is explained in detail below.

To obtain high accuracy estimates of HF and electronic correlation energies, extrapolation techniques can be applied, requiring large correlation-consistent basis sets.[139] We applied the extrapolation formulae proposed in W4 theory for the Hartree-Fock energies and the extrapolation formulae given in W3 theory for the correlation energies to obtain accurate *ab initio* thermochemistry properties. Theoretical results obtained using this approach are labeled "Best" in the remainder of the article. The Hartree-Fock energy extrapolation is based on the Karton-Martin modification[140] of Jensen's formula:[141]

$$E_{HF,"Best"} = E_X + \frac{E_X - E_{X-1}}{\frac{X \exp(9\sqrt{X} - \sqrt{X-1})}{X+1} - 1} \tag{2.7}$$

where the consecutive cardinal numbers $X-1$ and X are the maximum angular momentum quantum number X represented in correlation-consistent basis set (e.g., 3 for AVTZ, 4 for AVQZ, and 5 for AV5Z) [139]. $E_{HF,"Best"}$ represents the $E_{HF,Extrap}$ term in equation 2.6. Equation 2.7 was previously found to give an RMS error of 0.00628 kcal mol⁻¹ with respect to the Hartree-

Fock complete-basis set energy for a set of atoms and diatomic systems with the AV{Q,5}Z basis set pair.[142]

The correlation energy results are extrapolated separately from the Hartree-Fock components. The CCSD energy typically converges more slowly than the Hartree-Fock energy. [143, 144, 145] The extrapolations to the infinite basis-set limit for several correlation energy contributions were carried out with the two-term $A + B/L^\alpha$ expression used extensively in Wn theories[102, 103, 93, 97] and expressed in this form:

$$E_{CC,"Best"} = E_X + \frac{E_X - E_{X-1}}{(X/X-1)^\alpha - 1} \quad (2.8)$$

Equation 2.8 derives from the truncation of the partial-wave expansion of pair correlation energies to just the leading terms, as described by Klopper.[139] The α factor was set equal to 3, as given in the W3 protocol;[103] this contrasts with the W4 approach[93] where $\alpha = 5$ is used for triplet-coupled pair CCSD energies. Hence, the TA14 protocol uses equation 2.7 to extrapolate the Hartree-Fock energy ($E_{HF,Extrap}$ in equation 2.6) and applies equation 2.8 for some correlation energies ($\Delta E_{CCSD,Extrap}$, $\Delta E_{(T),Extrap}$, $\Delta E_{T-(T),Extrap}$) and for ΔE_{CORE} in equation 2.6 with $\alpha = 3$ throughout.

As recommended by Klopper and co-workers, [143] the (T) valence correlation energy contribution was evaluated separately from the CCSD contributions, with smaller basis sets. The more expensive (T) contribution converges to the basis set limit more quickly than the CCSD correlation energy.[143, 144] Our best estimate $\Delta E_{(T),Extrap}$ energy contributions were calculated with the AV{T,Q}Z basis set pair and were extrapolated using equation 2.8.

Post-CCSD(T) contributions to the electronic energy were determined with smaller basis sets. Higher-order correlated energies converge to the complete basis set limit more efficiently than the energies computed at CCSD(T) level.[96, 146] In the present work, the $\Delta E_{T-(T),Extrap}$ term was extrapolated from CCSDT-CCSD(T) energy differences with the PVTZ and PVQZ basis sets. However for NBrCl₂, NBr₂Cl, NHBr₂, NHBrCl and NBr₃, we instead used the PV{D,T}Z basis set pair, due to computational limitations.

Separately, we also applied the widely used extrapolation method of Halkier for the Hartree-Fock and CCSD, (T), and T-(T) correlation energies, leading to a second estimate of computed thermodynamic properties. Halkier et al. [145, 147] proposed applying two-term extrapolation procedures based on calculations with hierarchical correlation-consistent basis sets:

$$E_{HF/CC,"Halkier"} = \frac{E_X X^3 - E_{X-1}(X-1)^3}{X^3 - (X-1)^3} \quad (2.9)$$

Equation 2.9 was applied to approximate both Hartree-Fock energies and the above-listed correlation energies at the complete basis-set limit.[145, 148] We used the label "Halkier" for thermochemical quantities obtained by use of equation 2.9 to extrapolate Hartree-Fock and correlation energies.

As explained by Peterson et al.,[96] CCSDT(Q) corrections should always be included in order to counterbalance the CCSDT energy contributions, which are typically less close to the FullCI limit than CCSD(T) values. The $\Delta E_{(Q)}$ contributions were calculated as the CCSDT(Q)-CCSDT energy difference with the PVTZ basis set. For NBr_3 and NBr_2Cl , the $\Delta E_{(Q)}$ contribution was computed with the PVDZ basis set. $\Delta E_{Q-(Q)}$ was computed as the energy difference CCSDTQ-CCSDT(Q) with the PVDZ basis set. We chose to apply the UHF reference wave function on the ROHF oxygen molecule in the calculation of quadruple excitation correlation energy contributions. Due to its high computational cost, the CCSDTQ correlation energy was not computed for NBr_3 .

For most molecules, ΔE_{CORE} was assessed as the energy difference between all-electron CCSD(T)/AWCV{T,Q}Z and frozen-core CCSD(T)/AWCV{T,Q}Z calculations, applying equation 2.8 to extrapolate each energy to the complete basis-set limit. For NHBrCl the ΔE_{CORE} was computed at the AWCQVQZ level, whereas for NBr_3 and NBr_2Cl , this contribution was obtained at the AWCVTZ level, due to computational cost, and no extrapolation formula was applied.

Relativistic contributions were computed as follows. Scalar relativistic effects (ΔE_{REL}) are quantitatively recovered within the second-order Douglas-Kroll-Hess approximation,[149, 150, 151, 152, 153, 154] and these were obtained from the energy difference between relativistic CCSD(T)/AVQZ-DK and non-relativistic CCSD(T)/AVQZ calculations. Atomic first-order spin-orbit coupling terms, $\Delta E_{1^{\text{st}}\text{SO}}$, were taken from the experimental fine structure.[155] For heavy elements such as bromine, second-order molecular spin-orbit contributions have non-negligible contributions.[156, 95] These energy contributions, $\Delta E_{2^{\text{nd}}\text{SO}}$, were carried out with SO-DFT calculations at the B3LYP[157, 158] level. The CRENBL basis sets and AREPs (averaged relativistic effective potentials) with spin-orbit operators were employed for the non-hydrogen atoms.[159, 160, 161, 162, 163, 164] Although implemented with HF/AVTZ in the W4 scheme, post-HF contributions to the diagonal Born-Oppenheimer correction have been better reproduced when including the CCSD energy contribution.[165] ΔE_{DBOC} calculations thus were conducted at CCSD/AVDZ level, where the HF electronic energy contribution was calculated with the AVQZ basis set:

$$\Delta E_{\text{DBOC}} = \Delta E_{\text{DBOC}}^{\text{HF/AVQZ}} + \Delta \Delta E_{\text{DBOC}}^{\text{CCSD/AVDZ}} \quad (2.10)$$

2.3.5 Thermochemical Properties

To construct standard enthalpies of formation at 0 K and 298 K at 1 atm pressure, we determined the electronic energies and the total atomization energies of all species. Total atomization energies at the bottom of the theoretical potential energy well ($TAE_e(M)$) and at

0 K ($TAE_{0K}(M)$) were calculated *ab initio* as:

$$TAE_e^{TA14}(M) = \sum_i^N E_e^{TA14}(A_i) - E_e^{TA14}(M) \quad (2.11)$$

$$TAE_{0K}^{TA14}(M) = TA E_e^{TA14}(M) - ZPVE^{TA14}(M) \quad (2.12)$$

where $E_e^{TA14}(M)$ and $E_e^{TA14}(A_i)$ are the electronic energies of the molecule M and of the constituent atoms A_i , computed following the TA14 protocol, and $ZPVE^{TA14}(M)$ is the computed anharmonic zero-point vibrational energy of the molecule.

The method to calculate standard enthalpies of formation has been described previously by Curtiss et al.[166] Briefly the procedure was as follows. A theoretical enthalpy of formation of a molecule M at 0 K can be calculated as the difference between the summed experimental enthalpies of formation of the atoms contained in the molecule at 0 K, $\sum_i^N \Delta_f H_{0K}^0(A_i)$, and the theoretical atomization energy $TA E_{0K}(M)$ of the molecule. The superscript "0" refers to 1 atm standard state. For each molecule:

$$\Delta_f H_{0K}^{0,TA14}(M) = \sum_i^N \Delta_f H_{0K}^{0,Expt}(A_i) - TA E_{0K}^{TA14}(M) \quad (2.13)$$

A theoretical enthalpy of formation at 298 K was obtained by applying the following formula:

$$\begin{aligned} \Delta_f H_{298K}^{0,TA14}(M) &= \Delta_f H_{0K}^{0,TA14}(M) + \Delta \Delta H_{thermal}^{TA14}(M) \\ &\quad - \sum_i^N [H_{298K}(A_i) - H_{0K}(A_i)]^{0,Expt} \\ &\quad - ZPVE^{TA14}(M) \end{aligned} \quad (2.14)$$

where $\Delta \Delta H_{thermal}^{TA14}(M)$ is the computed thermal correction to the enthalpy for the molecule M obtained from computed vibrational frequencies, and $[H_{298K}(A_i) - H_{0K}(A_i)]^{0,Expt}$ is the experimental integrated heat capacity for each atom A_i at its standard state. The experimental

Table 2.2 Experimental Enthalpies of Formation $\Delta_f H_{0K}^{0,Expt}(A_i)$, Integrated Heat Capacities $[H_{298K}(A_i) - H_{0K}(A_i)]^{0,Expt}$ (kcal mol⁻¹), and Entropies (cal mol⁻¹K⁻¹) for Selected Diatomic Molecules at 298 K at their Standard State .

Element A_i	Reference State	$\Delta_f H_{0K}^{0,Expt}(A_i)$	$[H_{298K}(A_i) - H_{0K}(A_i)]^{0,Expt}$	$S_{298K}^{0,Expt}(D_i)$
H	H _{2,gas}	51.6336 ± 0.0014	1.012 ± 0.000	31.2333 ± 0.0007
N	N _{2,gas}	112.5287 ± 0.0956	1.036 ± 0.000	45.7957 ± 0.0010
O	O _{2,gas}	58.9842 ± 0.0239	1.037 ± 0.000	49.0325 ± 0.0012
Cl	Cl _{2,gas}	28.5901 ± 0.0019	1.097 ± 0.000	53.3176 ± 0.0024
Br	Br _{2,liq}	28.1836 ± 0.0287	2.930 ± 0.001	36.38

atomic enthalpy corrections and the integrated heat capacity values for each element are taken from the CODATA thermochemical database (Table 3.3).[105] In equation 2.14, computed zero-point vibrational energy contributions (already included in the total atomization energies) were subtracted from enthalpies of formation of the molecule at 0 K to avoid their double-counting.

We computed the Gibbs free energy of formation of each molecule as follows. We combined the computed entropy of formation, $\Delta_f S_{298K}^{0,TA14}(M)$, to the gas phase enthalpy of formation:

$$\Delta_f G_{298K}^{0,TA14}(M) = \Delta_f H_{298K}^{0,TA14}(M) - T \Delta_f S_{298K}^{0,TA14}(M) \quad (2.15)$$

where $\Delta_f S_{298K}^{0,TA14}(M)$ was calculated as follows:

$$\Delta_f S_{298K}^{0,TA14}(M) = S_{298K}^{TA14}(M) - \sum_i^N \nu_i S_{298K}^{0,Expt}(D_i) \quad (2.16)$$

For all polyatomic molecules, $S_{298K}^{TA14}(M)$ comprises computed anharmonic vibrational, rotational, and translational contributions to the molecular entropy at 298 K. For the diatomic molecules, the anharmonic contribution to vibrations was taken from experimental data, as discussed above. $S_{298K}^{0,Expt}(D_i)$ is the experimental entropy for each diatomic element at its standard state, as taken from the CODATA thermochemical database (Table 3.3),[105] and ν_i is the appropriate stoichiometric coefficient. For example, the $\Delta_f S_{298K}^{0,TA14}$ value of HOBr is:

$$\begin{aligned} \Delta_f S_{298K}^{0,TA14}(\text{HOBr}) &= S_{298K}^{TA14}(\text{HOBr}) - \frac{S_{298K}^{0,Expt}(\text{H}_2)}{2} \\ &\quad - \frac{S_{298K}^{0,Expt}(\text{O}_2)}{2} - \frac{S_{298K}^{0,Expt}(\text{Br}_2)}{2} \end{aligned} \quad (2.17)$$

The resulting $\Delta_f H_{298K}^{0,TA14}(M)$ and $\Delta_f G_{298K}^{0,TA14}(M)$ values are thus based on a combination of experimental data (e.g., $\Delta_f H_{0K}^{0,Expt}(A_i)$, $[H_{298K}(A_i) - H_{0K}(A_i)]^{0,Expt}$, and $S_{298K}^{0,Expt}(A_i)$) and computational results ($TAE_{0K}^{TA14}(M)$, $\Delta \Delta H_{thermal}^{TA14}(M)$, and $S_{298K}^{0,TA14}(M)$), but they are considered as theoretical values.

2.3.6 Diagnostics for Nondynamical Correlation Effects

Diagnostics for nondynamical correlation (NDC) effects provide an indication of the importance of post-CCSD(T) electronic contributions for thermochemical applications. Among several proposed diagnostics, the %TAE[HF] is the most affordable *a priori* energy-based diagnostic, and %TAE[(T)] is a more reliable indicator that also requires no post-CCSD(T) calculations.[93] %TAE[*post-CCSD(T)*] is an *a posteriori* diagnostic to evaluate the post-CCSD(T) contributions to total atomization energy.[93] These diagnostics are calculated as follows:

$$\%TAE[HF] = 100 \times \frac{TAE_e(HF)}{TAE_e(CCSD(T))} \quad (2.18)$$

$$\%TAE[(T)] = 100 \times \frac{TAE_e(CCSD(T)) - TAE_e(CCSD)}{TAE_e(CCSD(T))} \quad (2.19)$$

$$\begin{aligned} \%TAE[post - CCSD(T)] &= 100 \times \\ &\frac{TAE_e(post - CCSD(T)) - TAE_e(CCSD(T))}{TAE_e(post - CCSD(T))} \end{aligned} \quad (2.20)$$

where $TAE_e(HF)$, $TAE_e(CCSD)$ and $TAE_e(CCSD(T))$ represent the non-relativistic HF, CCSD, and CCSD(T) atomization energy components at the bottom of the well. $TAE_e(post - CCSD(T))$ contains the non-relativistic higher excitation energy contributions T-(T), (Q), and Q-(Q), but excludes core-valence and relativistic contributions.

2.4 Results and Discussion

We computed total atomization energies at 0 K, standard heats of formation at 0 K and at 298 K, and Gibbs free energies of formation at 298 K for bromamines, chloramines, bromochloramines, and other related molecules. First, we report total atomization energy data and discuss the electronic energy contributions to bond formation in these molecules. This is followed by a discussion of diagnostics for nondynamical correlation. Then, to assess the performance of the TA14 approach, we compare our computed property data to experimental data and other published benchmarks, where available. Finally we briefly discuss the implications of thermochemistry data for halamines.

2.4.1 Total Atomization Energies

Benchmark-level total atomization energies were obtained with the TA14 method, taking into account our best estimate CCSD(T) and post-CCSD(T) contributions, core-valence electronic correlation, relativistic effects and DBOC contributions. The component breakdown of the total atomization energies at the bottom of the potential energy well, TAE_e , and at 0 K, TAE_{0K} , is displayed in Table 2.3 for both chemical sets A and B.

Electron correlation is a substantial contributor to the bond formation of chloramines and bromamines. For the monohalogenated species, the $\Delta E_{CCSD,Extrap}$ and $\Delta E_{(T),Extrap}$ energy components together explain > 40% of the TAE_e . For the dihalogenated and trihalogenated species, the combined $\Delta E_{CCSD,Extrap}$ and $\Delta E_{(T),Extrap}$ contributions dominate over the $E_{HF,Extrap}$ energy component altogether. The $E_{HF,Extrap}$ component dwindles progressively with increasing halogenation. The chloramines and bromamines are thus relatively weakly bound molecules, held together largely by electron correlation forces, and presumably this accounts for their high reactivity.

For both NBr_3 and NBr_2Cl , the $E_{\text{HF},\text{Extrap}}$ component of the TAE_e is actually less than zero, indicating that these molecules are not predicted to be stable at the Hartree-Fock level. In other words, electronic correlation effects are entirely responsible for their stable formation. This is an unusual situation; a few other species have been reported to exhibit negative or near-zero Hartree-Fock contributions to the TAE_e , and many of them are halogen-containing molecules: O_3 , MgO , $\text{BN}(^1\Sigma^+)$, F_2 , FO_2 , F_2O_2 , FO , F_2O , OCIO , and CLOO are characterized by negative or near-zero Hartree-Fock atomization energies, and their stable formation is thus explained entirely by dynamical and nondynamical electron correlation effects.[93, 167] Dynamical and nondynamical correlation contributions are discussed further in the next section.

Post-CCSD(T) contributions to electronic correlation energies are varied. For example, $\Delta E_{T-(T),\text{Extrap}}$, $\Delta E_{(Q)}$, and $\Delta E_{Q-(Q)}$ contributions together account for $-0.49 \text{ kcal mol}^{-1}$ of the total atomization energy of NBr_2Cl . However for most of the halamines, the $\Delta E_{T-(T),\text{Extrap}}$, $\Delta E_{(Q)}$, and $\Delta E_{Q-(Q)}$ components tend to cancel each other. The $\Delta E_{T-(T),\text{Extrap}}$ energy components are destabilizing in all cases (< 0), whereas the quadruple excitation contributions uniformly stabilizing (> 0). This is consistent with the trends in post-CCSD(T) components found previously for other small molecules.[146, 93, 92]

Core-valence electronic correlation contributions to the total atomization energy are non-negligible for bromamines and chloramines. The ΔE_{CORE} values reported for chloramines range from $0.62 \text{ kcal mol}^{-1}$ to $0.74 \text{ kcal mol}^{-1}$. For bromamines and bromochloramines, values range from $0.66 \text{ kcal mol}^{-1}$ (NBrCl_2) to $3.24 \text{ kcal mol}^{-1}$ (NBr_3). Core-valence electronic correlation contributions thus have critical importance in achieving benchmark accuracy in the TAE.

Relativistic energy components also have an important role for estimating thermochemical properties of these molecules. The ΔE_{REL} and $\Delta E_{2^{\text{nd}}\text{SO}}$ components contribute quantitatively to the total atomization energies of halamines. The scalar relativistic effects, ΔE_{REL} , of halamines are negative with values that range from $-0.14 \text{ kcal mol}^{-1}$ (NBr_3) to $-0.63 \text{ kcal mol}^{-1}$ (NH_2Br). $\Delta E_{2^{\text{nd}}\text{SO}}$ values range from $-0.14 \text{ kcal mol}^{-1}$ (NCl_3) to $0.40 \text{ kcal mol}^{-1}$ (Br_2 and NHBr_2). These energy contributions, although small, have to be considered to achieve the desired accuracy in TAE calculations. The $\Delta E_{1^{\text{st}}\text{SO}}$ contribution is simply an additive function of the elemental composition of the molecule and therefore it is not discussed.

Finally, ΔE_{DBOC} components are the smallest energy contributions considered. Among the halamines, the largest values are $0.05 \text{ kcal mol}^{-1}$ found for NH_2Cl and NH_2Br .

Table 2.3 Component Breakdown of the Best Estimate Total Atomization Energies at the Bottom of the Well (TAE_e) and at 0 K (TAE_{0K}) [kcal mol⁻¹]

	HF ^a	CCSD ^b	(T) ^b	T-(T) ^b	(Q)	Q-(Q)	Core Shell ^b	Scalar Relat.	1st order Spin-Orbit	2nd Order Spin-Orbit	DBOC	TAE_e	ZPVE	TAE_{0K}
Set A														
H ₂	83.85	25.67	0.00	0.00	0.00	0.00	0.00	0.01	0.00	0.00	0.02	109.54	6.21 ^c	103.34
N ₂	115.42	102.22	9.46	-0.75	1.08	-0.15	1.07	-0.14	0.00	0.00	0.00	228.20	3.33 ^c	224.87
O ₂	18.77	91.70	9.24	-0.42	1.08	-0.12	0.45	-0.18	-0.45	0.00	0.00	120.07	2.19 ^c	117.88
Cl ₂	19.23	35.65	4.79	-0.44	0.43	-0.02	0.22	-0.18	-1.68	-0.09	0.00	57.91	0.79 ^c	57.12
Br ₂	16.09	32.08	4.17	-0.32	0.35	-0.02	0.54	-0.36	-7.02	0.40	0.00	45.91	0.47 ^c	45.44
HCl	77.08	28.75	1.60	-0.14	0.09	-0.00	0.26	-0.24	-0.84	-0.05	0.03	106.51	4.17 ^c	102.32
HBr	65.12	26.93	1.40	-0.08	0.08	-0.00	0.57	-0.49	-3.51	0.20	0.02	90.23	3.75 ^c	86.48
HOCl	78.82	80.11	6.93	-0.50	0.59	0.05	0.40	-0.31	-1.06	-0.05	0.03	165.01	7.92	157.09
HOBr	76.75	79.30	6.75	-0.46	0.59	-0.07	0.39	-0.65	-3.73	0.20	0.04	159.10	7.91	151.19
H ₂ O	155.92	73.14	3.59	-0.23	0.19	-0.02	0.48	-0.26	-0.22	0.00	0.09	232.67	13.22	219.454
NH ₃	201.12	92.28	3.92	-0.15	0.02	-0.02	0.79	-0.24	0.00	0.00	0.09	297.81	21.20	276.61
Set B														
NH ₂ Cl	142.01	98.49	6.95	-0.46	0.47	-0.04	0.74	-0.38	-0.84	-0.05	0.05	246.95	16.30	230.65
NHCl ₂	79.84	107.66	10.92	-0.89	0.93	-0.09	0.70	-0.39	-1.68	-0.09	0.02	196.92	10.45	186.48
NCl ₃	13.78	119.64	15.92	-1.46	1.58	-0.20	0.62	-0.29	-2.52	-0.14	0.01	146.45	3.84	143.11
NH ₂ Br	135.81	97.75	6.85	-0.41	0.48	-0.05	0.92	-0.63	-3.51	0.20	0.05	237.46	15.93	221.53
NHBr ₂	66.13	106.55	10.76	-0.81 ^d	0.97	-0.11	1.11	-0.54	-7.02	0.40	0.02	177.44	9.81	167.64
NBr ₃	-7.29	118.63	15.93	-1.39 ^d	1.29 ^e	N/A ^f	3.24 ^g	-0.14	-10.54	0.06	0.01	120.34	2.98	117.36
NHBrCl	73.51	107.14	10.87	-0.83 ^d	0.95	-0.10	1.22 ^h	-0.45	-4.35	0.15	0.02	188.12	10.13	177.99
NBrCl ₂	5.04	120.29	16.41	-1.41 ^d	1.74	-0.24	0.66	-0.20	-5.19	0.11	0.01	137.21	3.56	133.65
NBr ₂ Cl	-0.58	119.12	16.01	-1.67 ^d	1.22 ^e	-0.04	2.58 ^g	-0.15	-7.86	0.36	0.01	129.00	3.27	125.72

^aHartree-Fock energies extrapolated using equation 2.7. ^bCorrelation energies extrapolated using equation 2.8. ^cFor diatomic molecules, harmonic zero-point vibrational energy values were computed, and experimental anharmonicity contributions were added to these values. ^dFor NBrCl₂, NBr₂Cl, NHBr₂, NHBrCl and NBr₃ this contribution is computed with the pV(D,T)/Z basis set pair. ^eFor NBr₂Cl and NBr₃ this contribution is computed with the pVDZ basis set. ^fNot available. ^gFor NBr₂Cl and NBr₃ this contribution is computed with the AWCVTZ basis set, and no extrapolation to the complete basis set limit was applied. ^hFor NHBrCl this contribution is computed with the AWCVQZ basis set, and no extrapolation to the complete basis set limit was applied.

2.4.2 Importance of Nondynamical Correlation for Halamines

Nondynamical electron correlation (NDC) contributes substantially to the electronic structure of chloramines and bromamines, and this merits a brief discussion. The nondynamical electronic correlation refers to the interelectronic interactions for those systems where the reference configuration (defined as the HF wavefunction) is affected by quasidegeneracy and is not well-described by a single predominating configuration.[7] Chloramines and bromamines all exhibit nondynamical correlation (Table 2.4). This effect becomes increasingly important with increasing number of halogen atoms in the molecule. The wavefunctions of all four trihalamine species are dominated by multireference character as diagnosed by very low % $TAE[HF]$ values and high % $TAE[(T)]$ values. Monohalamines and dihalamines exhibit mild to moderate levels of nondynamical correlation.

These NDC diagnostics provide a rough indication of the reliability of single-reference approaches in the evaluation of the electronic structure. In order to provide a more detailed description of systems dominated by NDC, a multireference electronic structure method is generally required. However, the electronic energies of such systems can be quantitatively recovered with high-order coupled cluster methods based on a single-determinant HF reference.[103, 93, 98]

2.4.3 Comparison of Computed TAE_{0K} Values with Previous Experimental and Theoretical Data

Our best estimate total atomization energies at 0 K, $TAE_{0K, "Best"}^{TA14}$, are in excellent agreement with previously published experimental values, where available. For all species in set A there is agreement to within 0.23 kcal mol⁻¹ or less (Table 2.5). The average absolute deviation from experiments is 0.10 kcal mol⁻¹. The largest disagreement from experiment is for HOCl (0.23 kcal mol⁻¹), followed by HBr with a deviation of -0.14 kcal mol⁻¹. These results indicate that the *ab initio* protocol employed here has achieved ≤ 1 kJ mol⁻¹ accuracy for the small molecules of set A. This is consistent with previous high-level *ab initio* work using comparable methodologies.[93, 95]

Our $TAE_{0K, "Best"}^{TA14}$ results are also in very good agreement with previous theoretical values from W4 (TAE_{0K}^{W4}) and FPD calculations (TAE_{0K}^{FPD}), where comparisons can be made. $TAE_{0K, "Best"}^{TA14}$ and TAE_{0K}^{W4} agree to within 0.11 kcal mol⁻¹ for monochloramine. For molecule set A, the highest discrepancies between $TAE_{0K, "Best"}^{TA14}$ and TAE_{0K}^{W4} are found for N₂ (-0.14 kcal mol⁻¹) and HOCl (0.37 kcal mol⁻¹). These differences can be explained chiefly by a few energy contributions that were computed differently. First, Karton et al. employed a different definition of frozen-core electrons from that implemented in CFOUR, and, as a consequence, the estimates of the core-valence contributions differ by 0.14 kcal mol⁻¹ for HOCl. Second, the W4 estimate of the zero-point vibrational energy of HOCl was 8.18 kcal mol⁻¹, taken from theoretical data [168] calculated at the MRCI/AV(D,T,Q)Z level, and this differs from our VPT2-B2PLYPD/AVQZ value (7.92 kcal mol⁻¹) and from the experimental value of 7.97

Table 2.4 Diagnostics for Nondynamical Correlation (NDC)

Compound	%TAE[HF]	%TAE[(T)]	%TAE[<i>post</i> – CCSD(T)]	NDC evaluation based on %TAE[(T)] ^a
N ₂	50.9	4.16	0.076	mild NDC
O ₂	15.7	7.72	0.443	moderate NDC
Cl ₂	32.4	8.03	-0.051	moderate NDC
Br ₂	30.9	7.97	0.035	moderate NDC
HCl	71.8	1.49	-0.048	mild NDC
HBr	69.7	1.50	-0.006	mild NDC
HOCl	47.6	4.18	0.084	mild NDC
HOBr	47.2	4.14	0.037	mild NDC
H ₂ O	67.1	1.54	-0.029	mild NDC
NH ₃	67.7	1.32	-0.048	mild NDC
NH ₂ Cl	57.4	2.81	-0.012	mild NDC
NHCl ₂	40.3	5.50	-0.031	moderate NDC
NCl ₃	9.3	10.66	-0.049	severe NDC
NH ₂ Br	56.5	2.85	0.010	mild NDC
NHBr ₂	36.1	5.86	0.022	moderate NDC
NBr ₃	-5.8	11.52	-0.080	severe NDC
NHBrCl	38.5	5.68	0.008	moderate NDC
NBrCl ₂	3.6	11.58	0.065	severe NDC
NBr ₂ Cl	-0.4	11.90	-0.364	severe NDC

^aFollowing the qualitative interpretation proposed by Karton et al.,[93, 97] systems are dominated by dynamic correlation when the %TAE[(T)] value is below 2%, whereas a large nondynamical correlation contribution is indicated by a %TAE[(T)] value greater than 10%. %TAE[(T)] between 2% and 4-5% and between 4-5% and 10% suggest mild and moderate levels of nondynamical correlation, respectively. %TAE[HF] is a more generic and lower-cost predictor for NDC: a %TAE[HF] value above 66.7% indicates a system not affected by NDC, whereas a %TAE[HF] below 20% indicates a molecule dominated by a severe nondynamical correlation.

kcal mol⁻¹. [169, 170, 171] For N₂, discrepancies between the two theoretical methods are likely due to slightly different calculations of post-CCSD(T) contributions. In the W4 protocol, the quadruple excitation energies are calculated as 1.10[(CCSDTQ-CCSDT(Q))+(CCSDT(Q)-CCSDT)], whereas our estimates are calculated without the empirical scalar factor 1.10. Furthermore, CCSDTQ5 contributions were not included in our protocol. These dissimilarities between our method and W4 produce a discrepancy in the post-CCSD(T) energy value of N₂. Finally, for molecule set A, the largest discrepancies between $TAE_{0K, "Best"}^{TA14}$ and TAE_{0K}^{FPD} are for HCl and HOCl (0.17 and 0.15 kcal mol⁻¹, respectively). In summary, TA14 exhibits excellent agreement with W4 for monochloramine and excellent agreement with W4 and FPD values for molecules of set A, providing further confirmation that TA14 produces sub-kJ mol⁻¹ accuracy for atomization energies of small molecules containing atoms up to the third row. Based on comparisons between TA14 and these other theoretical methods, we conclude that the predominating sources of uncertainties in our TAE_{0K} values are in the calculations of the core-valence electron correlation energies and post-CCSD(T) energy treatments.

Table 2.5 Total Atomization Energies at 0 K: Experimental and Theoretical Values [kcal mol⁻¹]

Compound	TAE_{0K}^{TA14} <i>"Best"</i>	TAE_{0K}^{TA14} <i>"Halkier"</i>	TAE_{0K}^{W4} [93, 92]	TAE_{0K}^{FDPD} [95]	TAE_{0K}^{Expt}
Set A					
H ₂	103.34	103.36	103.29	103.27 ± 0.02	103.27 [109]
N ₂	224.87	224.93	225.01	224.88 ± 0.3	224.94 ± 0.01 [93]
O ₂	117.88	117.88	117.88	117.92 ± 0.2	117.99 ± 0.00 [93]
Cl ₂	57.12	57.81	57.03	57.23 ± 0.3	57.18 ± 0.00 [93]
Br ₂	45.44	45.50	N/A ^d	45.39 ± 0.3	45.46 ± 0.07 [109]
HCl	102.32	102.59	102.23	102.15 ± 0.2	102.21 ± 0.00 [93]
HBr	86.48	86.48	N/A ^d	86.47 ± 0.2	86.62 ± 0.05 [109]
HOCl	157.09	157.53	156.72	156.94 ± 0.4	156.86 ± 0.03 ^c
HOBr	151.19	151.23	N/A ^d	N/A ^d	151.28 ± 0.21 ^c
H ₂ O	219.45	219.46	219.36	219.38 ± 0.2	219.36 ± 0.01 [93]
NH ₃	276.61	276.66	276.60	276.48 ± 0.3	276.59 ± 0.01 [93]
Average Absolute Deviation ₁ ^a	0.09	0.22		0.06	
Average Absolute Deviation ₂ ^b	0.10	0.28	0.06	0.06	
Average Deviation ₁ ^a	0.00	0.18		-0.03	
Average Deviation ₂ ^b	0.03	0.25	-0.04	-0.02	
Signed Maximum Deviation ^a	0.23 (HOCl)	0.67 (HOCl)	-0.15 (Cl ₂)	-0.15 (HBr)	
Set B					
NH ₂ Cl	230.65	231.03	230.54	N/A ^d	N/A ^d
NHCl ₂	186.48	187.20	N/A ^d	N/A ^d	N/A ^d
NCl ₃	143.11	144.16	N/A ^d	N/A ^d	N/A ^d
NH ₂ Br	221.53	221.58	N/A ^d	N/A ^d	N/A ^d
NHBr ₂	167.64	167.70	N/A ^d	N/A ^d	N/A ^d
NBr ₃	117.36	117.49	N/A ^d	N/A ^d	N/A ^d
NHBrCl	177.99	178.38	N/A ^d	N/A ^d	N/A ^d
NBrCl ₂	133.65	134.34	N/A ^d	N/A ^d	N/A ^d
NBr ₂ Cl	125.72	126.15	N/A ^d	N/A ^d	N/A ^d

^aThe deviations were calculated considering all available experimental data. ^bOnly the compounds studied by Karton et al. are considered. ^cReference TAE_{0K} for HOCl and HOBr are calculated from experimental molecular $\Delta_f H_{0K}^0$ and experimental atomic heat capacities. ^dNot available.

Based on the above comparisons to experimental and previous theoretical data, we conclude that our best TA14 computations have 1 kJ mol^{-1} ($0.24 \text{ kcal mol}^{-1}$) uncertainty in the TAE_{0K} for the chloramines (NH_2Cl , NHCl_2 , and NCl_3) and for monobromamine (NH_2Br). We conservatively assign larger uncertainties of 3 kJ mol^{-1} ($0.72 \text{ kcal mol}^{-1}$) for the TAE_{0K} values of NHBr_2 , NBr_3 , NHBrCl , NBrCl_2 , and NBr_2Cl , which exhibit larger core-valence correlation and post-CCSD(T) energy contributions, and for which we were required to apply slightly lower levels of theoretical treatment.

For purposes of further comparisons, we additionally employed the Halkier extrapolation formula (equation 2.9) for the computations of Hartree-Fock and correlation energies. We compared these data with results obtained following our "Best" TA14 approach, which employs W4 extrapolation formulae (equations 2.7 and 2.8), as shown in Table 2.5. The $TAE_{0K, "Halkier"}^{TA14}$ values exhibit higher deviations with respect to experiments, with an average absolute deviation of $0.28 \text{ kcal mol}^{-1}$ in the TAE_{0K} . The largest disagreement is found for HOCl , which differs from the experimental data by $0.67 \text{ kcal mol}^{-1}$ using the Halkier extrapolation. Consistent with previous work,[103, 93] we find that equations 2.7 and 2.8 perform better than the Halkier's extrapolation formula for total atomization energies, with the large basis sets employed here.

2.4.4 Gas Phase Enthalpies of Formation at 0 K and at 298 K

Our computed gas phase enthalpies of formation at 0 K, $\Delta_f H_{0K, "Best"}^{0, TA14}$, are in excellent agreement with experimental data for molecule set A. Our best calculated values at 0 K exhibit an average absolute deviation of $0.11 \text{ kcal mol}^{-1}$ from experiment, indicating that the TA14 method achieves confident kJ mol^{-1} accuracy in the $\Delta_f H_{0K}^0$ for these systems. The computed enthalpy of formation at 0 K of HOCl is the most inaccurate, with a deviation of $-0.23 \text{ kcal mol}^{-1}$ from experiment and a discrepancy of $0.37 \text{ kcal mol}^{-1}$ with respect to the W4.2 value ($-17.51 \pm 0.14 \text{ kcal mol}^{-1}$). [97] This discrepancy from the W4.2 result arises from electronic and vibration contributions to the TAE_{0K} , discussed in the previous section. The computed enthalpies of formation at 0 K for HBr and N_2 are overestimated by about $0.20 \text{ kcal mol}^{-1}$ compared to experiment. These discrepancies arise primarily from the uncertainties in the calculations of the electronic contributions to total atomization energies, as discussed in the previous section.

For molecule set A, computed gas phase enthalpies of formation at 298 K, $\Delta_f H_{298K, "Best"}^{0, TA14}$, also exhibit sub- kJ mol^{-1} agreement with available experimental data (Table 2.6). The largest deviations from experiment were found for HOCl and N_2 , with differences of -0.20 and $0.18 \text{ kcal mol}^{-1}$, respectively. Errors in the computed gas phase enthalpy of formation are of similar magnitude at 0 K and at 298 K (Tables 2.7 and 2.6). It is worth noting that $\Delta_f H_{298K}^{0, Expt}$ values are probably not independent of reported $\Delta_f H_{0K}^{0, Expt}$ values. We did not verify whether the experimental data found in different databases, such as JANAF-Thermochemical Tables,[108] CODATA,[105] ATcT,[106, 107] and CCCBDB,[109] originate from experimental sources.

2.4. Results and Discussion

Table 2.6 Gas Phase Enthalpies of Formation at 298 K: Experimental and Theoretical values [kcal mol⁻¹]

Compound	$\Delta_f H_{298K, "Best"}^{0, TA14}$	$\Delta_f H_{298K}^{0, compt}$	$\Delta_f H_{298K}^{0, Expt}$
Set A			
H ₂	-0.03	0.00 ± 0.02[95]	0.00[106, 107]
N ₂	0.18	0.2 ± 0.3 [95]	0.00 [106, 107]
O ₂	0.09	0.0 ± 0.2 [95]	0.00 [106, 107]
Cl ₂	0.06	< 0.1 ± 0.3[95]	0.00 [106, 107]
Br ₂	7.38	7.4 ± 0.3 [95]	7.39 ± 0.03[108, 106, 107]
HCl	-22.14	-22.0 ± 0.2 [95]	-22.030 ± 0.001[106, 107]
HBr	-8.54	-8.5 ± 0.2[95]	-8.61 ± 0.03[106, 107]
HOCl	-18.56	-18.20 ± 0.14 [97] -18.1 ± 0.3 [172] -17.9 ± 0.3 [90] -18.1 ± 0.4 [95]	-18.357 ± 0.007[106, 107]
HOBr	-14.90	-15.3 ± 0.6 [172] -14.57 [88]	-15.00 ± 0.16[106, 107]
H ₂ O	-57.90	-57.8 ± 0.2 [95] -57.6 ± 0.3 [90]	-57.80 ± 0.01[108, 106, 107]
NH ₃	-10.86	-10.7 ± 0.3 [95] -10.3 ± 0.3 [90]	-10.889 ± 0.007[106, 107]
Average Absolute Deviation	0.07		
Average Deviation	0.03		
Signed Maximum Deviation	-0.20 (HOCl)		
Set B			
NH ₂ Cl	12.04	13.02[88] 12.4 [90]	N/A ^a
NHCl ₂	33.47	33.44[88] 32.5 [90]	N/A ^a
NCl ₃	54.36	53.56[88] 52.37 [90]	N/A ^a
NH ₂ Br	18.97	19.90[88]	N/A ^a
NHBr ₂	48.02	47.56 [88]	N/A ^a
NBr ₃	73.82	N/A ^a	N/A ^a
NHBrCl	39.80	N/A ^a	N/A ^a
NBrCl ₂	61.72	N/A ^a	N/A ^a
NBr ₂ Cl	91.00	N/A ^a	N/A ^a

^aNot available.

Chapter 3

Table 2.7 Gas Phase Enthalpies of Formation at 0 K: Experimental and Theoretical Values [kcal mol⁻¹]

Compound	$\Delta_f H_{0K}^{0,TA14}$ "Best"	$\Delta_f H_{0K}^{0,W4.2}$	$\Delta_f H_{0K}^{0,Exp}$
Set A			
H ₂	-0.07	N/A ^a	0.00 [105, 106, 107]
N ₂	0.19	N/A ^a	0.00[105, 106, 107]
O ₂	0.09	N/A ^a	0.00[105, 106, 107]
Cl ₂	0.06	N/A ^a	0.00[105, 106, 107]
Br ₂	10.93	N/A ^a	10.92 ± 0.03[105]
HCl	-22.10	N/A ^a	-22.02 ± 0.02[105]
HBr	-6.66	N/A ^a	-6.80 ± 0.04[105]
HOCl	-17.88	-17.51 ± 0.14[97]	-17.654 ± 0.007 [106, 107]
HOBr	-12.38	N/A ^a	-12.48 ± 0.16 [106, 107]
H ₂ O	-57.20	N/A ^a	-57.10 ± 0.01[173]
NH ₃	-9.18	N/A ^a	-9.31 ± 0.08[105]
Average Absolute Deviation	0.11		
Average Deviation	0.02		
Signed Maximum Deviation	-0.23 (HOCl)		
Set B			
NH ₂ Cl	13.74	N/A ^a	N/A ^a
NHCl ₂	34.87	N/A ^a	N/A ^a
NCl ₃	55.19	N/A ^a	N/A ^a
NH ₂ Br	22.45	N/A ^a	N/A ^a
NHBr ₂	52.89	N/A ^a	N/A ^a
NBr ₃	79.72	N/A ^a	N/A ^a
NHBrCl	42.95	N/A ^a	N/A ^a
NBrCl ₂	64.24	N/A ^a	N/A ^a
NBr ₂ Cl	95.21	N/A ^a	N/A ^a

^aNot available.

Chloramines and bromamines are found to be endothermic with respect to the elements in their standard states. $\Delta_f H_{298K}^{0,TA14}$ values range from 12.04 kcal mol⁻¹ to 91.00 kcal mol⁻¹ for chloramines, bromamines and bromochloramines (Table 2.6). No experimental heat of formation data are available for the halamines. Based on comparisons of our dataset with other computed and experimental data for molecule set A, we consider that the major sources of uncertainty in the $\Delta_f H_{298K}^{0,TA14}$ arise from the post-CCSD(T) electron correlation contributions to the TAE_{0K} . For the chloramines (NH₂Cl, NHCl₂, and NCl₃) and for monobromamine (NH₂Br), we estimate 1 kJ mol⁻¹ (0.24 kcal mol⁻¹) uncertainties in the computed $\Delta_f H_{0K}^0$ and $\Delta_f H_{298K}^0$ estimates. For NHBr₂, NBr₃, and for the bromochloramines,

we assign larger uncertainties of 2-3 kJ mol⁻¹ (0.48-0.72 kcal mol⁻¹) in computed $\Delta_f H_{0K}^0$ and $\Delta_f H_{298K}^0$ values, for reasons discussed in the section on TAE_{0K} data.

Recently, Rayne and Forest reported standard enthalpies of formation at 298K for chloramines computed at the G4MP2 and G4 levels and for monobromamine and dibromamine at the G4 level (Table 2.6).[88, 90] These protocols represent lower levels of theory than the methods employed here. The G4 and G4MP2 methods do not include any post-CCSD(T) energy calculations and do not employ basis sets larger than *6-31G(2df,p)* and *6-31+G(d)*. Reported G4 estimates of $\Delta_f H_{298K}^0$ deviate from our best estimates by 0.03 to 0.98 kcal mol⁻¹ for the chloramines, monobromamine, and dibromamine (Table 2.6). Reported G4MP2 data exhibit larger deviations from our best estimates, with a difference of 1.99 kcal mol⁻¹ found for the $\Delta_f H_{298K}^0$ value of trichloramine. Thus our computed enthalpy of formation values substantially improve upon these previously reported estimates.

2.4.5 Gibbs Free Energies of Formation at 298 K

For the molecule set A, our best estimate $\Delta_f G_{298K, "Best"}^{0, TA14}$ values show good agreement with experimental data, with an average absolute deviation of 0.09 kcal mol⁻¹ (Table 2.8). The $\Delta_f G_{298K, "Best"}^{0, TA14}$ of HOCl exhibits the largest disagreement from experiment, with a deviation of 0.19 kcal mol⁻¹. This is consistent with the accuracy found for the computed enthalpy of formation, $\Delta_f H_{298K, "Best"}^{0, TA14}$. A comparison of computed and experimental $\Delta_f S_{298K}^0$ values revealed an average absolute error of only 0.08 cal mol⁻¹K⁻¹ and a maximum unsigned deviation of 0.12 cal mol⁻¹K⁻¹ (for both H₂ and Br₂). Errors in the computed entropy thus contribute less than 0.04 kcal mol⁻¹ in the $\Delta_f G_{298K}^0$, for all molecules of set A.[109] Our computed vibrational frequencies are in excellent agreement with experiment, exhibiting an average absolute deviation value of 4 cm⁻¹, and a maximum deviation of -58 cm⁻¹ (for H₂), for set A.

For the computed $\Delta_f G_{298K, "Best"}^{0, TA14}$ values of set A, the most important sources of deviation from experiment were considered to be the uncertainties in the estimation of the core-valence correlation and post-CCSD(T) electronic correlation contributions to total atomization energies. These effects are discussed in previous section.

Halamine formation is endoergonic with respect to the elemental forms at standard state, with $\Delta_f G_{298K, "Best"}^{0, TA14}$ values ranging from 19.39 kcal mol⁻¹ to 93.46 kcal mol⁻¹. No experimental gas phase thermochemistry data are available for halamines. Based on results for molecule set A, we estimate 1 kJ mol⁻¹ (0.24 kcal mol⁻¹) uncertainties in the computed $\Delta_f G_{298K}^0$ values of the chloramines (NH₂Cl, NHCl₂, and NCl₃) and of monobromamine (NH₂Br). For NHBBr₂, NBr₃, and for the bromochloramines, we assign larger uncertainties of 3 kJ mol⁻¹ (0.72 kcal mol⁻¹) in computed $\Delta_f G_{298K}^0$ values, for reasons discussed in the section on TAE_{0K} data. It is worth noting that, unlike molecules of set A, the di- and tri-halogenated halamines contain some low frequencies, with the lowest frequencies ranging from 148 cm⁻¹ (NBr₃) to 283 cm⁻¹ (NHCl₂) (Table A.2 in the Appendix). However, the anharmonic corrections do not account more than 5

Chapter 3

cm^{-1} for the low-frequency bending modes of any of these species. Accurate gas phase Gibbs free energies of formation at 298 K are key thermodynamic properties for studying reaction chemistry involving halamines. This is illustrated further in the next section.

Table 2.8 Gas Phase Gibbs Free Energies of Formation at 298 K: Experimental and Theoretical Values [kcal mol^{-1}]

Compound	$\Delta_f G_{298\text{K}, \text{TA14}}^{0, \text{TA14}}$	$\Delta_f G_{298\text{K}}^{0, \text{Expt}}$
Set A		
H ₂	-0.03	0[105]
N ₂	0.18	0 [105]
O ₂	0.09	0 [105]
Cl ₂	0.06	0[105]
Br ₂	0.74	0.74 ± 0.03[105]
HCl	-22.85	-22.744 ± 0.001[105]
HBr	-12.55	-12.69 ± 0.03[105]
HOCl	-15.49	-15.30 ± 0.01[105]
HOBr	-15.14	-15.26 ^a
H ₂ O	-54.71	-54.63 ± 0.01[105]
NH ₃	-3.78	-3.83 ± 0.03[105]
Average Absolute Deviation	0.09	
Average Deviation	-0.02	
Signed Maximum Deviation	0.19 (HOCl)	
Set B		
NH ₂ Cl	19.39	N/A ^b
NHCl ₂	41.62	N/A ^b
NCl ₃	63.38	N/A ^b
NH ₂ Br	22.98	N/A ^b
NHBr ₂	49.46	N/A ^b
NBr ₃	73.15	N/A ^b
NHBrCl	44.19	N/A ^b
NBrCl ₂	67.56	N/A ^b
NBr ₂ Cl	93.46	N/A ^b

^aThe $\Delta_f S_{298\text{K}}^{0, \text{Expt}}$ value for HOBr was calculated using experimental rotational constants[174] and experimental vibrational frequencies,[175, 176] assuming an NVT ensemble, according to statistical mechanic expressions outlined in the Hill textbook.[137] ^bNot available.

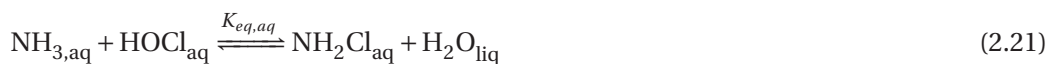
2.5 Implications for Aqueous Chemistry of Chloramines and Bromamines

The purpose of this study is to provide accurate thermochemistry data describing the formation of chloramines, bromamines, and bromochloramines. With the W4 and FPD procedures as a guiding basis, we successfully designed a computational method (TA14) that

2.5. Implications for Aqueous Chemistry of Chloramines and Bromamines

accomplished this goal. It was not our aim to test TA14 against a broad thermochemical database. However, our limited assessment of molecules that are structurally related to the halamines confirms that our approach successfully achieved the targeted level of accuracy in thermochemical properties.

The estimation of gas phase free energies of formation of chloramines, bromamines, and bromochloramines allows us to predict the equilibrium constants for the reactions involving these species. By combining gas phase $\Delta_f G_{298K, "Best"}^{0, TA14}$ data reported here together with experimental or computed estimates of solvation free energies for the pertaining species, it is possible to assess the equilibrium constants of the formation of chloramines, bromamines, and bromochloramines in aqueous phase. This can lead to further insights into the thermodynamics and the kinetics of the generation and decomposition processes affecting these reactive species during water treatment. As an illustrative example, we consider the generation of monochloramine from HOCl and NH_3 in water, which is an important reaction during water treatment:



where $K_{eq,aq}$ represents the aqueous equilibrium constant of the reaction shown by equation 2.21. A computational estimate of $K_{eq,aq}$ can be obtained by:

$$\log K_{eq,aq} = -2.303RT \ln \Delta_{rxn} G_{aq}, \quad (2.22)$$

where $\Delta_{rxn} G_{aq}$ is Gibbs free energy of reaction in aqueous phase. The $\Delta_{rxn} G_{aq}$ can be estimated from:

$$\Delta_{rxn} G_{aq} = \Delta_{rxn} G_{gas} + \Delta \Delta_{rxn} G_{solv}, \quad (2.23)$$

where $\Delta_{rxn} G_{gas}$ is the Gibbs free energy of reaction in gas phase and the $\Delta \Delta_{rxn} G_{solv}$ is the change in free energy of solvation upon converting reactants to products. For the reaction shown by equation 2.21, $\Delta \Delta_{rxn} G_{solv}$ was deduced from available experimental Henry's law constant data for NH_3 , [70] NH_2Cl , [70] and HOCl, [70] and using the value -6.31 for the ΔG_{solv} of H_2O in the 1 M standard state of the ideal dilute solution as proposed by Liptak and Shields. [177] The ΔG_{solv} for H_2O was also corrected for the conversion from the 1 M standard state to the 55.56 M pure liquid standard state, corresponding to a free energy change of 2.38 kcal mol⁻¹. [7]

Using our theoretical $\Delta_f G_{298K, "Best"}^{0, TA14}$ data to obtain $\Delta_{rxn} G_{gas}^{TA14}$ and combining this with experimental $\Delta \Delta_{rxn} G_{solv}^{Expt}$ data, we produce a theoretical estimated equilibrium constant of $\log K_{eq,aq}^{TA14} = 10.5$, according to equations 2.22 and 2.23 (Table 2.9). For comparison, Morris and Isaac [42] proposed an experimental value of 11.3 for the equilibrium constant, $K_{eq,aq}^{Expt}$, of monochloramine generation in aqueous phase (equation 2.21), derived from the ratio of the

Table 2.9 Experimental and Theoretical Equilibrium Constants for Generation of Monochloramine in Aqueous Phase

$\Delta_{rxn}G_{gas}^{TA14}$	$\Delta\Delta_{rxn}G_{solv}^{Expt}$	$\Delta_{rxn}G_{aq}^{TA14}$	$\Delta_{rxn}G_{aq}^{Expt}$	$\log K_{eq,aq}^{TA14}$	$\log K_{eq,aq}^{Expt}$
-16.1 ^a	1.8 ^a	-14.3 ^a	-15.6 ^a	10.5	11.3

^akcal mol⁻¹.

experimental forward rate constant, k_f , with the experimental reverse rate constant, k_r :

$$\log K_{eq,aq}^{Expt} = \log \frac{k_f}{k_r} \quad (2.24)$$

Our theoretical $\log K_{eq,aq}^{TA14}$ is in reasonable agreement with the experimental estimate (Table 2.9). We suspect that the discrepancy of 1.3 kcal mol⁻¹ in $\Delta_{rxn}G_{aq}^{TA14}$ arises mostly from uncertainties in the experimental Henry's law constant data used to estimate $\Delta\Delta_{rxn}G_{solv}$ or from experimental reaction rate constant data used to estimate $\Delta_{rxn}G_{aq}^{Expt}$.

Thermodynamic equilibria for hypothetical reactions of halamines with relevant species in natural water, such as inorganic anions and electron-rich organic nucleophiles, can now be determined based on free energies of formation of halamines supplied in the present study. Such reactions are relevant to understanding the chemical sinks of halamines during drinking water treatment as well as the pathways that could lead to the formation of toxic disinfection byproducts.

2.6 Acknowledgments

We thank Urs von Gunten (EPFL/EAWAG), Jennifer J. Guerard (UA Fairbanks), Peter R. Tentscher (EPFL), and David Feller (Washington State University) for helpful discussions. We also thank the EPFL centralized HPC facilities for computational resources.

3 Equilibria and Speciation of Chloramines, Bromamines, and Bromochloramines in Water

Daniela Trogolo^a and J. Samuel Arey^{*b}

Accepted in Environmental Science and Technology

Contributions:

I am the main author of this chapter. I carried out all quantum chemical simulations. Sam Arey provided guidance in the development of the computational methods and he substantially contributed to the manuscript writing and editing.

^a Environmental Chemistry Modeling Laboratory, École Polytechnique Fédérale de Lausanne (EPFL), Station 2, 1015 Lausanne, Switzerland.

^b Swiss Federal Institute of Aquatic Science and Technology (EAWAG), Dübendorf, Switzerland.

3.1 Abstract

The stabilities and speciation of the halamines in water are difficult to characterize experimentally. We provide theoretical estimates of aqueous standard free energies of formation for inorganic chloramines, bromamines, and bromochloramines, based on high-accuracy theoretical standard free energies of formation in gas phase combined with quantum chemical estimates of Henry's law constant. Based on comparisons between theoretical and experimental data, we assign an error of 1.1 – 1.2 log unit for equilibrium constants of several reactions leading to halamines in water. The reactions of ammonia with HOCl or HOBr that lead to dichloramine, trichloramine, and tribromamine are found to be thermodynamically more favorable than was previously believed. The newly reported equilibrium data also allow us to propose rate constant values for some hydrolysis and disproportionation reactions of dichloramine, monobromamine, and bromochloramine. Finally, theoretical results indicate aqueous acid dissociation constant (pK_a) values of 1.5 ± 1 for NH_3Cl^+ , 0.8 ± 1 for NH_3Br^+ , 11.8 ± 1 for NHCl_2 , and 12.5 ± 1 for NHBrCl . The present report provides a comprehensive dataset describing the free energies of the neutral inorganic halamines, the anionic conjugate base species, and the cationic conjugate acid species, with approximately uniform uncertainty bounds assigned throughout.

3.2 Introduction

Aqueous chloramines, bromamines, and bromochloramines, collectively termed halamines in the present work, typically arise from the N-substitution reactions of hypohalous acids with ammonia:[178, 40, 41, 43, 42, 179, 44, 56, 46, 53, 180, 54, 181, 182, 51, 183]



where X is either Cl or Br. Dichloramine,[42, 184, 179, 185] dibromamine,[56, 186, 182] and bromochloramine[57] can also form by disproportionation reactions. Chloramines are applied widely as disinfectants in water treatment facilities, and their decomposition is directly implicated in the production of potentially toxic disinfection byproducts (DBPs).[187, 63, 58, 36, 37, 188, 189, 190, 191, 192, 66, 65, 193, 194, 195, 196, 197, 67, 68, 198, 199, 200, 201, 202] During chloramination of natural waters, chloramines can provide the nitrogen source

for the formation of several families of nitrogenous disinfection byproducts, including halonitriles,[65, 197] halonitroalkanes,[65, 197] and nitrosamines.[65, 67, 68, 198, 199, 200, 201, 202, 193, 203] Chloramines can also participate in substitution and redox reactions with organic micropollutants.[61, 203, 204, 66, 198, 199]

The presence of naturally occurring bromide in fresh waters can potentially lead to the production of hypobromous acid, bromamines, and bromochloramines, during chlorination, chloramination, or ozonation of natural waters.[205, 47, 48, 50, 51, 186, 53, 54, 57, 56, 55, 206, 202] During oxidative water treatment of natural water, bromide can react with hypochlorous acid to produce HOBr,[207, 208] which can subsequently brominate ammonia and substituted amines, thereby producing bromamines (equations 3.1-3.3). These species can then further react rapidly to form dibromamine, tribromamine, and bromochloramines (equations 3.1-3.3).[49, 50, 69, 57, 55, 186] Bromamines and bromochloramines can lead to the production of potentially toxic DBPs in water as well.[60, 59, 209, 210] For example, NHBr_2 and NHBrCl are thought to be involved in the production of NDMA [209, 59] and of CNBr [210, 60] during water disinfection.

Chloramines and bromamines also arise in activated neutrophil and eosinophil cells during inflammatory disease affecting mammals, due to the reactions of HOCl or HOBr with nitrogen-containing biological molecules such as proteins and amino acids.[74, 80] Thus formed bromamines and chloramines can undergo oxidation reactions with O_2^- [80] or metal ions,[77, 211] generating nitrogen- and carbon-centered radicals. The spontaneous decomposition of such radical intermediates can damage the cell, inducing protein fragmentation, protein modification, and tissue damage.[77, 211]

Despite that the halamines have been studied for several decades, chemical equilibrium constants remain highly uncertain for relevant formation, disproportionation, and protonation/deprotonation reactions of many of these species. The rate constants and the equilibrium constants of the reactions involving chloramines are difficult to measure because several short-lived species can arise simultaneously, and in many cases these values must be constrained with kinetic models.[178, 212, 46, 185, 181, 41, 213, 57] The equilibria and the kinetics describing the production of bromamines and mixed halamines are also incomplete.[214, 215, 47, 180, 186, 50] Further complicating matters, the acid dissociation constant (pK_a) values remain unknown for most of the neutral chloramines, bromamines, and bromochloramines and also for their cationic conjugate acids.[43, 216]

Quantum chemical models provide an alternative approach for the determination of the aqueous equilibria of halamines. For example, chlorination reactions of amino functional groups were studied recently by computational chemical approaches.[217, 218, 219, 90] Rayson et al.[218] and Andrés et al.[217] investigated the oxidation of ammonia with HOCl by employing density functional methods. In other work, the G3B3[220] composite method was used to describe N-chlorination reactions of organic amines by HOCl.[219] Theoretical methods were also used by Rayne and Forest to estimate aqueous free energies

of reactions leading to chloramines (equations 3.1-3.3).[90] However, these approaches do not achieve sub-kcal mol⁻¹ accuracy in the free energies of the aqueous reactions leading to chloramines. For example, the gas phase theoretical enthalpies of reaction of Rayne and Forest exhibit discrepancies with respect to more accurate benchmark data published recently.[221, 222] Standard heats of formation (ΔH_f^o) and standard free energies of formation (ΔG_f^o) in gas phase were determined recently using high-accuracy theoretical methods for chloramines, bromamines, and bromochloramines, and these data were assigned uncertainties of 1-3 kJ mol⁻¹. [221, 222] However, the influence of aqueous solvent on these gas phase thermodynamic data remains to be established.

The goal of the present study is to establish reliable estimates of the standard free energies of formation and the acid dissociation constants of inorganic chloramines, bromamines, and bromochloramines in aqueous solution. We compare these theoretical results with available experimental data. Attention is paid to reporting realistic uncertainty bounds for these theoretically estimated thermodynamic properties. The results enable us to determine the aqueous equilibria for the principal pathways that generate halamines during drinking water treatment.

3.3 Methods

3.3.1 Computational Estimates of Free Energies of Solvation

The free energy of aqueous solvation of a chemical species, ΔG_{solv}^* , describes its equilibrium distribution between the gas and aqueous phases. According to the standard state convention used in the present study, ΔG_{solv}^* is defined as the energy required to transfer one mole of a chemical species from the gas phase to aqueous solution at a (hypothetically infinitely dilute) 1 M concentration in both phases.[223] The free energy of aqueous solvation is related to the experimentally measurable dimensionless Henry's law solubility constant, $K_H^{(-)}$:

$$\Delta G_{solv}^* = RT \ln K_H^{(-)} \quad (3.4)$$

More details on the conversion factors and the units of the Henry's law constant values are provided in the SIA.1.2.2. To estimate ΔG_{solv}^* values of the halamines, we considered several methodological approaches, including four implicit solvent models and also a cluster-continuum approach adapted from the method of Bryantsev and coworkers.[224]

3.3.2 Implicit Solvent Models: Methods and Basis Sets

Gas phase geometries for the halamines, HOCl, HOBr, NH₃, and H₂O were computed with the CCSD(T) electronic structure method and were taken from recent high-accuracy theoretical results.[221, 222] The gas phase geometries of Cl₂, Br₂, and NF₃ were optimized using the B2PLYPD[122, 123] DFT method with the aug-cc-pVQZ basis set,[126, 127, 225] as

implemented in Gaussian09.[124] Harmonic frequency analyses were subsequently carried out with the same electronic structure method used to obtain the geometries.

The implicit solvent models employed were the Universal Solvent Model based on the solute electron density[226] (SMD), the polarizable conductor calculation model (CPCM),[227, 228] and the polarizable conductor model (PCM)[229, 228, 230, 231] as implemented in Gaussian09,[124] and the COnductor-like Screening Model (COSMO)[232, 233] implemented in NWChem.[125] Free energies of solvation computed with these models are referred to as $\Delta G_{solv,SMD}^*$, $\Delta G_{solv,CPCM}^*$, $\Delta G_{solv,PCM}^*$, and $\Delta G_{solv,COSMO}^*$ respectively.

To obtain $\Delta G_{solv,SMD}^*$, $\Delta G_{solv,CPCM}^*$, $\Delta G_{solv,PCM}^*$, and $\Delta G_{solv,COSMO}^*$ for the species studied here, we performed B2PLYPD/aug-cc-pVQZ single point energy computations with the implicit solvent models SMD, CPCM, PCM, and COSMO, using the gas phase optimized geometries. The B2PLYPD method has been reported to give good performance for challenging multireference electronic structures such halogen oxides.[234, 235, 236, 97] To briefly test whether B2PLYPD is appropriate for the electronic structures of halamines and other halogen oxidants studied here, we evaluated gas phase total atomization energies and compared these results to recently published[221, 222] benchmark values (Table A.4 in SI). Based on the good performance of the B2PLYPD method for gas phase electronic structure predictions, we carried out free energy of solvation computations with B2PLYPD. Computations with the CPCM and PCM implicit solvent models were tried with different atomic radii (UFF, UAHE, and UAKS) as implemented in Gaussian09. To consistently calculate the solvent effect with the B2PLYPD method, we included the keyword *SCRF(ExternalIteration)*[237, 238] in the Gaussian09 input.

3.3.3 Cluster-continuum Solvent Models: Methods and Basis Sets

The cluster-continuum approach may allow a more accurate description of aqueous solvation effects, by including an explicit electronic treatment of interactions with one or more molecules of water.[224] Compared to implicit models, this approach has been found to give improved results for monoatomic ions.[224] The cluster-continuum approach has also been applied for neutral and charged organic molecules.[234] We obtained cluster-continuum results in combination with both the SMD and COSMO implicit solvent models. To apply this method, we employ a microsolvated cluster that contains the molecule of interest and one explicitly modeled molecule of water, together embedded in a conventional implicit solvent model. For the neutral halamine species studied here, a stable binary complex can be made between the halamine molecule and a single water molecule, in all cases by way of a hydrogen bond between the water H atom and the halamine N atom. Natural population analysis indicates that the N atom has a partial negative charge in all 9 inorganic chloramine, bromamine, and bromochloramine structures,[239] which facilitates this H-bond interaction with nearby aqueous solvent. Our cluster-continuum results assume that this hydrogen-bonded structure is representative of the interaction between a halamine solute

and a nearby water molecule in aqueous solvent. We did not see an advantage in increasing the number of explicit water molecules within the cluster-continuum framework. In our trial computations with a test set of neutral halogenated molecules including halamines, clusters containing the solute plus two explicitly modeled water molecules often exhibited shallow potential energy basins, and these clusters typically could occupy multiple stable geometric configurations that differed little in the potential energy (results not shown). We concluded that solvated clusters containing multiple water molecules were not suited to the cluster-continuum approach. The cluster-continuum model assumes that the geometric configuration of the cluster represents the most typical solvent structure near the solute, and the model also assumes that this configuration occupies a well-defined potential energy basin. The cluster-continuum estimate of the free energy of solvation can be obtained by an appropriate thermodynamic cycle,[224] explained further in the SIA.1.2.1. The free energies of solvation computed with the cluster-continuum approaches are referred to as $\Delta G_{solv,cluster-SMD}^*$ and $\Delta G_{solv,cluster-COSMO}^*$, depending on the implicit model used with the cluster.

To obtain free energies of solvation computed with the cluster-continuum approaches, $\Delta G_{solv,cluster-SMD}^*$ and $\Delta G_{solv,cluster-COSMO}^*$, it was necessary to compute several quantities, as shown in equations A.4 and A.5 in the SI. We conducted a gas phase geometry optimization of a cluster of the solute and one explicit molecule of water with the B2PLYPD/aug-cc-pVQZ model chemistry for chloramines, bromamines, bromochloramines, NH_3 , H_2O , $HOCl$, $HOBr$, Cl_2 , Br_2 , and NF_3 . In order to solve consistently the thermodynamic cycle on which the cluster-continuum approach is based, we performed additional gas phase geometry optimizations with B2PLYPD/aug-cc-pVQZ for all species. Harmonic vibrational frequency analyses were performed with B2PLYPD/aug-cc-pVQZ, used to compute gas phase thermal contributions to the free energies and to confirm the nature of the stationary points on the B2PLYPD potential energy surface. To evaluate the term in equation A.4, $\Delta G_{solv,SMD}^*(X(H_2O))$ that is used in the cluster-continuum-SMD approach (and the analogous term in the cluster-continuum-COSMO approach), we also carried out single point energy computations with SMD and COSMO implicit solvent models on gas phase geometries of a cluster of the solute and one explicit molecule of water.

3.3.4 Computational Estimates of Aqueous pK_a

We estimated aqueous acidity constant (pK_a) values for the deprotonation of both the neutral species and the cationic conjugate acid ammonium species, for several halamines. It is difficult to estimate pK_a values *a priori* with theoretical methods.[240, 241, 242] Therefore, we took advantage of the linear free energy relationship (LFER) that is commonly found between experimental and theoretical pK_a values within a family of structurally related acids.[240, 243, 244, 234, 245] We computed uncorrected quantum chemical acidity constant values according

to the equation:

$$pK_a^{uncorrected} = \frac{\Delta G_{aq}^{dep,uncorrected}}{2.303RT} \quad (3.5)$$

where $\Delta G_{aq}^{dep,uncorrected}$ is the raw quantum chemical estimate of the free energy of the aqueous deprotonation reaction. To obtain $\Delta G_{aq}^{dep,uncorrected}$, gas phase geometry optimizations, harmonic vibrational frequency analyses, and single point energy computations were conducted with the CBS-QB3[246, 247] composite method. The CBS-QB3 method has previously been shown to give good results for the proton affinities used in pK_a predictions.[248, 177, 249, 250, 234] Solvation free energies were computed with the SMD implicit solvent model and the M05[251]/aug-cc-pVTZ model chemistry. The SMD solvent method has been found to well perform in the calculations of free energies of solvation for pK_a predictions.[241, 242] Further details are provided in the SI. The resulting computed $pK_a^{uncorrected}$ values were substituted into the regression functions established by two linear free energy relationships, as explained below.

To construct a theoretical LFER for cationic ammonium functional groups, we fitted a linear regression between theoretical $pK_a^{uncorrected}$ values and previously reported experimental pK_a values for ammonium,[252] monochlorammonium,[43] chloromethylammonium,[43] methylammonium,[252] dimethylammonium,[253] bromodimethylammonium,[216] trimethylammonium,[254] anilinium,[255] 2-chloranilinium,[255] 2-bromoanilinium,[255] N-methylanilinium,[255] hydroxylammonium,[256] protonated hydrazine,[257] carbamidium (protonated urea),[258] acetamidium (protonated acetamide),[258] and thiocarbamidium (protonated thiourea).[258] This LFER was used to estimate the computed pK_a values of the cationic species monobromammonium, dibromammonium, dichlorammonium, bromomethylammonium, chloromethylammonium, dibromomethylammonium, and dichloromethylammonium.

To construct a theoretical LFER describing the acidity constant of the neutral amine functional group, we conducted a linear regression between theoretical $pK_a^{uncorrected}$ values and previously reported experimental pK_a data of hydrazoic acid,[259] acetamide,[259] sulfamide,[260] and trifluoromethanesulfamide.[259] The resulting LFER was employed to estimate the computed pK_a values of monochloramine, monobromamine, dichloramine, dibromamine, and bromochloramine.

3.4 Results and Discussion

3.4.1 Evaluation of Solvent Models for Halogen Species and Amines.

We evaluated six different solvent modeling approaches for their abilities to predict the free energies of solvation for species that are structurally related to the halamines. Four implicit solvent models (SMD, CPCM, PCM, and COSMO) and two cluster-continuum approaches

Table 3.1 Gibbs free energies of solvation for Cl₂, Br₂, NF₃, NH₃, H₂O, HOCl, inorganic chloramines, and methylated amines: experimental values and theoretical estimates. Values are in kJ mol⁻¹.

Compounds	$\Delta G_{solv,Expt}^*$	$\Delta G_{solv,SMD}^*$	$\Delta G_{solv,cluster-SMD}^*$	$\Delta G_{solv,half-and-half}^*$
Set A				
Cl ₂	-2.0 ^a ± 0.7	2.0	4.5	3.2
Br ₂	-7.1 ^a ± 0.7	-4.4	-3.7	-4.1
NF ₃	9.8 ^a ± 0.7	10.8	14.1	12.4
H ₂ O	-26.4 ^b	-28.6	-25.9	-27.3
NH ₃	-18.1 ^a ± 1.3	-13.1	-19.7	-16.4
NH ₂ CH ₃	-19.1 ^c ± 2.5	-15.2	-16.3	-15.8
NH(CH ₃) ₂	-17.9 ^c ± 2.5	-15.2	-13.7	-14.5
Set B				
NH ₂ Cl	-19.0 ^a ± 4.2	-16.3	-15.7	-16.0
NHCl ₂	-16.3 ^a ± 4.2	-10.2	-12.5	-11.3
NCl ₃	-2.2 ^a ± 4.2	2.6	4.8	3.7
HOCl	-24.0 ^a ± 4.2	-16.7	-21.8	-19.2
Set A				
Root Mean Square Error		3.3	3.8	3.2
Maximum Signed Deviation		5.0 (NH ₃)	6.5 (Cl ₂)	5.3 (Cl ₂)
Set B				
Root Mean Square Error		5.5	4.4	4.8
Maximum Signed Deviation		7.3 (HOCl)	7.0 (NCl ₃)	3.8 (HOCl)

^aExperimental free energies of solvation, based on Henry's law constant values, are taken from Sander's compilation.[261] ^bThe experimental free energy of solvation of H₂O is taken from Marenich et al.[262] ^cEstimates of Henry's law constant values were taken from Sander's compilation.[263]

were applied to Cl₂, Br₂, NF₃, NH₃, H₂O, NH₂CH₃ and NH(CH₃)₂ which we denoted as test set A (Table 3.1). Experimental Henry's law constants are available for these seven species (Table A.3),[261, 263, 262] with corresponding experimental free energy of solvation ($\Delta G_{solv,Expt}^*$) values that are considered to have uncertainties ranging from ± 0.7 kJ mol⁻¹ to ± 2.5 kJ mol⁻¹ (Table 3.1). We also tested the solvent models against experimental $\Delta G_{solv,Expt}^*$ values of the three chloramines and of hypochlorous acid, which have been assigned larger uncertainties of ± 4.2 kJ mol⁻¹. [261]

The SMD model and cluster-continuum-SMD approaches exhibit root mean square errors (RMSE) of 3.3 kJ mol⁻¹ and 3.8 kJ mol⁻¹, respectively, with respect to $\Delta G_{solv,Expt}^*$ values for set A (Table 3.1). However, the maximum deviations in the set were 7 kJ mol⁻¹ for both solvent models. The average unsigned error observed for SMD with test set A (3.1 kJ mol⁻¹) is very similar to the average unsigned errors that ranged from 2.5 to 3.8 kJ mol⁻¹ (depending on the DFT method) reported elsewhere[226] for SMD with a very large test set of small neutral molecules in water. The COSMO, CPCM, and PCM models produced worse results for this chemical test set (Table A.5), and these models were thus viewed as less appropriate for investigating the solvation of halamines in water.

Based on the above results, it is difficult to distinguish whether the SMD implicit model or the cluster-continuum-SMD approach would perform the best for estimating the free energies of solvation of bromamines, chloramines, and bromochloramines. Closer inspection of Table 3.1 results is revealing. Compared to the conventional SMD implicit model, the addition of an explicit water (i.e., cluster-continuum-SMD approach) improves, but "over-corrects", the predictions of Henry's law constants for the polar molecules NH_3 and H_2O . In contrast, the cluster-continuum-SMD approach appears to worsen slightly the results for the halogen-containing species (Cl_2 , Br_2 , NF_3), compared to conventional SMD. Taken together, these results suggest that a "half-and-half" approach, formulated as an average of the predictions by both solvent models, would produce the most accurate results overall for the related molecules, chloramines and bromamines. The "half-and-half" approach exhibits a RMSE of 3.2 kJ mol^{-1} in the free energies of solvation of set A. Based on these considerations, we propose that the error bounds expected to contain 95% of the deviations can be approximated by $2 \times \text{RMSE}$ found for the free energy of solvation data, and thus we assign an error of 6 kJ mol^{-1} to the free energy of solvation values estimated from the "half-and-half" approach for chloramines, bromamines, and bromochloramines (Table 3.2).

3.4.2 Estimated Aqueous Standard Free Energies of Formation for Chloramines, Bromamines, and Bromochloramines

We estimated aqueous standard free energies of formation of halamines and related compounds (Table 3.2) based on theoretically determined standard free energies of formation in gas phase, $\Delta_f G_{\text{gas,Comp}}^o(X)$, and computationally estimated free energies of solvation, $\Delta G_{\text{solv,half-and-half}}^*(X)$, according to:

$$\Delta_f G_{\text{aq,Comp}}^*(X) = \Delta_f G_{\text{gas,Comp}}^o(X) + \Delta G_{\text{solv,half-and-half}}^*(X) + \Delta G^{o \rightarrow *} \quad (3.6)$$

Theoretical benchmark $\Delta_f G_{\text{gas,Comp}}^o(X)$ values at 1 atm standard state were taken from recently published data.[221, 222] The $\Delta G_{\text{solv,half-and-half}}^*(X)$ values were obtained from an average of the SMD implicit solvent model results and the cluster-continuum-SMD results as discussed in the previous section. The term $\Delta G^{o \rightarrow *}$ represents the free energy required to transfer a molecule from the gas phase 1 atm standard state to the aqueous 1 M standard state.[223]

Table 3.2 Theoretical standard free energies of formation in gas phase ($\Delta_f G_{gas,Comp}^o$), theoretical free energies of aqueous solvation ($\Delta G_{solv,half-and-half}^*$), and theoretical and experimental aqueous standard free energies of formation ($\Delta_f G_{aq}^*$) for halamines and related compounds. Values are in kJ mol^{-1} .

Compounds	$\Delta_f G_{gas,Comp}^o$ ^a	$\Delta G_{solv,half-and-half}^*$ ^b	$\Delta_f G_{aq,Comp}^*$ ^b	$\Delta_f G_{aq,Expt}^*$
NH ₂ Cl	81.1 ± 1	-16.0 ± 6	73.1 ± 6	66.9 ^c , 84.0 ± 0.4 ^d
NHCl ₂	174.1 ± 1	-8.8 ± 6	173.3 ± 6	176.6 ^c , 209.2 ± 1.2 ^d
NCl ₃	267.1 ± 1	4.8 ± 6	279.8 ± 6	299.2 ^c , 341.4 ± 1.8 ^d
NH ₂ Br	96.2 ± 1	-14.9 ± 6	89.1 ± 6	77.0 ^c , 84.3 ± 0.5 ^d
NHBr ₂	206.9 ± 3	-9.4 ± 6	205.5 ± 7	181.1 ^c , 203.2 ± 1.5 ^d
NBr ₃	306.1 ± 3	0.4 ± 6	314.4 ^e ± 7	295.8 ^c , 329.6 ± 2.5 ^d
NHBrCl	184.9 ± 3	-8.8 ± 6	184.0 ± 7	
NBrCl ₂	282.7 ± 3	2.9 ± 6	293.5 ^e ± 7	
NBr ₂ Cl	292.9 ± 3	0.3 ± 6	301.2 ± 7	
NH ₃	-15.8 ± 1	-16.4 ± 6	-24.3 ± 6	-26.6 ^c
H ₂ O	-228.9 ± 1	-17.3 ± 6 ^f	-238.3 ± 6 ^f	-237.2 ^{cf}
HOCl	-64.8 ± 1	-19.2 ± 6	-76.1 ± 6	-79.9 ^c
HOBr	-63.4 ± 1	-16.2 ± 6	-71.7 ± 6	-82.4 ^c

^aThe gas phase standard free energies of formation at 298 K were taken from previous high-accuracy theoretical data.[221, 222] ^bThe error intervals reported for the theoretical standard free energy values are interpreted as error bounds that are expected to contain 95% of the deviations. ^cThese experimental aqueous standard free energies of formation were taken from Sugam and Helz.[215] No uncertainty bounds are available. ^dThese experimental aqueous standard free energies of formation were taken from Soulard and coworkers.[54] ^eExceptionally, the cluster-continuum component of the free energies of solvation for NBrCl₂ and NBr₃ was computed with the aug-cc-pVTZ basis set due to computational costs. ^fThe standard free energy of formation of H₂O in water is given at the 55.56 M pure liquid standard state instead of the 1 M aqueous standard state.

For computational $\Delta_f G_{aq,Comp}^*$ data, we assigned uncertainty bounds such that the computational predictions are expected to contain the correct experimental value in 95% of cases, as follows. In a previous study, we attributed an uncertainty of 1 kJ mol^{-1} to the $\Delta_f G_{gas,Comp}^o$ of the three chloramines and of monobromamine, whereas we assigned an uncertainty of 3 kJ mol^{-1} to the $\Delta_f G_{gas,Comp}^o$ values of bromochloramines, dibromamine, and tribromamine, based on comparisons between theoretical and experimental data discussed in that paper and citations therein.[221, 222] Based on the results discussed in the previous section (Table 3.1), the $\Delta G_{solv,half-and-half}^*$ values predicted with the "half-and-half" approach (an average of the SMD and the cluster-continuum-SMD values) are assigned an uncertainty of 6 kJ mol^{-1} . Based on propagation of error (equations A.11 and A.12), we estimated an error of 6 kJ mol^{-1} for the $\Delta_f G_{aq,Comp}^*$ values of chloramines, NH₃, H₂O, HOCl, HOBr, and NH₂Br, and an error of 7 kJ mol^{-1} for the $\Delta_f G_{aq,Comp}^*$ values of dibromamine, tribromamine, and the three bromochloramines. For the well-characterized molecules NH₃ and H₂O, the theoretical $\Delta_f G_{aq,Comp}^*$ values differ from the experimental $\Delta_f G_{aq,Expt}^*$ values by only 2.3 and 1.1 kJ mol^{-1} , respectively (Table 3.2). However for the chloramines and bromamines, there is less consistent agreement between theoretical and experimental results,

and some of the previously reported experimental data show large discrepancies from one another. A critical discussion of these different datasets is explored in the following section on aqueous equilibrium constants.

3.4.3 Aqueous Equilibrium Constants of Reactions that Produce to Chloramines, Bromamines, and Bromochloramines

Despite the wide importance of halamines in drinking water treatment, equilibrium constants have not been well-constrained for many of the reactions responsible for their occurrence. We determined equilibrium constants (K_{aq}^{Comp}) for several important reactions, based on theoretical $\Delta_f G_{aq,Comp}^*$ data (Table 3.2), and we compared these K_{aq}^{Comp} values to previously reported experimental estimates, where available.

For a reaction in aqueous solution, we can evaluate the aqueous free energy of reaction, ΔG_{aq}^* :

$$\Delta G_{aq}^* = \sum_i \nu_i \Delta_f G_{aq}^*(X_i) \quad (3.7)$$

where the ν_i is the stoichiometric coefficient of molecule X_i , and $\Delta_f G_{aq}^*(X_i)$ is the aqueous standard Gibbs free energy of formation for species X_i at 1 M standard state. For those reactions that generate water as a product, we applied a standard state conversion so that H_2O is at the liquid water (55.56 M) standard state (Table 3.2).[223] Further details on standard state conversion factors are provided in the SI. The computed aqueous equilibrium constant for a given reaction is obtained by:

$$K_{aq} = \exp\left(\frac{-\Delta G_{aq}^*}{RT}\right) \quad (3.8)$$

Theoretical equilibrium constant data, K_{aq}^{Comp} , reveal that reactions of ammonia with HOCl and HOBr that produce mono-, di-, and tri-halogenated species are highly favorable, with $\log K_{aq}^{Comp}$ values ranging from 8.1 to 11.8 (reactions 1-12, Table 3.3). The considered disproportionation reactions that involved neutral species (reactions 13-17, Table 3.3) were found to have $\log K_{aq}^{Comp}$ values ranging from -3.0 to 1.1. Based on the uncertainties ascribed to $\Delta_f G_{aq,Comp}^*$ values (Table 3.2), we assigned an error of ± 1.1 to ± 1.2 logarithmic unit to $\log K_{aq}^{Comp}$ values, depending on the reaction.

In previous reports, equilibrium constants have been estimated based on experimental data for several reactions that produce halamines. Morris and Isaac reported an aqueous equilibrium constant value, K_{aq}^{Exp} , of $10^{11.3}$ for the reaction leading to NH_2Cl (reaction 1, Table 3.3), a value of $10^{8.7}$ for the reaction leading to $NHCl_2$ (reaction 2), and a value of $10^{4.7}$ for the reaction leading to NCl_3 (reaction 3).[42] However, Kumar and coworkers[212] proposed an estimate of $10^{8.2}$ for K_3 , four orders of magnitude higher than the value suggested by Morris and Isaac.

The equilibrium constants reported by Morris and Isaac[42] and by Kumar et al.[12] were deduced based on the measurements of forward and reverse rate constants for these reactions. This discrepancy between different studies reflects the difficulties encountered during the measurements of rate constants used to deduce the equilibrium constants of these reactive species in water. Hofmann and Andrews estimated aqueous equilibrium constants for the production of bromamines,[214] based on estimated standard free energies of formation of bromamines taken from Sugam and Helz's work.[215] The aqueous equilibrium constants of one disproportionation reaction was estimated: the disproportionation of two molecules of monochloramine to form dichloramine (reaction 13).[42] The origins of some of these equilibrium constant data are discussed further in the section about rate constants, below.

We compared our theoretical aqueous equilibrium constant values, K_{aq}^{Comp} , with available estimates obtained from reported experimental data, K_{aq}^{Expt} . We found good agreement between our theoretical aqueous equilibrium constants and previously reported experimental values for the reactions leading to monochloramine (reaction 1), monobromamine (reaction 4), and dibromamine (reaction 5): the experimental and computational equilibrium constants for these reactions agree within 1 order of magnitude, which falls within the error bounds of the theoretical values (Table 3.3). We viewed that the experimental equilibrium constants reported for reactions 1 and 4 were reliable values, since both the forward and reverse rate constants can be measured under well-controlled conditions for these two reactions. We consider these findings as a validation of the theoretical approach, further confirming the validations of $\Delta_f G_{gas,Comp}^o$, $\Delta G_{solv,half-and-half}^*$, and $\Delta_f G_{aq,Comp}^*$ data, discussed above. However, the agreement between experimental and theoretical results decreases substantially for the reactions that produce dichloramine (reaction 2, Table 3.3), trichloramine (reaction 3), and tribromamine (reaction 6), as well as the disproportionation reaction 13. Theoretical $\log K_{aq}^{Comp}$ values for these reactions are ~ 2 to 5 orders of magnitude higher than the experimental equilibrium constants. The discrepancies observed for reactions 2, 3, 6, and 13 might be attributed to the difficulty in performing well-controlled experiments on these species.[42] The experimental equilibrium constant values for reactions 2, 3, 6, and 13 are not direct measurements; rather, they are constrained from kinetic and thermodynamic models that involve multiple reactions.[42, 215] Based on the expected uncertainty of our theoretical data, we infer that the theoretical equilibrium constant values have higher confidence than the previously reported experimental estimates for the reactions 2, 3, 6, and 13. These findings imply that the reactions that produce dichloramine, trichloramine, and tribromamine are more thermodynamically favorable than was previously estimated. Therefore, under circumneutral conditions conducive to the production of chloramines and/or bromamines, the equilibrium concentrations of the dichloramine, trichloramine, and tribromamine species are higher than what previous models have suggested.

Table 3.3 Equilibrium constants ($\log K_{aq}$) for reactions leading to halamines in water: computational and experimental estimates.

#	Reactions	$\log K_{aq}^{Comp a}$	$\log K_{aq}^{eq.3.9 b}$	$\log K_{aq}^{Expt}$
Chloramines				
1	$\text{NH}_{3,aq} + \text{HOCl}_{aq} \xrightleftharpoons{K_1} \text{NH}_2\text{Cl}_{aq} + \text{H}_2\text{O}_l$	11.4 ± 1.1	10.6 ± 0.8	$11.3^c, 8.2^d$
2	$\text{NH}_2\text{Cl}_{aq} + \text{HOCl}_{aq} \xrightleftharpoons{K_2} \text{NHCl}_{2,aq} + \text{H}_2\text{O}_l$	10.9 ± 1.1	10.7 ± 0.8	8.7^c
3	$\text{NHCl}_{2,aq} + \text{HOCl}_{aq} \xrightleftharpoons{K_3} \text{NCl}_{3,aq} + \text{H}_2\text{O}_l$	9.7 ± 1.1	8.7 ± 0.8	$4.7^c, 8.2^e, 7.5^d$
Bromamines				
4	$\text{NH}_{3,aq} + \text{HOBr}_{aq} \xrightleftharpoons{K_4} \text{NH}_2\text{Br}_{aq} + \text{H}_2\text{O}_l$	9.3 ± 1.1		10.5^f
5	$\text{NH}_2\text{Br}_{aq} + \text{HOBr}_{aq} \xrightleftharpoons{K_5} \text{NHBr}_{2,aq} + \text{H}_2\text{O}_l$	8.8 ± 1.2		8.7^f
6	$\text{NHBr}_{2,aq} + \text{HOBr}_{aq} \xrightleftharpoons{K_6} \text{NBr}_{3,aq} + \text{H}_2\text{O}_l$	$10.1^g \pm 1.2$		6.7^f
Bromochloramines				
7	$\text{NH}_2\text{Br}_{aq} + \text{HOCl}_{aq} \xrightleftharpoons{K_7} \text{NHBrCl}_{aq} + \text{H}_2\text{O}_l$	11.8 ± 1.2		
8	$\text{NH}_2\text{Cl}_{aq} + \text{HOBr}_{aq} \xrightleftharpoons{K_8} \text{NHBrCl}_{aq} + \text{H}_2\text{O}_l$	9.8 ± 1.2		
9	$\text{NHBrCl}_{aq} + \text{HOCl}_{aq} \xrightleftharpoons{K_9} \text{NBrCl}_{2,aq} + \text{H}_2\text{O}_l$	$9.2^g \pm 1.2$		
10	$\text{NHBrCl}_{aq} + \text{HOBr}_{aq} \xrightleftharpoons{K_{10}} \text{NBr}_2\text{Cl}_{aq} + \text{H}_2\text{O}_l$	8.7 ± 1.2		
11	$\text{NHCl}_{2,aq} + \text{HOBr}_{aq} \xrightleftharpoons{K_{11}} \text{NBrCl}_{2,aq} + \text{H}_2\text{O}_l$	$8.1^g \pm 1.2$		
12	$\text{NHBr}_{2,aq} + \text{HOCl}_{aq} \xrightleftharpoons{K_{12}} \text{NBr}_2\text{Cl}_{aq} + \text{H}_2\text{O}_l$	11.7 ± 1.2		
Disproportionation reactions				
13	$\text{NH}_2\text{Cl}_{aq} + \text{NH}_2\text{Cl}_{aq} \xrightleftharpoons{K_{13}} \text{NHCl}_{2,aq} + \text{NH}_{3,aq}^h$	-0.5 ± 1.1	0.1 ± 0.8	-2.6^i
14	$\text{NH}_2\text{Br}_{aq} + \text{NH}_2\text{Br}_{aq} \xrightleftharpoons{K_{14}} \text{NHBr}_{2,aq} + \text{NH}_{3,aq}^j$	-0.5 ± 1.2		0.5^k
15	$\text{NH}_2\text{Cl}_{aq} + \text{NH}_2\text{Br}_{aq} \xrightleftharpoons{K_{15}} \text{NHBrCl}_{aq} + \text{NH}_{3,aq}$	0.4 ± 1.2		
16	$\text{NHBrCl}_{aq} + \text{HOCl}_{aq} \xrightleftharpoons{K_{16}} \text{NHCl}_{2,aq} + \text{HOBr}_{aq}$	1.1 ± 1.2		
17	$\text{NHBrCl}_{aq} + \text{HOBr}_{aq} \xrightleftharpoons{K_{17}} \text{NHBr}_{2,aq} + \text{HOCl}_{aq}$	-3.0 ± 1.2		
18	$2 \text{NH}_2\text{Cl}_{aq} + \text{Br}_{aq}^- + \text{H}_{aq}^+ \xrightleftharpoons{K_{18}} \text{NHBrCl}_{aq} + \text{NH}_{4,aq}^+ + \text{Cl}_{aq}^-$	12.0^l		

^aThese estimates were calculated using equations 3.6 and 3.7. Uncertainty bounds are assigned such that the prediction is expected to contain the correct experimental value in 95% of cases. ^bThese estimates were calculated using equation 3.9. ^cThis $\log K_{aq}^{Expt}$ value was obtained from Morris and Isaac's fitting model.[42] ^dThese values were taken from Soulard et al.[54] ^eThis experimental value was taken from Kumar and coworkers.[212] ^fThese values were taken from Hofmann and Andrews' review.[214] ^gExceptionally, the free energies of solvation for the reactions leading to NBrCl_2 and NBr_3 were computed with the aug-cc-pVTZ basis set, due to the computational cost of computations with larger basis sets. ^hThis reaction can take place by two parallel pathways: a neutral uncatalyzed pathway and also an acid-catalyzed pathway. The computed and experimental equilibrium constant values reported here refer to the uncatalyzed reaction.[264] ⁱThese values were taken from Morris and Isaac's work.[42] ^jThis reaction can take place by two parallel pathways: a neutral uncatalyzed pathway and also an acid-catalyzed pathway. The computed and experimental equilibrium constant values reported here refer to the uncatalyzed reaction.[56] ^kThis value was taken from Lei et al.[56] ^lThis value was derived using the theoretical aqueous standard free energy of formation for NH_2Cl and NHBrCl (Table 3.2) and the previously reported experimental standard free energy of formation[265] for H_{aq}^+ , Br_{aq}^- , $\text{NH}_{4,aq}^+$, and Cl_{aq}^- .

For further validation of our theoretical equilibrium constant values, K_{aq}^{Comp} , we compare them to a second set of estimates, referred to as $K_{aq}^{eq.3.9}$. These values were determined based on theoretical $\Delta_f G_{gas,Comp}^o$ values (Table 3.2) combined with previously reported experimental Henry's law constants, where available:

$$K_{aq}^{eq.3.9} = \exp \left(\frac{-\sum_i \nu_i (\Delta_f G_{gas,Comp}^o(X_i) + \Delta G_{solv,Expt}^*(X_i) + \Delta G^{o \rightarrow *})}{RT} \right) \quad (3.9)$$

Based on available experimental reports of Henry's law constants, we determined the $K_{aq}^{eq.3.9}$ for reactions involving chloramines (reactions 1, 2, 3, and 13, Table 3.3). We assigned an uncertainty of 0.8 log unit to the $\log K_{aq}^{eq.3.9}$ values based on the uncertainty of 1 kJ mol⁻¹ attributed to $\Delta_f G_{gas,Comp}^o$ and the uncertainty of 4.2 kJ mol⁻¹ associated with the $\Delta G_{solv,Expt}^*$.

The resulting $K_{aq}^{eq.3.9}$ values for reaction 1, 2, 3, and 13 (Table 3.3) all exhibit good agreement with K_{aq}^{Comp} estimates obtained from the theoretical ΔG_{aq}^* given by equation 3.6, which offers mutual validation of these two datasets. In contrast, the $K_{aq}^{eq.3.9}$ values for reactions 2, 3, and 13 are up to 4 orders of magnitude higher than the reported experimental estimates. These data further confirm the above conclusion that the theoretical estimates of the present study improve upon the previously reported experimental estimates for reactions 2, 3, 6, and 13.

We also estimated the aqueous equilibrium constant for the disproportionation reaction between two molecules of NH₂Cl and Br⁻ (reaction 18, Table 3.3). We combined theoretical aqueous standard free energies of formation for the NH₂Cl and NHBrCl species from Table 3.2 together with reported experimental aqueous standard free energies of formation[265] for the remaining compounds, H⁺, Br⁻, NH₄⁺, and Cl⁻. Since we could not find uncertainty bounds for the experimental aqueous standard free energy of formation data, we did not assign an uncertainty value to this equilibrium constant.

3.5 Implications for Reaction Rate Constants

Based on the theoretical aqueous equilibrium constants presented here (Table 3.3), we can re-evaluate rate constant data for some of the decomposition reactions for chloramines, bromamines, and bromochloramines. For this purpose, we took advantage of the relationship between the reaction equilibrium constant, the forward reaction rate constant, and the reverse reaction rate constant:[266]

$$k_r^{eq.3.10} = \frac{k_f^{Expt}}{K_{aq}^{Comp}} \quad (3.10)$$

3.5. Implications for Reaction Rate Constants

Table 3.4 New estimates of reverse rate constant values for selected reactions that produce chloramines, bromamines, and bromochloramines.

# ^a	Reaction	$k_{f,rxn}^{Expt}$	$k_{r,rxn}^{eq.3.10}{}^b$	$k_{r,rxn}^{Expt}$
1	$\text{NH}_{3,\text{aq}} + \text{HOCl}_{\text{aq}} \xrightleftharpoons[k_{-1}]{k_1} \text{NH}_2\text{Cl}_{\text{aq}} + \text{H}_2\text{O}_l$	$4.2 \times 10^6 \text{ M}^{-1}\text{s}^{-1}{}^c$	$2 \times 10^{-5} \text{ s}^{-1}$	$2.1 \times 10^{-5} \text{ s}^{-1}{}^c$
2	$\text{NH}_2\text{Cl}_{\text{aq}} + \text{HOCl}_{\text{aq}} \xrightleftharpoons[k_{-2}]{k_2} \text{NHCl}_2\text{aq} + \text{H}_2\text{O}_l$	$3.5 \times 10^2 \text{ M}^{-1}\text{s}^{-1}{}^c$	$5 \times 10^{-9} \text{ s}^{-1}$	$7.6 \times 10^{-7} \text{ s}^{-1}{}^c$
4	$\text{NH}_{3,\text{aq}} + \text{HOBr}_{\text{aq}} \xrightleftharpoons[k_{-4}]{k_4} \text{NH}_2\text{Br}_{\text{aq}} + \text{H}_2\text{O}_l$	$7.50 \pm 0.4 \times 10^7 \text{ M}^{-1}\text{s}^{-1}{}^d$	$4 \times 10^{-2} \text{ s}^{-1}$	
8	$\text{NH}_2\text{Cl}_{\text{aq}} + \text{HOBr}_{\text{aq}} \xrightleftharpoons[k_{-8}]{k_8} \text{NHBrCl}_{\text{aq}} + \text{H}_2\text{O}_l$	$2.86 \pm 0.06 \times 10^5 \text{ M}^{-1}\text{s}^{-1}{}^e$	$5 \times 10^{-5} \text{ s}^{-1}$	
13	$\text{NH}_2\text{Cl}_{\text{aq}} + \text{NH}_2\text{Cl}_{\text{aq}} \xrightleftharpoons[k_{-13}]{k_{13}} \text{NHCl}_2\text{aq} + \text{NH}_{3,\text{aq}}{}^f$	$5.6 \times 10^{-2} \text{ M}^{-1}\text{s}^{-1}{}^c$	$0.2 \text{ M}^{-1} \text{ s}^{-1}$	$24 \text{ M}^{-1}\text{s}^{-1}{}^c$

^aReaction number is taken from Table 3.3. ^bEstimates were calculated using equation 3.10. ^cExperimental values were taken from Morris and Isaac's work.[42] ^dExperimental value was taken from Wajon and Morris.[180] ^eExperimental value was taken from Gazda and Margerum.[50] ^fThis reaction can take place by two parallel pathways: a neutral uncatalyzed pathway and also an acid-catalyzed pathway. The calculated and experimental rate constant values reported here refer to the uncatalyzed reaction.[264]

We assumed that the forward experimental rate constant (k_f^{Expt}) had been determined reliably by experiment in previous reports for the five reactions shown in Table 3.4. Equilibrium constant values (K_{aq}^{Comp}) were taken from our theoretical results (Table 3.3). We compared our theoretically supported estimates of the reverse rate constant for the production of monochloramine, $k_{-1}^{eq.3.10}$, to the previously reported experimental value, k_{-1}^{Expt} . By way of equation 3.10, our theoretical estimate, $k_{-1}^{eq.3.10} = 2 \times 10^{-5} \text{ s}^{-1}$, is in good agreement with the experimental value, $k_{-1}^{Expt} = 2.1 \times 10^{-5} \text{ s}^{-1}$. [42] The agreement between k_{-1}^{Expt} and $k_{-1}^{eq.3.10}$ is consistent with the observed agreement between K_1^{Comp} and K_1^{Expt} for this reaction (Table 3.3). For the chlorination reaction of monochloramine to form dichloramine, we determined a theoretical reverse rate constant of $k_{-2}^{eq.3.10} = 5 \times 10^{-9} \text{ s}^{-1}$, based on the reported experimental value of the forward reaction (Table 3.4) and the theoretical equilibrium constant, $K_{aq}^{Comp} = 10^{10.9 \pm 1.1}$ (Table 3.3). The resulting value of $5 \times 10^{-9} \text{ s}^{-1}$ for the rate constant of the hydrolysis of dichloramine, $k_{-2}^{eq.3.10}$, disagrees with the experimental value ($7.6 \times 10^{-7} \text{ s}^{-1}$) by a factor of 152. The origin of this discrepancy is explained as follows. Morris and Isaac determined the equilibrium constant for reaction 2 as a ratio of the experimental equilibrium constant (K_1^{Expt}) of the formation of monochloramine ($10^{11.3}$, Table 3.4) and the experimental equilibrium constant, $K_{13}^{Expt} = 10^{-2.6}$ of the disproportionation of NH_2Cl to NHCl_2 (reaction 13). These authors then used their estimate of the equilibrium constant of reaction 2 together with their experimental forward rate constant (Table 3.4) to deduce an experimental reverse rate constant for reaction 2. However the value of K_{13}^{Expt} of reaction 13 deviates from our theoretical equilibrium constant ($K_{13}^{Comp} = 10^{-0.5 \pm 1.1}$). The discrepancy observed for the experimental equilibrium constant for the disproportionation reaction of monochloramine (reaction 13) propagates to the aqueous equilibrium constant for the chlorination reaction of monochloramine (reaction 2). Based on these considerations, we

propose our value of the reverse rate constant, $k_{-2}^{eq.3.10} = 5 \times 10^{-9} \text{ s}^{-1}$, as a better alternative to the previous estimate, $7.6 \times 10^{-7} \text{ s}^{-1}$.

For the disproportionation reaction of two molecules of monochloramine to form dichloramine (reaction 13), we estimated a theoretical reverse rate constant, $k_{-13}^{eq.3.10}$, of $0.2 \text{ M}^{-1}\text{s}^{-1}$, based on the rate constant for the forward reaction reported by Morris and Isaac, $k_{13}^{Expt} = 5.6 \times 10^{-2} \text{ M}^{-1}\text{s}^{-1}$, and the theoretical aqueous equilibrium constant of $K_{13}^{Comp} = 10^{-0.5 \pm 1.1}$. The resulting theoretically supported value of $k_{-13}^{eq.3.10}$, $0.2 \text{ M}^{-1}\text{s}^{-1}$, is two orders of magnitude lower than the experimental estimate ($k_{-13}^{Expt} = 24 \text{ M}^{-1}\text{s}^{-1}$). We interpret that this discrepancy arises from the experimental aqueous equilibrium constant, $K_{13}^{Expt} = 10^{-2.6}$, [42] which is two orders of magnitude lower than the theoretical value, $K_{13}^{Comp} = 10^{-0.5 \pm 1.1}$. Hence, using similar reasoning as for reaction 2 (above), we propose our theoretically supported value of $k_{-13}^{eq.3.10}$ as an alternative to the experimentally derived estimate.

Further taking advantage of equation 3.10, here we provide theoretical estimates of the reverse rate constants for the bromination reactions of ammonia and monochloramine (reactions 4 and 8), based on the previously determined k_f^{Expt} values and our theoretical K_{aq}^{Comp} values (Table 3.3) for these reactions. For reaction 4, we used the forward rate constant value proposed by Wajon and Morris, [180] $k_4^{Expt} = 7.5 \pm 0.4 \times 10^7 \text{ M}^{-1}\text{s}^{-1}$. This value was confirmed later by Inman and Johnson [186] who reported a kinetic constant of $4 \times 10^7 \text{ M}^{-1}\text{s}^{-1}$, and by Heeb [239] who proposed a value of $5.5 \times 10^7 \text{ M}^{-1}\text{s}^{-1}$. Our resulting estimate of $k_{-4}^{eq.3.10} = 4 \times 10^{-2} \text{ s}^{-1}$ is reasonably consistent (within an expected uncertainty of an order of magnitude) with the value originally reported by Haag and Lietzke, $1.5 \times 10^{-3} \text{ s}^{-1}$. [213] For reaction 8, which describes the production of chlorobromamine from the reaction of NH_2Cl with HOBr , we assumed the forward rate constant measured by Gazda and Margerum, $k_8^{Expt} = 2.86 \pm 0.06 \times 10^5 \text{ M}^{-1}\text{s}^{-1}$. [50] This value implies a reverse rate constant of $k_{-8}^{eq.3.10} = 5 \times 10^{-5} \text{ s}^{-1}$. Based on the theoretical aqueous equilibrium constants reported here, we were thus able to (re)assess the rate constants of some decomposition and disproportionation reactions involving chloramines, bromamines, and bromochloramines. Similar exercises could be applied to other available rate constant data involving halamines, based on the thermodynamic property data that we have provided in the present work.

3.5.1 pK_a Values for Chloramines, Bromamines, and Bromochloramines: Theoretical Estimates

Dissociation constants of chloramines and bromamines are difficult to measure experimentally due to the high reactivities of these molecules in water. We estimated acid dissociation constant values for both the cationic conjugate acid and neutral amine functional group of chloramines, bromamines, bromochloramines, and selected methyl-substituted halamines.

We established a quantum chemical LFER (Table A.7 in SI) based on previously reported experimental pK_a values of 16 substituted ammonium groups. We found a correlation coefficient of $R^2 = 0.98$ for the regression line of this computational LFER (Figure 3.1).

The following equation was used to determine the computed pK_a values of several chlorammonium and bromammonium species (Table 3.5):

$$pK_a^{Quantum\ Chemical\ LFER} = 1.83 \times pK_a^{uncorrected} - 6.25 \quad (3.11)$$

We also constructed a quantum chemical LFER (Table A.8) based on theoretical and experimental pK_a data of 4 neutral amine functional groups. The regression line of the LFER (equation A.13) established to estimate the pK_a values for neutral halamines had a correlation coefficient R^2 of 0.93 (Figure A.1). This relationship was used to predict the pK_a values for neutral chloramines, bromamines, and bromochloramines (Table 3.5). Uncertainties of the predicted pK_a values were assigned as ± 1 log unit, based on previous work on LFER prediction of pK_a values[240, 243, 244, 234] and on the observed scatter in the fitted LFER data (Tables A.7 and A.8).

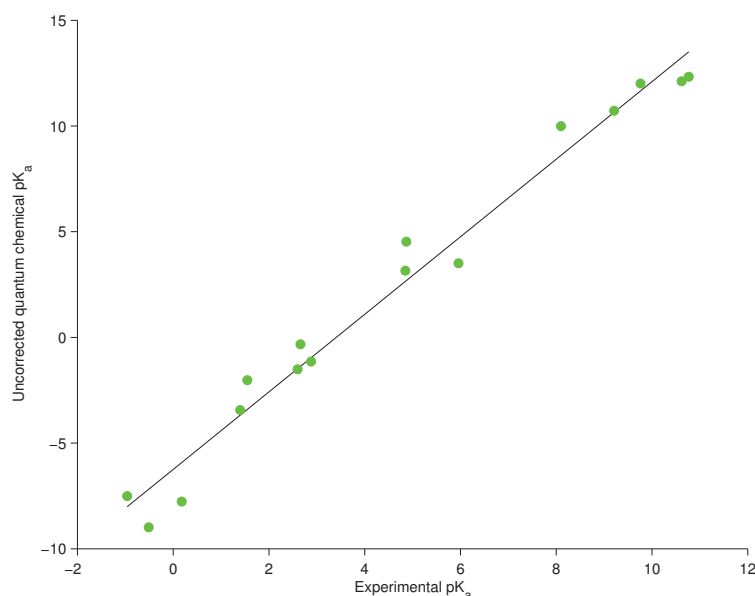


Fig. 3.1 Correlation between the experimental pK_a values and the uncorrected quantum chemical $pK_a^{uncorrected}$ results for the ammonium functional group of several compounds, including some halamines for which data are available (Table A.7).

Table 3.5 Estimated pK_a values for the cationic conjugate acid and neutral chloramines, bromamines, bromochloramines, and methylated halamines, according to quantum chemical LFER results (Tables A.7, A.8, Figure 3.1 and Figure A.1).

Deprotonation reactions	pK_a X = Cl	pK_a X = Br	pK_a X = Cl and Br
$\text{NH}_3\text{X}^+ \xrightleftharpoons{K_a^{\text{NH}_3\text{X}^+}} \text{NH}_2\text{X} + \text{H}^+$	$1.5 \pm 1^a, 1.44^b$	0.8 ± 1^a	
$\text{NH}_2\text{X}_2^+ \xrightleftharpoons{K_a^{\text{NH}_2\text{X}_2^+}} \text{NHX}_2 + \text{H}^+$	-6.0 ± 1^a	-7.8 ± 1^a	-7.1 ± 1^a
$\text{NH}_2\text{XCH}_3^+ \xrightleftharpoons{K_a^{\text{NH}_2\text{XCH}_3^+}} \text{NHXCH}_3 + \text{H}^+$	$2.3 \pm 1^a, 1.55^b$	1.3 ± 1^a	
$\text{NHX}(\text{CH}_3)_2^+ \xrightleftharpoons{K_a^{\text{NHX}(\text{CH}_3)_2^+}} \text{NX}(\text{CH}_3)_2 + \text{H}^+$		$2.8 \pm 1^a, 2.88^c$	
$\text{NHX}_2\text{CH}_3^+ \xrightleftharpoons{K_a^{\text{NHX}_2\text{CH}_3^+}} \text{NX}_2\text{CH}_3 + \text{H}^+$	-5.0 ± 1^a	-5.9 ± 1^a	-5.4 ± 1^a
$\text{NH}_2\text{X} \xrightleftharpoons{K_a^{\text{NH}_2\text{X}}} \text{NHX}^- + \text{H}^+$	19.7 ± 1^d	24.7 ± 1^d	
$\text{NHX}_2 \xrightleftharpoons{K_a^{\text{NHX}_2}} \text{NX}_2^- + \text{H}^+$	11.8 ± 1^d	19.6 ± 1^d	12.5 ± 1^d

^aThe regression line used for this quantum chemical LFER is equation 3.11.

^bExperimental values were taken from Margerum and Gray.[43]

^cExperimental value was taken from Antelo and coworkers.[216]

^dThe regression line used for this quantum chemical LFER is equation A.13.

Dissociation constants for chloramines, bromamines, bromochloramines, and methyl-substituted halamines reveal the pH -dependent speciation of these reactive molecules in water. Computed pK_a data show that chloramines and bromamines are predominantly in neutral form at circumneutral pH . However, selected cationic species and anionic species are still relevant for certain reactions. For example, NH_3Br^+ was found to predominate over NH_2Br in reactions with substituted phenols studied by Heeb et al. at neutral pH , despite the low pK_a of monobromammonium (~ 0.8), due to the much higher electrophilicity of monobromammonium relative to monobromamine.[239] On the other hand, the computed pK_a values of NHCl_2 and NHClBr (~ 11.8 and ~ 12.5 , respectively) are down-shifted relative to the less acidic monohalogenated species, due to the stabilization of the anion by the presence of an additional electron-withdrawing substituent. These anionic species may be relevant for reactions with electrophiles. For example, recent theoretical work indicated that ozone oxidizes primarily the deprotonated anionic form of bromo- N,N -dimethylsulfamide rather than the neutral species ($pK_a \sim 9.0$), due to the higher nucleophilicity of the anionic form.[234]

3.6 Acknowledgment

The authors thank Urs von Gunten (Eawag and EPFL) and Michèle B. Heeb (EPFL) for comments on the manuscript and for helpful discussions, as well as Giovanni Cangiani (EPFL) and Jennifer Guerard (UA Fairbanks). We also thank the EPFL centralized HPC facilities for computational resources and support.

4 Molecular Mechanism of *NDMA* Formation from *N,N*-Dimethylsulfamide During Ozonation: Quantum Chemical Insights into a Bromide-Catalyzed Pathway

Daniela Trogolo^a, Brijesh Kumar Mishra^a, Michèle B. Heeb^b, Urs von Gunten,^{b,c} and J. Samuel Arey^{a,c}

Adapted from:

Environ. Sci. Technol., 2015, 49 (7), 4163 - 4175

DOI: 10.1021/eNDMA-S504407h

Contributions:

I am the main author of this chapter. I carried out most of the calculations. Brijesh Kumar Mishra performed the initial transition state searches and the IRC calculations. Michèle B. Heeb and Urs von Gunten developed the experimental section of the chapter. Michèle B. Heeb performed the experiments. Urs von Gunten contributed to the interpretation of results and participated in the text editing. Sam Arey provided guidance in the computational methods and interpretation of results, and he substantially contributed to the manuscript writing and editing.

^a Environmental Chemistry Modeling Laboratory, École Polytechnique Fédérale de Lausanne (EPFL), Station 2, 1015 Lausanne, Switzerland.

^b Laboratory for Water Quality and Treatment, École Polytechnique Fédérale de Lausanne (EPFL), Station 2, 1015 Lausanne, Switzerland.

^c EAWAG, Swiss Federal Institute of Aquatic Science and Technology, Dübendorf, Switzerland.

4.1 Abstract

During ozonation of drinking water, the fungicide metabolite *N,N*-dimethylsulfamide (DMS) can be transformed into a highly toxic product, *N*-nitrosodimethylamine (NDMA). We used quantum chemical computations and stopped-flow experiments to evaluate a chemical mechanism proposed previously to describe this transformation. Stopped-flow experiments indicate a $pK_a = 10.4$ for DMS. Experiments show that hypobromous acid (HOBr), generated by ozone oxidation of naturally occurring bromide, brominates the deprotonated DMS^- anion with a near-diffusion controlled rate constant ($7.1 \pm 0.6 \times 10^8 \text{ M}^{-1} \text{ s}^{-1}$), forming Br-DMS^- anion. According to quantum chemical calculations, Br-DMS has a $pK_a \sim 9.0$ and thus remains partially deprotonated at neutral pH. The anionic Br-DMS^- bromamine can react with ozone with a high rate constant ($10^{5 \pm 2.5} \text{ M}^{-1} \text{ s}^{-1}$), forming the reaction intermediate $(\text{BrNO})(\text{SO}_2)\text{N}(\text{CH}_3)_2^-$. This intermediate resembles a loosely bound complex between an electrophilic nitrosyl bromide (BrNO) molecule and an electron-rich dimethylaminosulfinate ($-(\text{SO}_2)\text{N}(\text{CH}_3)_2$) fragment, based on inspection of computed natural charges and geometric parameters. This fragile complex undergoes immediate ($10^{10 \pm 2.5} \text{ s}^{-1}$) reaction by two branches: an exothermic channel that produces NDMA, and an entropy-driven channel giving non-NDMA products. Computational results bring new insights into the electronic nature, chemical equilibria, and kinetics of the elementary reactions of this pathway, enabled by computed energies of structures that are not possible to access experimentally.

4.2 Introduction

The formation of toxic disinfection byproducts during chlorination of drinking water has led to the use of less reactive chloramine as a treatment agent.[267] However, the switch toward chloramine has been found to promote the formation of toxic and mutagenic *N*-nitrosodimethylamine (NDMA) and other nitrosamines.[267, 268, 200, 269] NDMA formation during chloramination of either drinking water or wastewater has been attributed to both naturally occurring and anthropogenic precursors,[270, 271, 272] including dimethylamine (DMA),[268, 200] compounds substituted with a DMA functional group,[273, 204] 1,1-dimethylhydrazine (UDMH),[274, 275, 190, 192] amine-containing pharmaceuticals and personal care products,[274, 275, 190, 192, 276] amine-containing herbicides and pesticides,[190, 276, 277] and amine-based commercial polymers used during water treatment.[278, 279]

Ozonation has been suggested as an alternative disinfection strategy that destroys several important NDMA precursors,[280, 281, 282] and hence ozonation is expected to lead to decreased formation of NDMA compared to chloramination.[272, 283, 65] However, other types of precursors can produce NDMA during ozonation. *N,N*-dimethylsulfamide, a prevalent environmental metabolite of the fungicide tolylfluanid, was found to lead to high yields of NDMA formation in ozone-based drinking water plants in Germany.[284] Resulting high

concentrations (>100 ng/L) of NDMA in drinking water caused the shutdown of at least one full-scale ozonation treatment plant.[284] Further studies showed that compounds containing hydrazine functional groups or *N,N*-dimethylsulfamide functional groups could produce NDMA in high yields during ozonation of natural waters.[284, 285, 286] A recent report investigated the role of hydroxylamine and brominated nitrogenous oxidants in NDMA formation during ozonation.[287]

The chemical mechanism governing the transformation of *N,N*-dimethylsulfamide into NDMA during ozonation was investigated in a previous study.[288] The transformation could not be explained either by the reaction of *N,N*-dimethylsulfamide with ozone, which proceeded slowly ($k_{\text{apparent}} \sim 20 \text{ M}^{-1} \text{ s}^{-1}$ at pH 8), nor by reactions with OH radical, which failed to yield NDMA. Rather, the presence of either bromide or HOCl during ozonation was necessary to transform *N,N*-dimethylsulfamide into NDMA. At levels occurring naturally in water ($15\text{--}20 \mu\text{g L}^{-1}$), bromide led to an overstoichiometric formation of NDMA. This is consistent with a bromide-catalyzed pathway: ozone reaction with bromide ($k = 160 \text{ M}^{-1} \text{ s}^{-1}$ at 20°C) forms HOBr, followed by bromination of a precursor that subsequently decomposes to regenerate bromide.[282, 289] Taken together, these observations suggested that the reaction of *N,N*-dimethylsulfamide with HOBr is the initial step of the NDMA-formation pathway. Further experiments demonstrated that *N,N*-dimethylsulfamide produced an NDMA yield of up to 54% in the presence of bromide, ozone, and tert-butyl alcohol (present as an OH radical scavenger).[288] Most (39%) of the remaining (non-NDMA) oxidized nitrogen could be explained by produced nitrate.[288] Replacing the O_3 +bromide treatment by an O_3 +HOCl treatment (absent bromide) also produced NDMA from *N,N*-dimethylsulfamide, but with a lower yield (30%), indicating that initial halogenation by HOCl (instead of by HOBr) produced a reaction intermediate that was less favorable for NDMA formation. The entire transformation pathway was rapid, taking place within minutes under conditions considered typical for drinking water treatment.

Based on these observations, a detailed pathway for the transformation of *N,N*-dimethylsulfamide into NDMA was proposed (Supporting Information Figure A.2),[288] as follows. Ozone reaction with bromide generates HOBr, which then brominates the sulfamoyl ($-(\text{SO}_2)\text{NH}_2$) nitrogen in *N,N*-dimethylsulfamide (DMS) to form Br-DMS. Deprotonation of Br-DMS produces an anionic amine, Br-DMS^- , which reacts rapidly with ozone. The resulting oxygenated intermediate (labeled “B” in the Appendix Figure A.2) decomposes either to form NDMA or to form non-NDMA products that lead to nitrate, thus explaining the partial yields of NDMA (54%) and nitrate (39%) from *N,N*-dimethylsulfamide observed in the experiments.

In the present study, we assess the previously proposed NDMA formation mechanism, using quantum chemical computational methods. The previous experimental study detected and quantified two end products: NDMA and nitrate.[288] However, none of the other inferred short-lived intermediates were measured directly. By modeling both the thermodynamics and kinetics of elementary steps along the pathway, we evaluated the detailed mechanism and proposed intermediate structures involved. An improved understanding of this pathway

provides insight into other potential nitrosamine formation pathways.

The chemical systems involved in this study bring nontrivial challenges to molecular modeling. A recent computational study of NDMA formation from tertiary amines[204] employed the widely popular density functional theory (DFT) method, B3LYP.[158, 157] However, the electronic structures of nitroso-containing compounds and of oxidized forms of chlorine, bromine, and sulfur often involve multireference character,[290, 93, 97, 98] and this may or may not be adequately captured by some widely applied single-determinant electronic structure methods.[97, 98, 235, 291, 236] The biradical character of ozone is particularly difficult for mainstream quantum chemical approaches.[93, 5, 8] For example, Zhao and co-workers demonstrated that B3LYP produces an error of 6–8 kcal mol⁻¹ for the electronic energy barrier of the ozone reaction with ethylene or acetylene.[5] Additionally, B3LYP does not perform as well as some recently developed functionals for predicting electronic energy barriers of reactions.[292] These potential difficulties motivated us to prescreen the electronic structure methods (“model chemistries”) that we applied, and to evaluate the NDMA formation mechanism using multiple, complementary model chemistries.

4.3 Materials and Methods

4.3.1 Selection of Model Chemistries

All computations were performed using the Gaussian09 suite of programs.[124] We employed the M05[251] and B2PLYPD[293, 123] model chemistries, both of which are competitive for diverse applications in chemistry.[291, 236] These methods additionally have been reported to give good performance with the potentially difficult electronic structures of ozone, halogen oxides, and nitroso-containing compounds. The developers of M05 recommended this cost-effective global hybrid meta-GGA correlation functional for systems having multireference character.[294] For reaction energies and barrier heights involving ozone with ethylene/acetylene, a severe multireference system, the M05 method gave performance superior to several other popular DFT methods, including the M06 suite of functionals.[5] M05 also performed well in electronic energy barrier height and reaction energy calculations for species with low-to-moderate multireference character.[251, 295, 296] The B2PLYP[293] and B2PLYPD double-hybrid functionals are among the most reliably accurate DFT methods for both single-reference and multireference systems.[98, 235, 236] In a study of total atomization energies (TAE) of several chlorine and fluorine oxides, B2PLYP was one of the best-performing DFT methods among those evaluated, and M05 also performed reasonably well.[97] In our own total atomization energy calculations with the aug-cc-pVTZ basis set[297, 126, 128, 127] used throughout, we observed that the B2PLYPD and M05 model chemistries provided maximum error-per-bond values of 3.4 kcal mol⁻¹ and 7.5 kcal mol⁻¹, respectively, of the benchmark for the set O₃, NO, HNO, N₂O, and Br₂, and gave somewhat larger errors (7.2 and 8.2 kcal mol⁻¹) for SO₂, when compared to published W4[93] and FPD[95] high-accuracy theoretical benchmarks (Appendix Table A.2).

The above methods have differing requirements for the computer time needed, with M05 < B2PLYP ~ B2PLYPD, in computational expense, and this constraint also guided our modeling strategy. Based on the literature described above, we concluded that M05 would be appropriate for geometry optimizations of both stable structures and transition state structures. All geometries were optimized in gas phase. On the M05 geometries, single point calculations with the more accurate B2PLYPD method were conducted to confirm and improve the electronic energy differences computed with M05. All geometry optimizations, other structure searches, and energy single point calculations were conducted with the Dunning aug-cc-pVTZ basis set (Tables 4.1, 4.2, and Appendix Tables A.12 and A.13).^[297, 126, 128, 127] Finally, for one reaction (step *b*), we additionally employed M06-L,^[295] MP2,^[83] and CCSD(T)^[110, 87] computations to provide further method comparisons.

4.3.2 Computation of the Aqueous Free Energy of Reaction for Elementary Reaction Steps

Aqueous Gibbs free energies of reaction, $\Delta G_{aq,rxn}$ (1 M standard state), were computed based on quantum chemical calculations of stationary structures (i.e., reactants, stable intermediates, and products). Aqueous solvent effects were expected to play an important role in the reaction thermodynamics studied here. Two different strategies were employed to handle solvation modeling, depending on the elementary reaction step, described below.

For reaction steps *c*, *f*, *j*, and *n* (Figure 4.1), all species were modeled as monomeric (gas-like) solutes, and aqueous solvation was treated with the Universal Solvation Model based on Solute Electron Density (SMD) implicit solvation^[226] model. Thus:

$$\Delta G_{aq,rxn} = \sum_i \nu_i (E_{gas,elec}(A_i) + G_{gas,therm}(A_i) + \Delta G_{SMD}(A_i) + \Delta G_{standard\ state}) \quad (4.1)$$

where $E_{gas,elec}(A_i)$ is the total electronic energy of species A_i in gas phase, and $G_{gas,therm}(A_i)$ is the thermal contribution to the free energy arising from translations, rotations, and vibrations in gas phase, computed from statistical thermodynamics according to the quantum harmonic oscillator, classical rigid-rotor approximations.^[137] $\Delta G_{SMD}(A_i)$ is the SMD estimate of free energy of transfer from the gas phase into aqueous solution, ν_i is the stoichiometric coefficient of species A_i for the reaction step, and $\Delta G_{standard\ state}$ accounts for any relevant standard state changes of the solute (see Appendix section A.1.3.1). Each of these terms was computed individually, using different model chemistries (Table 4.1 and Appendix Table A.12).

For reaction steps *b*, *g*, *k*, *l*, *m*, *o*, and *p* (Figure 4.1), we suspected that direct involvement of the solvent may be important (see the Results section for explanation). For these cases, the cluster-continuum approach of Bryantsev et al. was used to compute free energies in solution.^[224] Each species was modeled as a microsolvated cluster that contained the solute plus several explicitly modeled water molecules, further embedded in SMD implicit continuum model

4.3.3 Computation of Aqueous Reaction Gibbs Free Energies of Activation and Estimation of Reaction Rate Constants

For several elementary reaction steps we also computed Gibbs free energies of activation and reaction rate constants. For a given reaction step, minimum energy pathway calculations were used to estimate a free energy of activation, defined as the difference between the estimated highest free energy value along the profile of the reaction coordinate and the free energy of the preceding stable reactant or stable intermediate structure. This technique is described further in the Appendix section A.1.3.4.

For the steps *k*, *l*, *m*, *o*, and *p* (Figure 4.1), the free energy of activation was calculated as

$$\Delta G_{aq,rxn}^{\ddagger} = E_{gas,elec}^{\ddagger}(TS(H_2O)_5) + \Delta G_{SMD}^{\ddagger}(TS(H_2O)_5) - E_{gas,elec}(R(H_2O)_5) + \Delta G_{SMD}(R(H_2O)_5) \quad (4.3)$$

where the superscript \ddagger indicates the computed property of the transition structure, and *R* indicates the preceding stationary structure. Since the number of species remains unchanged upon going from reactant to transition structure, the $\Delta G_{cluster\ correction}$ and $\Delta G_{standard\ state}$ terms are both zero, analogous to the eq A.24 in the Appendix. We considered it impractical to attempt to find true saddle points (transition structures) for these very fast reactions, all of which involved loosely bound solvated clusters. For these cases we did not conduct a frequency analysis at the top of the electronic energy barrier, and we thus neglected thermal contributions.

For reaction steps *b*, *f*, *g*, *j*, and *n* (Figure 4.1), the computed activation free energy was further refined by use of a transition state search. Steps *f*, *j*, and *n* did not include explicit water clusters, whereas the transition structure for step *b* included three explicit molecules of water (explained in Results and Discussion), and the transition structure for step *g* included one explicit molecule of water (explained in the Appendix sections A.1.3.3 and A.1.3.7). For these cases, the saddle point was confirmed as a transition structure having a single imaginary vibrational frequency. The activation free energy was defined as

$$\Delta G_{aq,rxn}^{\ddagger} = E_{gas,elec}^{\ddagger}(TS) + G_{gas,therm}^{\ddagger}(TS) + \Delta G_{SMD}^{\ddagger}(TS) - \sum_i (E_{gas,elec}(R_i) + G_{gas,therm}(R_i) + \Delta G_{SMD}(R_i)) + \Delta G_{standard\ state} \quad (4.4)$$

where $G_{gas,therm}^{\ddagger}(TS)$ and $G_{gas,therm}(R_i)$ are determined based on the computed rotations, vibrations, and translations in gas phase for the transition structure (\ddagger) and for the preceding stationary structure(s), *R_i*. In the calculations of $\Delta G_{aq,rxn}^{\ddagger}$ of reaction steps *b* and *g*, the cluster-continuum approach was applied. The notation in eq 4.4 does not show these explicitly modeled waters. Further details are explained in the Appendix section A.1.3.3.

Approximate reaction rate constants were estimated from computed activation free energies based on transition state theory.[137, 298] We used the Eyring–Polanyi equation to estimate a

transition-state theory (TST) rate constant:

$$k_{TST} = \frac{k_B T}{h} e^{\frac{-\Delta G_{aq,rxn}^\ddagger}{RT}} \quad (4.5)$$

where k_B is the Boltzmann constant, h is Planck's constant, T is temperature, R is the molar gas constant, and $\Delta G_{aq,rxn}^\ddagger$ is determined by either eqs 4.4 or 4.5. In eq 4.5, the transmission coefficient (not shown) is assigned as unity, corresponding to the assumption that neither recrossing nor tunneling phenomena are important.[299] The k_{TST} given by eq 4.5 can have units of s^{-1} (first order) or $M^{-1} s^{-1}$ (second order), as prescribed by the reactant stoichiometry contained in $\Delta G_{aq,rxn}^\ddagger$. Equation 4.5 was used to estimate rate constant values for all reactions that are formally first-order, including decomposition reactions and intramolecular reactions. For second-order (bimolecular) reactions, the hypothetical TST rate may exceed the maximum rate allowed by diffusive transport between reactive species, and for these cases the second order reaction rate constant, k , was estimated as[300]

$$\frac{1}{k} = \frac{1}{k_{TST}} + \frac{1}{k_{diffusion}} \quad (4.6)$$

where the limiting second order diffusion-controlled rate constant, $k_{diffusion}$, was assigned a value of $10^{10} M^{-1} s^{-1}$. We assigned a total uncertainty of ± 2.5 in the $\log k$ for all computed rate constants, based on our expectation that the applied model chemistries (SMD/B2PLYPD/aug-cc-pVTZ) would produce an uncertainty of ± 3 kcal mol^{-1} in the $\Delta G_{aq,rxn}^\ddagger$ and that the approximations inherent in transition state theory may lead to an additional factor of 2-3 error[301] in the final rate constant. Nonetheless these approximate rate constant estimates provide useful insights into the plausibilities of several hypothesized reaction pathways.

4.3.4 Computational Estimates of Aqueous pK_a Values

For DMS, Br-DMS, and Cl-DMS, it was desirable to estimate the aqueous pK_a of deprotonation of the neutral amine group. It is difficult to estimate accurate absolute aqueous pK_a values *a priori* by *ab initio* methods.[240] Instead, pK_a values were estimated by taking advantage of the linear free energy relationship (LFER) that is generally observed between experimental and computed pK_a data within a compound family.[240, 243] To establish the LFER, we considered four neutral compounds having known experimental pK_a values with nitrogen as the deprotonating functional group, including hydrazoic acid,[259] sulfamide,[260] acetamide,[259] and trifluoromethanesulfamide.[259] Uncorrected theoretical pK_a values were calculated as follows:

$$pK_a^{uncorr} = \frac{\Delta G_{aq,rxn}^{dep}}{2.303RT} \quad (4.7)$$

where $\Delta G_{aq,rxn}^{dep}$ is the Gibbs free energy of the aqueous deprotonation reaction. For calculation of $\Delta G_{aq,rxn}^{dep}$, gas phase geometries and Gibbs free energies of the acid species and conjugate

base species were carried out with the CBS-QB3 composite method,[247, 246] which gives reliable gas phase deprotonation energy data used in pK_a estimation.[248, 177, 249, 250] Solvation free energies were obtained with the SMD continuum solvation model with the M05/aug-cc-pVTZ electronic density. Further details are provided in the Appendix section A.1.3.5.

4.3.5 Natural Population Analysis (NPA)

To gain more insight into the chemical nature of several intermediate species, we conducted a Natural Population Analysis (NPA)[302, 303, 304, 305, 306, 307] as implemented in Gaussian09. Based on the number of electrons populating each natural orbital (natural orbital occupancies), NPA assigns a partial charge to each atom in the molecule. The natural charge of each atom is obtained from the atomic nuclear charge minus the sum of the populations of the natural atomic orbitals assigned to that atom. NPA charges were computed with an M05/aug-cc-pVTZ electron density and with SMD to represent aqueous solvent, using gas phase M05/aug-cc-pVTZ geometries.

4.3.6 Experimental Determination of the Rate Constant for the Reaction of HOBr with *N,N*-Dimethylsulfamide

For experimental measurement of the rate constant of HOBr reaction with DMS, kinetic experiments on a Hi-Tech Scientific SF-61DX2 Stopped-flow spectrometer were performed. This was done by recording the change in absorbance at pH values of 6.5 to 7.8 (increase of absorbance at 240 nm due to Br–DMS), and 11.5 to 12.5 (decrease of absorbance at 330 nm due to OBr[−]), working under pseudo first-order conditions (5-10 fold excess of DMS over HOBr). The experiments were performed at room temperature and at an ionic strength of 0.12 ± 0.06 M (NaClO₄), using phosphate buffer to maintain the pH. The kinetic data was analyzed using the software Kinetic Studio 2.x.

4.4 Results and Discussion

We explore an *N,N*-dimethylsulfamide transformation pathway that was proposed previously.[288] We first report our analysis of each reaction step in Figure 4.1 and associated intermediate structures. An overall interpretation of the pathway is discussed at the end of the article, as well as implications for other NDMA formation pathways.

4.4.1 Quantum Chemical LFER for Estimation of pK_a Values of DMS, Cl – DMS, and Br – DMS

We generated a quantum chemical linear free energy relationship (LFER) between known experimental pK_a values and computed pK_a values (eq 4.7) for the four neutral nitrogen acid

compounds hydrazoic acid, sulfamide, acetamide, and trifluoromethanesulfamide, finding a squared correlation coefficient of $r^2 = 0.93$ for the regression line (Appendix Table A.14, Figure A.7). Previous work has established that quantum chemical computed pK_a values correlate well with experimental pK_a values within a compound family,[240, 243] and this has been demonstrated for many compound families, including amines.[244] Therefore, although the presently proposed LFER is fitted using only four values, we interpret that the resulting regression parameters are valid for DMS, Cl–DMS, and Br–DMS. This LFER was used to estimate $pK_a = 10.3$ for DMS, $pK_a = 9.0$ for Br–DMS, and $pK_a = 7.9$ for Cl–DMS, by substituting the quantum chemical computed values (pK_a^{uncorr}) for these compounds into the regression function. Expected uncertainties in resulting pK_a estimates are roughly ± 1 unit.

4.4.2 Reaction Steps *a*, *b*, *c*, and *d* in the Presence of Ozone and Bromide. Bromination of DMS versus DMS^- , and Speciation Equilibria of DMS/ DMS^- and BrDMS/BrDMS $^-$

It was proposed previously that *N,N*-dimethylsulfamide initially undergoes electrophilic attack by HOBr, resulting in the halogenation of the sulfamoyl ($-(SO_2)NH_2$) nitrogen.[288] However, neutral *N,N*-dimethylsulfamide, hereafter denoted DMS, can deprotonate to form the DMS^- anion (Figure 4.1, reaction *a*). It has remained unclear whether *N,N*-dimethylsulfamide bromination would arise predominantly from the reaction of HOBr with neutral DMS to form Br–DMS (reaction *b*) or due to the HOBr reaction with the deprotonated DMS^- anion to form Br– DMS^- (reaction *c*). Additionally, Br–DMS/Br– DMS^- can undergo acid–base chemistry (reaction *d*). We investigated the equilibria and predominating chemical fluxes along these four reaction channels (*a*, *b*, *c*, *d*). The reaction of *N,N*-dimethylsulfamide with HOBr was measured at pH conditions ranging from 6.5 to 12.5, using stopped-flow experiments. HOBr was expected to be the principal oxidant, since it is more electrophilic than OBr^- . [4] Additionally, compared to neutral DMS, the deprotonated nitrogen atom of the DMS^- anion was expected to exhibit faster reactivity with HOBr.[4] These expectations were supported by observed trends in stopped-flow data, which indicated that the reaction of HOBr with DMS was not relevant over the investigated pH range. We thus interpret that HOBr reaction with the DMS^- anion (pathway *a-c*) was the predominant pathway for bromination of *N,N*-dimethylsulfamide throughout the investigated pH range, and we neglect consideration of the reactions of either HOBr or OBr^- with neutral DMS (pathway *b-d*). Accordingly, the following model was used to interpret the apparent second order rate constant measured by stopped-flow experiments:

$$k_{apparent} = \alpha_{HOBr}(1 - \alpha_{DMS})k_c \quad (4.8)$$

where α_{HOBr} represents the fraction of hypobromous acid in the protonated state under specified pH conditions, based on $pK_a = 8.8$ for HOBr;[308] α_{DMS} is the fraction of DMS in the neutral (protonated) state; and k_c is the species-specific second order rate constant for the reaction of HOBr with DMS^- anion. Values of α_{DMS} and k_c were fitted such that eq 4.8

produced the best match to experimentally measured k_{apparent} values.

Table 4.1 Best Estimates^a for Aqueous Free Energies of Reaction ($\Delta G_{\text{aq},\text{rxn}}$) for Elementary Reaction Steps of the NDMA Formation Pathway

Reaction step ^b	Number of explicit waters included	Estimated Total $\Delta G_{\text{aq},\text{rxn}}$ (kcal mol ⁻¹)	
		X ^c = Br	X ^c = Cl
b	3	-8.0	-11.2
c	0	-17.9	-21.5
f	0	1.9	-
g	1	-20.1	-
j	0	-30.7	-34.2
k	5	-4.0	-4.0
l	5	-26.2	-31.3
m	5	6.2	2.1
n	0	-34.6	-
o	5	-2.8	-1.4
p	5	1.2	2.6

^aA complete listing of all computed $\Delta G_{\text{aq},\text{rxn}}$ results is given in the Appendix Table A.12. Shown here are results obtained with M05 for geometries, B2PLYPD for $\Delta E_{\text{gas},\text{elec}}$, M05 for $\Delta G_{\text{gas},\text{therm}}$, and SMD/M05 for ΔG_{SMD} . The aug-cc-pVTZ basis set was used for all computations. ^bElementary reaction step as depicted in Figure 4.1.

^cResults are shown for both the O₃ + Br⁻-catalyzed pathway (X = Br) and the O₃ + HOCl system pathway (X=Cl).

The reaction of HOBr with the DMS⁻ anion (pathway *c*) was assigned a species-specific rate constant of $k_c = 7.1 \pm 0.6 \times 10^8 \text{ M}^{-1} \text{ s}^{-1}$, according to fitting of eq 4.8 to experimental data.[309] Hence reaction *c* is near the diffusion-limited rate. According to results from quantum chemical computations, this reaction is exothermic and has a free energy of reaction of $\Delta G_{\text{aq},\text{rxn}} = -17.9 \text{ kcal mol}^{-1}$ (Table 4.1). Thus, based on stopped-flow experimental results and quantum chemical calculations, reaction *c* may be considered as very fast, thermodynamically favorable, and irreversible. The observed good fit statistics of eq 4.8 supported our interpretation that HOBr reaction with DMS⁻ anion is the principal pathway for bromination of *N,N*-dimethylsulfamide. This interpretation is further supported by quantum chemical calculations of the rate constant for reaction *b*, discussed in the next section. Based on the fitted value of k_c and the experimental conditions used, we also ruled out the possible influence of other bromine species[4] such as Br₂, BrCl, or Br₂O.

Deprotonation of DMS was assigned an experimental pK_a value of 10.4 (reaction pathway *a*), based on the fitted value of α_{DMS} obtained with eq 4.8. This was corroborated by our quantum chemical pK_a estimate of 10.3 ± 1 for DMS (above). The pK_a of DMS is similar to that of the structural analogue sulfamide (pK_a = 10.42).[260] Under conditions typical for drinking water treatment (pH 6 to 8), *N,N*-dimethylsulfamide thus exists mostly in the neutral state. However,

Chapter 2

the reaction of HOBr with the DMS⁻ anion nonetheless dominates over HOBr reaction with neutral DMS at pH 7, as explained above.

Finally, a $pK_a = 9.0 \pm 1$ was estimated for Br–DMS (reaction *d*) based on quantum chemical LFER estimates (above). Owing to the stabilization of the deprotonated sulfamoyl anion by the electron-withdrawing Br substituent, the pK_a of Br–DMS is downshifted compared to that of DMS. Hence under typical drinking water conditions (pH 6–8), brominated *N,N*-dimethylsulfamide is present predominantly in the neutral form. However, the deprotonated species, Br–DMS⁻, likely has a much higher reactivity toward electrophiles and was assumed to be the principal species that reacts with ozone, discussed further below.

In summary, the bromination of *N,N*-dimethylsulfamide occurs principally by a fast reaction of HOBr with the DMS⁻ anion ($k_c = 7.1 \pm 0.6 \times 10^8 \text{ M}^{-1} \text{ s}^{-1}$), despite that neutral DMS is the predominant species at neutral pH. This produces Br–DMS/Br–DMS⁻ ($pK_a = 9.0$). According to NPA calculations (Figure 4.2), the negative charge of Br–DMS⁻ is fully localized on the Br-substituted N atom ($-1.01 e$). This electron-rich nitrogen is thus susceptible to further reaction with oxidants such as ozone. Analogous results are found for the chlorination of DMS/DMS⁻ that arises in a system containing ozone and HOCl (absent bromide), which is discussed further in the Appendix section A.1.3.8.

Table 4.2 Best Estimates^a of Activation Free Energies ($\Delta G_{aq,rxn}^\ddagger$) for Elementary Reaction Steps of the NDMA Formation Pathway

Reaction step ^b	Number of explicit waters included	Estimated Total $\Delta G_{aq,rxn}^\ddagger$ (kcal mol ⁻¹)	
		X ^c = Br	X ^c = Cl
b	3	17.9	-
g	1	33.9	-
j	0	10.6	10.5
k	5	3.6	4.2
l	5	<1.0	<1.0
m	5	12.2	3.6
n	0	3.1	-
o	5	3.0	2.5
p	5	5.1	11.4

^aA complete listing of all computed $\Delta G_{aq,rxn}^\ddagger$ results is in given in the Appendix Table A.13. Shown here are results obtained with M05 for minimum energy pathway calculations, B2PLYPD for $\Delta E_{gas,elec}^\ddagger$, and SMD/M05 for ΔG_{SMD}^\ddagger . For reactions *b*, *g*, *j*, and *n*, M05 was used to compute the transition state search and $\Delta G_{gas,therm}^\ddagger$. The aug-cc-pVTZ basis set was used for all computations. ^bElementary reaction step as depicted in Figure 4.1. ^cResults are shown for both the O₃ + Br⁻-catalyzed pathway (X = Br) and the O₃ + HOCl system pathway (X=Cl).

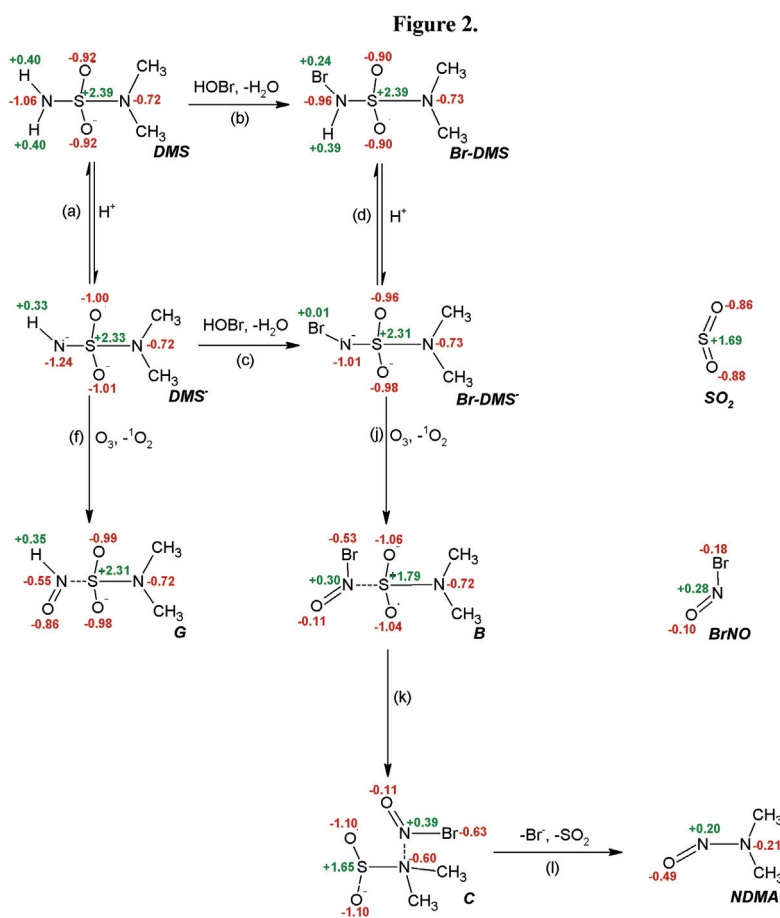


Fig. 4.2 Partial charges assigned to each atom, for several key structures in the NDMA formation pathway during ozonation of waters containing Br^- and DMS^- , according to natural population analysis (NPA). Computed partial charges for nitrosyl bromide (BrNO) and sulfur dioxide (SO_2) are shown for comparison.

4.4.3 Quantum Chemical Modeling of the rate constant of reaction step *b*

The bromination of neutral DMS by HOBr (reaction *b*, Figure 4.1) was difficult to investigate by experimental means. At neutral and high pH conditions, pathway *c* dominates over pathway *b*, according to stopped-flow results. At low pH conditions, competition from other halogenating species may become important.[310, 311] Thus, we evaluated the rate constant of reaction step *b* using quantum chemical computations. Previous experimental and theoretical studies have suggested that three structured water molecules facilitate the halogenation of substituted amines by HOCl.[312, 218] We hypothesized that a similar mechanism may arise for the reaction of HOBr with DMS. Consistent with these previous studies, we found that the inclusion of explicitly modeled water molecules substantially lowered the computed activation free energy, compared to computations without explicit waters, for reaction step *b*. This reaction involves a proton transfer through the proximate water molecules (Appendix Figure A.3). Thus, explicit modeling of the involved water molecules is crucial for this reaction

step. With three explicit water molecules, our estimate for the activation free energy was 17.9 kcal mol⁻¹ (Table 4.2). Intrinsic reaction coordinate (IRC) calculations confirmed that the identified transition structure connected the reactants and products.[313, 314, 315] Based on the computed activation free energy for step *b*, the species-specific rate constant estimate is $k_b \sim 10^{0 \pm 2.5} \text{ M}^{-1} \text{ s}^{-1}$ using eq 4.6. On the suggestion of a reviewer, we further validated this result by applying the same computational methodology to the reaction of HOBr with ammonia, for which the rate constant is known experimentally. Our computational estimate of $k_{\text{HOBr}+\text{NH}_3} = 10^{5 \pm 2.5} \text{ M}^{-1} \text{ s}^{-1}$ is consistent with the reported experimental[180] values of $4 \times 10^7 \text{ M}^{-1} \text{ s}^{-1}$ and $7.5 \times 10^7 \text{ M}^{-1} \text{ s}^{-1}$. Similarly, our computational estimate of the rate constant for the HOBr reaction with dimethylamine, $k_{\text{HOBr}+\text{NH}(\text{CH}_3)_2} = 10^{9 \pm 2.5} \text{ M}^{-1} \text{ s}^{-1}$, agrees well with the reported experimental[180] value of $3 \times 10^9 \text{ M}^{-1} \text{ s}^{-1}$ (see SI). These results provide validation for the theoretical estimate of reaction rate constant k_b . Computational results also support the expectation that the strongly electron-withdrawing sulfonyl (-SO₂) group in DMS decreases the reactivity of the amine group toward electrophiles. In summary, quantum chemistry results offer further support to stopped-flow experimental data, indicating that reaction pathway *b* does not compete with pathway *c* under neutral or high pH conditions.

To further confirm the appropriateness of our modeling approach for reaction step *b*, we conducted additional computations of the free energy of this reaction using other model chemistries. These results are discussed in the Appendix section A.1.3.6.

4.4.4 Reaction Steps *e* and *f*. Oxidation of DMS and DMS⁻ by Ozone

A previous study reported a measured species-specific rate constant of $k_e = 1.24 \pm 0.10 \text{ M}^{-1} \text{ s}^{-1}$ for the reaction of O₃ with neutral DMS (reaction *e*).⁽²⁷⁾ This rate constant is noticeably lower than that for the reaction of O₃ with ammonia (20 to 44 M⁻¹ s⁻¹),^[316] again owing to the presence of the electron-withdrawing sulfonyl group. Based on the previously measured apparent second order rate constant of the O₃ reaction with *N,N*-dimethylsulfamide (pK_a ~ 10.4) under conditions ranging from pH 5.0 to 10.2,^[288] and assuming typical treatment conditions of [O₃] ~ 20 μM and [HOBr] ~ 0.2 μM, we deduced that the reaction of O₃ with either DMS or DMS⁻ anion does not compete with the reaction of HOBr with the DMS⁻ anion. Thus, reactions *e* and *f* are not considered further.

4.4.5 Reaction Step *g*. Can Br – DMS Undergo SO₂ Extrusion to Form Br – UDMH?

Although it has not been proposed previously, we investigated whether Br–DMS could undergo extrusion of SO₂ to form 1,1-dimethyl-2-bromohydrazine (Br–UDMH). It has been reported that Cl–UDMH can rapidly produce NDMA in high yield in the presence of diatomic oxygen (³O₂),^[68] and it has been proposed that Br–UDMH would lead to NDMA formation by the same mechanism.^[59, 209] Therefore, the transformation of Br–DMS to Br–UDMH (reaction step *g*) was evaluated as another potential pathway leading to the formation of

NDMA. The free energy of activation was computed using one explicitly modeled water molecule, and this is explained further in the Appendix section A.1.3.7. Although reaction step *g* is thermodynamically favorable (Table 4.1), computations indicate an activation free energy of $\Delta G_{aq,rxn}^\ddagger = 33.9 \text{ kcal mol}^{-1}$ for formation of Br-UDMH from Br-DMS (Table 4.2), corresponding to a first order rate constant $k_g \sim 10^{-12 \pm 2.5} \text{ s}^{-1}$. This implies a half-life of $10^{5 \pm 2.5}$ years. Thus, reaction *g* is considered kinetically implausible. We did not perform computations of the analogous activation free energy for Cl-DMS, assuming that this reaction would also be kinetically unfeasible. This is consistent with the previously reported observation that NDMA did not noticeably form from *N,N*-dimethylsulfamide during HOCl treatment, in the absence of ozone.[284]

4.4.6 Reaction Steps *h*, *i*, and *j*. Ozone Reaction with Br – DMS[−] (or Cl – DMS[−])

It was proposed previously that the electron-rich, deprotonated sulfamoyl nitrogen of the Br-DMS[−] anion (or Cl-DMS[−] anion) may be rapidly attacked by ozone.[288] This was proposed to lead to formation of the ozonide intermediate A, which would subsequently decompose into intermediate B and singlet oxygen (reactions *h* and *i*, Figure 4.1). We evaluated these reaction steps using quantum chemical calculations.

Exploring the O-N interatomic distance as a reaction coordinate, we find that the proposed ozonide structure A does not exist as a stable intermediate. We attempted to optimize structure A both in gas phase with M05/aug-cc-pVTZ and in aqueous phase with SMD/M05/cc-pVTZ, for the cases of both X = Br and X = Cl. Suspecting that explicit treatment of solute-solvent interactions may be important, we also attempted to optimize structure A with a cluster-continuum treatment using SMD together with up to four explicit water molecules. However, the ozonide intermediate A was found to be unstable in all of these environments, according to the M05/aug-cc-pVTZ model chemistry. Thus, we tentatively propose that structure A does not exist as an intermediate structure. Structure A and reaction steps *h* and *i* are tentatively rejected in favor of pathway *j*, in which ozonation of X-DMS[−] leads directly to intermediate B (Figure 4.1).

Further investigation of pathway *j* indicates that ozone attack on X-DMS[−] has a low barrier (Table 4.2) and is concerted with the release of singlet oxygen, ¹O₂, leading to the weakly bound anion intermediate B. Using the N-O interatomic distance as a reaction coordinate, we find that formation of the N=O double bond is concerted with spontaneous release of ¹O₂, with estimated rate constants of approximately $k_j \sim 10^{5 \pm 2.5} \text{ M}^{-1} \text{ s}^{-1}$ for the reaction of O₃ with either Br-DMS[−] or Cl-DMS[−]. To further validate the computational estimate of k_j , we also computed the rate constant for the previously studied reaction of O₃ with another anion, bromide. Our computed estimate of $k_{\text{O}_3+\text{Br}^-} = 10^{4 \pm 2.5} \text{ M}^{-1} \text{ s}^{-1}$ agrees reasonably with the experimental value[316] of $1.60 \times 10^2 \text{ M}^{-1} \text{ s}^{-1}$. Finally, quantum chemical estimates of $\Delta G_{aq,rxn}$ for step *j* are $-30.7 \text{ kcal mol}^{-1}$ and $-34.2 \text{ kcal mol}^{-1}$ for Br-DMS[−] and Cl-DMS[−], respectively (Table 4.1), indicating a thermodynamically favorable reaction in both cases. In

summary, computations indicate that ozone attack on X-DMS⁻ is fast and irreversible. This reaction produces the intermediate structure B.

4.4.7 Cluster-Continuum Modeling of the Fragile Intermediate B and Subsequent Reaction Intermediates

The intermediate B, produced by ozone reaction with Br-DMS⁻, was found to be a fragile, loosely bound structure that exists only fleetingly. We viewed that specific interactions with the solvent were likely to be important for stabilizing this charged molecule and directing its chemistry. We found that five explicitly modeled molecules of water could fulfill hydrogen-bonding sites with the four atoms of structure B having substantial (-0.5 *e*) negative NPA charges (Figure 4.2 and Appendix Figure A.4), and this stabilized the fragile intermediate. In the absence of such an explicitly solvated cluster, the bromine atom is found to spontaneously cleave from intermediate B during the gas phase geometry optimization, using the M05/aug-cc-pVTZ model chemistry. Thus, we simulated the chemistry of structure B and subsequent anionic intermediates with a cluster-continuum approach using five explicitly modeled water molecules. Based on gas phase geometry optimizations with M05/aug-cc-pVTZ starting from several different trial structures of the hydrated cluster, we found a stable minimum energy structure that we label B(H₂O)₅ (Appendix Figure A.4).

Applying minimum energy pathway calculations to the B(H₂O)₅ structure, we explored the potential energy profiles associated with the N-S distance, N-O distance, and N-S-N angle. Extensive searches led to the stable intermediate structures C(H₂O)₅, D(H₂O)₅, and F(H₂O)₅, as well as NDMA, and the transition structures associated with the connecting reaction steps *k*, *l*, *m*, *o*, and *p*, discussed further below. Owing to the inclusion of explicitly modeled water molecules, these stable clusters and the intervening transition structures occupy a high-dimensional, rugged, shallow potential energy surface. Thus, it is difficult to ensure that all of the most relevant (i.e., minimum energy) geometric configurations and lowest energy barriers have been explored exhaustively. Nonetheless, based on minimum energy pathway calculations involving these clusters, we propose estimates of activation free energies and reaction free energies for the steps *k*, *l*, *m*, *o*, and *p*. This enables several useful insights about the overall NDMA-formation pathway, outlined below.

4.4.8 Reactions of the Brominated Intermediate B: a Branching in the Pathway

In the optimized structure of the hydrated B(H₂O)₅ cluster, the N-Br bond and the S-N bond are both found to be elongated, exhibiting bond lengths of 2.39 and 2.66 Å, respectively (Figure A.4). This inspires the expectation that structure B may decompose according to the branching in the bifurcated pathway proposed previously (Figure A.2).^[288] Resulting reaction branches could lead either to the formation of NDMA or to the formation of nitrate. The kinetics and/or equilibria of these competing reactions are expected to control the final yields of NDMA and nitrate resulting from the precursor DMS. We discuss each of these pathways below, as well as

the previously hypothesized protonation reaction (step *q*).

What is the chemical nature of intermediate B? NPA charges of $B(H_2O)_5$ reveal that the Br-substituted nitrogen atom is highly electron-deficient (+0.30 *e*); the bromine atom bears a substantial partial negative charge of -0.53 *e*; and the newly added oxygen atom exhibits little excess electron density (-0.11 *e*) (Figure 4.2). Structure B thus displays a dramatic shift in charge density compared to the $Br-DMS^-$ anion, which had a full negative charge (-1.01 *e*) located on the Br-substituted sulfamoyl nitrogen. Instead, structure B resembles an electrostatic complex between an electrophilic nitrosyl bromide ($BrNO$) molecule and an electron-rich dimethylaminosulfinate anion ($(SO_2)N(CH_3)_2^-$). Indeed, the computed NPA partial charges, bond lengths, and bond angle of $BrNO$ compare well with those found for the analogous atoms in structure B (Appendix Figure A.5). The NPA partial charges and bond length of the N–O group in $B(H_2O)_5$ are consistent with a nitrosyl (N=O) moiety, which is considered too acidic to become protonated at neutral pH, thereby ruling out pathway *q*. Finally, the sulfonyl group of structure B has gained nearly an entire electron (change of -0.86 *e*) compared to DMS (interpreted as S(VI)), indicating a change in the oxidation state of sulfur. This brings the sulfonyl group much closer to the electronic arrangement of free sulfur dioxide (S(IV)), as judged by NPA charges (Figure 4.2), consistent with the imminent departure of SO_2 by way of extrusion (upcoming steps *k*, *l*).

Analysis of reaction *o* (Figure 4.1) confirms that the $BrNO$ molecule is only loosely bound to the dimethylaminosulfinate, and these fragments can cleave readily. For step *o*, we explored the already-elongated N–S bond as a reaction coordinate, applying minimum energy pathway calculations to the $B(H_2O)_5$ cluster. Reaction *o* is found to have a very low activation free energy of 3.0 kcal mol⁻¹ (Table 4.2), corresponding to a nearly thermally controlled reaction rate ($10^{11\pm1.5}$ s⁻¹). The free energy of reaction ($\Delta G_{aq,rxn} = -2.8$ kcal mol⁻¹) is driven primarily by the increase in translational degrees of freedom, or the increase in entropy of mixing, arising from the decomposition of a single molecule into two dilute products. Reaction *o* leads away from NDMA formation. Thus, another fast reaction must compete with reaction *o* to explain the observed 54% yield of NDMA from *N,N*-dimethylsulfamide during ozonation; this is the role of reaction *k*.

Reaction *k* arises as an electrophilic attack of the $BrNO$ nitrogen on the electron-rich nitrogen of the dimethylaminosulfinate anion. Reaction *k* is closely analogous to the known nitrosation reaction of dimethylamine by $BrNO$, which rapidly produces NDMA according to a measured[317] rate constant of $k_{rxn} = 3.6 \times 10^7$ M⁻¹ s⁻¹ in water at 25 °C. Applying minimum energy pathway calculations to the N–S–N angle as a reaction coordinate of the brominated $B(H_2O)_5$ complex, we find a very low activation free energy of 3.6 kcal mol⁻¹ (Table 4.2) for the intramolecular rearrangement reaction *k*, corresponding a nearly thermally limited reaction rate of $k_k \sim 10^{10\pm2.5}$ s⁻¹ (Appendix Figure A.6). Reaction thermochemistry calculations of the hydrated $B(H_2O)_5$ and $C(H_2O)_5$ clusters confirm that reaction *k* is mildly favorable, with a $\Delta G_{aq,rxn}$ of -4.0 kcal mol⁻¹ (Table 4.1). This reaction step is enthalpy-driven, as judged by the change in the electronic energy (the term $E_{gas,elec}(A_i(H_2O)_x)$, in eq 4.2) of the cluster upon

rearrangement. Thus, simulations indicate that reaction *k* is thermodynamically favorable and very fast. The resulting structure C, although observed as a technically stationary structure in simulations, would exist only fleetingly at environmentally relevant temperatures. The SO₂ group and the Br atom both simultaneously and spontaneously cleave from this structure with an activation free energy of <1 kcal mol⁻¹, in an entropy-driven reaction that has a favorable $\Delta G_{aq,rxn}$ value of -26.2 kcal mol⁻¹ (reaction *l*). Thus, reaction *l* is interpreted to produce NDMA irreversibly at a thermally controlled rate ($k_l \sim 10^{11 \pm 1.5} \text{ s}^{-1}$).

Finally, intermediate B might also decompose by reaction pathway *m*, corresponding to departure of the bromide anion. However, minimum energy pathway calculations of the N–Br interatomic distance reveal an activation free energy of 12.5 kcal mol⁻¹ (Table 4.2), suggesting that this reaction would be too slow ($\leq 10^5 \text{ s}^{-1}$) to compete with the much faster reactions *k* and *o*. In summary, upon exploring the potential energy profiles of the steps *k* and *o* of the hydrated B(H₂O)₅ cluster, we find that these two reactions both feature very low activation free energies of 3.6 and 3.0 kcal mol⁻¹, respectively. Reaction *k* is interpreted as an exothermic intramolecular nitrosation of the electron-rich dimethylaminosulfinate anion by the electrophile BrNO, followed by the departure of both the Br⁻ anion and SO₂ to produce NDMA (reaction *l*). Reaction *o* simply corresponds to the entropy-driven departure of the BrNO from the weakly bound dimethylaminosulfinate anion. Reaction steps *m* and *p* appear unable to compete with steps *k*, *l*, and *o*. Within the uncertainties of the computational methods applied, the activation free energy of steps *k*, *l*, and *o* were considered equivalent and would correspond to near-thermally controlled reaction rates ($k_k \sim k_l \sim k_o \sim 10^{10 \pm 2.5} \text{ s}^{-1}$). The facile branching of the decomposition of intermediate B is consistent with the previously observed split yields of NDMA (54%) and nitrate (39%) with respect to DMS. Theoretical branching ratios for the decomposition of intermediate B are reported in the Appendix section A.1.3.11. However, the limited accuracy of the computational methods employed here preclude meaningful quantitative apportionments of the yields of the competing pathways for decomposition of structure B. Finally, analogous pathways arise for structure B under chlorinating conditions (O₃ + HOCl, absence of bromide), and this is discussed further in the Appendix sections A.1.3.9–A.1.3.10.

4.4.9 Overall Interpretation of the Pathway

Based on quantum chemical simulations and new experiments reported here, we confirm and further illuminate a previously proposed reaction pathway for the formation of NDMA from *N,N*-dimethylsulfamide during ozonation of natural water. Detailed analyses of the elementary reaction steps illustrate a pathway that is both thermodynamically favorable and kinetically feasible.

Several new insights are gained into the detailed mechanism of this NDMA formation pathway. Neutral *N,N*-dimethylsulfamide has a p*K_a* of approximately 10.4, and thus a fraction of these molecules can deprotonate to form the DMS⁻ anion at neutral pH. The electron-

rich, deprotonated sulfamoyl nitrogen can undergo a fast reaction with HOBr ($k_c = 7.1 \pm 0.6 \times 10^8 \text{ M}^{-1} \text{ s}^{-1}$). The bromination step produces Br–DMS[−], for which the conjugate acid (Br–DMS) has an estimated pK_a of 9.0. The deprotonated form, Br–DMS[−], can react with ozone ($k_j = 10^{5 \pm 2.5} \text{ M}^{-1} \text{ s}^{-1}$) to produce the fragile intermediate structure B. Electronically, the intermediate B resembles a loosely bound complex between an electrophilic nitrosyl bromide (BrNO) molecule and an electron-rich dimethylaminosulfinate fragment. Compared to Br–DMS, structure B displays a decreased oxidation state in the sulfonyl group, changing from $\sim \text{S(VI)}$ (in Br–DMS) closer to S(IV) (in free SO_2). This altered electronic arrangement facilitates the fast extrusion of SO_2 from structure B, which occurs in $\leq 10^{-8} \text{ s}$. By comparison, the extrusion of SO_2 from Br–DMS is kinetically impossible (half-life of $\geq 10^3$ years). Thus, calculations predict that structure B exhibits a dramatic $\geq 10^{17}$ -fold acceleration of the SO_2 extrusion rate compared to Br–DMS. The fast electrophilic attack of the BrNO fragment on the dimethylaminosulfinate nitrogen (reaction *k*) may be compared with the previously documented rapid nitrosation of *N,N*-dimethylamine by BrNO,(95) which also produces NDMA.

The fleeting intermediate B immediately decomposes according to one of two pathways: an enthalpy-driven pathway that leads to NDMA (reaction *k*) and an entropy-driven pathway that leads to the non-NDMA product, nitrate (reaction *o*). Our quantum chemical calculations are insufficiently accurate to distinguish a preferential channel in the delicate branching of these two decomposition reactions of intermediate B. However, our results are qualitatively consistent with the observed dual yields of NDMA (54%) and nitrate (39%) from *N,N*-dimethylsulfamide. Both pathways release bromide, which acts as a catalytic reagent that can again become oxidized by ozone to form HOBr and react with another molecule of DMS[−]. According to the results obtained here, the conversion of *N,N*-dimethylsulfamide to NDMA is expected to transpire within minutes under conditions that would be typical for ozonation of drinking water. Assuming treatment conditions of $[\text{O}_3] \sim 20 \text{ }\mu\text{M}$ and $[\text{Br}^-] \sim 0.2 \text{ }\mu\text{M}$, the limiting step of the transformation pathway is the rate at which HOBr is produced by ozone reaction with bromide. This is consistent with the previous interpretation of the kinetics of NDMA formation from *N,N*-dimethylsulfamide.[288]

What strategies could be taken to improve the *a priori* theoretical estimates of rate constants for the reactions studied here? The uncertainty in the computed free energy of activation is the dominating source of error (a factor of ~ 160) in *a priori* estimates of the rate constants. To substantially improve the accuracy of the activation energy, more theoretically rigorous model chemistries would be needed, requiring a more computationally intensive effort than the already-expensive study presented here. The TST approximation, although unsophisticated, contributes less uncertainty to final rate constant estimate (perhaps a factor of ~ 2 -3).[301] Relatively efficient algorithms have been developed that can provide improved results compared to TST,[301] and this would lead to slightly better rate constant estimates. In the present study, these uncertainties in the theoretical rate constants do not affect the predicted overall rate of NDMA formation from DMS during ozonation, because the rate-limiting step in the pathway is the experimentally known reaction of Br^- with O_3 to form HOBr. However, the

present theoretical approach does not have useful accuracy to resolve the branching ratio of the decomposition of intermediate B (and thus yield of NDMA from *N,N*-dimethylsulfamide), as explained above.

4.5 Implications for Other NDMA Pathways

The presented mechanism illustrates a few themes that are potentially relevant to other disinfection byproduct formation pathways. This expands the knowledge base upon which to develop strategies for the minimization of such toxic compounds during water disinfection processes.

Acid–base chemistry of the precursor molecule, *N,N*-dimethylsulfamide, facilitates dramatically accelerated oxidation reactions in the NDMA formation pathway. DMS and Br-DMS are both electron-deficient amines that may be considered as mild nucleophiles. However, the respective deprotonated conjugate bases, DMS^- and Br-DMS^- , are electron-rich anionic amines that can react according to high rate constants with HOBr and O_3 , respectively. Acid–base chemistry also arises as an oxidation “accelerant” in other disinfection byproduct formation pathways.[318, 319]

The nitrosamine formation potential of a precursor is usually associated with the presence of reduced alkyl-substituted amine substructures. However, we might also screen the nitrosamine formation potential of a candidate precursor by its capacity to produce “electrophilic nitrogen”. Electrophilic nitrogen appears as a common actor among several apparently different nitrosamine formation pathways. In the pathway studied here, electrophilic oxidants (HOBr and O_3) successively substitute an initially reduced nitrogen (sulfamide) group with electron-withdrawing substituents (Br and O). This produces a strongly electrophilic nitrogen group that is structurally resemblant to BrNO. This electrophilic nitrogen then reacts with a proximate alkyl-substituted amine to form NDMA. Analogous motifs arise in other nitrosamine formation pathways, in which a precursor amine group is transformed into reactive electrophilic nitrogen (e.g., a chloramine, bromamine, hydroxylamine, or nitrosyl substructure) that subsequently reacts with an electron-rich alkyl-substituted amine, thereby producing a partially oxidized unsymmetrically substituted hydrazine substructure that may readily convert into NDMA in high yield.[65, 287, 68, 59, 209]

The pathway that connects DMS to NDMA contains several very high elementary reaction rate constants. Analogous NDMA-formation pathways involving related precursors thus may be difficult to study by experimental approaches only, and molecular modeling provides a useful complementary means to investigate the linkages in such pathways. Quantum chemical modeling of reaction chemistry in water requires careful attention to several methodological details. However, the technical approaches outlined in this study are intended to provide guidance for similar efforts by other groups (e.g., see Appendix sections A.1.3.1-A.1.3.7).

4.6 Acknowledgments

We gratefully acknowledge support from Swiss National Science Foundation Division II Project Grant 200021_126893. We also thank the Swiss National Supercomputing Center (CSCS) and EPFL centralized HPC facilities for computing resources.

5 Mechanisms of OCS Formation in Seawater from DMS, Biogenic Thiols, and Polysulfides

Daniela Trogolo^a, Davide V. Vione^b, and J. Samuel Arey^c

Contributions:

I am the main author of this chapter. I carried out all quantum chemical simulations. Davide Vione carried out the APEX photochemical model calculations and substantially contributed to the manuscript writing and editing. Sam Arey provided guidance in the computational methods and interpretation of results, and he substantially contributed to the manuscript writing and editing.

^a Environmental Chemistry Modeling Laboratory, École Polytechnique Fédérale de Lausanne (EPFL), Station 2, 1015 Lausanne, Switzerland.

^b Università degli Studi di Torino (UNITO), Torino, Italy

^c Swiss Federal Institute of Aquatic Science and Technology (EAWAG), Dübendorf, Switzerland.

5.1 Abstract

We investigated the molecular pathways that produce carbonyl sulfide (OCS) from the reaction of carbon monoxide (CO) with reactive intermediates formed from thiol, polysulfide, and dimethylsulfide precursors in seawater. The oceans are a major source of atmospheric OCS, most likely produced from photochemical and also from dark, abiotic transformations of sulfur-containing compounds in seawater near the ocean surface. However, the combination(s) of precursors, reactive species, and mechanisms that contribute the principal formation pathways of oceanic OCS remain relatively unexplored. Hypothesized radical and anionic molecular mechanisms involving biogenic thiols, dimethylsulfide, polysulfides, and CO were explored using quantum chemical molecular modeling computations. To investigate these pathways, aqueous Gibbs free energies of reaction and kinetic rate constants were determined with density functional theory electronic structure methods. Based on quantum chemical models, thiyl radicals, which might be produced from the one-electron oxidation of thiolates or from the homolytic bond cleavage of dimethylsulfide, are key intermediates that could lead to OCS formation in seawater. Sulfide and polysulfide species such as HS^- , $\text{S}^{\cdot-}$, S^{2-} , and S_2^{2-} are found to be involved in the formation of OCS in the surface ocean as well, based on computational thermodynamic and kinetic results. To investigate the role of the photo-produced species, OH^\cdot , $^1\text{O}_2$, $\text{CO}_3^{\cdot-}$, and $\text{Br}_2^{\cdot-}$ in the oxidation of dimethylsulfide, methionine, cysteine, and glutathione, we conducted simulations of coupled photochemistry and reaction kinetics with the Aqueous Photochemistry of Environmentally-occurring Xenobiotics (APEX) model. The results indicate that $\text{Br}_2^{\cdot-}$ is the principal reactive species that facilitates the oxidation of sulfur-containing precursors in seawater, thereby leading to OCS formation. The results of the study have implications for our understanding of the role of OCS in ocean biogeochemistry and climate.

5.2 Introduction

The ocean is believed to be one of the most important sources of OCS in the atmosphere,[320, 30, 321, 14, 22, 322, 323] most likely originating from sunlight-driven transformations of phytoplankton-produced sulfur precursor compounds in the surface ocean water column (Figure 5.1).[15, 16, 17, 18, 19, 22] Oceans contribute to the atmospheric pool by direct outgassing of OCS and also by emissions of CS_2 and DMS that are then oxidized to OCS in the troposphere (Figure 5.1).[324, 325, 326, 327, 328, 30, 329, 321, 330] Since it is relatively inert in the troposphere (half-lifetime of > 8 months),[323] OCS can transport into the lower layer of the stratosphere, where it is photooxidized by ultraviolet light (Figure 5.1).[27, 331, 332] Oxidation of stratospheric OCS thus leads to sulfur dioxide, which is in turn rapidly oxidized to sulfate, contributing to the stratospheric sulfate aerosol layer.[27, 331, 28] Atmospheric sulfate condenses into particles that seed clouds, influencing the Earth's radiation budget as well as ozone levels in the stratosphere.[27, 333] Other inputs to atmospheric OCS include anoxic soils, wetlands, atmospheric DMS and CS_2 oxidation, biomass burning, and other

anthropogenic sources.[14, 334, 30] Sinks for OCS include atmospheric oxidation, uptake by plants[334, 335, 321, 336] and by oxic soils.[334, 335, 321]

The annual net flux of OCS from oceans to atmosphere has been estimated in several studies, but it still contains large uncertainties.[320, 321, 14, 334, 30] Recently, Berry and coworkers proposed a value of 736 Gg S yr^{-1} for the flux of OCS from the ocean to the atmosphere,[321] whereas Launois and coworkers reported a value of 813 Gg S yr^{-1} . [320] Different possible parametrizations of the transport model developed by Launois and coworkers lead to estimates of the air-sea flux of OCS that range from 573 Gg S yr^{-1} to $3997 \text{ Gg S yr}^{-1}$. Despite the large uncertainties of these values, these estimates of the flux of OCS from the ocean to the atmosphere imply that the oceans are one of the largest global sources of atmospheric OCS.

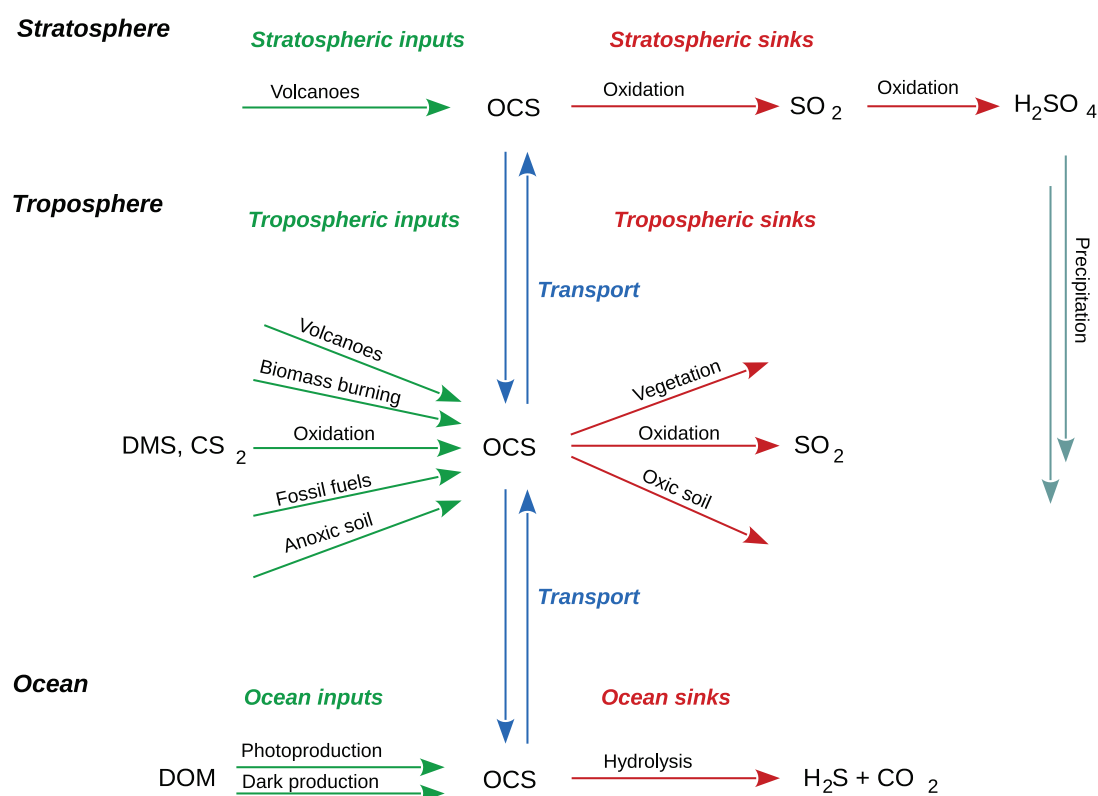


Fig. 5.1 Sources and sinks of OCS in the oceans and atmosphere.

Chemical Formation of OCS in the Ocean

The observation of a strong diurnal cycle of OCS concentration in the surface ocean suggests that photochemical production is the major source of marine OCS, but the molecular mechanisms and the dominant precursor(s) involved remain unclear.[21, 337, 328, 22, 19, 338, 15] After sunrise, the photoproduction of OCS exceeds losses due to hydrolysis and outgassing, thus concentrations increase during the day.[328, 15] The rates of loss of OCS

from the surface ocean by hydrolysis, gas exchange, and downward mixing are all expected to increase approximately in proportion to the OCS concentration near the sea surface.[20, 15] Thus when photoproduction stops in late afternoon, the concentration of OCS decreases until the next morning.[328] The photoproduction of OCS in seawater depends mainly on the presence of photosensitizing or chromophoric compounds, some of which are produced by phytoplankton.[334] Apparent quantum yield measurements of OCS in seawater samples collected from the sea surface to the upper thermocline showed that the OCS photochemical production reaches the maximum near the surface and then exponentially decreases with depth in the photic zone.[328, 15] This exponential trend is consistent with the attenuation of UV radiation in water.[328] However, OCS formation can also occur in the dark.[20, 21] Although the concentrations of OCS decrease with depth, deep water (200-1100 m) contains measurable amounts of OCS, suggesting that a non-photochemical production mechanism takes place in addition to the photochemical mechanism operating in surface seawaters.[16] In the aphotic zone, phytoplankton produce low levels of aqueous reactive species that participate in non-photochemical processes.[339] Experiments showed that the pathway of OCS production in seawater anoxic (dark) sediment is mainly coupled to bacterial sulfate reduction.[340] Oceanic OCS production is thus regulated mostly by photochemical formation pathways during the day and by non-photochemical formation pathways during the night. In both cases, reactive species are thought to mediate the transformation of dissolved organic sulfur compounds into OCS.[18] However, the OCS formation mechanisms that take place in the presence and in the absence of light have not been established yet, nor have the key reactive intermediates been identified.

Chromophoric dissolved organic matter (CDOM) likely plays a key role in photochemical production of OCS in the ocean, whereas its role in the non-photochemical OCS production has not been confirmed.[20, 15] The rate of photoproduction of OCS is increased by the addition of CDOM[341] or DOM standards (with photo-sensitizer properties similar to CDOM),[18] and depends on the nature of CDOM.[342, 15] These observations are consistent with the spatial variability in the observed concentration distribution of OCS:[342, 343] marine OCS concentrations are higher in coastal and shelf regions (see Table 5.1), where natural DOM is more prevalent compared to open seawaters.[22, 340] Non-photochemical OCS production is likely related to the DOM concentration as well.[328, 20] Non-photochemical OCS production is higher in those zone where the CDOM concentration is higher.[328] Moreover, von Hobe et al. found that non-photochemical OCS production is first-order with respect to the chromophoric dissolved organic matter (CDOM) absorbance at 350 nm in seawater samples.[20] On the other hand, lower rates of non-photochemical OCS production in the deep ocean may be explained by bacterial production of both sulfur precursors and reactive species. Given the well-known role of bacteria in OCS production from sediments,[340] there is no conclusive evidence of a direct role of DOM in dark production.

Table 5.1 Summary of OCS sea surface measurements taken between 1987-1996.[14]

OCS / $10^{-12} \text{ mol L}^{-1}$	Area
Open Ocean	
51	North Atlantic Ocean[344]
6	North Atlantic Ocean[16]
20	C/S Pacific Ocean[345]
60	Indian Ocean[346]
19	North Atlantic Ocean (September) [338]
15	North Atlantic Ocean (April)[338]
5	North Atlantic Ocean (January)[338]
Coastal	
18	Mediterranean Sea[346]
23	Ionian Sea[347]
142	North Sea and English Channel[348]
41	Aegean Sea[347]
112	Caribbean Sea[322]
156	African Coast and Amsterdam Is.[346]
Estuarine	
1800	Yarmouth, UK (September)[348]
400	Yarmouth, UK (March)[348]

OCS in the surface ocean is removed by two major sinks, which are the air-sea gas exchange and the temperature-dependent and pH-dependent hydrolysis of OCS to CO_2 and H_2S . [21, 322, 341, 349] The kinetics of OCS hydrolysis is described as the sum of two contributing mechanisms: reaction with water and reaction with hydroxyl anion:[33]



These reactions are pH- and temperature-dependent.[350, 351, 33] The rate constants are $k_{\text{H}_2\text{O}} = (4.37 \pm 0.28) \times 10^{-5} \text{ s}^{-1}$ and $k_{\text{OH}^-} = 34.5 \pm 2.2 \text{ M}^{-1} \text{ s}^{-1}$ for reactions 5.1 and 5.1 at 30°C in artificial polysulfide solutions.[33] The temperature-dependent rate law established by

Kamyshny and coworkers is

$$k_{tot} = k_{H_2O} + k_{OH^-} [OH^-] = (4.19 \pm 0.34 s^{-1}) \times 10^{12} \exp\left(\frac{-12110K}{T}\right) + (1.41 \pm 0.11 M^{-1} s^{-1}) \times 10^{18} \exp\left(\frac{-11580K}{T}\right) [OH^-] \quad (5.3)$$

s^{-1} in artificial polysulfide solutions.[33] At pH 8.03 and 20°C, the total estimated hydrolysis rate constant is $k_{tot} = (2.1 \pm 0.2) \times 10^{-5} s^{-1}$, corresponding to a half-life time of 9 hours in artificial seawater samples, assuming no other loss processes.[33] By comparison, Elliott and coworkers reported apparent half-life times that ranged from 6 hours at 10°C to ~2 days at 25°C for OCS in open surface seawater.[350]

Plausible Molecular Precursors of OCS Formation

Although the mechanisms of OCS formation are not known, it has been proposed that OCS is formed by reaction of CO with sulfur radical species (Table 5.2).[17, 32, 33, 18] Pos et al. proposed a mechanism of formation of OCS where a thiyl radical reacts with a carbonyl group.[17] It has been suggested that a molecular mechanism of OCS production involves the formation of thiyl radical from sulfur-containing compounds, followed by reaction of the thiyl radical with CO.[18, 33] Flöck and co-workers suggested that the naturally occurring methanethiol (CH_3SH) and the most frequently detected thiols in natural aquatic systems (Table 5.3),[352, 353, 354, 355] glutathione (GSH), cysteine (CYS), 3-mercaptopropionic acid (3-MPA), can undergo a hydrogen abstraction from the thiol group in the presence of a radical reactive species, denoted X^\cdot :[18]



The thus formed thiyl radical could then react with CO to form OCS:

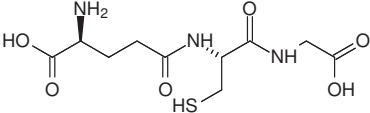
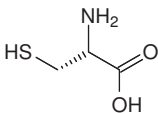
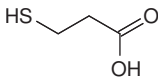
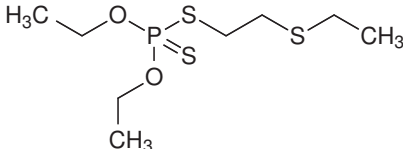
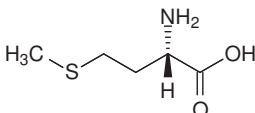


Polysulfides may play a role in OCS formation as well (Table 5.2).[32, 33] Kamyshny et al. reported that the dark reaction between CO and polysulfides to form OCS exhibits second order kinetics under laboratory conditions.[33] Sulfhydryl radicals react with CO to form OCS in water, according to a mechanism analogous to that proposed for thiols:[32, 33]



where X^\cdot is a radical reactive species able to abstract a hydrogen atom from the polysulfides.

Table 5.2 Plausible Sulfur-containing Precursors to OCS formation.

Organic thiols		
		
Glutathione ^a	Cysteine ^{b,c}	3-mercaptopropionic acid ^{d,e}
CH ₃ -SH		
Methanethiol		
Polysulfides		
H ₂ S	HS-SH	HS-S-SH
Hydrogen sulfide	Hydrogen disulfide	Hydrogen trisulfide
HS-S-SH	HS-S-S-SH	HS-S-S-S-SH
Hydrogen tetrasulfide	Hydrogen pentasulfide	Hydrogen hexasulfide
HS-S-S-S-SH		
Hydrogen heptasulfide		
Thioethers		
CH ₃ -S-CH ₃		
Dimethylsulfide	Disulfoton	Methionine

^aNomenclature used in the chapter for Glutathione: the term GSH refers to thiol (i.e., with the neutral thiol functional group -SH); the term GS⁻ refers to thiolate (i.e., with the deprotonated thiol functional group -S⁻); and the term GS[•] refers to thiyl radical (i.e., with the radical center on the thiol functional group -S[•]). ^bCysteine is a zwitterionic species at the pH of the sea (~ 8.3) with the chemical formula of ⁻OOC-CH(NH₃)⁺-CH₂-SH. ^cNomenclature used in the chapter for Cysteine: the term CYS refers to thiol (i.e., with the neutral thiol functional group -SH); the term CYS⁻ refers to thiolate (i.e., with the deprotonated thiol functional group -S⁻); and the term CYS[•] refers to thiyl radical (i.e., with the radical center on the thiol functional group -S[•]). ^d3-mercaptopropionic acid is an anionic species at the pH of the sea (~ 8.3) with the chemical formula of ⁻OOC-CH₂-CH₂-SH. ^eNomenclature used in the chapter for 3-mercaptopropionic acid: the term 3-MPA refers to thiol (i.e., with the neutral thiol functional group -SH); the term 3-MPA⁻ refers to thiolate (i.e., with the deprotonated thiol functional group -S⁻); and the term 3-MPA[•] refers to thiyl radical (i.e., with the radical center on the thiol functional group -S[•]).

Table 5.3 Distribution and Concentrations of Organic Thiols.

Campaign	Total thiols nmol L ⁻¹	GSH nmol L ⁻¹	CYS nmol L ⁻¹	3-MPA nmol L ⁻¹
Coastal Western North Sea and English Channel[353]	0.77-3.54			
Subarctic Pacific Ocean[355]		0.10	1.35	
Open North East Atlantic Ocean[356]		1-15		
Galveston Bay (Texas)[352]		0.23-6.23		
Linsley Pond Lake (Connecticut)[354]		5		2-3

The formation of thiyl radicals from thiols and thioethers and the formation of sulfhydryl radicals from polysulfides have not been fully investigated. Abiotic degradation of thiols has to be activated chemically in ocean surface waters, because thiols do not absorb solar UV radiation at wavelengths above 280 nm. The formation of thiyl radicals from the reaction of aqueous hydroxyl radical OH[•] with GSH, CYS, and 3-MPA has been confirmed by pulse radiolysis experiments:[357]



This reaction is very fast with a rate constant of $\sim 3 \times 10^{10} \text{ M}^{-1} \text{ s}^{-1}$, [357] at the diffusion-controlled limit (which ranges from 10^8 to 10^{10} in water at 298 K, depending on the molecular charges and the sizes of the reactants[358]). However, Zepp and Andreae showed that OH[•] and ¹O₂ are not directly implicated in the OCS formation in coastal seawater samples.[19] They observed that OCS photoproduction in seawater samples and in synthetic seawater solutions containing organosulfur compounds did not substantially increase by saturating the seawater samples with oxygen, indicating that oxygen species such as OH[•] and ¹O₂ are not involved in reactions leading to the formation of OCS. They suggested that other aqueous reactive species such as Br₂^{•-} and CO₃^{•-} were more likely to be responsible for the formation of the thiyl radicals.[19]

The formation of thiyl radicals may also result from the one-electron oxidation of polysulfide anions, thiolates, and thiols.[18, 359, 360, 361] Pos et al.[17] performed a one-electron oxidation of disulfide (HS⁻) to the sulfhydryl radical (HS[•]) using a Ce(IV) salt in a solution of potassium acetylacetonate as a source of carbonyl for OCS production. They observed an instantaneous production of OCS, confirming that sulfur radicals can participate in the formation of OCS. Having one-electron oxidation potential values of 0.7 - 0.8 V versus the NHE electrode (Table 5.4), thiolates can thus react with electron acceptors such as transition metal ions[362, 360] and with oxidizing radicals that exhibit higher one-electron reduction potentials.[361] For example, Br₂^{•-}, which has a one-electron potential, $E^0(\text{Br}_2^{\bullet-}|\text{2Br}^-)$, of

1.62, [363, 364] can easily oxidize GS^- ($E^0(\text{GS}^\bullet|\text{GS}^-) = 0.8 \text{ V}$) [365] to the corresponding thiyl radical, GS^\bullet , under laboratory conditions. [365] However, since Br_2^- oxidizes the sulfur atom of cysteamine anion to thiyl radical and the oxygen atom of phenolate to oxyradical (Table 5.5), here we assume that the thiyl radical CYS^\bullet is a product of the oxidation of CYS^- by Br_2^- . Recently, Chu et al. investigated the photochemical and non-photochemical transformation of CYS^- , showing that the main products of the photo-oxidation of CYS^- in irradiated $^3\text{CDOM}^*$ are cystine ($\text{C}_6\text{H}_{12}\text{N}_2\text{O}_4\text{S}_2$) and a sulfinic acid ($\text{C}_3\text{H}_7\text{NO}_4\text{S}$). [196] Having one-electron oxidation potential values of 0.9 - 1.5 V versus the NHE electrode (Table 5.4), thiols can thus react with electron acceptors such as oxidizing radicals that exhibit sufficiently high one-electron reduction potentials as well. Previously published rate constants for the reactions between Br_2^- and CO_3^- with thiols such as CYS, GSH, and 3-MPA, MET, and phenol in aqueous solution are in the range of 10^6 - $10^9 \text{ M}^{-1} \text{ s}^{-1}$ (Table 5.5). The reactions of CO_3^- with CYS, GSH, 3-MPA, and the reaction of Br_2^- with GSH lead to the formation of the thiyl radical GS^\bullet . No information exists about the structures of the products of the oxidation of CYS by Br_2^- . However, since Br_2^- oxidizes the sulfur atom of GSH to thiyl radical and the oxygen atom of phenol to oxyradical (Table 5.5), here we assume that the thiyl radical CYS^\bullet is a product of the oxidation of CYS by Br_2^- . Having a one-electron reduction potential higher than 1.36 V vs NHE [366] and lower than 1.7 V vs NHE (Table 5.4), [367] the excited triplet state dissolved organic matter ($^3\text{DOM}^*$) can also be involved in the oxidation of thiols and thiolates.

OCS can be also produced from thioether precursors such as MET, DMS, and disulfoton in synthetic and natural seawater under laboratory conditions, but the reaction mechanism remains unknown. [19, 18] The oxidation of DMS by reactive species could potentially represent a substantial source of OCS, since DMS is the predominant volatile sulfur species in open oceans. [22] Br_2^- can oxidize DMS and MET with rate constants in the order of magnitude of $10^9 \text{ M}^{-1} \text{ s}^{-1}$ (Table 5.5). However, the initial chemical steps of DMS oxidation and the nature of the transient species formed are not completely known. Based on the limited information available, the direct products of the oxidation of these two thioethers are a bromine-adducts: [368] DMSBr^\bullet and MET-Br^\bullet (Table 5.5). Zepp and Andreae inferred that oxygen-dependent reactive species such as $^1\text{O}_2$ and OH^\bullet are not responsible for the formation of OCS in coastal seawater samples. [19] Since Br_2^- derives from the reaction between bromide and $^3\text{DOM}^*$, [369] and CO_3^- is mostly produced by the rapid reactions of carbonate with OH^\bullet , [370, 371, 372] and since both react rapidly with organosulfur species such as DMS [373] and neutral protonated GSH, [365] Zepp and Andreae [19] and Boullion and Miller [374] inferred that Br_2^- and CO_3^- could be plausible reactive species responsible for the photo-induced degradation of organic sulfur-containing marine species.

As discussed above, ample evidence indicates that sunlight-generated reactive species play a role in OCS formation. [19, 374] However it is not clear which reactive species are the most important. The interaction of sunlight and DOM at the ocean surface produces a variety of reactive species, including photoactivated $^3\text{DOM}^*$, $^1\text{O}_2$, ROO^\bullet , OH^\bullet , CO_3^- , O_2^- , and several reactive halogen species (Table 5.6). [375] It remains unknown which radical oxidant(s) would play the most important role in generating thiyl radical in (dark or sunlit) seawater.

Chapter 5

Table 5.4 Previously reported one-electron potentials of thiols, thiolates, and hydrogen sulfide. Values are reported in Volts.

Reduction couple	$E^0(\text{RS}^\cdot \text{RS}^-)$	Compounds	$E^0(\text{RS}^\cdot, \text{H}^+ \text{RSH})$
GS^-	0.8[365] ^a	GSH	0.92±0.03[365]
CYS^-	0.73[376]	CYS	1.1[377]
CH_3S^-	0.73[378]	CH_3SH	N/A ^a
3-MPA ⁻	N/A ^a	3-MPA	1.359[377]
HS^-	1.15[379], 1.13[364]	H_2S	1.54[364]

^aNot available.

Table 5.5 Previously reported rate constants of reactions of Br_2^- and CO_3^- with CYS, GSH, 3-MPA, DMS, MET, phenol, phenolate, and cysteamine anion in aqueous solution.

Reactions	$k [\text{M}^{-1} \text{s}^{-1}]$	pH
Oxidant + Thiol		
$\text{CO}_3^- + \text{GSH} \longrightarrow \text{HCO}_3^- + \text{GS}^\cdot$ ^a	5.3×10^6 [368]	pH=7
$\text{CO}_3^- + 3\text{-MPA} \longrightarrow \text{HCO}_3^- + 3\text{-MPA}^\cdot$ ^a	$\sim 3 \times 10^7$ [368]	pH~7
$\text{CO}_3^- + \text{CYS} \longrightarrow \text{HCO}_3^- + \text{CYS}^\cdot$ ^a	4.6×10^7 [368]	pH~7
$\text{Br}_2^- + \text{H}_2\text{NCH}_2\text{CH}_2\text{S}^- \longrightarrow 2 \text{Br}^- + \text{H}_2\text{NCH}_2\text{CH}_2\text{S}^\cdot$	$\sim 2 \times 10^9$ [368]	pH=9.6
$\text{Br}_2^- + \text{GSH} \longrightarrow 2 \text{Br}^- + \text{H}^+ + \text{GS}^\cdot$ ^a	$6.5 \pm 0.1 \times 10^8$ [365]	
$\text{Br}_2^- + \text{CYS} \longrightarrow \text{Products}$	1.8×10^8 [368]	pH=6.6
Oxidant + Thiolate		
$\text{Br}_2^- + \text{CYS}^- \longrightarrow \text{Products}$	$\sim 2 \times 10^9$ [368]	pH=10-11 ^b
$\text{CO}_3^- + \text{CYS}^- \longrightarrow \text{CO}_3^{2-} + \text{CYS}^\cdot$ ^a	3.5×10^8 [368]	pH~10
$\text{CO}_3^- + 3\text{-MPA}^- \longrightarrow \text{CO}_3^{2-} + 3\text{-MPA}^\cdot$ ^a	2.4×10^8 [368]	pH=12 ^c
Oxidant + Thioether		
$\text{CO}_3^- + \text{MET} \longrightarrow \text{CO}_3^{2-} + \text{MET}^{\cdot+}$ ^d	2×10^7 [368]	pH=7
	5×10^7 [368]	pH=11
$\text{Br}_2^- + \text{DMS} \longrightarrow \text{Br}^- + \text{DMS}-\text{Br}^\cdot$ ^e	3.2×10^9 [368]	pH<3.6
$\text{Br}_2^- + \text{MET} \longrightarrow \text{Br}^- + \text{MET}-\text{Br}^\cdot$ ^e	1.7×10^9 [368]	pH=5
	2×10^9 [368]	pH=11
Oxidant + Phenol		
$\text{CO}_3^- + \text{C}_6\text{H}_5\text{OH} \longrightarrow \text{HCO}_3^- + \text{C}_6\text{H}_5\text{O}^\cdot$	2.2×10^7 [368]	pH=7
$\text{Br}_2^- + \text{C}_6\text{H}_5\text{OH} \longrightarrow 2 \text{Br}^- + \text{H}^+ + \text{C}_6\text{H}_5\text{O}^\cdot$	2.2×10^7 [368]	pH=7
Oxidant + Phenolate		
$\text{Br}_2^- + \text{C}_6\text{H}_5\text{O}^- \longrightarrow 2 \text{Br}^- + \text{C}_6\text{H}_5\text{O}^\cdot$	4.7×10^8 [368]	pH=11.2
$\text{CO}_3^- + \text{C}_6\text{H}_5\text{O}^- \longrightarrow \text{CO}_3^{2-} + \text{C}_6\text{H}_5\text{O}^\cdot$	4.7×10^8 [368]	pH=11.2

^aCYS[·], GS[·], and 3-MPA[·] are the thiyl radical derived from CYS, GSH, and 3-MPA. ^bThe thiol functional group of cysteine is deprotonated at the pH 10. ^cThe thiol functional group of 3-mercaptopropionic acid is deprotonated at the pH 12. ^dMET^{·+} is the radical cation of MET. ^eDMS-Br[·] and MET-Br[·] are bromine-adducts of DMS and MET, respectively.

The proposed mechanisms that involve sulfur-containing species and CO to form OCS in seawater merit further confirmation, and the relevance of potential competing mechanisms remains relatively unexplored. Without an understanding of the precursors, species, and mechanisms involved in oceanic OCS formation, it is difficult to fully assess how OCS is coupled with ongoing changes in the Earth's oceans.

Objectives of the Present Study

The main objective of this study was to identify the combination(s) of precursors, reactive species, and mechanisms that most likely contribute the principal formation pathways of oceanic OCS. We investigated the reaction mechanisms of several candidate precursor molecules and reactive oxidants for their capacities to form OCS. Plausible reduced sulfur precursors included prominent marine thiols, thioethers, and polysulfides (Table 5.2).

To investigate these pathways, reaction equilibrium constants and rate constants were determined or estimated based on existing experimental data, further supplemented with quantum chemical molecular modeling computations conducted in the present study. The resulting information about reaction equilibria, rates, and mechanisms have been analyzed together with data on the environmental abundances of candidate precursors and aqueous reactive transients in the surface ocean. This allowed us to identify the most important pathways that lead to oceanic OCS formation. The results of the project have broad implications for our understanding of the role of OCS in ocean biogeochemistry and climate.

Table 5.6 Aqueous reactive species in surface seawater.

Reactive species	Concentration [M]	Reactive species	Concentration [M]
$^1\text{O}_2$	$10^{-14} / 10^{-13}$ [380]	Cl^\bullet	1.73×10^{-15} [381]
$\text{O}_2^{\bullet-}$	$20 - 167 \times 10^{-12}$ [382]	$\text{Cl}_2^{\bullet-}$	1.80×10^{-12} [381]
$\text{CO}_3^{\bullet-}$	2.99×10^{-7} [381]		$10^{-14} / 10^{-12}$ [383]
OH^\bullet	$10^{-18} / 10^{-17}$ [380]	Br^\bullet	4.10×10^{-12} [381]
	1.51×10^{-13} [381]	$\text{Br}_2^{\bullet-}$	8.59×10^{-9} [381]
NO^\bullet	$0.12 \pm 0.01 \times 10^{-9}$ [384]		$10^{-15} / 10^{-14}$ [380]
	$2.4 - 32 \times 10^{-11}$ [385]	$\text{BrCl}^{\bullet-}$	3.12×10^{-9} [381]
e_{aq}^-	10^{-17} [380]		

5.3 Methods

5.3.1 Model Chemistries and Basis Sets

All computations were carried out with the Gaussian09 program.[124] Aqueous phase molecular geometries for all species involved in this study were optimized with M06-2X[386] density functional method combined with the Universal Solvent Model based on Solute Electron Density (SMD).[226] M06-2X was designed for main-group thermochemistry.[386] In previous reports, M06-2X also gave good performance in the prediction of geometries and frequencies of small radicals,[387] in the prediction of binding energies of radicals with solvent molecules[388] as well as energies of bond dissociation reactions leading to radicals.[292] We optimized the molecular geometries with the SMD implicit solvent model, since the geometries of zwitterionic species such as amino acids can be substantially influenced by the presence of aqueous solvent.[7] Harmonic vibrational frequency analyses were conducted to confirm the nature of the stationary points on the potential energy surfaces with the same method used for the geometry optimizations. Structures corresponding to minimum points in the potential energy surfaces are characterized by all positive vibrational frequencies, whereas structures corresponding to transition states exhibit one negative (imaginary) vibrational frequency.[7] Single point energy computations with the B2PLYPD[122, 123] electronic structure method combined with SMD implicit solvent model were performed on the optimized geometries to obtain a more accurate prediction of the aqueous phase electronic energy than M06-2X electronic structure results. To briefly test whether B2PLYPD and M06-2X are appropriate for the electronic structures of sulfur-containing molecules, we evaluated gas phase total atomization energies and compared these results to published benchmark values[93] (Table 5.8). To consistently calculate the solvent effect with the B2PLYPD functional, we included the keyword *SCRF(ExternalIteration)*[237, 238] in the Gaussian09 input. The aug-cc-pVTZ basis set[126, 127, 225] was employed throughout.

5.3.2 Computational Estimates of Aqueous Phase Gibbs Free Energies of Reaction

The aqueous phase Gibbs free energy of reaction at a (hypothetically infinitely dilute) 1 M standard state,[223] $\Delta G_{aq,rxn}^*$, can be obtained from aqueous phase free energies. For any reaction in aqueous solution, we can determine the aqueous free energy of reaction:

$$\Delta G_{aq,rxn}^* = \sum_i \nu_i G_{aq}^*(X_i) \quad (5.9)$$

where ν_i is the stoichiometric coefficient of molecule X_i , and $G_{aq}^*(X_i)$ is the aqueous Gibbs free energy of species X_i at 1 M standard state. The superscript * indicates that the thermochemical property is reported at the (hypothetically infinitely dilute) 1 M standard state[223]. In the present work, $G_{aq}^*(X_i)$ is determined as the sum of aqueous electronic energy contribution and thermal contributions to the Gibbs free energy, which is derived from the vibrational

frequency analysis calculation:

$$G_{aq}^*(X_i) = E_{SMD}^*(X_i) + \Delta G_{thermal,SMD}^*(X_i) \quad (5.10)$$

where $E_{SMD}^*(X_i)$ is the total electronic energy corresponding to the molecular electronic structure of species X_i including the energy of interaction with the solvent according to the SMD implicit solvent model, and $\Delta G_{thermal,SMD}^*(X_i)$ is the thermal contribution to the Gibbs free energies for species X_i . The subscript *SMD* indicates that the energetic property has been computed within the SMD approach (*i.e.*, in aqueous phase). We employed two different density functional methods, M06-2X and B2PLYPD, to estimate G_{aq}^* for species involved in the reactions leading to OCS in water. The aqueous free energies computed with the SMD/M06-2X/aug-cc-pVTZ model chemistry, $G_{aq}^{*M06-2X}$ are the sum of the following contributions:

$$G_{aq}^{*M06-2X}(X_i) = E_{SMD}^{*M06-2X}(X_i) + \Delta G_{thermal,SMD}^{*M06-2X}(X_i) \quad (5.11)$$

where $E_{SMD}^{*M06-2X}(X_i)$ is the electronic energy corresponding to the molecular electronic structure of species X_i , and $\Delta G_{thermal,SMD}^{*M06-2X}(X_i)$ is the thermal contribution to the Gibbs free energies for species X_i computed with the SMD/M06-2X/aug-cc-pVTZ method. The molecular geometry of species X_i was optimized with the SMD/M06-2X/aug-cc-pVTZ model chemistry. We performed additional energy single point calculations with SMD/B2PLYPD/aug-cc-pVTZ electronic structure method to obtain more accurate electronic energy predictions than M06-2X estimates:

$$G_{aq}^{*B2PLYPD}(X_i) = E_{SMD}^{*B2PLYPD}(X_i) + \Delta G_{thermal,SMD}^{*M06-2X}(X_i) \quad (5.12)$$

where $E_{SMD}^{*B2PLYPD}(X_i)$ is the B2PLYPD electronic energy estimate associated to the molecular electronic structure of species X_i , and $\Delta G_{thermal,SMD}^{*M06-2X}(X_i)$ is the thermal contribution to the Gibbs free energies for species X_i computed with the SMD/M06-2X/aug-cc-pVTZ method. The molecular geometry of species X_i was optimized with the SMD/M06-2X/aug-cc-pVTZ model chemistry.

5.3.3 Computational Estimates of Aqueous Phase Gibbs Free Energies of Activation

We estimated the aqueous Gibbs free energies of activation for several reactions that were hypothesized to lead to the formation of OCS from thiols and polysulfides. In the transition state theory,[137, 298] the aqueous Gibbs free energy of activation at 1 M standard state for a reaction is defined as the difference between the aqueous free energy of the transition state structure (*i.e.* the highest free energy value along the profile of the reaction coordinate) and the aqueous free energy of the reactants:

$$\Delta G_{aq,rxn}^\ddagger = G_{aq}^\ddagger(TS) - \sum_i \nu_i G_{aq}^*(R_i) \quad (5.13)$$

where $G_{aq}^\ddagger(TS)$ is the aqueous Gibbs free energy associated with the transition state structure TS , the ν_i is the stoichiometric coefficient of the reactant R_i , and $G_{aq}^*(R_i)$ is the aqueous Gibbs free energy of species R_i at 1 M standard state. We computed aqueous free energies of activation with two DFT methods, M06-2X and B2PLYPD. The aqueous free energies of activation computed with the SMD/M06-2X/aug-cc-pVTZ model chemistry, $\Delta G_{aq,rxn}^{\ddagger M06-2X}$ is the sum of the following contributions:

$$\Delta G_{aq,rxn}^{\ddagger M06-2X} = \left(E_{SMD}^{\ddagger M06-2X}(TS) + \Delta G_{thermal,SMD}^{\ddagger M06-2X}(TS) \right) - \sum_i \nu_i \left(E_{SMD}^{* M06-2X}(R_i) + \Delta G_{thermal,SMD}^{* M06-2X}(R_i) \right) \quad (5.14)$$

where $E_{SMD}^{\ddagger M06-2X}(TS)$ and $E_{SMD}^{* M06-2X}(R_i)$ each denote the total value of the electronic energy computed with the SMD/M06-2X/aug-cc-pVTZ model chemistry for the transition state and reactants species, and $\Delta G_{thermal,SMD}^{\ddagger M06-2X}(TS)$ and $\Delta G_{thermal,SMD}^{* M06-2X}(R_i)$ are the thermal corrections to the Gibbs free energies for species TS and R_i computed with the SMD/M06-2X/aug-cc-pVTZ method. We performed additional energy single point calculations with the SMD/B2PLYPD/aug-cc-pVTZ electronic structure method to obtain more accurate electronic energy predictions than M06-2X estimates:

$$\Delta G_{aq,rxn}^{\ddagger B2PLYPD} = \left(E_{SMD}^{\ddagger B2PLYPD}(TS) + \Delta G_{thermal,SMD}^{\ddagger M06-2X}(TS) \right) - \sum_i \nu_i \left(E_{SMD}^{* B2PLYPD}(R_i) + \Delta G_{thermal,SMD}^{* M06-2X}(R_i) \right) \quad (5.15)$$

where $E_{SMD}^{\ddagger B2PLYPD}(TS)$ and $E_{SMD}^{* B2PLYPD}(R_i)$ are the B2PLYPD electronic energy estimates associated with the molecular electronic structure of species TS and R_i , respectively, where the geometry has been optimized with the SMD/M06-2X/aug-cc-pVTZ model chemistry, and $\Delta G_{thermal,SMD}^{\ddagger M06-2X}(TS)$ and $\Delta G_{thermal,SMD}^{* M06-2X}(R_i)$ are the thermal contributions to the Gibbs free energies for the transition state structure TS and the reactants R_i , respectively, computed with the SMD/M06-2X/aug-cc-pVTZ method.

5.3.4 Aqueous Equilibrium Constants of Reactions Leading to OCS Formation

We computed aqueous equilibrium constants for the reactions that are hypothesized to produce OCS from thiol and polysulfide precursors. No experimental equilibrium constant data are available for the reactions evaluated here. We determined equilibrium constants (K_{aq}^{Comp}) for several important reactions, based on theoretical aqueous free energy of reaction, $\Delta G_{aq,rxn}^*$, data:

$$K_{aq}^{Comp} = \exp \left(\frac{-\Delta G_{aq,rxn}^*}{RT} \right) \quad (5.16)$$

5.3.5 Aqueous Rate Constants of Reactions Leading to OCS Formation

Reaction rate constants were estimated from computed activation free energies based on transition state theory.[137, 298] We employed the Eyring-Polanyi equation to estimate a transition-state theory rate constant:

$$k_{TST} = \frac{k_B T}{h} \exp\left(\frac{-\Delta G_{aq,rxn}^\ddagger}{RT}\right) \quad (5.17)$$

where k_B is the Boltzmann constant, h is Planck's constant, T is temperature, and R is the molar gas constant. The k_{TST} from equation 5.17 has units of s^{-1} in the case of first order reactions, whereas it has units of $M^{-1} s^{-1}$ for second order reactions, consistent with the stoichiometry of the partition functions that are used to determine $\Delta G_{aq,rxn}^\ddagger$. For second order reactions the theoretical k_{TST} value can exceed the rate allowed by diffusion of the reactive species ($\sim 10^{10} M^{-1} s^{-1}$). In these cases, we assumed that the diffusion-controlled reaction rate, $k_{diffusion}$, is the rate-limiting reaction step and we estimated the second order reaction rate constant, k , as:[300]

$$\frac{1}{k} = \frac{1}{k_{TST}} + \frac{1}{k_{diffusion}} \quad (5.18)$$

We assigned a value of $10^{10} M^{-1} s^{-1}$ to $k_{diffusion}$.

5.3.6 Description of the Profile of the Reaction Potential Energy Surface (Relaxed Scan)

A relaxed scan describes the profile of the system electronic energy at several selected values of a chosen reaction coordinate. We used the interatomic distance (bond length) between the C atom of the CO and the S atom of the sulfur-containing species involved in the reaction atoms as the reaction coordinate. At each selected value of the reaction coordinate, a partially constrained geometry optimization of the system is conducted, maintaining a fixed value of the reaction coordinate while the remainder of the molecular system geometry is relaxed to an energy minimum configuration. The resulting energy profile describes the minimum energy pathway along the reaction coordinate. Relaxed scan calculations were conducted with the SMD/M06-2X/aug-cc-pVTZ model chemistry in Gaussian09. Further single point energy calculations with the SMD/B2PLYPD/aug-cc-pVTZ model have been performed to obtain a more accurate electronic energy. Thermal contributions to the free energy are not included in the energy profile.

5.3.7 Natural Population Analysis to Estimate Atomic Charge Distribution

A natural population analysis (NPA), as implemented in Gaussian09,[302, 303, 304, 305, 306, 307] was performed to gain more insight into the chemical nature of transition state structures

of reactions involving polysulfides and CO. Based on the natural orbital occupancies, the NPA algorithm partitions the electron density of the entire molecule to each of the different atoms. The natural charge on each atom is given by the difference between the atomic nuclear charge and the sum of the populations of the natural atomic orbitals assigned to that atom. The resulting assigned natural charges were computed with the SMD/M06-2X/aug-cc-pVTZ electronic structure method, using SMD/M06-2X/aug-cc-pVTZ for geometry optimizations, also conducted with Gaussian09.

5.3.8 NPA spin density analyses to locate the unpaired electron in open shell systems

Atomic spin density calculations, carried out within the NPA framework as implemented in Gaussian09, enable us to locate the unpaired electron and understand whether it is delocalized over several atoms in the molecule or localized on a single atom.[7, 389] The spin density calculation indicates the difference between the populations of α -spin and β -spin electrons of each atom.[7] In open shell systems, the α electrons and the β electrons are distributed differently throughout the molecule, and population analysis can thus be conducted separately for both densities. The difference between α - and β -spin densities, q^α and q^β , corresponds to the unpaired spin density (SD) at a given center x :

$$SD_x = q_x^\alpha - q_x^\beta \quad (5.19)$$

In the case of the NPA population analysis, q^α and q^β are combined with half of the nuclear atomic charge, $q_x^{nucleus}$, to produce the corresponding natural atomic charge, NPA_x^α and NPA_x^β :

$$NPA_x^\alpha = \frac{q_x^{nucleus}}{2} - q_x^\alpha \quad (5.20)$$

$$NPA_x^\beta = \frac{q_x^{nucleus}}{2} - q_x^\beta \quad (5.21)$$

The unpaired NPA spin densities SD_x are obtained from:

$$SD_x = NPA_x^\beta - NPA_x^\alpha \quad (5.22)$$

5.3.9 Photochemical Modeling with the Aqueous Photochemistry of Environmentally-occurring Xenobiotics (APEX) Software

We sought to assess the relative importance of the reactions between sulfur-containing molecules and some reactive oxidants under environmentally relevant conditions, focusing on molecules and reactive species for which reasonably accurate experimental data of the

second-order reaction rate constants are available. The chosen sulfur-containing molecules were DMS, MET, CYS, and GSH, and the reactive oxidants were OH^\cdot , $\text{CO}_3^{\cdot-}$, $^1\text{O}_2$, and $\text{Br}_2^{\cdot-}$ (Table 5.7).[390, 368, 391, 365] The reactions that involve the thiolate species were ignored, and only the neutral thiol species were considered. It was for instance not possible to carry out an assessment of the role of $^3\text{DOM}^*$ reactions because, although these processes may be important in seawater photochemistry,[375] the relevant second-order reaction rate constants are not available. We are aware that $\text{BrCl}^{\cdot-}$ species might be also important; despite its relevance in marine and natural water chemistry,[381, 392] the relevant second-order reaction rate constants for the reactions of $\text{BrCl}^{\cdot-}$ with DMS, MET, and the thiols CYS and GSH are not available. Therefore, we assumed that $\text{BrCl}^{\cdot-}$ contribution to the phototransformation of sulfur-containing compounds is taken into account as $\text{Br}_2^{\cdot-}$ contribution in the kinetic model. The steady-state concentrations of OH^\cdot , $\text{CO}_3^{\cdot-}$, and $^1\text{O}_2$ were modeled directly (*vide infra*), whereas $[\text{Br}_2^{\cdot-}]$ was calculated by assuming that $\text{Br}_2^{\cdot-}$ is formed by reaction between OH^\cdot and Br^- , [370, 371] and $\text{Br}_2^{\cdot-}$ is eliminated by disproportionation and by reactions with nitrite and DOM.[390, 368, 393, 394, 2]

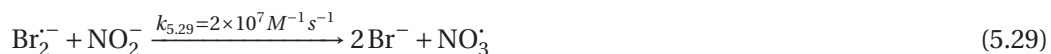
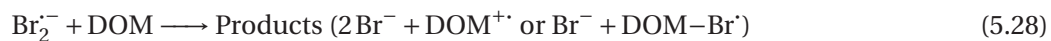
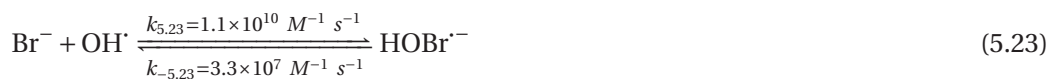


Table 5.7 Previously reported rate constants of reactions of $\text{Br}_2^{\cdot-}$, $\text{CO}_3^{\cdot-}$, OH^{\cdot} , and $^1\text{O}_2$ with CYS, GSH, DMS, and MET in aqueous solution.

Compounds	$k_{\text{Br}_2^{\cdot-}} [\text{M}^{-1} \text{s}^{-1}]$	$k_{\text{CO}_3^{\cdot-}} [\text{M}^{-1} \text{s}^{-1}]$	$k_{\text{OH}^{\cdot}} [\text{M}^{-1} \text{s}^{-1}]$	$k_{^1\text{O}_2} [\text{M}^{-1} \text{s}^{-1}]$
CYS	1.8×10^8 [368]	5×10^7 [368]	2×10^{10} [390]	8.3×10^6 ^a [391]
GSH	$6.5 \pm 0.1 \times 10^8$ [365]	5.3×10^6 [368]	1.4×10^{10} [390]	2.4×10^6 ^a [391]
MET	1.7×10^9 [368]	3×10^7 [368]	8.3×10^9 [390]	2.1×10^7 [391]
DMS	3.2×10^9 [368]	4×10^7 ^b	1.9×10^{10} [390]	5.8×10^7 ^c [391]

^aThe experimental value was measured in a D_2O solution. ^bValue was estimated according to equation 5.32. ^cThe experimental value was measured in a CH_3OH solution.

The oxidation reaction of bromide by $^3\text{DOM}^*$ is potentially important in seawater conditions,[393, 392] but its rate constant is still poorly known. A rough estimate is available as $k_{5,25} = 3.5 \times 10^9 \text{ M}^{-1} \text{s}^{-1}$, [393], but there is evidence that such a value overestimates the real rate constant.[392] In this work we applied two different approaches to account for the contribution of $^3\text{DOM}^*$ to the system. In the first approach (*a*), we totally neglect reaction 5.25, which would cause the $\text{Br}_2^{\cdot-}$ formation rate to be underestimated, whereas in the second approach (*b*), we study the behavior of the system as a function of $k_{5,25}$, making the latter vary over a wide range of orders of magnitude.

The rate constant of reaction 5.28 is also not exactly known, but an estimate was obtained by considering the reaction rate constants between $\text{Br}_2^{\cdot-}$ and phenolic compounds ($k_{5,28} = 2 \times 10^7 \text{ M}^{-1} \text{s}^{-1}$ or, in more manageable units, $k_{5,28} = 3 \times 10^2 \text{ L (mg C)}^{-1} \text{s}^{-1}$).[393] The mg C L^{-1} units are more straightforward to use than the molar ones when the DOM is measured as the dissolved organic carbon (DOC, expressed in mg C L^{-1}). Our estimate of $k_{5,28}$ is actually an upper limit because phenolic compounds are assumed more reactive than average organic molecules toward $\text{Br}_2^{\cdot-}$. [368] Therefore, by omitting a potentially important source ($^3\text{DOM}^* + \text{Br}^-$) and by overestimating the $\text{Br}_2^{\cdot-}$ consumption by DOM, we obtain a lower limit for the steady-state $[\text{Br}_2^{\cdot-}]$ under environmental conditions. From the reaction sequence (5.23 - 5.29), by applying the steady-state approximation to all radical species we obtain the following result:

$$[\text{Br}_2^{\cdot-}] = \frac{-(k_{5,28}\text{DOC} + k_{5,29}[\text{NO}_2^-])}{4k_{5,27}} + \frac{\sqrt{(k_{5,28}\text{DOC} + k_{5,29}[\text{NO}_2^-])^2 + 8k_{5,27}[\text{Br}^-](k_{5,23}k_{5,24}(k_{-5,23} + k_{5,24})^{-1}[\text{OH}^{\cdot}] + k_{5,25}[^3\text{DOM}^*])}}{4k_{5,27}} \quad (5.30)$$

where the $k_{5,25}[^3\text{DOM}^*]$ term was initially omitted, and it was considered only in a second moment.

The assessment of $[\text{OH}^{\cdot}]$ and $[^3\text{DOM}^*]$, together with $[^1\text{O}_2]$ and $[\text{CO}_3^{\cdot-}]$, was carried out with

the APEX software (Aqueous Photochemistry of Environmentally-occurring Xenobiotics).[395] APEX predicts the steady-state concentration of transient species as a function of water chemistry and depth, for a given sunlight irradiance and spectrum. The sunlight data we chose correspond a UV irradiance of 22 W m^{-2} , which can be observed during a clear-weather summer day in mid-morning or mid-afternoon (e.g., July 15 at 9 am or 3 pm solar time).[395] Water photoreactivity and absorption data were based on previously published saltwater irradiation results.[396] Key input data for APEX are the water depth, the concentration values of nitrate and nitrite (which are OH^\cdot sources) and of bromide (the main OH^\cdot scavenger in seawater),[397] the concentration of inorganic carbon (carbonate and bicarbonate, which scavenge OH^\cdot to produce $\text{CO}_3^{\cdot-}$)[373, 398], and the DOC which includes both DOM (important scavenger of OH^\cdot and $\text{CO}_3^{\cdot-}$) and CDOM (chromophoric DOM, a source of $^1\text{O}_2$, OH^\cdot , and $^3\text{DOM}^*$). On this basis, APEX predicts $[\text{OH}^\cdot]$, $[^1\text{O}_2]$, and $[\text{CO}_3^{\cdot-}]$ under the given irradiation conditions. The values of $[\text{Br}_2^{\cdot-}]$ were then calculated with equation 5.30 on the basis of the modeled $[\text{OH}^\cdot]$, and of input DOC, nitrite, and bromide concentrations.

We assumed that a sulfur-containing compound w (where $w = \text{DMS, MET, CYS, or GSH}$) reacts with the reactive species y with known second-order reaction rate constant, $k_{w,y}$. We also assumed that the relevant set of reactive species (which include y) are $j = \text{OH}^\cdot, ^1\text{O}_2, \text{CO}_3^{\cdot-}, \text{ or } \text{Br}_2^{\cdot-}$, with known second-order rate constants $k_{w,j}$. On this basis, the fraction of the overall extent of phototransformation of w by the reactive species y with respect to the set of considered reactive species, j , is determined as follows

$$\psi_{w,y} = \frac{k_{w,y}[y]}{\sum_j k_{w,j}[j]} \quad (5.31)$$

where $[y]$ and $[j]$ are the (modeled) steady-state concentrations of these reactive oxidant species. It is important to note that reaction with j does not necessarily account for the totality or even the majority of w phototransformations. Therefore, the calculated values of $\psi_{w,y}$ represent the relative importance of the studied reactive species, based on their relative contributions to the reaction with each sulfur-containing compound, w . The trends of $\psi_{w,y}$ were modeled at water column depth of 10 m and with assumed input parameter values of: $10 \mu\text{M}$ nitrate, $1 \mu\text{M}$ nitrite, 2 mM bicarbonate, and $20 \mu\text{M}$ carbonate, which are considered typical of seawater.[399] Simulations were conducted with varied concentrations of bromide, from 0 to 1 mmol L^{-1} , and with varied concentrations of DOC, from 0 to 2 mg C L^{-1} . Shortly before the submission deadline of the finally formatted thesis, it was noticed that the reaction rate constant employed in APEX simulations for the reaction of $\text{Br}_2^{\cdot-}$ with GSH had been assigned a value that was too low ($7 \times 10^7 \text{ M}^{-1} \text{ s}^{-1}$) by about a factor of 10 compared to the correct value ($6.5 \pm 0.1 \times 10^8 \text{ M}^{-1} \text{ s}^{-1}$)[365]. In future work, the APEX simulations could be updated to incorporate the corrected rate constant. However, at a qualitative level, the corrected results and conclusions for APEX simulations are expected to be similar to what is reported here.

The reaction rate constant between DMS and $\text{CO}_3^{\cdot-}$ is not known, although the process

is expected to be important.[374] Based on structural analogies,[374] it is very likely that $k_{\text{DMS}+\text{CO}_3^-} \sim k_{\text{CYS}+\text{CO}_3^-}$ and/or $k_{\text{MET}+\text{CO}_3^-}$, considering that $k_{\text{CYS}+\text{CO}_3^-} \sim k_{\text{MET}+\text{CO}_3^-}$. [368] For this reason, we assumed hereafter that:

$$k_{\text{DMS}+\text{CO}_3^-} = \frac{1}{2}(k_{\text{CYS}+\text{CO}_3^-} + k_{\text{MET}+\text{CO}_3^-}) = 4 \times 10^7 \text{ M}^{-1} \text{ s}^{-1} \quad (5.32)$$

5.4 Results and Discussion

5.4.1 Assignment of Error Bounds for the Theoretical Aqueous Thermochemical Properties

We briefly evaluate the reliabilities of the chemistry models employed to predict thermodynamic and kinetic properties, based on comparisons to previously reported theoretical benchmark total atomization energies and experimental data, $\Delta G_{\text{sol},\text{Expt}}$, for selected small molecules. We found that the M06-2X/aug-cc-pVTZ and B2PLYPD/aug-cc-pVTZ model chemistries are both appropriate for evaluating the electronic structures of a test set of sulfur-containing molecules (Table 5.8), with the B2PLYPD electronic structure method providing better performance than M06-2X, on average. Gas phase total atomization energies (TAEs) predicted by B2PLYPD and M06-2X methods for SO_2 , CS_2 , COS , CO_2 , H_2S , CS , CO , HS^\cdot , and HSS^\cdot were compared to high-accuracy theoretical benchmarks that are available in the literature[93] (Table 5.8). The error-per-bond statistic was defined as the absolute value of $\frac{|(\text{TAE}_{\text{DFT}} - \text{TAE}_{\text{Benchmark}})|}{\text{total number of bonds}}$ for each molecule, and with the term DFT we refer to M06-2X/aug-cc-pVTZ and B2PLYPD/aug-cc-pVTZ model chemistries. We observed that the B2PLYPD method exhibits an average error-per-bond value of 10.1 kJ mol⁻¹, a root mean square error-per-bond of 13.1 kJ mol⁻¹, and a root mean square error of 23.6 kJ mol⁻¹ of the gas phase TAEs for this test set (Table 5.8). The M06-2X model chemistry has an average error-per-bond value of 8.0 kJ mol⁻¹, a root mean square error-per-bond of 13.7 kJ mol⁻¹, and a root mean square error of 25.6 kJ mol⁻¹ of the TAEs for the same chemical set.

The magnitude of root mean square error of the TAEs found here for the B2PLYPD/aug-cc-pVTZ and M06-2X/aug-cc-pVTZ model chemistries is similar to values reported for other datasets. Goerigk and Grimme[235] reported a root mean square error of 18.0 kJ mol⁻¹ for B2PLYPD/def2-QZVP[400] for the W4-08 total atomization energy dataset (which also contains sulfur species). Based on the reasonable performance of the B2PLYPD and M06-2X functionals for the datasets discussed above, these model chemistries were viewed as appropriate for investigating electronic structures of sulfur-containing molecules.

To evaluate the performance of the SMD/B2PLYPD model chemistry for the handling of aqueous solvent, we evaluated the free energies of solvation of CO_2 , CO , and 6 sulfur-containing molecules for which experimental data have been measured previously (Table 5.9). For each solute, the free energy of solvation was calculated as the difference between the free energy computed with the SMD/B2PLYPD model chemistry and the free energy computed

Table 5.8 Evaluation of M06-2X and B2PLYPD electronic structure models for total atomization energies (TAE) at 0 K and average error-per-bond values, for selected sulfur and oxygen species, in kJ mol^{-1} .

Compounds	TAE_{W4}^a	TAE_{M06-2X}	Error per bond $_{M06-2X}^b$	$TAE_{B2PLYPD}$	Error per bond $_{B2PLYPD}^b$
SO ₂	1086.2	1012.8	36.7	1026.4	29.9
CS ₂	1167.7	1158.4	4.6	1155.1	6.3
OCS	1398.8	1397.1	0.9	1393.7	2.5
CO ₂	1624.8	1626.5	0.8	1624.8	0.7
H ₂ S	768.1	758.1	5.0	751.5	8.3
CS	717.1	700.8	16.3	699.9	17.2
CO	1082.5	1080.3	2.2	1074.4	8.1
HS [*]	366.4	364.4	2.0	360.6	5.7
HSS [*]	689.1	681.6	3.7	665.1	12.0
MUE per bond ^c			8.0		10.1
RMSE		25.6		23.6	
RMSE per bond			13.7		13.1

^aThe TA14 theoretical benchmarks of the total atomization energies at 0 K were taken from Karton et al., [93] and the values shown here exclude the zero-point vibrational energy, core-valence correlation contribution, scalar relativistic contribution, first and second order spin-orbit couplings, and diagonalized Born-Oppenheimer contribution. ^berror per bond = $|(TAE_{W4} - TAE_{B2PLYPD})| / (Total\ number\ of\ atoms - 1)$. ^cMean unsigned error (MUE) is the average of the absolute error-per-bond values over the molecular set, in kJ mol^{-1} .

Table 5.9 Evaluations of SMD/B2PLYPD model for free energies of solvation for CO, CO₂, and selected sulfur neutralspecies, in kJ mol⁻¹.

	$\Delta G_{solv,Expt}^a$	$\Delta G_{solv,Comp}$
Neutral compounds		
CO	9.2 ± 0.2	23.4
CO ₂	0.5 ± 0.2	14.4
SO ₂	-8.7 ± 0.7	-9.2
H ₂ S	-2.3 ± 1.3	-5.2
CS ₂	-1.0 ± 4.2	5.3
OCS	1.7 ± 4.2	11.3
CH ₃ SH	-5.6 ± 8.4	-3.6
DMS	-6.4 ± 8.4	-2.5
MUE		6.7
MSE		-5.8
MAD		14 (CO)
RMSE		8.3

^aExperimental values were taken from Sander's database.[261]

with the B2PLYPD model chemistry in gas phase:

$$\Delta G_{solv,Comp}(X_i) = G_{SMD}^{*B2PLYPD}(X_i) - G_{gas}^{*B2PLYPD}(X_i) \quad (5.33)$$

The SMD/B2PLYPD model exhibits a root mean square error (RMSE) of 8.3 kJ mol⁻¹ and a mean unsigned error (MUE) of 6.7 kJ mol⁻¹ for this test set which includes CO₂, CO, and neutral sulfur-containing compounds (Table 5.9). The MUE found for our test set is higher than the mean unsigned error of 3.6 kJ mol⁻¹ of the SMD model reported by Marenich et al.[226] for a much larger test set of small neutral molecules in aqueous solvent.

In this project, we are also dealing with radical and anionic molecules in water, and the assessment of the uncertainties of free energy properties of these species is more difficult. From previous theoretical study on the weak interactions of radicals with water, we know that the binding energy between a neutral carbon-centered radical and a single molecule of water is in the order of -7 kJ mol⁻¹, whereas the binding energy of a neutral halogen atom with a single molecule of water is in the range of -15 kJ mol⁻¹. [388] Based on this, we assume that the interactions between a neutral sulfur-centered radical and a single molecule of water are relatively weak as well. Since the free energies of solvation of neutral radicals are assumed to be much smaller than the values for anions, we assume that implicit solvent models can predict the solvation energies for neutral radicals more accurately than the solvation energies for closed-shell ionic species. However, no previous computational assessment of the error of free energies of solvation values for neutral radical species has been made. The uncertainties assigned to quantum chemical results for these reactions are thus discussed on a case by case basis. We suggest that the error bounds expected to contain 70% of the deviations can be

approximated by $1.04 \times \text{RMSE}$ found for the free energies of solvation for neutral close- and open-shell species, and thus we assign an error of 9 kJ mol^{-1} to the free energy of solvation values to neutral close- and open-shell compounds. Marenich et al. reported a mean unsigned error of 19 kJ mol^{-1} for the free energies of aqueous solvation for small ionic molecules.[226] The RMSE values for a given dataset is always larger than the MUE values; while MUE gives the same weight to all the errors, the RMSE gives errors with larger absolute values more weight than errors with smaller absolute values.[401] Since no RMSE value is available for the free energies of aqueous solvation of the dataset used by Marenich et al., we tentatively assign uncertainty bounds (expected to contain 70% of the deviations) of $\geq 1.04 \times \text{MUE}$ (20 kJ mol^{-1}) to the free energies of solvation of the anions and radical anions considered in this project. It is unclear how to interpret the performance of the SMD/B2PLYPD model to predict aqueous free energies of solvation for radical anions species, where additional errors may arise from the specific interactions between radicals and solvent. We are unaware of a systematic assessment of SMD/DFT methods for a set of radical anions.

To assign the uncertainty bounds for the $\Delta G_{aq,rxn}^\ddagger$ and $\Delta G_{aq,rxn}^*$ values, we estimated the overall uncertainty as a combination of the average error of the electronic structure method (B2PLYPD/aug-cc-pVTZ) and the average error associated with the implicit solvent model (SMD/B2PLYPD/aug-cc-pVTZ). We estimated the error bounds that are expected to contain 70% of the deviations for the aqueous free energy of reaction and for the aqueous free energy of activation, as follows.

$$\Delta_f G_{aq,exact}^{*/\ddagger} = \Delta_f G_{aq,Comp}^{*/\ddagger} \pm z_{0.15} \times s \quad (5.34)$$

where $\Delta_f G_{aq,exact}^{*/\ddagger}$ is the correct experimental value, estimated from the aqueous standard free energy of reaction or activation, $\Delta_f G_{aq,Comp}^{*/\ddagger}$, with the error bounds that are expected to contain 70% of the deviations. s is the expected standard error of the computational approach, and $z_{0.15}$ is the critical value of a normal distribution associated with the probability $\frac{(1-0.70)}{2}$, equal to -1.04. We estimated s based on a propagation of the expected errors of the gas phase prediction and the solvation energy prediction:

$$s = \sqrt{(\text{RMSE}_{\Delta G_{solv,Comp}^*})^2 + (\text{RMSE per bond}_{B2PLYPD,gas})^2} \quad (5.35)$$

where the $\text{RMSE}_{\Delta G_{solv,Comp}^*}$ is 8.3 kJ mol^{-1} for neutrally charged sulfur-containing molecules. The $\text{RMSE per bond}_{B2PLYPD,gas}$ (Table 5.8) is 13.1 kJ mol^{-1} for sulfur- and oxygen-containing species. We thus assigned a total uncertainty of ± 2.7 in the $\log k$ for computed rate constants and in the $\log K_{eq}$ for the theoretical aqueous equilibrium constants of reactions involving neutrally charged species, based on our expectation that the applied model chemistry (SMD/B2PLYPD/aug-cc-pVTZ) would produce an uncertainty of $\pm 23 \text{ kJ mol}^{-1}$ in the $\Delta G_{aq,rxn}^\ddagger$ and in the $\Delta G_{aq,rxn}^*$. The so-estimated uncertainty bounds were applied to the neutral species that are investigated.

Other reactions studied here involve the radical or the anionic center of the molecules directly,

but the nature of the radical/anion is not changed during the reaction. With this reasoning, we can expect that the high uncertainty associated to the solvation approach is partially canceled out. We applied equation 5.35 to calculate the uncertainty for aqueous standard free energy of reaction or activation, $\Delta_f G_{aq,Comp}^{*/\ddagger}$, with the error bounds that are expected to contain 70% of the deviations. Rather than the $RMSE_{\Delta G_{sol,Comp}^*}$ value used for the neutrally charged molecules, we employed the $MUE_{\Delta G_{sol,Comp}^*}$ value determined by Marenich et. al for a small set of anionic molecules: 19 kJ mol^{-1} . We thus assigned a total uncertainty of ± 4 units in the $\log k$ for computed rate constants and in the $\log K_{eq}$ for the theoretical aqueous equilibrium constants of reactions involving anions and radical anions, based on our expectation that the applied model chemistries (SMD/B2PLYPD/ aug-cc-pVTZ) would produce an uncertainty of $\pm 23 \text{ kJ mol}^{-1}$ in the $\Delta G_{aq,rxn}^\ddagger$ and in the $\Delta G_{aq,rxn}^*$. The so-estimated uncertainty bounds were applied to the open- and closed-shell anionic species that are investigated.

5.4.2 First Step of the OCS Formation: Formation of Thiyl/Sulfhydryl Radicals and Anions

Formation of Thiyl Radical from Thiols

We considered three different sulfur-containing nucleophiles that can be produced from thiols and that might play a role in the formation of OCS in seawater: thiyl radicals, RS^\cdot , the sulfide anion, HS^- , and thiolates, RS^- . Figure 5.2 shows plausible molecular pathways that lead from a thiol to the formation of a thiyl radical, a thiolate, or a sulfide anion.

The pK_a values of thiols studied here are in the range of 8.2 to 10.4 (Table 5.10), and thus these sulfur compounds are partly dissociated at the pH conditions of seawater (~ 8.3):



where R is an organic fragment or H atom that is bound to the SH group of GSH, CYS, 3-MPA, CH_3SH , and H_2S .

The so-formed thiolate group can thus undergo one-electron oxidation to form the thiyl radical:



Since the thiols are partially deprotonated in seawater, we assume that the oxidation of thiolate functional group is a potential source of thiyl radical from thiols (reaction 5.37). Thiolates have one-electron potentials $\sim 0.8 \text{ V}$ (Table 5.4), and can be oxidized by electron acceptors such as transition metal ions[362, 360] and by reactive species that exhibit higher one-electron reduction potentials.[361] Thus, reactive species with sufficiently high electron potential (Table 5.11), such as Cl^\cdot , Br^\cdot , $Br_2^{\cdot-}$, $CO_3^{\cdot-}$, and $^3DOM^*$ are possible oxidants that can react with the deprotonated thiolate species of CYS, GSH, 3-MPA, and CH_3SH , leading to the formation

of the corresponding thiyl radical.

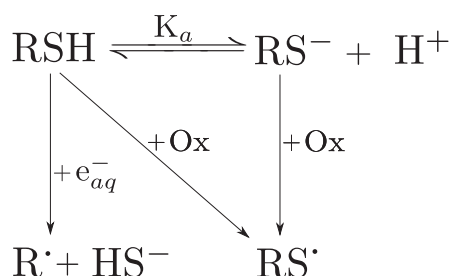


Fig. 5.2 Considered pathways to the formation of thiyl radicals, thiolate, and sulfide anion from thiols. The thiol group (-SH) is partially deprotonated at the pH of the sea (Table 5.10). The thiolate group can undergo oxidation reaction and form the thiyl radical.[359, 18, 362, 360, 361] Pulse radiolysis experiments showed that the thiol functional group can also react with the aqueous free electron leading to the formation of an organic radical and sulfide anion, which can further react and oxidize to sulfhydryl radical.[402]

Table 5.10 Aqueous pK_a values of naturally occurring organic thiols in the sea.

Compounds	pK_a
GSH	8.7-9.3[18], 9.3[378]
CYS	8.2-8.7[18], 8.5[378]
CH_3SH	10.2[18], 10.3[378]
3-MPA	10.4[18]

Table 5.11 Aqueous one-electron reduction potentials of some reactive species in water. Values are in Volts.

Reduction couple	E^0
$\text{Br}_2^{\cdot-} / 2\text{Br}^-$	1.63 ± 0.02 [363, 364]
$\text{Br}^\cdot / \text{Br}^-$	1.96 ± 0.02 [364]
$\text{Cl}_2^{\cdot-} / 2\text{Cl}^-$	2.0 [403], 2.126 ± 0.017 [364]
$\text{Cl}^\cdot / \text{Cl}^-$	2.432 ± 0.018 [364]
$\text{CO}_3^{\cdot-} / \text{CO}_3^{2-}$	1.57 ± 0.03 [364]
$\text{O}_2^{\cdot-} / {}^1\text{O}_2$	0.18 ± 0.02 [364]
${}^3\text{DOM}^\cdot$	$1.36 < E^0 < 1.7$ [366, 367]

The portion of thiols that are not deprotonated can react with aqueous free electron e_{aq}^- , [363, 364] to produce sulfide anion and organic radicals (equation 5.38), [402]



or they can be oxidized to thiyl radicals by oxidants arising in water (equation 5.39):



The rate constant for equation 5.38 was previously measured for 3-MPA ($2.5 \times 10^8 \text{ M}^{-1}\text{s}^{-1}$), GSH ($4.5 \times 10^8 \text{ M}^{-1}\text{s}^{-1}$), and the zwitterionic form of CYS ($1.3 \times 10^{10} \text{ M}^{-1}\text{s}^{-1}$). [402] However, these fast reactions with aqueous free electron e_{aq}^- are likely not competitive with other OCS formation mechanisms, due to the low concentration of e_{aq}^- in water ($[e_{aq}^-] = 10^{-17} \text{ M}$ in freshwater). [404] Thiols exhibit higher one-electron potentials than thiolates, with values ranging from 0.92 to 1.359 V (Table 5.4). This implies that the oxidation of thiols is less thermodynamically favorable than the oxidation of thiolates. Nonetheless, Br_2^- ($E^0 = 1.63 \text{ V}$) [363, 364], CO_3^- ($E^0 = 1.57 \text{ V}$) [364], and $^3\text{DOM}^*$ ($1.36 < E^0 < 1.7 \text{ V}$) [366, 367] can oxidize thiols, leading to the formation of thiyl radicals as well (equation 5.39).

Formation of Thiyl Radical from DMS: Bond Dissociation Energies of $S-H$, $S-S$, and $C-S$ Bonds to Evaluate the Stability of Thiyl/sulphydryl Radicals

The evaluation of previously reported experimental BDE values allows us to consider another possible thiyl radical formation pathway: the homolytic cleavage of the $C-S$ bond of thioethers and thiols. $C-S$ bonds have gas phase BDE values of about 300 kJ mol^{-1} (Table 5.12). A closer look at Table 5.12 reveals that the experimental bond dissociation energies at 298 K in gas phase of the bond $C-S$ of thioethers and thiols are lower than the BDE of the bond $S-H$. The formation of the thiyl radical from the cleavage of the $C-S$ of DMS is more thermodynamically feasible than from the hydrogen abstraction from thiols. Based on these observations, we could suggest homolytic decomposition of DMS and thioethers in water leading to an organic carbon-centered radical and the thiyl radical can be more feasible than the homolytic cleavage of $H-S$ thiol bonds:



where R is an organic fragment.

5.4. Results and Discussion

Table 5.12 Previously reported experimental bond dissociation energies at 0 K and 298 K in gas phase and in water for a set of thiols, polysulfides, and thiyl/sulfhydryl radicals. Values are in kJ mol⁻¹.

Compounds	S-H bonds		S-C bonds		S-S bonds
	BDE ^{0K} _{gas}	BDE ^{298K} _{gas}	BDE ^{0K} _{gas}	BDE ^{298K} _{gas}	BDE ^{298K} _{gas}
HS [•]	348.2 ± 3.3 [405]	352.0 ± 3.1 [405] 350 ± 4 [406]			
H ₂ S	376.2 ± 3.8 [405]	381.5 ± 3.6 [405] 385 ± 4 [406] 381.6 ± 0.4 [407]			
CH ₃ SH	359.7 ± 2.8 [405] 360.2 ± 2.1 [408]	365.5 ± 2.4 [405] 365.7 ± 2.1 [408] 385 ± 6 [406]	303.7 ± 4.4 [405]	311.6 ± 4.2 [405]	
CH ₃ S [•]			292.2 ± 3.3 [405]	298.1 ± 2.9 [405]	
DMS			301.9 ± 3.6 [405]	307.8 ± 3.1 [405] 314 ± 6 [406]	
HSSH		293 ± 6 [406]			276 ± 8 [406]
HSS [•]		253 ± 6 [406]			331 ± 4 [406]
HS ₃ H		293 ± 6 [406]			209 ± 8 [406]
HS _{3+n} H		293 ± 6 [406]			
HS ₂ -S ₂ H					141 ± 8 [406]
	BDE^{298K}_{water}				
GSH	365 [378]				
CYS	353 [378]				
H ₂ S	385 [378]				
CH ₃ SH	363 [378]				
HOCH ₂ CH ₂ SH	362 [378]				
C ₆ H ₅ SH	338 [378]				
4-CH ₃ C ₆ H ₄ SH	344 [378]				
4-CH ₃ OC ₆ H ₄ SH	328 [378]				
4-BrC ₆ H ₄ SH	336 [378]				

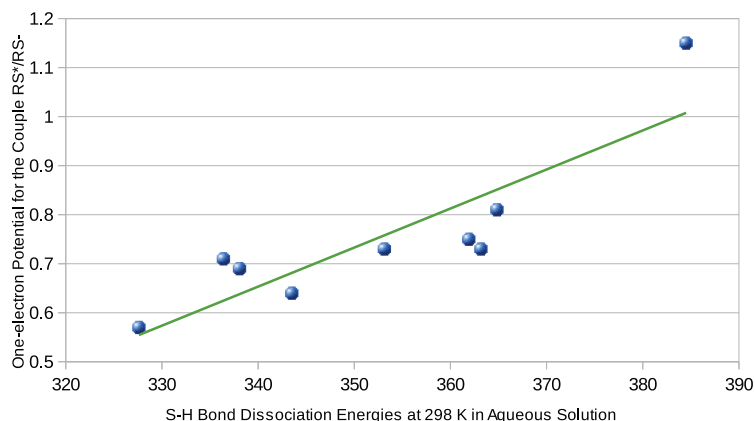


Fig. 5.3 Correlation between the experimental bond dissociation energies of the S-H bond in water at 298 K (Table 5.12) and the aqueous one-electron reduction potentials for the couple RS^{\bullet}/RS^{-} for a set of thiolates, including GS^{-} , CYS^{-} , HS^{-} , CH_3S^{-} , $HOCH_2CH_2S^{-}$, $C_6H_5S^{-}$, $4-CH_3C_6H_4S^{-}$, $4-CH_3OC_6H_4S^{-}$, and $4-BrC_6H_4S^{-}$.

The experimental bond dissociation energies at 298 K in gas phase of the bonds $S-H$, $C-S$, and $S-S$, and the experimental bond dissociation energies at 298 K in water of the $S-H$ bonds range from 141 to 385 kJ mol^{-1} (Table 5.12). This implies that the homolytic cleavage of $X-S$ bonds (where X can be S, H, or C) would not take place spontaneously in water. However, we speculate that thioethers might interact with radical oxidants, metals, or excited state compounds (such as $^3DOM^*$) that can catalyze the homolytic cleavage. We found a correlation between the experimental $S-H$ bond dissociation energies of thiols in water at 298 K and the one-electron potential for the couple RS^{\bullet}/RS^{-} for the thiolates including GS^{-} , CYS^{-} , HS^{-} , CH_3S^{-} , $HOCH_2CH_2S^{-}$, $C_6H_5S^{-}$, $4-CH_3C_6H_4S^{-}$, $4-CH_3OC_6H_4SH$, and $4-BrC_6H_4SH$ (Figure 5.3). A correlation coefficient of $R^2 = 0.76$ was found for this regression line (Figure 5.3).

Limited information is available to understand whether oxidation products of DMS by reactive species such as $Br_2^{\bullet-}$ might be lead to thiyl radicals. The first step of the oxidation of DMS by $Br_2^{\bullet-}$ involves the formation of the bromine-adduct $DMS-Br^{\bullet}$:



This reaction is feasible having an aqueous equilibrium constant of 4[409] and a rate constant of $3.2 \times 10^9 \text{ M}^{-1}\text{s}^{-1}$. [368] Since the aqueous one-electron oxidation potential of DMS $E_{DMS|DMS^+}^0$ is 1.66 V[363] and the aqueous one-electron reduction potential $Br_2^{\bullet-}$ is 1.63 V, DMS can be oxidized to DMS^+ species. Therefore, the $Br^{\bullet-}$ species might cleave from the bromine-adduct $DMS-Br^{\bullet}$ to form DMS^+ :



Table 5.13 NPA partial atomic charge distributions of DMS, DMS-Br \cdot , and DMS $^{+}$, and spin densities of DMS-Br \cdot , and DMS $^{+}$. NPA partial charge values are in e^{-} .

	DMS		DMS-Br \cdot		DMS $^{+}$	
	NPA charge		NPA charge	Spin Density	NPA charge	Spin Density
C	-0.7		-0.7	0.0	-0.8	0.0
S	0.1		0.5	0.5	0.9	0.9
C	-0.7		-0.7	0.0	-0.8	0.0
H	0.2		0.2	0.0	0.3	0.0
H	0.2		0.2	0.0	0.3	0.0
H	0.2		0.2	0.0	0.3	0.0
H	0.2		0.2	0.0	0.3	0.0
H	0.2		0.2	0.0	0.3	0.0
H	0.2		0.2	0.0	0.3	0.0
Br			-0.5	0.5		

Additional natural population analysis calculations of the DMS, DMS-Br \cdot , and DMS $^{+}$ have been performed to gain further insight into the electronic structures of these species (Table 5.13). C – S bond lengths have been computed with the SMD/M06-2X/aug-cc-pVTZ model chemistry; the C – S bond of DMS $^{+}$ (1.77Å) is slightly contracted compared to the C – S bonds of DMS (1.80Å) and DMS-Br \cdot (1.81Å).

Formation of Sulfhydryl Radical and Polysulfide Anions

Polysulfides can react with CO to form OCS, but the detailed molecular mechanism(s) remain unclear.[32, 33] Polysulfides are assumed to exhibit acid/base equilibria with polysulfide anions:[410, 411]



with n ranging from 0 to 6. We took into account polysulfide compounds with a chain of up to 7 atoms of sulfur, since heptasulfide species was detected in μM concentrations in sulfide-rich water wells.[412]

To determine the most predominant sulfide and polysulfide species in seawater, we considered previously reported experimental acid dissociation equilibrium constants, pK_a , and thermodynamic speciation models based on measurements of the concentrations of sulfide and polysulfide in seawater and distilled water. The polysulfide distribution is

largely dependent on the pH and the total sulfide and polysulfide concentration.[413] Their acid dissociation constants decrease with an increase of the chain length (Table 5.14).[414] According to the first acid dissociation constant values, pK_{a1} , and the second acid dissociation constants, pK_{a2} , of polysulfides (Table 5.14), both the acidic extremities of the polysulfide chain are mostly deprotonated at the pH condition of the sea (~ 8.3). Exceptionally, H_2S exhibits a second acid dissociation constant, pK_{a2} , of 14,[414] indicating that HS^- is the predominating species at the pH of the seawater. High pH and high sulfide-to-polysulfide ratio lead to a distribution of polysulfides having shorter chain lengths.[413] Gun et al. found that, under low level of dissolved sulfur species conditions, the disulfide is the most concentrated over the other polysulfides.[32] Hydrogen sulfide is found to be one of the most abundant volatile sulfur species in surface seawater, having nanomolar concentration.[415] The marine sulfide concentration reaches the maximum at the top of the thermocline (50 m) and then decreases with depth.[415] Based thermodynamic models on polysulfide speciation at seawater conditions[32] and concentration measurements of hydrogen sulfide in surface seawater,[415] we assumed that the sulfide species (HS^- , HS^\cdot , $S^{\cdot-}$, and S^{2-}) and the disulfide species (HS_2^- , HS_2^\cdot , $S_2^{\cdot-}$, and S_2^{2-}) are the most predominating sulfide species in surface seawater and, thus, the most plausible precursors of OCS among the polysulfides. However, further investigations on the steady-state concentrations on the polysulfide species are required to identify the most predominant reactions.

The formation of sulphydryl radicals from polysulfides can happen through two differing molecular pathways: a hydrogen abstraction from the neutral thiol group (equations 5.45 and 5.46) and a one-electron oxidation from the thiolate functional group (equations 5.47 and 5.48). The hydrogen abstraction can involve neutral polysulfide chain and partially deprotonated polysulfides:



Table 5.14 Experimental 1st and 2nd Aqueous Acid Dissociation Constant Values of Polysulfides.

Compounds	pK_{a1}	pK_{a2}
hydrogen sulfide	6.83[414]	14[414]
hydrogen disulfide	5 [414]	9.7[414]
hydrogen trisulfide	4.2 [414]	7.5 [414]
hydrogen tetrasulfide	3.8 [414]	6.3 [414]
hydrogen pentasulfide	3.5 [414]	5.7 [414]



where X^\cdot is the aqueous reactive species that abstracts a hydrogen from the polysulfides, HS_{1+n}H and HS_{1+n}^- .

We considered the reactions described by equation 5.45 as being not as relevant in the formation of OCS as the reactions defined by equation 5.46, since the polysulfides are present principally in ionic form, according to the pK_a values. HS_{1+n}^- and S_{1+n}^{2-} can also undergo one-electron oxidation in water:



with n ranging from 0 to 6. The one-electron potentials of hydrogen sulfide are 1.15 V for the couple $\text{HS}^\cdot | \text{HS}^-$ [379] and 0.92 V for the couple $\text{HS}^\cdot, \text{H}^+ | \text{H}_2\text{S}$ [416] (Table 5.4). No experimental reduction potentials of the polysulfides species are available. However, Nagy reported that the one-electron potential of polysulfide increases with chain length, [417] based on Lessner et al.' results. [418] Aqueous oxidants having one-electron potentials higher than 1.15 V can oxidize H_2S and HS^- to HS^\cdot . Pulse radiolysis and laser flash photolysis studies demonstrated that HS^- reacts with organic and inorganic oxidants, such as $\text{SO}_4^{\cdot-}$, $\text{CO}_3^{\cdot-}$, and I_2^- , to form HS^\cdot with rate constants in the order of 10^8 - $10^9 \text{ M}^{-1} \text{ s}^{-1}$. [416] To sum up, the reactions between polysulfide anions and sufficiently strong oxidants can take place in water and lead to the sulfhydryl radicals. Hydrogen sulfide species (H_2S , HS^- , S^{2-}) can react with several naturally occurring marine oxidants in water to lead to sulfhydryl radicals, and the corresponding reactions for the disulfide species (H_2S_2 , HS_2^- , S_2^{2-}) are likely to be feasible as well.

5.4.3 The relative importance of different possible natural oxidants for marine sulfur species: APEX photochemical model results

We evaluated the role that 4 aqueous reactive species (OH^\cdot , $^1\text{O}_2$, $\text{CO}_3^{\cdot-}$, and Br_2^-) play in the photo-oxidation of MET, CYS, GSH, and DMS in seawater. Using the APEX photochemical model we can establish which species oxidize(s) thiols and DMS in seawater at several realistic concentrations of DOC and bromide. We thus hypothesized that OH^\cdot , $^1\text{O}_2$, $\text{CO}_3^{\cdot-}$, and Br_2^- might be responsible of the photo-oxidation of MET, CYS, GSH, and DMS in seawater, and thus might participate in the formation of OCS.

DOC may depend on seawater productivity, [419] whereas bromide is closely connected with salinity. [420] In estuarine/coastal environments, bromide increases along the transects going from freshwater to seawater. The fractions $\psi_{w,y}$ of $w = \text{DMS, MET, CYS, and GSH}$

phototransformation that are accounted for by $y = \text{OH}^\cdot$, $^1\text{O}_2$, $\text{CO}_3^{\cdot-}$, and $\text{Br}_2^{\cdot-}$ are reported in Figure 5.4 as a function of the DOC, for a water column depth of 10 m. Other conditions typical of seawater were fixed: we assumed 10 μM nitrate, 1 μM nitrite, 2 mM bicarbonate, 20 μM carbonate, and 0.8 mM bromide.[399] Figure 5.4 reveals that, among the studied reactive species, $\text{Br}_2^{\cdot-}$ plays by far the main role in the transformation of the reduced sulfur compounds under consideration. In the interpretation of these results, it should be considered that our approach would actually underestimate the importance of $\text{Br}_2^{\cdot-}$ reactions in seawater. Moreover, a decrease of nitrate and nitrite concentration by two orders of magnitude (down to 0.1 μM and 10 nM, respectively) would produce relatively limited effects that can be summarized as an overall decrease in the importance of the $\text{CO}_3^{\cdot-}$ reactions.

DOC and bromide levels determine which reactive oxidants predominantly transform the reduced sulfur compounds considered here (Figures 5.4 and 5.6). According to the APEX model, the role of OH^\cdot in phototransformation would be minor although not totally negligible (Figures 5.4 and 5.6); this simulation result is in agreement with Zepp and coworkers, who stated that the role of OH^\cdot in OCS photogeneration in seawater is unimportant, although the hydroxyl radical is able to oxidize thiols into thiyl radicals that are potential OCS precursors.[19] The radical $\text{CO}_3^{\cdot-}$ can play some role at low DOC values in the phototransformation of MET, CYS and GSH, but not for DMS. The importance of the $\text{CO}_3^{\cdot-}$ reactions decreases with increasing DOC because DOM acts as a powerful $\text{CO}_3^{\cdot-}$ inhibitor, by directly scavenging $\text{CO}_3^{\cdot-}$ itself and by consuming OH^\cdot that is a major $\text{CO}_3^{\cdot-}$ precursor.[373, 398] Finally, the role of $^1\text{O}_2$ is expected to be negligible under all conditions for all of the studied compounds. The above considerations are supported by the plot of the steady-state concentrations of the transient species as a function of the DOC, shown in Figure 5.5. The scavenging by DOM explains why OH^\cdot , $\text{CO}_3^{\cdot-}$ and $\text{Br}_2^{\cdot-}$ decrease with increasing DOC. In contrast, $^1\text{O}_2$ and $^3\text{DOM}^*$ increase with increasing DOC because DOM is their only source but it is not an important scavenger.[397]

The trends of $\psi_{w,y}$ as a function of bromide are reported in Figure 5.6 (other conditions assumed are 1 mg C L^{-1} DOC, 10 m depth, 10 μM nitrate, 1 μM nitrite, 2 mM bicarbonate and 20 μM carbonate). Without bromide or with low bromide (up to some μM concentration), the radicals OH^\cdot and $\text{CO}_3^{\cdot-}$ would play the main roles in the phototransformation processes of CYS and GSH. The important role of $\text{CO}_3^{\cdot-}$ at low bromide concentration is consistent with assumptions that the $\text{CO}_3^{\cdot-}$ -induced processes could play a significant role in the degradation of easily oxidized sulfur-containing compounds in freshwater.[421, 422] However, the reaction with $\text{Br}_2^{\cdot-}$ prevails at high bromide concentration for CYS and GSH and under almost all conditions for MET and DMS. Under seawater conditions (0.8 mM Br^-) the reaction with $\text{Br}_2^{\cdot-}$ would prevail in all the cases, and relatively small $[\text{Br}^-]$ variations are unable to considerably modify the $\psi_{w,y}$ values. Therefore, at least with the studied compounds and transients, we can predict that the relative importance of $\text{Br}_2^{\cdot-}$ would not be modified by differences in salinity among the world's oceans.[420] In contrast, the reported results as a function of $[\text{Br}^-]$ are of significance for environments where there is transition from freshwater to saltwater (i.e., from very low to elevated bromide concentration), such as estuaries. We also note that bromide as a major OH^\cdot scavenger strongly inhibits the OH^\cdot reactions,[397] which explains why OH^\cdot

would play an important role in the phototransformation of all of the compounds investigated in freshwater, whereas its role becomes negligible at the 0.8 mM bromide concentration that is typical of seawater.

Figure 5.7 reports the transients steady-state concentrations as a function of bromide. The figure plot shows that $^3\text{DOM}^*$ and $^1\text{O}_2$ are unaffected by bromide (the reaction between $^3\text{DOM}^*$ and Br^- was not taken into account in this modeling), $[\text{OH}^\bullet]$ decreases with increasing bromide that is a major OH^\bullet scavenger and, because OH^\bullet is strongly involved in $\text{CO}_3^{\bullet-}$ formation, its decrease causes $[\text{CO}_3^{\bullet-}]$ to decrease as well. Finally, $\text{Br}_2^{\bullet-}$ increases with increasing bromide. The results reported so far were obtained by neglecting the reaction between $^3\text{DOM}^*$ and Br^- as $\text{Br}_2^{\bullet-}$ source, for which insufficient knowledge is available concerning the rate constant. Starting from the upper limit $k_{5.25} = 3.5 \times 10^9 \text{ M}^{-1} \text{ s}^{-1}$, [393] the rate constant was varied over a very wide range of values and the results concerning the relative role of the transients in substrate phototransformation are reported in Figure 5.8. As expected the role of $\text{Br}_2^{\bullet-}$, already substantial when neglecting reaction (5.25), can only increase when $k_{5.25}$ assumes values higher than $10^7 \text{ M}^{-1} \text{ s}^{-1}$. The steady-state concentrations $[\psi]$ are reported in 5.9, which shows that $^3\text{DOM}^*$ and $\text{Br}_2^{\bullet-}$ are the only transients affected by a change in $k_{5.25}$. In particular, $^3\text{DOM}^*$ decreases and $\text{Br}_2^{\bullet-}$ increases when $k_{5.25} > 10^7 \text{ M}^{-1} \text{ s}^{-1}$.

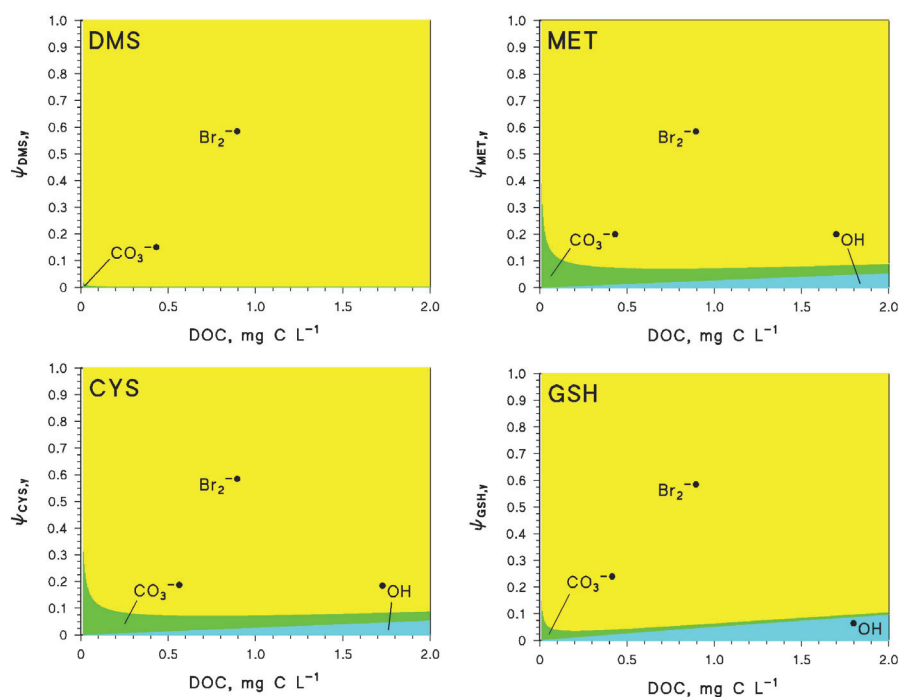


Fig. 5.4 Modeled fractions of DMS, MET, CYS, and GSH phototransformation accounted for by OH^\bullet , $^1\text{O}_2$, $\text{CO}_3^{\bullet-}$, and $\text{Br}_2^{\bullet-}$, as a function of the water DOC under 22 W m^{-2} UV irradiance of sunlight. Other water conditions that we assumed: 10 m depth, $10 \mu\text{M}$ nitrate, $1 \mu\text{M}$ nitrite, 2 mM bicarbonate, $20 \mu\text{M}$ carbonate, and 0.8 mM bromide.

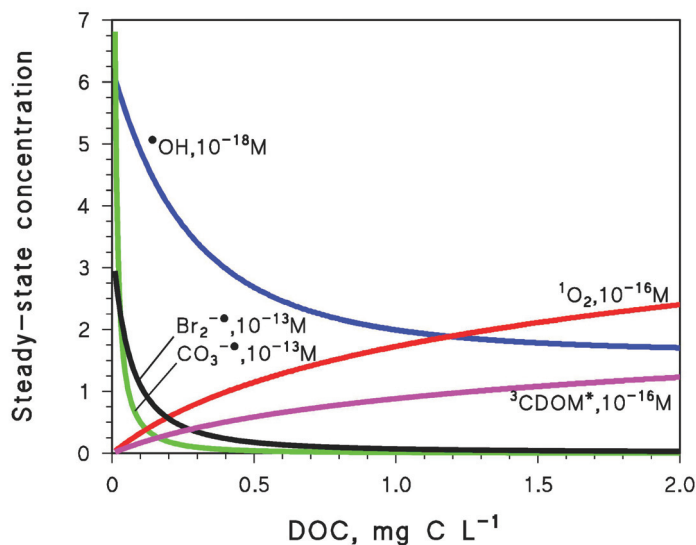


Fig. 5.5 Modeled steady-state concentrations of OH^\bullet , $^1\text{O}_2$, $\text{CO}_3^{\bullet-}$, $^3\text{DOM}^*$ and $\text{Br}_2^{\bullet-}$, as a function of the water DOC under 22 W m^{-2} UV irradiance of sunlight. Other water conditions that we assumed: 10 m depth, $10 \mu\text{M}$ nitrate, $1 \mu\text{M}$ nitrite, 2 mM bicarbonate, $20 \mu\text{M}$ carbonate, and 0.8 mM bromide.

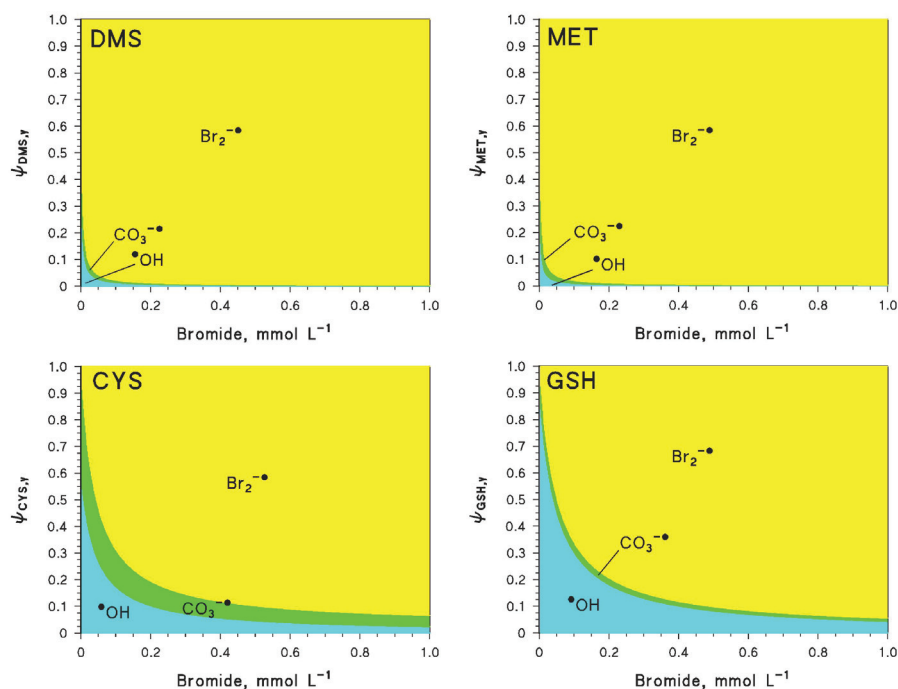


Fig. 5.6 Modeled fractions of DMS, MET, CYS, and GSH phototransformation accounted for by OH^\bullet , $^1\text{O}_2$, $\text{CO}_3^{\bullet-}$, and $\text{Br}_2^{\bullet-}$, as a function of bromide concentration under 22 W m^{-2} UV irradiance of sunlight. Other water conditions that we assumed: 10 m depth, 1 mg C L^{-1} DOC, $10 \mu\text{M}$ nitrate, $1 \mu\text{M}$ nitrite, 2 mM bicarbonate, and $20 \mu\text{M}$ carbonate.

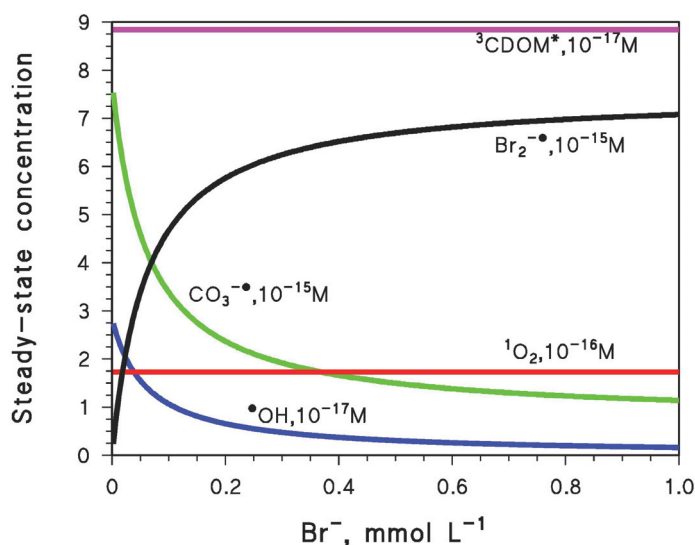


Fig. 5.7 Modeled steady-state concentrations of OH^\bullet , $^1\text{O}_2$, $\text{CO}_3^{\bullet-}$, $^3\text{DOM}^*$ and $\text{Br}_2^{\bullet-}$, as a function of bromide concentration under 22 W m^{-2} UV irradiance of sunlight. Other water conditions that we assumed: 10 m depth, $10 \mu\text{M}$ nitrate, $1 \mu\text{M}$ nitrite, 2 mM bicarbonate, $20 \mu\text{M}$ carbonate, and 1 mg C L^{-1} DOC.

Increasing water depth would mainly enhance the relative importance of $^1\text{O}_2$, compared to other reactive oxidants, for the transformation of the sulfur species considered here. The rationale is that singlet oxygen is produced by CDOM that is activated by visible light, which has higher penetration in the water columns compared to UV radiation.[423] However, although the water depth has a limited impact on the $\psi_{w,y}$ values, it affects the photochemical reaction rates such that photoinduced processes are much more important in shallow than in deep water.[397, 423] Finally, a decrease of nitrate and nitrite concentration by two orders of magnitude (down to $0.1 \mu\text{M}$ and 10 nM , respectively) would decrease the importance of the $\text{CO}_3^{\bullet-}$ reactions and increase the importance of $^1\text{O}_2$ reactions.

According to APEX model calculation results, we infer that $\text{Br}_2^{\bullet-}$, $\text{CO}_3^{\bullet-}$, and OH^\bullet are predominantly responsible for the photo-oxidation of organic sulfur-containing compounds in seawater. APEX model calculations identified the $\text{Br}_2^{\bullet-}$ species, among the studied transients, as the most important in the photochemical transformation of DMS, MET, CYS, and GSH in seawater. The already important role of $\text{Br}_2^{\bullet-}$ cannot undergo a considerable further enhancement by the oxidation of bromide by $^3\text{DOM}^*$, although this process could play a significant role in seawater if its rate constant is higher than $10^7 \text{ M}^{-1} \text{ s}^{-1}$ (note that the upper limit for the rate constant is $3.5 \times 10^9 \text{ M}^{-1} \text{ s}^{-1}$)[393]. At low bromide (e.g., under freshwater conditions) $\text{CO}_3^{\bullet-}$, and OH^\bullet would prevail in the phototransformation of CYS and GSH. However, under seawater conditions the role of $\text{Br}_2^{\bullet-}$ would be important enough so as not to be impacted by differences in salinity among the world's oceans. $\text{CO}_3^{\bullet-}$ could play a significant role in the photo-oxidation of CYS and GSH at low DOC conditions. These findings

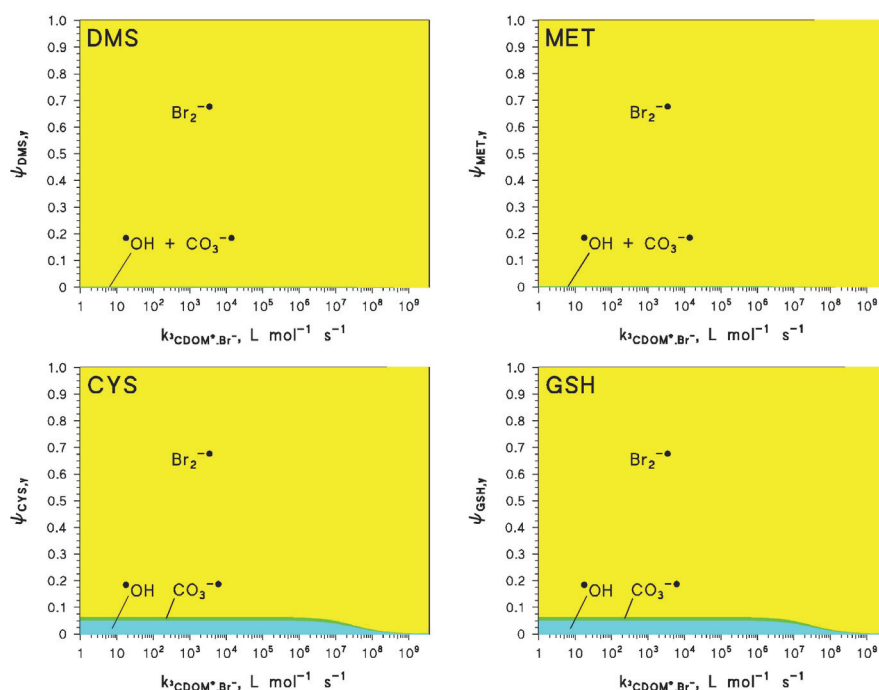


Fig. 5.8 Modeled fractions of DMS, MET, CYS, and GSH phototransformation accounted for by OH^\bullet , $^1\text{O}_2$, $\text{CO}_3^{\bullet-}$, and $\text{Br}_2^{\bullet-}$, as a function of the rate constant value for the reaction between $^3\text{DOM}^*$ and bromide, under 22 W m^{-2} UV irradiance of sunlight. Other water conditions that we assumed: 10 m depth, 1 mg C L^{-1} DOC, $10 \mu\text{M}$ nitrate, $1 \mu\text{M}$ nitrite, 2 mM bicarbonate, $20 \mu\text{M}$ carbonate, and 0.8 mM bromide.

validate the interpretation of Boullion and Miller, who suggested that $\text{Br}_2^{\bullet-}$ and $\text{CO}_3^{\bullet-}$ were plausible reactive species responsible for the photo-induced degradation of sulfur-containing organic marine species.[374] Shortly before the submission deadline of the finally formatted thesis, it was noticed that the reaction rate constant employed in APEX simulations for the reaction of $\text{Br}_2^{\bullet-}$ with GSH had been assigned a value that was too low ($7 \times 10^7 \text{ M}^{-1} \text{ s}^{-1}$) by about a factor of 10 compared to the correct value ($6.5 \pm 0.1 \times 10^8 \text{ M}^{-1} \text{ s}^{-1}$)[365]. In future work, the APEX simulations could be updated to incorporate the corrected rate constant. However, at a qualitative level, the corrected results and conclusions for APEX simulations are expected to be similar to what is reported here.

Our APEX model calculation results enable us to take one more step forwards in the assessment of the precursors of OCS in seawater. Zepp and Andreae suggested that $\text{Br}_2^{\bullet-}$ and $\text{CO}_3^{\bullet-}$ could react with GSH, CYS, and 3-MPA to form thiyl radical and participate in the formation of OCS in seawater.[19] According to the previously reported experimental one-electron potentials of GSH, CYS, and CH_3SH (Table 5.4), these thiolates and thiols can be oxidized to thiyl radicals by $\text{Br}_2^{\bullet-}$ and $\text{CO}_3^{\bullet-}$, which exhibit much higher reduction potentials, $1.63 \pm 0.02 \text{ V}$ and $1.57 \pm 0.03 \text{ V}$, respectively (Table 5.11).[364] APEX model calculations predicted that $\text{Br}_2^{\bullet-}$, OH^\bullet , and $\text{CO}_3^{\bullet-}$ participate in the photo-oxidation of DMS, MET, CYS, and GSH in seawater. Previously

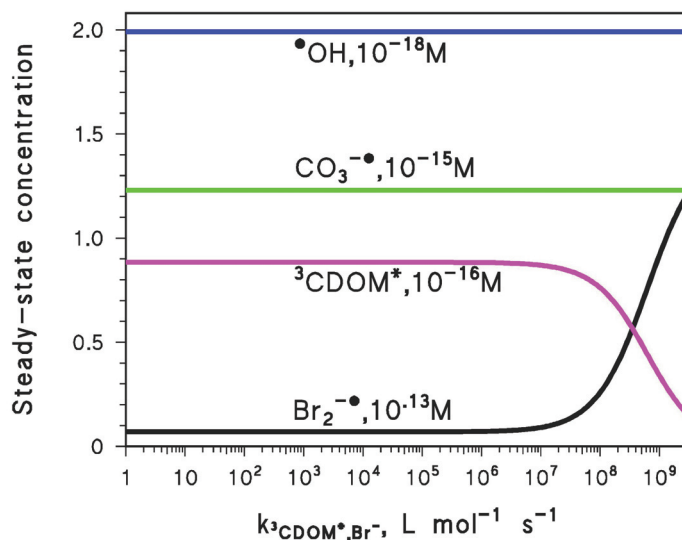


Fig. 5.9 Modeled steady-state concentrations of OH^\bullet , $^1\text{O}_2$, $\text{CO}_3^{\bullet-}$, $^3\text{DOM}^*$ and $\text{Br}_2^{\bullet-}$, as a function of the rate constant value for the reaction between $^3\text{DOM}^*$ and bromide under 22 W m^{-2} UV irradiance of sunlight. Other water conditions that we assumed: 10 m depth, $10 \mu\text{M}$ nitrate, $1 \mu\text{M}$ nitrite, 2 mM bicarbonate, $20 \mu\text{M}$ carbonate, 1 mg C L^{-1} DOC, and 0.8 mM bromide.

published experimental rate constants for the reactions of $\text{CO}_3^{\bullet-}$ with CYS, GSH, 3-MPA, and for the reactions of $\text{Br}_2^{\bullet-}$ with CYS, GSH, 3-MPA, and DMS are in the order of magnitude of 10^6 - $10^9 \text{ M}^{-1} \text{ s}^{-1}$ (Table 5.5). The reactions of $\text{CO}_3^{\bullet-}$ with CYS, GSH, 3-MPA, and the reaction of $\text{Br}_2^{\bullet-}$ with GSH lead to the formation of thiyl radical in aqueous solution, whereas the reactions of $\text{Br}_2^{\bullet-}$ with the thioethers MET and DMS produce a bromine-adduct (Table 5.5). No information is available about the products of the reaction between $\text{Br}_2^{\bullet-}$ and CYS. However, we can reasonably argue that the thiyl radical is formed from the oxidation of CYS, since $\text{Br}_2^{\bullet-}$ oxidizes the sulfur atom of GSH to thiyl radical. Flöck and coworkers suggested that thiyl radicals formed from sulfur-containing compounds (equation 5.5) react with CO leading to OCS in water.[18] Based on the above findings and observations, we can conclude that $\text{Br}_2^{\bullet-}$, OH^\bullet , and $\text{CO}_3^{\bullet-}$ facilitate OCS production in seawater.

5.4.4 Second Step of the OCS Formation: Reactions of Reactive Sulfur-containing Species with CO to produce OCS

Reactions of $\text{RS}^-/\text{RS}^\bullet$ with CO to Form OCS

As explained previously, thiyl radicals are products of the photo-oxidation of thiols and (possibly also) DMS catalyzed by reactive species in seawater. We considered two different molecular mechanisms that lead from thiyl radicals or thiolates to the formation of OCS (Table 5.15). We computed the Gibbs free energies of reaction and the rate constants of both the hypothesized mechanisms in order to assess the feasibility of these reactions. The

hypothesized radical pathway involves the RS^\cdot and CO. According to our quantum chemical simulation results, the formation of the radical adduct $[\text{RSCO}]^\cdot$ could be followed by the C – S bond cleavage with the production of OCS and R^\cdot :



The computed thermodynamic and kinetic properties for the radical mechanism involving thiyl radicals and CO indicated that the radical pathway (equations 5.49 and 5.50) is feasible in seawater (Table 5.15). The aqueous free energies values, $\Delta G_{rxn,aq}^{*B2PLYPD}$, for the first step of the reactions (reactions 1a, 2a, and 3a in Table 5.15) involving thiyl radicals are slightly positive, with values ranging from 16 kJ mol⁻¹ for 3-MPA $^\cdot$ to 25 kJ mol⁻¹ for CYS $^\cdot$, whereas the second step of the radical mechanism (equation 5.50 and reactions 1b, 2b, and 3b in Table 5.15) is more favorable with negative $\Delta G_{rxn,aq}^{*B2PLYPD}$. The formation of the radical adducts, where CO is bound to the S of the thiyl radical, from 3-MPA $^\cdot$ and CH₃S $^\cdot$ is kinetically plausible (equation 5.49 and reactions 2a and 3a in Table 5.15), with rate constants in the order of magnitude of 10⁵ M⁻¹s⁻¹. The thiyl radical CYS $^\cdot$ exhibits a lower reactivity towards CO, which is reflected in a rate constant of 3 × 10^{4±2.7} M⁻¹s⁻¹. The second step of the radical pathway (reactions 1b, 2b, and 3b in Table 5.15) is thermodynamically feasible and kinetically relevant for all thiyl radical precursors considered here. The rate constants of this second step (reactions 1b, 2b, and 3b in Table 5.15) are on the order of 10^{4±2.7}-10^{5±2.7} s⁻¹.

In the hypothesized anionic pathway, CO could attack the RS^- species, leading to OCS and an anionic organic byproduct.



According to our quantum chemical simulation results, the hypothesized anionic pathway is a one-step concerted mechanism, where the addition of CO to the thiolate and the C – S bond cleavage take place in the same kinetic step. We attempted to optimize an anionic intermediate where CO was linked to the sulfur fragments in aqueous phase with SMD/M06-2X/aug-cc-pVTZ model chemistry, as a possible intermediate of a two-step mechanism (in analogy with the radical pathway). However, these CO-adducts were found to be unstable in water, according to the SMD/M06-2X/aug-cc-pVTZ model chemistry. Thus, we propose that these CO-adducts do not exist as intermediate structures.

We also computed the aqueous free energies of reaction and the aqueous free energies of activation for the anionic pathways (equation 5.51). The results are reported in Table 5.15. Based on these newly computed thermodynamic and kinetic data, the anionic one-step mechanism is not thermodynamically feasible nor kinetically relevant. The aqueous free

Table 5.15 Aqueous free energies of reaction, aqueous free energies of activation, and rate constants for the reaction of thiols with CO leading to OCS: computational estimates. Values are in kJ mol^{-1} .

#	Reactions	$\Delta G_{rxn,aq}^{*B2PLYPD}$	$\Delta G_{aq}^{\ddagger B2PLYPD}$	$k_{aq}^{B2PLYPD}$
Radical Pathway				
CYS^a				
1a	$\text{OOC-CH(NH}_3\text{)}^+ \text{-CH}_2\text{-S}^\cdot + \text{CO} \rightleftharpoons \text{OOC-CH(NH}_3\text{)}^+ \text{-CH}_2\text{-SCO}^\cdot$	25 ± 16	70 ± 16	$3 \times 10^0 \pm 2.7 \text{ M}^{-1} \text{ s}^{-1}$
1b	$\text{OOC-CH(NH}_3\text{)}^+ \text{-CH}_2\text{-SCO}^\cdot \rightleftharpoons \text{OOC-CH(NH}_3\text{)}^+ \text{-CH}_2^\cdot + \text{OCS}$	-54 ± 16^b	41 ± 16^b	$4 \times 10^5 \pm 2.7 \text{ s}^{-1} \text{ }^{bd}$
3-MPA^c				
2a	$\text{OOC-CH}_2\text{-CH}_2\text{-S}^\cdot + \text{CO} \rightleftharpoons \text{OOC-CH}_2\text{-CH}_2\text{-SCO}^\cdot$	16 ± 16	43 ± 16	$2 \times 10^5 \pm 2.7 \text{ M}^{-1} \text{ s}^{-1}$
2b	$\text{OOC-CH}_2\text{-CH}_2\text{-SCO}^\cdot \rightleftharpoons \text{OOC-CH}_2\text{-CH}_2^\cdot + \text{OCS}$	-43 ± 16^b	41 ± 16^b	$5 \times 10^5 \pm 2.7 \text{ s}^{-1} \text{ }^d$
CH₃SH				
3a	$\text{CH}_3\text{S}^\cdot + \text{CO} \rightleftharpoons \text{CCH}_3\text{O}^\cdot$	18 ± 16	43 ± 16	$2 \times 10^5 \pm 2.7 \text{ M}^{-1} \text{ s}^{-1}$
3b	$\text{CH}_3\text{SCO}^\cdot \rightleftharpoons \text{CH}_3^\cdot + \text{OCS}$	-31 ± 16^b	48 ± 16^b	$2 \times 10^4 \pm 2.7 \text{ s}^{-1} \text{ }^d$
Anionic Pathway				
CYS^a				
4	$\text{OOC-CH(NH}_3\text{)}^+ \text{-CH}_2\text{-S}^- + \text{CO} \rightleftharpoons \text{OOC-CH(NH}_3\text{)}^+ \text{-CH}_2^- + \text{OCS}$	111 ± 23	168 ± 23	$2 \times 10^{-17} \pm 4 \text{ M}^{-1} \text{ s}^{-1}$
3-MPA^c				
5	$\text{OOC-CH}_2\text{-CH}_2\text{-S}^- + \text{CO} \rightleftharpoons \text{OOC-CH}_2\text{-CH}_2^- + \text{OCS}$	133 ± 23	N/A ^e	N/A ^e
CH₃SH				
6	$\text{CH}_3\text{S}^- + \text{CO} \rightleftharpoons \text{CH}_3^- + \text{OCS}$	103 ± 23	131 ± 23	$8 \times 10^{-11} \pm 4 \text{ M}^{-1} \text{ s}^{-1}$

^aCysteine is a zwitterionic species at the pH of the sea (~ 8.3) with the chemical formula of $\text{OOC-CH(NH}_3\text{)}^+ \text{-CH}_2\text{-SH}$. ^bThese free energies of reaction and activation of the second step of the radical pathways is calculated using the adduct as reactant, and not the sum of CO and thiyl radical. ^c3-mercaptopropionic acid is an anionic species at the pH of the sea (~ 8.3) with the chemical formula of $\text{OOC-CH}_2\text{-CH}_2\text{-SH}$. ^dThese rate constants are computed using the adduct as reactant. ^eNot available.

energies of reaction range from $103 \pm 23 \text{ kJ mol}^{-1}$ for the reaction involving CH_3S^- to $133 \pm 23 \text{ kJ mol}^{-1}$ for the CYS^- . According to these thermodynamic properties, we infer that the thiolates CYS^- , 3-MPA^- , and CH_3S^- do not directly lead to the formation of OCS in seawater.

In conclusion, we infer that the thiyl radicals formed from thiols and (potentially from) DMS are plausible intermediates that lead to OCS formation in seawater. According to our theoretical predictions, the reactions of thiyl radicals with CO are thermodynamically feasible in water. The reactions of 3-MPA^\cdot and $\text{CH}_3\text{S}^\cdot$ with CO have rate constants in the order of $10^5 \text{ M}^{-1}\text{s}^{-1}$ (reactions 2a, 2b, 3a, and 3b) and are faster than the reaction involving CYS^\cdot having rate constant of the rate-limiting step in the order of $10^0 \text{ M}^{-1}\text{s}^{-1}$ (reaction 1a). 3-MPA^\cdot , CYS^\cdot , and $\text{CH}_3\text{S}^\cdot$ (which can be produced from CH_3SH or DMS) are thus likely to be directly involved in the formation of oceanic OCS.

Reactions of Sulfhydryl Radicals and Polysulfide Anions with CO to Form OCS

In analogy with the organic thiols, we considered both radical and anionic molecular mechanisms that from sulfhydryl radicals/anions lead to OCS. In the hypothesized radical mechanism, the sulfhydryl radicals, HS_{1+n}^\cdot , might react with CO, forming OCS in one concerted kinetic step:



In a previous section, we concluded that the most predominant radical species among the sulfides and polysulfides in seawater typically are HS^\cdot , $\text{S}^{\cdot-}$, HS_2^\cdot , and $\text{S}_2^{\cdot-}$.

According to quantum chemical modeling results, among reactions 7 to 13, reaction 7, which involves HS^\cdot , appears most likely to contribute to the formation of OCS in seawater. Except for the formation of the radical adduct OCSH^\cdot that exhibits a slightly positive $\Delta G_{rxn,aq}^{*B2PLYPD}$ (reaction 7), the reactions involving a partially deprotonated sulfhydryl radical are thermodynamically feasible in water with $\Delta G_{rxn,aq}^{*B2PLYPD}$ values ranging from $-14 \pm 16 \text{ kJ mol}^{-1}$ to $-71 \pm 16 \text{ kJ mol}^{-1}$. Reactions 8-13 have rate constants that range from $1 \times 10^{-1} \pm 2.7 \text{ M}^{-1} \text{ s}^{-1}$ to $7 \times 10^{-4} \pm 2.7 \text{ M}^{-1} \text{ s}^{-1}$ indicating that these reactions are slower but might still contribute to the formation of OCS in water. The production of the radical adduct OCSH^\cdot from reaction between HS^\cdot and CO has a $\Delta G_{rxn,aq}^{*B2PLYPD}$ value of $16 \pm 16 \text{ kJ mol}^{-1}$ and a $\Delta G_{rxn,aq}^{\ddagger B2PLYPD}$ value of $26 \pm 16 \text{ kJ mol}^{-1}$. This energy barrier corresponds to a rate constant of $2 \times 10^8 \pm 2.7 \text{ M}^{-1} \text{ s}^{-1}$.

We also considered that the fully deprotonated sulfhydryl radical anions, $\text{S}_{1+n}^{\cdot-}$, might be involved in a radical reaction with CO (reactions 14-20) as well:



where n ranges from 0 to 6.

Table 5.16 Aqueous free energies for the reactions, aqueous free energies of activation, and rate constants for the reactions of polysulfides with CO leading to OCS: computational estimates. Values are in kJ mol⁻¹ for the free energies and in M⁻¹ s⁻¹ for the rate constants.

#	Reactions	$\Delta G_{rxn,aq}^{*B2PLYPD}$	$\Delta G_{rxn,aq}^{\ddagger B2PLYPD}$	$k_{aq}^{\ddagger B2PLYPD}$
Radical Reactions				
7	$HS^{\bullet} + CO \rightleftharpoons OCSH^{\bullet}$	16 ± 16	26 ± 16	$2 \times 10^{8 \pm 2.7}$
8	$HS_2^{\bullet} + CO \rightleftharpoons OCS + HS^{\bullet}$	-14 ± 16	84 ± 16	$1 \times 10^{-1 \pm 2.7}$
9	$HS_3^{\bullet} + CO \rightleftharpoons OCS + HS_2^{\bullet}$	-67 ± 16	88 ± 16	$2 \times 10^{-2 \pm 2.7}$
10	$HS_4^{\bullet} + CO \rightleftharpoons OCS + HS_3^{\bullet}$	-70 ± 16	88 ± 16	$2 \times 10^{-3 \pm 2.7}$
11	$HS_5^{\bullet} + CO \rightleftharpoons OCS + HS_4^{\bullet}$	-72 ± 16	71 ± 16	$2 \times 10^{0 \pm 2.7}$
12	$HS_6^{\bullet} + CO \rightleftharpoons OCS + HS_5^{\bullet}$	-73 ± 16	86 ± 16	$5 \times 10^{-3 \pm 2.7}$
13	$HS_7^{\bullet} + CO \rightleftharpoons OCS + HS_6^{\bullet}$	-69 ± 16	91 ± 16	$7 \times 10^{-4 \pm 2.7}$
14	$S^{\bullet-} + CO \rightleftharpoons OCS^{\bullet-}$	-69 ± 23	17 ± 23	$6 \times 10^{9 \pm 4}$
15	$S_2^{\bullet-} + CO \rightleftharpoons OCS + S^{\bullet-}$	29 ± 23	80 ± 23	$5 \times 10^{-2 \pm 4}$
16	$S_3^{\bullet-} + CO \rightleftharpoons OCS + S_2^{\bullet-}$	-22 ± 23	112 ± 23	$2 \times 10^{-7 \pm 4}$
17	$S_4^{\bullet-} + CO \rightleftharpoons OCS + S_3^{\bullet-}$	-90 ± 23	89 ± 23	$1 \times 10^{-3 \pm 4}$
18	$S_5^{\bullet-} + CO \rightleftharpoons OCS + S_4^{\bullet-}$	-122 ± 23	62 ± 23	$8 \times 10^{1 \pm 4}$
19	$S_6^{\bullet-} + CO \rightleftharpoons OCS + S_5^{\bullet-}$	-68 ± 23	56 ± 23	$1 \times 10^{3 \pm 4}$
20	$S_7^{\bullet-} + CO \rightleftharpoons OCS + S_6^{\bullet-}$	-51 ± 23	70 ± 23	$4 \times 10^{0 \pm 4}$
Anionic Reactions				
21	$HS^- + CO \rightleftharpoons OCSH^-$	N/A ^a		
22	$HS_2^- + CO \rightleftharpoons OCS + HS^-$	-81 ± 23	58 ± 23	$4 \times 10^{2 \pm 4}$
23	$HS_3^- + CO \rightleftharpoons OCS + HS_2^-$	-53 ± 23	76 ± 23	$3 \times 10^{-1 \pm 4}$
24	$HS_4^- + CO \rightleftharpoons OCS + HS_3^-$	-64 ± 23	75 ± 23	$4 \times 10^{-1 \pm 4}$
25	$HS_5^- + CO \rightleftharpoons OCS + HS_4^-$	-69 ± 23	73 ± 23	$1 \times 10^{0 \pm 4}$
26	$HS_6^- + CO \rightleftharpoons OCS + HS_5^-$	-69 ± 23	76 ± 23	$3 \times 10^{-1 \pm 4}$
27	$HS_7^- + CO \rightleftharpoons OCS + HS_6^-$	-71 ± 23	74 ± 23	$6 \times 10^{-1 \pm 4}$
28	$S^{2-} + CO \rightleftharpoons OCS^{2-}$	6 ± 23	24 ± 23	$4 \times 10^{8 \pm 4}$
29	$S_2^{2-} + CO \rightleftharpoons OCS + S^{2-}$	1 ± 23	33 ± 23	$1 \times 10^{7 \pm 4}$
30	$S_3^{2-} + CO \rightleftharpoons OCS + S_2^{2-}$	-0 ± 23	59 ± 23	$2 \times 10^{2 \pm 4}$
31	$S_4^{2-} + CO \rightleftharpoons OCS + S_3^{2-}$	-51 ± 23	48 ± 23	$3 \times 10^{4 \pm 4}$
32	$S_5^{2-} + CO \rightleftharpoons OCS + S_4^{2-}$	-30 ± 23	71 ± 23	$2 \times 10^{0 \pm 4}$
33	$S_6^{2-} + CO \rightleftharpoons OCS + S_5^{2-}$	-59 ± 23	77 ± 23	$2 \times 10^{-1 \pm 4}$
34	$S_7^{2-} + CO \rightleftharpoons OCS + S_6^{2-}$	-67 ± 23	73 ± 23	$9 \times 10^{-1 \pm 4}$

^aThe adduct $OCSH^-$ was not found in the potential energy surface described by the SMD/M06-2X electronic structure method.

According to thermodynamic and kinetic properties, reaction 14 contributes to the production of OCS with negative $\Delta G_{rxn,aq}^{*B2PLYPD}$ value and rate constant in the order of 10^9 M⁻¹ s⁻¹. Except for reaction 15, all the reactions of this set are thermodynamically favorable with $\Delta G_{rxn,aq}^{*B2PLYPD}$ values ranging from -22 ± 23 kJ mol⁻¹ to -122 ± 23 kJ mol⁻¹. Reaction 14 is extremely fast with a rate constant of $6 \times 10^{9 \pm 2.7}$ M⁻¹ s⁻¹, followed by reaction 19 with a rate constant value of

$1 \times 10^3 \pm 4 \text{ M}^{-1} \text{ s}^{-1}$. The profile of the potential energy surface of reaction 14 is represented in Figure A.8. Reactions 18 and 19 appear unlikely to compete with reaction 14, since they exhibit much slower rate constants (Table 5.16). Moreover, reaction 14 involves $\text{S}^{\cdot-}$ species that is much more abundant in seawater than hexasulfide or pentasulfide.[32, 415]

The natural population analyses and spin density calculations revealed that the nature of the transition state structures of reactions 14 to 20 is mostly radical with the anionic charge not directly involved in the reaction (Table A.16). In the transition structure of reaction 14, the unpaired electron is already transferred from the sulfhydryl fragment to the positively charged CO, and the negative partial charge is totally localized on the sulfur atom, which has a charge of $-1.9 e^-$. The CO fragment of the transition state structure of reaction 19 is overall neutral, with C atom being positively charged ($0.5 e^-$) and O atom negatively charged ($-0.6 e^-$). The unpaired electron is delocalized on the three sulfur atoms. The S atom that is involved in reaction 19 shows a negative partial charge of ($-0.5 e^-$), indicating that in the case of reaction 19 the reaction mechanism is not completely radical and that the anionic charge might be involved.

We also investigated an anionic molecular mechanism involving polysulfides and CO that leads to the formation of OCS in seawater. Partially and fully deprotonated polysulfides might be directly involved in the anionic reaction with CO in water:



where n ranges from 0 to 6. According to thermodynamic speciation models and concentrations measurements,[32, 415] HS^- , S^{2-} , HS_2^- , and S_2^{2-} are the most common anionic sulfur species in seawater conditions.

According to computed aqueous Gibbs free energies of reaction, the anionic reactions (22-34) are thermodynamically feasible or slightly infeasible. The $\Delta G_{rxn,aq}^{*B2PLYPD}$ values range from $6 \pm 23 \text{ kJ mol}^{-1}$ for reaction 28 to $-81 \pm 23 \text{ kJ mol}^{-1}$ for reaction 22. Reactions 28 and 29 exhibit slightly positive $\Delta G_{rxn,aq}^{*B2PLYPD}$ values, $6 \pm 23 \text{ kJ mol}^{-1}$ and $1 \pm 23 \text{ kJ mol}^{-1}$, respectively. The anionic adduct OCSH^- produced by reaction 21 was not located in the potential energy surface described by the SMD/M06-2X/aug-cc-pVTZ electronic structure method. A closer look at the potential energy surface of reaction 21 (Figure A.9) suggests that the adduct OCSH^- is not formed in water.

Reactions 28, 29, and 31 might contribute substantially to the production of OCS in seawater. Although having aqueous Gibbs free energies of reaction slightly positive, reactions 28 and 29 have high rate constants on the order of 10^7 - $10^8 \text{ M}^{-1} \text{ s}^{-1}$. The profile of the potential energy surface of reaction 28 is reported in Figure A.10. Reaction 31 has negative $\Delta G_{rxn,aq}^{*B2PLYPD}$ value

of $-51 \pm 23 \text{ kJ mol}^{-1}$ and a rate constant of $3 \times 10^4 \pm 4 \text{ M}^{-1}\text{s}^{-1}$. Reactions 28 and 29 involve S^{2-} and S_2^{2-} that have been assumed to be abundant in seawater.[32, 415]

The electronic nature of the transition state structures for the set of the anionic reactions has been investigated by performing natural population analyses to obtain the charge distribution (Table A.17). The negative charge of transition state structures of reactions 22-27 is mostly localized on the oxygen atom; the negative partial charge on the oxygen atom ranges from $-0.8 e^-$ for reaction 22 to $-0.3 e^-$ for reaction 24. The carbon atom of the CO fragment is partially positively charged, whereas the sulfur atom directly involved in the reaction is negatively charged with charges varying from $-0.3 e^-$ to $-0.1 e^-$. The transition state structures of reactions 28-34 are similar to the ones determined for reactions 22-27; the only remarkable difference is that the sulfur atom at the non-reactive extremity of the polysulfide chain is negatively charged, with charges that range from $-1.4 e^-$ for reaction 28 to $-0.5 e^-$ for reaction 32.

Based on our findings, S^- , S^{2-} and S_2^{2-} can be direct precursors of OCS in the oceans. S^- , S^{2-} and S_2^{2-} are abundant in seawater, [32, 415] and they can react rapidly with CO with rate constants in range of 10^7 - $10^8 \text{ M}^{-1}\text{s}^{-1}$, according to our computations. However, further investigation on the concentrations of these reactive sulfur species are required to understand which species play the predominant role in OCS formation in water.

5.5 Implications

Carbonyl sulfide (OCS) is a volatile gas that links ocean biogeochemistry with climate, creating the potential for feedbacks in the ongoing changes of the ocean and climate systems. The oceans are a major source of OCS entering the atmosphere, most likely originating from sunlight-driven transformations of sulfur precursor compounds produced by phytoplankton in the surface seawaters. Oceanic OCS ventilates into the atmosphere where it is oxidized to sulfate and contributes to cloud condensation nuclei formation. According to the CLAW hypothesis,[24, 25] changes in oceanic sulfur species production may therefore influence cloud cover, which in turn would affect phytoplankton growth and OCS production, thus representing a feedback between ocean biogeochemistry and the climate system.

By elucidating the principal OCS formation pathways, we shed light on the influence of future changes in the surface ocean. A possible feedback between atmospheric chemistry and air-sea exchange of OCS is related to the production of OCS in seawater. Stratospheric ozone depletion, which is caused by stratospheric OCS oxidation, may lead to increased production of OCS in surface water and hence increased flux of OCS into the atmosphere.[424] An increased atmospheric OCS could enhance the formation of stratospheric sulfate layer and reduce stratospheric ozone concentrations.[424] Other ocean changes such as decreased pH, increased stratification, and decreased phytoplankton growth, may affect the production and concentration of oceanic OCS as well. We took an important step forward, which is to determine the most important precursors, mechanisms, and reactive species that contribute to oceanic OCS.

Table 5.17 Reactions that from thiols and polysulfides lead to OCS in the ocean with the highest computed rate constants selected from previous tables.

# ^a	Reactions	$k_{aq}^{\ddagger B2PLYPD}$
1a	$\text{OOC-CH(NH}_3\text{)}^+-\text{CH}_2-\text{S}^\cdot + \text{CO} \rightleftharpoons \text{OOC-CH(NH}_3\text{)}^+-\text{CH}_2-\text{SCO}^\cdot$	$3 \times 10^0 \pm 2.7 \text{ M}^{-1} \text{ s}^{-1}$
1b	$\text{OOC-CH(NH}_3\text{)}^+-\text{CH}_2-\text{SCO}^\cdot \rightleftharpoons \text{OOC-CH(NH}_3\text{)}^+-\text{CH}_2 + \text{OCS}$	$4 \times 10^5 \pm 2.7 \text{ s}^{-1} \text{ }^b$
2a	$\text{OOC-CH}_2-\text{CH}_2-\text{S}^\cdot + \text{CO} \rightleftharpoons \text{OOC-CH}_2-\text{CH}_2-\text{SCO}^\cdot$	$2 \times 10^5 \pm 2.7 \text{ M}^{-1} \text{ s}^{-1}$
2b	$\text{OOC-CH}_2-\text{CH}_2-\text{SCO}^\cdot \rightleftharpoons \text{OOC-CH}_2-\text{CH}_2 + \text{OCS}$	$5 \times 10^5 \pm 2.7 \text{ s}^{-1} \text{ }^b$
3a	$\text{CH}_3\text{S}^\cdot + \text{CO} \rightleftharpoons \text{CCH}_3\text{O}^\cdot$	$2 \times 10^5 \pm 2.7 \text{ M}^{-1} \text{ s}^{-1}$
3b	$\text{CH}_3\text{SCO}^\cdot \rightleftharpoons \text{CH}_3 + \text{OCS}$	$2 \times 10^4 \pm 2.7 \text{ s}^{-1} \text{ }^b$
7	$\text{HS}^\cdot + \text{CO} \rightleftharpoons \text{COSH}^\cdot$	$2 \times 10^8 \pm 2.7 \text{ M}^{-1} \text{ s}^{-1}$
14	$\text{S}^{\cdot-} + \text{CO} \rightleftharpoons \text{COS}^{\cdot-}$	$6 \times 10^9 \pm 4 \text{ M}^{-1} \text{ s}^{-1}$
28	$\text{S}_2^{\cdot-} + \text{CO} \rightleftharpoons \text{COS}^{\cdot-}$	$4 \times 10^8 \pm 4 \text{ M}^{-1} \text{ s}^{-1}$
29	$\text{S}_2^{\cdot-} + \text{CO} \rightleftharpoons \text{OCS} + \text{S}^{\cdot-}$	$1 \times 10^7 \pm 4 \text{ M}^{-1} \text{ s}^{-1}$
31	$\text{S}_4^{\cdot-} + \text{CO} \rightleftharpoons \text{OCS} + \text{S}_3^{\cdot-}$	$3 \times 10^4 \pm 4 \text{ M}^{-1} \text{ s}^{-1}$

^aThe numbers of reactions is taken from Tables 5.15 and 5.16. ^bThese rate constants are computed using the adduct as reactant.

With this study we successfully provided new insights into the precursors and mechanisms of formation of OCS in the ocean surface. Aqueous short-lived oxidants such as $\text{Br}_2^{\cdot-}$, $\text{CO}_3^{\cdot-}$, and $^3\text{DOM}^*$ are implicated in the photooxidation of sulfur-containing species. Among the studied transients (OH^\cdot , $^1\text{O}_2$, $\text{CO}_3^{\cdot-}$, and $\text{Br}_2^{\cdot-}$), $\text{Br}_2^{\cdot-}$ is expected to play the main role in the photochemical transformation of sulfur-containing compounds such as DMS, MET, CYS, and GSH in seawater. This finding is strengthened by the fact that in our approach we considered a lower limit for $\text{Br}_2^{\cdot-}$ concentration in seawater. $\text{CO}_3^{\cdot-}$ could play a significant role in the photooxidation of CYS and GSH as well. Thiyl and sulphydryl radicals, and sulphydryl radical anions are the products of the reactions between aqueous reactive species and thiols, polysulfides, and (possibly also) DMS. They are the source of sulfur atom in OCS, according to the pathways that we evaluated here.

Quantum chemical modeling estimates of aqueous free energies of reaction and rate constant allowed us to identify the most relevant pathways that lead from thiols, DMS, and polysulfides to OCS in water. In Table 5.17 we reported the most kinetically relevant reactions that from thiyl/sulphydryl radicals and CO lead to the formation of OCS in water. According to our quantum chemical simulations and to acid/base speciation based on previously reported experimental pK_a values, we inferred that the thiyl radicals, which can be generated by oxidation of thiolates or homolytic bond cleavage of thiols, can react with CO to form OCS via a radical two-kinetic steps-pathway. The first step (reactions 1a, 2a, and 3a) generates an intermediate where CO is bound to the S atom of the thiyl radical. The second step (reactions 1b, 2b, and 3b) is the cleavage of the bond between the S atom and the C atom of the organic fragment. Both steps are kinetically and thermodynamically feasible.

5.6 Acknowledgments

We thank Kristopher McNeill (ETH Zurich), Urs von Gunten (Eawag/EPFL), and Lenny Winkel (Eawag/ETH Zurich) for their constructive comments. We acknowledge financial support by Italian MIUR-PNRA. The authors also thank the EPFL centralized HPC facilities for computational resources and support.

6 Conclusions

6.1 Main Results

The present thesis provides new thermodynamic and kinetic data for reactions involving reactive species in water. The new TA14 computational protocol was designed to obtain gas phase total atomization energies, standard enthalpies of formation and standard Gibbs free energies of formation for halamines in gas phase within uncertainty bounds of 1-3 kJ mol⁻¹ (chapter 2). In chapter 3, I reported theoretical estimates of aqueous equilibrium constants of reactions of halamines with an expected accuracy of ~ 1 logarithmic unit. Then I established linear free energy relationships (LFERs) between previously reported experimental data and new computational aqueous free energies of deprotonation to assess acid dissociation constants of chloramines, bromamines, and bromochloramines. Thanks to these newly computed aqueous equilibrium data, I also revised the rate constant values for reactions leading to halamines in water. In chapter 4, I computed the free energies of reaction and rate constants for the multistep mechanism that involves bromide and ozone, as aqueous reactive species, and *N,N*-dimethylsulfamide, as reaction substrate. By using DFT methods that were previously validated for multireference species such as ozone, ozone adducts, and transition state structures in general, the results of my simulations achieved an accuracy of 2-3 orders of magnitude in the rate constant estimates, allowing us to deduce the most favorable pathway(s) that lead from *N,N*-dimethylsulfamide to NDMA. In chapter 5, I computed Gibbs free energies of reactions and rate constants for aqueous reactions between thiyl or sulfhydryl radicals and CO within uncertainty bounds of 15.5 kJ mol⁻¹. In conclusion, the results of the present thesis show that current quantum chemical models can substantially aid in the interpretation of chemical pathways involving reactive species in water.

6.2 Main Challenges

The computational treatment of solvent-solute interactions was one of the main challenges I encountered in this thesis work. In order to obtain aqueous free energies of reaction, I

combined gas phase reaction free energy estimates with experimental (when available) or computed free energies of solvation. The theoretical free energy of solvation values contain most of the uncertainty assigned to the aqueous thermochemical properties. To treat the solvent-solute interactions, I used two different solvation approaches: the implicit solvent models, such as SMD and COSMO, and the cluster-continuum solvation approach in which one molecule of solvent was explicitly modeled with the solute. In chapter 4, I studied the formation of a loosely bound reaction intermediate containing an electrophilic fragment BrNO and an electron-rich fragment. This intermediate is (micro)solvated by 5 molecules of water, which stabilize the fragile cluster by holding together the two fragments. It was not possible to simulate this reaction intermediate without explicitly adding 5 molecules of water. In chapter 3, I proposed an ‘half and half’ approach based on the average of free energies of solvation estimated with the implicit solvent model SMD and with the cluster-continuum model to obtain free energies of reaction within uncertainty bounds of 6-7 kJ mol⁻¹. Computational approaches to properly account for the solvation effects have to be chosen on a case-by-case basis.

The second main challenge I had to deal with consists in the computational treatment of reactive species having multireference character. Ozone, ozonides, and halamines are molecules in which the reference configuration is affected by quasi-degeneracy and cannot be completely described by a single predominating configuration. Single-reference methods such as DFT methods and some of the post-HF wavefunction methods give erratic performance in the prediction of thermodynamic and kinetic properties of such multireference systems. In chapter 4, ozone plays a key role in the molecular mechanism studied. Ozone is a closed-shell singlet with a pronounced diradical character. The M05 density functional was chosen to treat ozone, the ozone adducts, and other reactive species that arose. Previous validation tests showed that this functional performed well in the prediction of thermodynamic properties and barrier heights of reactions involving multireference systems. In chapter 2, I dealt with the electronic structures of chloramines, bromamines, and bromochloramines. My total atomization energy results showed that these species exhibit from low to severe multireference character, leading to the conclusions that halamines are fragile species, whose N-Cl and N-Br bonds are held together by electronic correlation forces. To study these ‘delicate’ halogen oxidants, I chose extremely expensive high-level wave function methods able to describe the electronic correlation energy. In conclusion, multireference species require tailored computational treatments.

6.3 Future Developments and Improvements

In this thesis, I have employed several quantum chemical modeling approaches to obtain accurate thermodynamic and kinetic properties for reactive species in water. These approaches can be improved or used as they are to investigate other aquatic systems:

- The TA14 benchmark protocol, designed in chapter 2, can potentially be used to assess

the performance of other quantum chemical methods in the prediction of the electronic structure properties and the gas phase thermochemistry of species containing halogens in water. For example, by comparing total atomization energies computed with a chosen DFT method, TAE_{DFT} , with the TAE_{TA14} estimates, it is possible to understand whether the chosen DFT method would give reasonable results in prediction of the electronic structures of halogen-containing species.

- The computational procedures employed here to predict the thermochemistry and the kinetics of reactions involving halamines (chapters 2 and 3) or sulfur-containing species (chapter 5) can be used to investigate other similar aqueous systems. For example, the $\Delta_f G_{aq}$ values computed for halamines can be further used to determine aqueous equilibrium constants of reactions involving halamines, as I did in chapter 3, where I took advantage of these thermodynamic data to assess the equilibria of chlorination and bromination reactions of ammonia that lead to halamines. This approach can be thus applied to investigate the thermodynamics of other hypothetical reactions of halamines with relevant species in water.
- The computational treatment to account for the solvent-solute interactions can be further improved. I often used implicit solvent models combined with the cluster-continuum approach when I added one explicitly modeled molecule of water to increase the quality of the free energies of solvation estimates. The addition of more molecules of water in the system might lead to more accurate predictions of the solvent-solute interactions, but this would also raise questions about whether different geometric configurations of the microsolvated system had been adequately sampled.
- Concerning the formation of OCS in the ocean, I investigated computationally the reactions of thiyl and sulfhydryl radicals with CO in water. Previous experimental data and the results of the APEX photochemical model demonstrated that sulfur-containing compounds react with aqueous reactive species, such as Br_2^- and CO_3^- , and could lead to the formation of thiyl radicals. Further quantum chemical simulations of the molecular mechanism of the oxidation of sulfur-containing compounds by aqueous reactive species would provide additional insights in the sulfur chemistry of ocean.

A Appendix A

A.1 Supporting Information

This appendix contains the supporting information sections of Chapter 2, Chapter 3, Chapter 4, and Chapter 5.

A.1.1 Benchmark Thermochemistry of Chloramines, Bromamines, and Bromochloramines: Halogen Oxidants Stabilized by Electron Correlation - SUPPORTING INFORMATION

Table A.1 Optimized Geometries, with coordinates in Bohr. ^a

Compound			
H ₂	(AE-CCSD(T)/aug-cc-pVQZ)		
H	0.00000000	0.00000000	0.70108673
H	0.00000000	0.00000000	-0.70108673
N ₂	(AE-CCSD(T)/aug-cc-pVQZ)		
N	0.00000000	0.00000000	1.03764068
N	0.00000000	0.00000000	-1.03764068
O ₂	(AE-CCSD(T)/aug-cc-pVQZ)		
O	0.00000000	0.00000000	1.13922333
O	0.00000000	0.00000000	-1.13922333
Cl ₂	(AE-CCSD(T)/aug-cc-pVQZ)		
Cl	0.00000000	0.00000000	1.88919509

Appendix A

Table A.1 Optimized Geometries, with coordinates in Bohr. ^a

Compound				
Cl		0.00000000	0.00000000	-1.88919509
Br ₂	(AE-CCSD(T)/aug-cc-pVQZ)			
Br		0.00000000	0.00000000	2.15289952
Br		0.00000000	0.00000000	-2.15289952
HCl	(AE-CCSD(T)/aug-cc-pVQZ)			
H		0.00000000	0.00000000	-2.34371101
Cl		0.00000000	0.00000000	0.06754727
HBr	(AE-CCSD(T)/aug-cc-pVQZ)			
H		0.00000000	0.00000000	-2.62480873
Br		0.00000000	0.00000000	0.03352007
HOCl	(AE-CCSD(T)/aug-cc-pVQZ)			
H		-2.61817495	1.63840308	0.00000000
O		-2.14218076	-0.11860230	0.00000000
Cl		1.05530087	0.00702940	0.00000000
HOBr	(AE-CCSD(T)/aug-cc-pVQZ)			
H		-3.30726752	1.63594240	0.00000000
O		-2.82221738	-0.11762873	0.00000000
Br		0.61423334	0.00294884	0.00000000
H ₂ O	(AE-CCSD(T)/aug-cc-pVQZ)			
H		0.00000000	-1.43048941	0.98402826
O		0.00000000	0.00000000	-0.12400545
H		0.00000000	1.43048941	0.98402826
NH ₃	(AE-CCSD(T)/aug-cc-pVQZ)			
N		0.00000000	-0.00000007	-0.12755526
H		0.52290825	-0.90130902	0.59076593
H		0.01910294	1.76953179	0.59076553

Table A.1 Optimized Geometries, with coordinates in Bohr. ^a

Compound			
H		-1.54201116	-0.86822179 0.59076594
NH ₂ Cl	(AE-CCSD(T)/aug-cc-pVQZ)		
N		2.23834626	0.00035926 -0.14938635
H		2.75235390	-1.52668576 0.88990901
H		2.77931371	1.51166594 0.89918960
Cl		-1.05575901	0.00028902 0.00825791
NHCl ₂	(AE-CCSD(T)/aug-cc-pVQZ)		
N		0.00029142	-1.60102491 -0.16108085
H		-0.09791735	-2.55978615 1.50251967
Cl		2.65526471	0.35593995 0.01139714
Cl		-2.65255937	0.35895588 0.00980316
NCl ₃	(AE-CCSD(T)/aug-cc-pVQZ)		
N		-1.07140387	0.00000003 0.00000000
Cl		0.14301248	-1.54542252 2.67675026
Cl		0.14301249	3.09084503 0.00000000
Cl		0.14301248	-1.5454225 2 -2.67675026
NH ₂ Br	(AE-CCSD(T)/aug-cc-pVQZ)		
N		-0.14731129	2.94534561 0.00000000
H		0.89705829	3.44615957 -1.52710267
H		0.89705820	3.44615930 1.52710281
Br		0.00322682	-0.61063305 0.00000000
NHBr ₂	(AE-CCSD(T)/aug-cc-pVQZ)		
N		0.00018299	-1.91523168 -0.15770407
H		-0.11697966	-2.87207630 1.50607992
Br		2.88430786	0.18747499 0.00476453
Br		-2.88284644	0.18903676 0.00398472
NBr ₃	(AE-CCSD(T)/aug-cc-pVTZ)		

Appendix A

Table A.1 Optimized Geometries, with coordinates in Bohr. ^a

Compound			
N	-0.00000010	-0.00000011	-1.19775081
Br	2.42495000	-2.35936212	0.07084198
Br	0.83079273	3.27974917	0.07084197
Br	-3.25574271	-0.92038704	0.07084198
NHBrCl (AE-CCSD(T)/aug-cc-pVQZ)			
N	1.18723587	-1.66610171	-0.16159297
H	1.23545984	-2.52767504	1.55701050
Cl	3.75319661	0.40413037	0.01043165
Br	-1.88948559	0.14883771	0.00416660
NBrCl ₂ (AE-CCSD(T)/aug-cc-pVTZ)			
N	-1.13390506	-1.02781227	0.00000000
Br	0.06123594	2.43641543	-0.00000001
Cl	0.15793366	-2.54348239	-2.69794123
Cl	0.15793366	-2.54348234	2.69794126
NBr ₂ Cl (AE-CCSD(T)/aug-cc-pVTZ)			
N	-0.80436316	-1.15422838	0.00000000
Br	0.92761792	0.06539392	2.93260742
Br	0.92761790	0.06539392	-2.93260743
Cl	-3.86482701	0.16703972	0.00000003

^aThe model chemistry is indicated in parenthesis.

A.1. Supporting Information

Table A.2 Computed anharmonic Frequencies for the halamines and the hypohalous acids (in cm^{-1}).
Method: B2PLYPD/aug-cc-pVQZ

NH_2Cl	NHCl_2	NCl_3	NH_2Br	NHBr_2	NBr_3	NHBrCl	NBrCl_2	NBr_2Cl	HOCl	HOBr
3383.2	3286.7	629.1	3383.6	3284.4	556.2	3281.6	618.1	607.1	3601.3	3607.0
3305.1	1298.1	628.6	3304.4	1227.1	555.7	1268.0	609.8	570.2	1231.9	1156.9
1542.5	995.4	535.8	1502.4	915.0	435.5	951.9	489.8	459.1	733.6	634.5
1168.3	662.4	350.7	1097.6	589.9	210.5	647.2	317.8	267.8		
1023.2	609.4	254.9	973.4	504.1	147.7	538.3	211.7	193.1		
675.9	283.5	255.2	581.3	170.2	148.1	226.1	209.4	160.7		

A.1.2 Equilibria and Speciation of Chloramines, Bromamines, and Bromochloramines in Water

- SUPPORTING INFORMATION

A.1.2.1 Computational Modeling of Free Energies of Solvation and Aqueous Free Energies of Reaction To describe solvation effects, we employed two different types of computational approaches: implicit solvent models and cluster-continuum approaches. We first explain the computational derivation of the free energy values obtained with the implicit solvent models: $\Delta G_{solv,SMD}^*$, $\Delta G_{solv,COSMO}^*$, $\Delta G_{solv,CPCM}^*$, and $\Delta G_{solv,PCM}^*$. For a given molecule X , the Gibbs free energy of solvation $\Delta G_{solv,Implicit}^*(X)$ can be obtained from the difference between the aqueous free energy and gas phase free energy:

$$\Delta G_{solv,Implicit}^*(X) = G_{aq,Implicit}^*(X) - G_{gas}^*(X) \quad (A.1)$$

The superscript $*$ denotes the 1 M standard state. $G_{gas}^*(X)$ is computed as follows:

$$G_{gas}^*(X) = G_{gas}^o(X) + \Delta G^{o \rightarrow *} \quad (A.2)$$

where the $G_{gas}^o(X)$ is the gas phase free energy of the compound X at 1 atm, and $\Delta G^{o \rightarrow *}$ term accounts for the free energy change of transferring 1 mole of ideal gas from 1 atm ($\frac{1}{RT} = 0.04087 \frac{[atm]}{[M]}$) to 1 M ($\frac{1}{1} = \frac{[M]}{[M]}$) at 298 K:

$$\Delta G^{o \rightarrow *} = -RT \ln \left(\frac{0.04087/1}{1/1} \right) = 7.9 \text{ kJ mol}^{-1} \quad (A.3)$$

We derived the free energies of solvation computed with the cluster-continuum-SMD approach as follows. According to the cluster-continuum framework developed by Bryantsev et al.[224] for the case of one explicit molecule of water, the Gibbs free energy of solvation for a given compound X can be estimated by:

$$\begin{aligned} \Delta G_{solv,Cluster-SMD}^*(X) = & \Delta G_{gas,bind}^{0,II}(X) + \Delta G_{solv,SMD}^*(X(H_2O)) - \Delta G_{solv,SMD}^*(H_2O) \\ & - \Delta G^{o \rightarrow *} - RT \ln([H_2O]_l) \end{aligned} \quad (A.4)$$

The term $[H_2O]_l$ represents the molar concentration of water at liquid state, 55.56 M, at 298 K. The terms $\Delta G_{solv,SMD}^*(X(H_2O))$ and $\Delta G_{solv,SMD}^*(H_2O)$ are the free energies required to transfer the cluster $X(H_2O)$ and the single molecule of water H_2O from the gas phase to the aqueous phase at the 1 M standard state. The aqueous free energies of the cluster, $\Delta G_{solv,SMD}^*(X(H_2O))$, and the molecule of water, $\Delta G_{solv,SMD}^*(H_2O)$, in equation A.4 were computed using the SMD implicit solvent model. The development of the cluster-continuum-COSMO approach is analogous to that shown in eq A.4, where the terms with subscript "SMD" would be replaced with subscript "COSMO". According to the *cluster cycle II* presented in Bryantsev et al., the term $\Delta G_{gas,bind}^{0,II}(X)$ corresponds to the free energy of binding the gas phase molecule X and

explicitly modeled water molecule (H_2O):

$$\Delta G_{gas,bind}^{0,II}(X) = G_{gas}^0(X(H_2O)) - G_{gas}^0(H_2O) - G_{gas}^0(X) \quad (A.5)$$

Many of the reactions investigated in the present paper generated a water molecule as a reaction product (Table 3.3). The aqueous free energy of the water molecule computed at 1 M standard state was converted to the pure liquid (55.56 M) standard state, according to:

$$\begin{aligned} \Delta_f G_l(H_2O) &= \Delta_f G_{gas}^0(H_2O) + \Delta G_{solv}^*(H_2O) + \Delta G^{o \rightarrow *} + \Delta G^{* \rightarrow l} \\ &= \Delta_f G_{gas}^0(H_2O) + \Delta G^{o \rightarrow *} + \Delta G^{* \rightarrow l} \end{aligned} \quad (A.6)$$

where

$$\Delta G^{o \rightarrow l} = \Delta G^{o \rightarrow *} + \Delta G^{* \rightarrow l} \quad (A.7)$$

The term $\Delta G^{o \rightarrow l}$ refers to the free energy required to transfer 1 atm of ideal gas into 1 M ideal gas ($\frac{[1M]}{[1M]}$), and 1 M of ideal gas into 55.56 M ($\frac{[55.56M]}{[1M]}$) liquid water at 298 K:

$$\Delta G^{o \rightarrow l} = -RT \ln \left(\frac{1/1}{55.56/1} \right) = 9.9 \text{ kJ mol}^{-1} \quad (A.8)$$

A.1.2.2 Henry's Law Constant: Experimental Data and Conversion Factors Experimental Henry's law constant values for several compounds are reported in Sander's database[261, 263] in $\frac{mol}{m^3 \cdot Pa}$.

Table A.3 Experimental Henry's law solubility constants $K_H^{(-)}$ for a selected set of molecules. $K_H^{(-)}$ has units of $\frac{M}{M}$.

Compounds	$K_H^{(-)}$
HOCl	6.2×10^{-5a}
HOBr	3.1×10^{-4a}
Cl ₂	0.44 ^a
Br ₂	0.06 ^a
NF ₃	51.06 ^a
NH ₃	6.8×10^{-4a}
NH ₂ Cl	4.7×10^{-4a}
NHCl ₂	1.4×10^{-3a}
NCl ₃	0.41 ^a
NH ₂ CH ₃	4.5×10^{-4b}
NH(CH ₃) ₂	7.2×10^{-4b}

^aThe experimental data are taken from Sander's compilation.[261] ^bThe experimental data are taken from Sander's compilation.[263]

Appendix A

These values were converted to dimensionless units $K_H^{(-)}$, using equations A.9 and A.10:

$$K_H^{(-)} = K_H \left[\frac{\text{mol}}{\text{m}^3 \cdot \text{Pa}} \right] \times 101.325 \left[\frac{\text{m}^3 \cdot \text{Pa}}{\text{L} \cdot \text{atm}} \right] \quad (\text{A.9})$$

where the factor $101.325 \left[\frac{\text{m}^3 \cdot \text{Pa}}{\text{L} \cdot \text{atm}} \right]$ converts $\text{m}^3 \cdot \text{Pa}$ to $\text{L} \cdot \text{atm}$, and:

$$K_H^{(-)} = K_H \left[\frac{\text{mol}}{\text{L} \cdot \text{atm}} \right] \times \frac{1}{RT} \quad (\text{A.10})$$

where R is the ideal gas constant ($0.08205736 \text{ L atm K}^{-1} \text{ mol}^{-1}$) and T is 298.15 K. $K_H^{(-)}$ has units of $\frac{M}{M}$.

A.1.2.3 Assignment of the Error Bounds for the Computed Aqueous Standard Free Energies of Formation We estimated the error bounds that are expected to contain 95% of the deviations for the computed aqueous standard free energies of formation, as follows.

$$\Delta_f G_{aq,exact}^* = \Delta_f G_{aq,Comp}^* \pm z_{0.025} \times s \quad (\text{A.11})$$

where $\Delta_f G_{aq,exact}^*$ is the hypothetical exact experimental value and $\Delta_f G_{aq,Comp}^*$ is the computational estimate. The term s is the expected standard error of the computational approach, and $z_{0.025}$ is the critical value of a normal distribution associated with the probability $\frac{(1-0.95)}{2}$, equal to -1.960. We estimated s based on a propagation of the expected errors of the computational gas phase prediction and the computational solvation energy prediction:

$$s = \sqrt{(RMSE_{\Delta G_{solv,half-and-half}^*}^o)^2 + (SE_{\Delta_f G_{gas,Comp}^o}^o)^2} \quad (\text{A.12})$$

The $RMSE_{\Delta G_{solv,half-and-half}^*}^o$ refers to the root mean squared error of computational predictions of the free energy of aqueous solvation, found to be 3.2 kJ mol^{-1} for test set A (Table 3.1 in the main text), and $SE_{\Delta_f G_{gas,Comp}^o}^o$ is the expected standard error of the gas phase standard free energies of formation, assigned as $\frac{1}{2} \text{ kJ mol}^{-1}$ for chloramines and monobromamines and $\frac{3}{2} \text{ kJ mol}^{-1}$ for dibromamine, tribromamine, and bromochloramines.

A.1.2.4 Aqueous Free Energy of the Proton A value of $-1119.2 \text{ kJ mol}^{-1}$ was employed for the free energy of proton, $G_{aq}^*(H^+)$, in the 1 M aqueous standard state. This value results from the sum of the free energy of the proton in gas phase, $G_g^o(H^+)$, which is equal to $-26.3 \text{ kJ mol}^{-1}$, [248] the solvation free energy of the proton, $\Delta G_{solv}^o(H^+)$, $-1100.9 \text{ kJ mol}^{-1}$, [425] and the factor $\Delta G^{o \rightarrow *}$ that converts the 1 atm standard state to the 1 M standard state at 298 K. The $G_{aq}^*(H^+)$ value contributes to the uncorrected pK_a value, which is determined from $\Delta G_{aq}^{dep,uncorrected}$ in equation 3.5 in the main text. However, the contribution from $G_{aq}^*(H^+)$ cancels out in the LFER used to produce the final computational estimate of the pK_a .

Table A.4 Evaluation of B2PLYPD method for total atomization energies (TAE) at 0 K and average error-per-bond values, for NH₃, H₂O, and selected halogen species, in kJ mol⁻¹.

Compounds	TAE_{TA14}^a	$TAE_{B2PLYPD}$	Error per bond ^b
NH ₃	1250.1	1243.4	2.2
H ₂ O	967.2	973.1	3.0
HOCl	682.8	694.5	5.9
NH ₂ Cl	1034.1	1035.2	0.4
NHCl ₂	824.3	829.9	1.9
NCl ₃	608.7	624.5	5.3
HOBr	675.9	681.4	2.7
NH ₂ Br	1010.4	1006.0	1.5
NHBr ₂	775.2	767.7	2.5
NBr ₃	536.2	532.0	1.4
NHBrCl	799.5	801.4	0.6
NBrCl ₂	584.3	593.4	3.0
NBr ₂ Cl	560.1	560.9	0.3
MUE per bond^c			2.4
RMSE per bond^d			2.9

^aThe TA14 theoretical benchmarks of the total atomization energies at 0 K were taken from Trogolo and Arey,[221, 222] and the values shown here exclude the zero-point vibrational energy, core-valence correlation corrections, scalar relativistic correction, first and second order spin-orbit couplings, and diagonalized Born-Oppenheimer correction, since these energy contributions are not considered in the B2PLYPD computations. ^bError per bond = $|TAE_{TA14} - TAE_{B2PLYPD}| / (Total\ number\ of\ atoms - 1)$. ^cMean unsigned error (MUE) is the average of the absolute error-per-bond values over the set of molecules, in kJ mol⁻¹. ^dRoot mean squared error (RMSE) is the root mean square of the error-per-bond values over the set of molecules, in kJ mol⁻¹.

A.1.2.5 Evaluation of the B2PLYPD Method for the Total Atomization Energy We find that the B2PLYPD/aug-cc-pVQZ model chemistry is appropriate for evaluating the electronic structures of halamines and other halogen oxidants studied here. Gas phase total atomization energies (TAEs) predicted by the B2PLYPD method for the chloramines, bromamines, bromochloramines, H₂O, NH₃, HOCl, and HOBr were compared to previously reported high-accuracy theoretical TA14 data:[221, 222] we observed that the B2PLYPD method performed well, exhibiting an average error-per-bond value of 2.4 kJ mol⁻¹ for this chemical set (Table A.4). The error-per-bond statistic was defined as the absolute value of $\frac{|TAE_{B2PLYPD} - TAE_{benchmark}|}{total\ number\ of\ bonds}$ for each molecule. The maximum error-per-bond value, 5.9 kJ mol⁻¹, was observed for HOCl (Table A.4).

A.1.2.6 Evaluation of the Implicit Solvent Models, SMD, COSMO, PCM, and CPCM, for Free Energies of Solvation and Aqueous Equilibrium Constants

Table A.5 Evaluation of the implicit solvent models, SMD, COSMO, PCM, and CPCM, for the prediction of free energy of solvation values using the B2PLYPD/aug-cc-pVQZ model chemistry for selected molecules, in kJ mol^{-1} .

	Expt	SMD [226]	COSMO[232, 233]	CPCM[227, 228]/UAHF ^a	CPCM/UAKS ^b	PCM[229, 228, 230, 231]/UAHF ^a	PCM/UAKS ^b
Set A							
NH ₃	-18.1 ^c	-13.1	-20.1	-29.4	-29.4	-29.1	-29.1
H ₂ O	-26.4 ^d	-28.6	-27.9	-42.1	-42.1	-41.7	-41.7
NH ₂ CH ₃	-19.1 ^e	-15.2	-17.8	-34.0	-34.0	-33.7	-33.7
NH(CH ₃) ₂	-17.9 ^e	15.2	-15.3	-34.7	-34.7	-34.3	-34.3
Cl ₂	-2.0 ^c	2.0	-3.0	-2.3	-2.3	-2.3	-2.3
Br ₂	-7.1 ^c	-4.4	-2.9	-3.4	-3.4	-3.4	-3.4
NF ₃	9.7 ^c	10.8	-1.8	-2.9	-2.9	-2.9	-2.9
Set B							
HOCl	-24.0 ^c	-16.7	-20.2	-39.1	-39.1	-38.7	-38.7
NH ₂ Cl	-19.0 ^c	-16.3	-22.5	-42.4	-42.4	-42.0	-42.0
NHCl ₂	-16.3 ^c	-10.2	-17.0	-40.5	-40.5	-40.0	-40.0
NCl ₃	-2.2 ^c	2.6	-4.4	-3.5	-3.5	-3.5	-3.5
HOBr	-20.0 ^c	-14.5	-20.1	-38.1	-38.1	-37.7	-37.7
NH ₂ Br	N/A ^f	-14.3	-21.9	-41.1	-41.1	-40.7	-40.7
NHBr ₂	N/A ^f	-10.1	-17.7	-39.1	-39.1	-38.6	-38.6
NBr ₃	N/A ^f	-6.2	N/A ^f	-5.1	-5.1	-5.0	-5.0
NHBrCl	N/A ^f	-9.8	-17.2	-39.9	-39.9	-39.4	-39.4
NBrCl ₂	N/A ^f	-0.3	-5.2	-4.0	-4.0	-4.0	-4.0
NBr ₂ Cl	N/A ^f	-3.3	-5.9	-4.6	-4.6	-4.5	-4.5
Set A							
Root Mean Square Error		3.3	4.9	12.3	12.3	12.0	12.0

^aThe implicit solvent model was applied using the UAHF atomic radii. ^bThe implicit solvent model was applied using the UAKS atomic radii. ^cThe experimental values are taken from Sander's compilation.[261] ^dThe free energy of solvation of H₂O was taken from Marenich et al.[262] ^eThe experimental values are taken from Sander's compilation.[263] ^fNot available.

Table A.6 Theoretical gas phase equilibrium constants, $\log K_{gas}^{Comp}$, and aqueous equilibrium constants, $\log K_{aq,Comp}$, for the halamines, using the SMD implicit solvent model, COSMO implicit solvent model, and cluster-continuum-SMD approach.

Reactions	$\log K_{gas}^{Comp}{}^a$	$\log K_{aq}^{SMD}{}^b$	$\log K_{aq}^{cluster-SMD}{}^b$	$\log K_{aq}^{COSMO}{}^b$
Chloramines				
$NH_{3,aq} + HOCl_{aq} \rightleftharpoons NH_2Cl_{aq} + H_2O_l$	11.77±0.18	12.7	10.1	11.8
$NH_2Cl_{aq} + HOCl_{aq} \rightleftharpoons NHCl_{2,aq} + H_2O_l$	12.46±0.18	11.7	10.0	11.1
$NHCl_{2,aq} + HOCl_{aq} \rightleftharpoons NCl_{3,aq} + H_2O_l$	12.48±0.18	10.6	8.9	9.9
Bromamines				
$NH_{3,aq} + HOBr_{aq} \rightleftharpoons NH_2Br_{aq} + H_2O_l$	9.39±0.18	10.3	8.3	9.3
$NH_2Br_{aq} + HOBr_{aq} \rightleftharpoons NHBr_{2,aq} + H_2O_l$	9.6±0.53	9.6	8.0	8.5
$NHBr_{2,aq} + HOBr_{aq} \rightleftharpoons NBr_{3,aq} + H_2O_l$	11.6±0.53	11.7	8.5	N/A ^c
Bromochloramines				
$NH_2Br_{aq} + HOCl_{aq} \rightleftharpoons NHBrCl_{aq} + H_2O_l$	13.2±0.53	12.8	10.8	12.0
$NH_2Cl_{aq} + HOBr_{aq} \rightleftharpoons NHBrCl_{aq} + H_2O_l$	10.8±0.53	10.4	9.1	9.5
$NHBrCl_{aq} + HOCl_{aq} \rightleftharpoons NBrCl_{2,aq} + H_2O_l$	11.6±0.53	10.3	8.2	9.1
$NHBrCl_{aq} + HOBr_{aq} \rightleftharpoons NBr_2Cl_{aq} + H_2O_l$	10.1±0.53	9.7	7.7	7.7
$NHCl_{2,aq} + HOBr_{aq} \rightleftharpoons NBrCl_{2,aq} + H_2O_l$	10.0±0.53	9.0	7.2	7.5
$NHBr_{2,aq} + HOCl_{aq} \rightleftharpoons NBr_2Cl_{aq} + H_2O_l$	13.7±0.53	12.8	10.5	11.2
Disproportionation reactions				
$NH_2Cl_{aq} + NH_2Cl_{aq} \rightleftharpoons NHCl_{2,aq} + NH_{3aq}$	0.69±0.18	-0.9	-0.1	-0.7
$NH_2Br_{aq} + NH_2Br_{aq} \rightleftharpoons NHBr_{2,aq} + NH_{3aq}$	0.2±0.53	-0.8	-0.3	-0.8
$NH_2Cl_{aq} + NH_2Br_{aq} \rightleftharpoons NHBrCl_{aq} + NH_{3aq}$	1.4±0.53	0.1	0.8	0.2
$NHBrCl_{aq} + HOCl_{aq} \rightleftharpoons NHCl_{2,aq} + HOBr_{aq}$	1.6±0.53	1.3	0.9	1.6
$NHBrCl_{aq} + HOBr_{aq} \rightleftharpoons NHBr_{2,aq} + HOCl_{aq}$	-3.6±0.53	-3.2	-2.8	-3.5

^aThe gas phase equilibrium constants were computed using gas phase free energies of formation taken from benchmark-quality theoretical results.[221, 222] ^bAll of the reactions that have H_2O as a reaction product are reported with H_2O at the 55.56 M standard state. The remaining reactions (*i.e.* the disproportionation reactions) are in the 1 M standard state. ^cNot available.

Appendix A

A.1.2.7 Regression Results for Quantum Chemical LFERs Used to Estimate pK_a Values.

The following equation was used to determine the pK_a values of neutral chloramine and bromamine species (Table A.8).

$$pK_a^{\text{Quantum Chemical LFER}} = 1.78 \times pK_a^{\text{uncorrected}} - 0.32 \quad (\text{A.13})$$

Table A.7 Experimental pK_a data and quantum chemical LFER pK_a estimates for the ammonium functional group of several compounds, including halamines.

	Experimental pK_a value ^a	Uncorrected quantum chemical pK_a value ^b	Quantum Chemical LFER pK_a estimate ^c
Calibration set			
$\text{NH}_2\text{-CS-NH}_3^+/\text{NH}_2\text{-CS-NH}_2$	-0.96[258]	-7.5	-0.7
$\text{CH}_3\text{-CO-NH}_3^+/\text{CH}_3\text{-CO-NH}_2$	-0.51 [258]	-9.0	-1.5
$\text{NH}_2\text{-CO-NH}_3^+/\text{NH}_2\text{-CO-NH}_2$	0.18 [258]	-7.8	-0.8
$\text{Br}(\text{CH}_3)_2\text{NH}^+/\text{Br}(\text{CH}_3)_2\text{N}$	2.88 [216]	-1.1	2.8
$2\text{-BrC}_6\text{H}_4\text{NH}_3^+/2\text{-BrC}_6\text{H}_4\text{NH}_2$	2.60[255]	-1.5	2.6
$2\text{-ClC}_6\text{H}_4\text{NH}_3^+/2\text{-ClC}_6\text{H}_4\text{NH}_2$	2.66[255]	-0.3	3.2
$\text{C}_6\text{H}_5\text{NH}_2\text{CH}_3^+/\text{C}_6\text{H}_5\text{NHCH}_3$	4.85[255]	3.2	5.1
$\text{C}_6\text{H}_5\text{NH}_3^+/\text{C}_6\text{H}_5\text{NH}_2$	4.87[255]	4.5	5.9
$\text{HONH}_3^+/\text{HONH}_2$	5.96[256]	3.5	5.3
$\text{H}_2\text{N-NH}_3^+/\text{H}_2\text{N-NH}_2$	8.10[257]	10.0	8.9
$\text{NH}_4^+/\text{NH}_3$	9.21[252]	10.7	9.2
$\text{CH}_3\text{NH}_3^+/\text{CH}_3\text{NH}_2$	10.62[252]	12.1	10.0
$(\text{CH}_3)_2\text{NH}_2^+/(\text{CH}_3)_2\text{NH}$	10.77[253]	12.3	10.1
$(\text{CH}_3)_3\text{NH}^+/(\text{CH}_3)_3\text{N}$	9.76[254]	12.1	10.0
$\text{ClNH}_3^+/\text{ClNH}_2$	1.44[43]	-3.4	1.5
$\text{ClCH}_3\text{NH}_2^+/\text{ClCH}_3\text{NH}$	1.55[43]	-2.0	2.3
Prediction set			
$\text{Cl}_2\text{NH}_2^+/\text{Cl}_2\text{NH}$		-17.2	-6.0
$\text{BrClNH}_2^+/\text{BrClNH}$		-19.3	-7.1
$\text{Cl}_2\text{CH}_3\text{NH}^+/\text{Cl}_2\text{CH}_3\text{N}$		-15.4	-5.0
$\text{BrClCH}_3\text{NH}^+/\text{BrClCH}_3\text{N}$		-16.24	-5.4
$\text{BrNH}_3^+/\text{BrNH}_2$		-4.8	0.8
$\text{Br}_2\text{NH}_2^+/\text{Br}_2\text{NH}$		-20.6	-7.8
$\text{BrCH}_3\text{NH}_2^+/\text{BrCH}_3\text{NH}$		-3.9	1.3
$\text{Br}_2\text{CH}_3\text{NH}^+/\text{Br}_2\text{CH}_3\text{N}$		-17.1	-5.9

^aEach experimental value is provided with the appropriate reference. ^bComputed according to equation 3.5 in the main text. ^cThe quantum chemical LFER pK_a values are estimated using equation 3.11 in the main text.

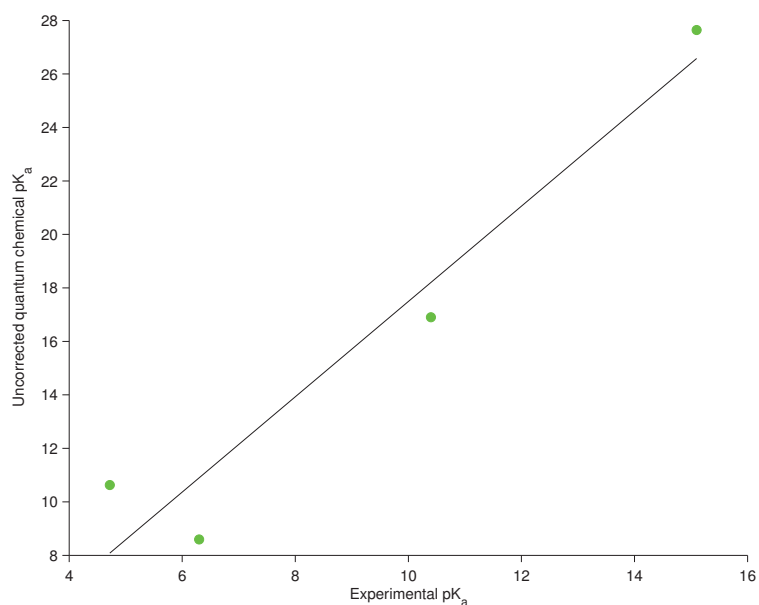


Fig. A.1 Correlation between the experimental pK_a values and the uncorrected quantum chemical $pK_a^{uncorrected}$ results for hydrazoic acid, sulfamide, acetamide, and trifluoromethanesulfamide (Table A.8).

Table A.8 Experimental pK_a data and quantum chemical LFER pK_a estimates for the amine functional group.

	Experimental pK_a value ^a	Uncorrected quantum chemical pK_a value ^b	Quantum Chemical LFER pK_a estimate ^c
Calibration set			
$CF_3-SO_2-NH_2/CF_3-SO_2-NH^-$	6.30[259]	8.6	5.0
$H_2N-SO_2-NH_2/H_2N-SO_2-NH^-$	10.40[260]	16.9	9.7
$CH_3-CO-NH_2/CH_3-CO-NH^-$	15.1[259]	27.6	15.7
$NNNH/NNN^-$	4.72[259]	10.6	6.1
Prediction set			
$ClNH_2/ClNH^-$		34.7	19.7
Cl_2NH/Cl_2N^-		20.7	11.8
$BrClNH/BrClN^-$		21.9	12.5
$BrNH_2/BrNH^-$		43.7	24.7
Br_2NH/Br_2N^-		34.7	19.6

^aEach experimental values is provided with the appropriate reference. ^bComputed according to equation 3.5 in the main text. ^cThe quantum chemical LFER pK_a values are estimated using equation A.13.

A.1.3 Molecular Mechanism of NDMA Formation from *N,N*-Dimethylsulfamide During Ozonation: Quantum Chemical Insights into a Bromide-Catalyzed Pathway

- SUPPORTING INFORMATION

A.1.3.1 Standard State Terms Entering the $\Delta G_{aq,rxn}$ Calculation by eq 4.1. Following previous conventions,[223] here we consider that the free energies of gas phase species are given in the 1 atm gaseous standard state, denoted “*o*”, free energies of aqueous species are given in the “infinitely dilute”(i.e., not self-interacting) 1 M aqueous standard state, denoted “***”, and water is given in the pure liquid 55.56 M standard state, denoted “*l*”.

The Gibbs free energy of solvation, $\Delta G_{solv}^*(A_i)$, is defined as the free energy of transferring of a mole of A_i from the gas phase into aqueous solution, at infinitely dilute 1 M concentrations in both phases:

$$\begin{aligned}\Delta G_{solv}^*(A_i) &= G_{aq}^*(A_i) - G_{gas}^*(A_i) \\ &= G_{aq}^*(A_i) - (G_{gas}^o(A_i) + \Delta G^{o \rightarrow *})\end{aligned}\tag{A.14}$$

where $\Delta G^{o \rightarrow *}$ corresponds to the free energy change of compressing 1 mol of an ideal gas from 1 atm (0.04087 M) to 1 M at 298 K, or $-RT \ln(0.04087/1) = 1.89 \text{ kcal mol}^{-1}$. [426] The gas phase free energy at 1 M concentration, $G_{gas}^*(A_i)$, is obtained from the gas phase free energy at 1 atm, $G_{gas}^o(A_i)$, according to the relation $G_{gas}^*(A_i) = G_{gas}^o(A_i) + \Delta G^{o \rightarrow *}$. For any reaction in aqueous phase, we can therefore write:

$$\begin{aligned}\Delta G_{aq,rxn}^* &= \sum_i \nu_i G_{aq}^*(A_i) \\ &= \sum_i \nu_i (G_{gas}^*(A_i) + \Delta G_{solv}^*(A_i))\end{aligned}\tag{A.15}$$

where ν_i is the stoichiometric coefficient of species A_i for the reaction step of interest.

Accordingly, for the reaction steps *f* and *j*, equation 4.1 would be written as:

$$\begin{aligned}\Delta G_{aq,rxn}^* &= \sum_i \nu_i (E_{gas,elec}(A_i) + G_{gas,therm}^o(A_i) \\ &\quad + \Delta G_{solv}^*(A_i) + \Delta G^{o \rightarrow *})\end{aligned}\tag{A.16}$$

where $G_{gas}^*(A_i) = E_{gas,elec}(A_i) + G_{gas,therm}^o(A_i) + \Delta G^{o \rightarrow *}$ and where $\Delta G_{solv}^*(A_i) = \Delta G_{SMD}^*(A_i)$. In practice, the term $\Delta G_{SMD}^*(A_i)$ is given by the energy difference of two single point calculations of the static solute: one with the SMD model and one without. The term $\sum_i \nu_i (\Delta G^{o \rightarrow *})$ corresponds to the $\Delta G_{standard\ state}$ contribution to free energy of reaction, and thus eq A.16 can be written as:

$$\begin{aligned}\Delta G_{aq,rxn}^* &= \sum_i \nu_i (E_{gas,elec}(A_i) + G_{gas,therm}^o(A_i) \\ &\quad + \Delta G_{SMD}^*(A_i) + \Delta G_{standard\ state})\end{aligned}\tag{A.17}$$

The $\Delta G_{aq,rxn}^*$ value provided by eq A.17 thus gives an equilibrium constant that is in the 1 M

aqueous standard state. For reaction steps *b* and *c*, which both generate H_2O as a product of the reaction, the free energy term of the generated water molecule is exceptionally converted to the pure liquid (55.56 M) standard state:

$$G_{H_2O}^l = E_{gas,elec}(H_2O) + G_{gas,therm}^o(H_2O) + \Delta G_{SMD}^*(H_2O) + \Delta G^{o \rightarrow *} + \Delta G^{* \rightarrow l} \quad (A.18)$$

where $\Delta G^{o \rightarrow *} + \Delta G^{* \rightarrow l}$ accounts for compressing a 1 atm (0.04087 M) ideal gas into 55.56 M liquid water at 298 K, or $-RT \ln(0.04087/55.56) = 4.27 \text{ kcal mol}^{-1}$. Thus, for reaction steps *b* and *c*, $\Delta G_{aq,rxn}^*$ is still provided by eq A.17 for non- H_2O solutes, but the free energy term for the H_2O solute, G_{H_2O} , is substituted by eq A.18. This gives an equilibrium constant in which the non- H_2O species are in the 1 M aqueous standard state and H_2O is in the pure liquid standard state. For these cases, the $\Delta G_{standard\ state}$ contribution also includes the $\Delta G^{* \rightarrow l}$ term.

A.1.3.2 Application of the Cluster-continuum Solvation Approach for $\Delta G_{aq,rxn}^*$ Calculations According to eq 4.2. For quantum chemistry simulation of ions in aqueous solution, specific solute-solvent interactions in the first solvation shell are typically quite important. Implicit solvent models are known to have difficulty capturing this effect. Bryantsev, Diallo, and Goddard have shown that a combined “cluster-continuum” solvation approach can lead to an improved description of equilibrium aqueous solvation free energies of ions.[224] According to the cluster-continuum method, the molecule of interest is treated as a geometry-optimized “cluster” of the solute together with a limited number of explicitly modeled water molecules. This cluster is further embedded in an implicit continuum dielectric field, taken to model the extant solvent. The previous work of Bryantsev et al.[224] explains how to obtain the Gibbs free energy of solvation for a molecule of interest (specifically, for ions), based on cluster-continuum calculations.

In the following section, we show how the cluster-continuum framework is extended to reactions. First we derive the expression for an intramolecular reaction (reaction step *k*), which is the simplest case. Then we evaluate the cases of step *o* and *p*, in which the solute dissociates into two product molecules, but the water cluster does not dissociate. Finally we consider a dissociation reaction (steps *l*, *m*), where the modeled water cluster itself becomes dissociated. The consequences of the cluster dissociation must be considered carefully in order obtain the correctly computed free energy of reaction in solution ($\Delta G_{aq,rxn}^*$) and also the correctly computed change in solvation free energy of the reaction ($\Delta \Delta G_{solv,rxn}^* = \Delta G_{aq,rxn}^* - \Delta G_{gas,rxn}^*$), according to the cluster-continuum framework. For ease of comparisons with the previous work, we adopt notation similar to that used by Bryantsev et al.[224]

According to the cluster-continuum framework presented by Bryantsev et al.,[224] the Gibbs

Appendix A

free energy of solvation of molecule A may be computed by:

$$\Delta G_{solv}^*(A) = \Delta G_{gas,bind,x}^{o,II}(A) + \Delta G_{SMD}^*(A(H_2O)_x) - \Delta G_{SMD}^*((H_2O)_x) - \Delta G^{o \rightarrow *} - RT \ln \left(\frac{[H_2O]}{x} \right) \quad (A.19)$$

where $\Delta G_{solv}^*(A)$ is the free energy of solvation based on the infinitely dilute 1 M standard state. The term $\Delta G_{gas,bind,x}^{o,II}(A)$ is the free energy of binding between the gas phase molecule A and the gas phase cluster of water molecules, $(H_2O)_x$, following “cluster cycle II” in that paper:

$$\Delta G_{gas,bind,x}^{o,II}(A) = G_{gas}^o(A(H_2O)_x) - G_{gas}^o((H_2O)_x) - G_{gas}^o(A) \quad (A.20)$$

In eqs A.19 and A.20, the lone species (A) indicates the unclustered molecule of interest, the species $A(H_2O)_x$ indicates a cluster of molecule A together with x explicit water molecules, and $[H_2O]$ represents the molar concentration of liquid water, 55.56 M. In eq A.19, the terms $\Delta G_{SMD}^*(A(H_2O)_x)$ and $\Delta G_{SMD}^*((H_2O)_x)$ represent the free energies required to bring the clusters $A(H_2O)_x$ and $(H_2O)_x$ from gas phase into aqueous phase, as evaluated by the implicit solvent model (SMD, in the present work). We refer the reader to the previous paper[224] for complete explanation on the origins of the above equations.

First we evaluate $\Delta G_{aq,rxn}^*$ for an intramolecular rearrangement, which illustrates the cluster-continuum approach used for step k (Figure 4.1). Consider a reactant molecule A that is converted into product molecule P:

$$\Delta G_{aq,rxn}^* = G_{aq}^*(P) - G_{aq}^*(A) \quad (A.21)$$

Following eqs A.14 and A.15, eq A.21 can be re-written in terms of free energies of the gas phase species, G_{gas}^* , plus the aqueous solvation free energy, ΔG_{solv}^* , of each species:

$$\Delta G_{aq,rxn}^* = G_{gas}^o(P) + \Delta G^{o \rightarrow *} + \Delta G_{solv}^*(P) - G_{gas}^o(A) - \Delta G^{o \rightarrow *} - \Delta G_{solv}^*(A) \quad (A.22)$$

It is worth noticing that in eq A.22 the $\Delta G_{standard\ state} = \sum_i \nu_i (\Delta G^{o \rightarrow *})$ term cancels to zero. Upon substituting eqs A.19 and A.20 for the ΔG_{solv}^* terms in eq A.22, several terms cancel to zero, and we arrive at:

$$\Delta G_{aq,rxn}^* = G_{gas}^o(P(H_2O)_x) + \Delta G_{solv}^*(P(H_2O)_x) - G_{gas}^o(A(H_2O)_x) - \Delta G_{solv}^*(A(H_2O)_x) \quad (A.23)$$

where x corresponds to the number of explicit water molecules associated with the cluster containing each solute. By recognizing that $G_{gas}^o = E_{gas,elec} + G_{gas,therm}^o$, eq A.23 can be

re-written as:

$$\begin{aligned}\Delta G_{aq,rxn}^* &= E_{gas,elec}(P(H_2O)_x) - E_{gas,elec}(A(H_2O)_x) \\ &\quad + G_{gas,therm}^o(P(H_2O)_x) - G_{gas,therm}^o(A(H_2O)_x) \\ &\quad + \Delta G_{solv}^*(P(H_2O)_x) - \Delta G_{solv}^*(A(H_2O)_x)\end{aligned}\quad (A.24)$$

Eq A.24 is equivalent to eq 4.2 in the main text, where the $\Delta G_{standard\ state}$ term and $\Delta G_{cluster\ correction}$ term of eq 4.2 are both zero. Eq A.24 eliminates the need to consider the unclustered gas phase product and reactant molecules. In other words, the reaction thermochemistry can be evaluated entirely by way of solvated clusters.

Eq A.24 was applied to reaction step k . For the dissociation reaction steps g , o , and p , we also used eq A.24, because in these cases the water cluster remains associated with a product fragment and does not break apart. However due to the fact that two product molecules are formed from the reaction steps g , o , and p , we had also to take into account an additional standard-state factor $\Delta G^{o \rightarrow *}$.

Next we consider $\Delta G_{aq,rxn}^*$ for a reaction in which the cluster dissociates, which illustrates the cluster-continuum approach used for step m (Figure 4.1). In this case, reactant molecule A is converted into the product molecules P_1 and P_2 :

$$\Delta G_{aq,rxn}^* = G_{aq}^*(P_1) + G_{aq}^*(P_2) - G_{aq}^*(A) \quad (A.25)$$

We anticipate that the aqueously solvated species P_1 , P_2 , and A can be modeled as the clusters $P_1(H_2O)_y$, $P_2(H_2O)_z$, and $A(H_2O)_x$, where y is the number of explicit water molecules associated with the cluster containing P_1 , z is the number of explicit water molecules in the cluster containing P_2 , and x is the number of explicit water molecules in the cluster containing A. In order to maintain a balanced reaction, $x = z + y$.

Now, if we follow manipulations analogous to eqs A.21-A.24 above, fewer beneficent cancellations occur, and we find the expression:

$$\begin{aligned}\Delta G_{aq,rxn}^* &= (E_{gas,elec}(P_1(H_2O)_y) + E_{gas,elec}(P_2(H_2O)_z) - E_{gas,elec}(A(H_2O)_x)) \\ &\quad + (G_{gas,therm}^o(P_1(H_2O)_y) + G_{gas,therm}^o(P_2(H_2O)_z) - G_{gas,therm}^o(A(H_2O)_x)) \\ &\quad + (\Delta G_{solv}^*(P_1(H_2O)_y) + \Delta G_{solv}^*(P_2(H_2O)_z) - \Delta G_{solv}^*(A(H_2O)_x)) \\ &\quad + \Delta G_{cluster\ correction}\end{aligned}\quad (A.26)$$

Appendix A

where:

$$\begin{aligned}\Delta G_{cluster\ correction} = & - \left(E_{gas,elec}((H_2O)_y) + E_{gas,elec}((H_2O)_z) - E_{gas,elec}((H_2O)_x) \right) \\ & - \left(G_{gas,therm}^o((H_2O)_y) + G_{gas,therm}^o((H_2O)_z) - G_{gas,therm}^o((H_2O)_x) \right) \\ & - \left(\Delta G_{solv}^*((H_2O)_y) + \Delta G_{solv}^*((H_2O)_z) - \Delta G_{solv}^*((H_2O)_x) \right) \\ & - RT \ln \left(\frac{x[H_2O]}{yz} \right)\end{aligned}\tag{A.27}$$

Eq A.26 is equivalent to eq 4.2 in the main text, where $\Delta G_{cluster\ correction}$ is given by eq A.27, and the $\Delta G_{standard\ state}$ term (not shown) has canceled to zero.

Eq A.26 is a convenient way to represent $\Delta G_{aq,rxn}^*$, because each major term is an intuitive result of straightforward simulations:

- The first three terms (first three lines of eq A.26) are obtained by electronic, vibrational, and implicit solvent model calculations of the solvated clusters $P_1(H_2O)_y$, $P_2(H_2O)_z$, and $A(H_2O)_x$.
- The $\Delta G_{cluster\ correction}$ term (eq A.27) is a less intuitive contribution that arises purely from the construction of the cluster-continuum framework. Collectively, the first three lines represent the free energy cost of dissociating the $(H_2O)_x$ water cluster into the two sub-clusters, $(H_2O)_y$ and $(H_2O)_z$, all embedded in implicit solvent. This must be computed based on individually geometry-optimized water clusters having number x , z , and y . Conceptually, this term is viewed as a correction for the artifactual decrease in the number of inter-molecular contacts that result from the dissociation of the $A(H_2O)_x$ cluster into the two product clusters. Lastly, the term $-RT \ln \left(\frac{x[H_2O]}{yz} \right)$ comes from the standard state conversion of the water clusters into 55.56 M liquid water.[224]
- Eqs A.26 and A.27 eliminate the need to consider the unclustered gas phase product and reactant molecules. In other words, the reaction thermochemistry can be evaluated entirely by way of solvated clusters.

The magnitude of the $\Delta G_{cluster\ correction}$ term was 2.35 kcal mol⁻¹ for the dissociation reaction m , according to eq A.27. For this reaction, the explicit water clusters had populations of $x = 5$, $z = 3$, and $y = 2$. Geometries of the water clusters $(H_2O)_5$, $(H_2O)_3$, and $(H_2O)_2$ were optimized based on initial guess structures taken from Day et al.[427]

Finally, three product molecules were formed by the decomposition reaction l , but only two product species (Br^- and SO_2) were associated with water clusters. In this particular case, the $\Delta G_{aq,rxn}^*$ also contained the term $G_{aq}^*(P_3)$:

$$\Delta G_{aq,rxn}^* = G_{aq}^*(P_1) + G_{aq}^*(P_2) + G_{aq}^*(P_3) - G_{aq}^*(A)\tag{A.28}$$

For the dissociation reaction l , we combined eqs A.24 and A.28 as follows:

$$\begin{aligned}\Delta G_{aq,rxn}^* &= (E_{gas,elec}(P_1(H_2O)_y) + E_{gas,elec}(P_2(H_2O)_z) - E_{gas,elec}(A(H_2O)_x)) \\ &+ (G_{gas,therm}^o(P_1(H_2O)_y) + G_{gas,therm}^o(P_2(H_2O)_z) - G_{gas,therm}^o(A(H_2O)_x)) \\ &+ (\Delta G_{solv}^*(P_1(H_2O)_y) + \Delta G_{solv}^*(P_2(H_2O)_z) - \Delta G_{solv}^*(A(H_2O)_x)) \\ &+ (E_{gas,elec}(P_3) + G_{gas,therm}^o(P_3) + \Delta G^{o \rightarrow *} + \Delta G_{solv}^*(P_3)) \\ &+ \Delta G_{cluster\ correction}\end{aligned}\quad (A.29)$$

where the $\Delta G_{cluster\ correction}$ is given by eq A.27.

A.1.3.3 Standard State Contributions to $\Delta G_{aq,rxn}^\ddagger$ According to eq 4.4. For the reaction steps f and j , we compute the free energies of activation by applying equation 4.4:

$$\begin{aligned}\Delta G_{aq,rxn}^\ddagger &= E_{gas,elec}^\ddagger(TS) + G_{gas,therm}^\ddagger(TS) + \Delta G_{SMD}^\ddagger(TS) - \sum_i (E_{gas,elec}(R_i) \\ &+ G_{gas,therm}(R_i) + \Delta G_{SMD}(R_i)) + \Delta G_{standard\ state}\end{aligned}\quad (A.30)$$

where, R_i are the reactant species, TS is the transition state structure, and the contribution to free energy of activation is defined as $\sum_i \nu_i (\Delta G^{o \rightarrow *})$ as for eq A.17. Finally, for reaction steps b and g , a cluster of water molecules was included in the simulations of both the reactant and the transition structure. For reaction b , the $\Delta G_{aq,rxn}^\ddagger$ was defined in a similar way as eq A.24:

$$\begin{aligned}\Delta G_{aq,rxn}^\ddagger &= E_{gas,elec}^\ddagger(TS(H_2O)_x) - E_{gas,elec}(R_1(H_2O)_x) \\ &+ G_{gas,therm}^\ddagger(TS(H_2O)_x) - G_{gas,therm}^o(R_1(H_2O)_x) \\ &+ \Delta G_{solv}^\ddagger(TS(H_2O)_x) - \Delta G_{solv}^*(R_1(H_2O)_x) \\ &- (E_{gas,elec}(R_2) + G_{gas,therm}^o(R_2) + \Delta G^{o \rightarrow *} + \Delta G_{solv}^*(R_2))\end{aligned}\quad (A.31)$$

The cluster of water does not dissociate in going from reactants to the transition state. For reaction step b , since there are two reactants and one transition state species, the $\Delta G_{standard\ state}$ term is $-\Delta G^{o \rightarrow *}$.

Reaction step g has one reactant, and the $\Delta G_{aq,rxn}^\ddagger$ was defined as follows:

$$\begin{aligned}\Delta G_{aq,rxn}^\ddagger &= E_{gas,elec}^\ddagger(TS(H_2O)_x) - E_{gas,elec}(R_1(H_2O)_x) \\ &+ G_{gas,therm}^\ddagger(TS(H_2O)_x) - G_{gas,therm}^o(R_1(H_2O)_x) \\ &+ \Delta G_{solv}^\ddagger(TS(H_2O)_x) - \Delta G_{solv}^*(R_1(H_2O)_x)\end{aligned}\quad (A.32)$$

For step g , the $\Delta G_{standard\ state}$ term is canceled out.

A.1.3.4 Description of Minimum Energy Pathway Calculation (Relaxed Scan). A relaxed scan describes the profile of the system electronic energy at several selected values of a chosen reaction coordinate. We used either the interatomic distance (bond length) or the angle

Appendix A

between three bonded atoms as the reaction coordinate, depending on the reaction step. At each selected value of the reaction coordinate, a partially constrained geometry optimization of the system was conducted, maintaining a fixed value of the reaction coordinate while the remainder of the molecular system geometry is relaxed to an energy minimum. The resulting energy profile describes the minimum energy pathway along the reaction coordinate. M05 us the model chemistry employed to perform relaxed scan computations, for $\Delta E_{gas,elec}^\ddagger$. The aug-cc-pVTZ basis set was used throughout.

A.1.3.5 Free Energy of the Proton in Aqueous Phase. The free energy of the proton in gas phase was assigned a value of $G(H^+)_{gas} = -6.28 \text{ kcal mol}^{-1}$. [248] This was converted from 1 atm to the 1 M standard state at 298 K by adding $\Delta G^{o \rightarrow *} = 1.89 \text{ kcal mol}^{-1}$. To this we added the free energy of solvation of the proton, $G(H^+)_{solv} = -263.12 \text{ kcal mol}^{-1}$. [425] The resulting value of $-267.51 \text{ kcal mol}^{-1}$ was employed for $G(H^+)_{aq}$ in the 1 M aqueous standard state and was used for computations of free energy of aqueous deprotonation reaction in eq 4.7. However the value for $G(H^+)_{aq}$ is cancelled out in the LFER used to estimate pK_a .

A.1.3.6 Considerations on the validity of the quantum chemical modeling approach for aqueous reaction chemistry.

Table A.9 Previously reported and computed rate constant values for the reactions of HOBr with NH_3 , HOBr with $\text{NH}(\text{CH}_3)_2$, and ozone with bromide.

Reaction	Computed $k \text{ (M}^{-1} \text{ s}^{-1})$	Experimental $k \text{ (M}^{-1} \text{ s}^{-1})$
$\text{HOBr} + \text{NH}_3$	$10^{5 \pm 2.5}$	7.5×10^7 Ref.[180]
$\text{HOBr} + \text{NH}(\text{CH}_3)_2$	$10^{9 \pm 2.5}$	3.0×10^9 Ref.[180]
$\text{O}_3 + \text{Br}^-$	$10^{4 \pm 2.5}$	2.58×10^2 Ref.[316]

Comparison of theoretical and experimental reaction rate constants for selected reactions. The theoretical rate constants for these three reactions were in agreement with the experimental estimates, to within expected errors of the modeling approach. This provides validation for the theoretical method applied to the related reactions *b* and *j*. To further evaluate the appropriateness of our modeling approach, we also applied several other electronic structure methods to the free energy of reaction for step *b* (Table A.12). The results obtained using other methods for geometry optimizations (B2PLYP, B2PLYPD, MP2, M06-L) are consistent with the values obtained with M05 geometries. Additionally, the reliable CCSD(T) wavefunction method confirms our energy results obtained by B2PLYPD. Finally, $\Delta G_{aq,rxn}^*$ results obtained with three explicit molecules of water are consistent with results obtained without explicit molecules of water. This suggests that the implicit solvent model (SMD) sufficiently accounts for the influence of directed solute-solvent interactions on the thermochemistry of this reaction.

In this study, we chose to optimize all geometries in gas phase. Geometry optimization and the vibrational analysis using implicit solvent models are often difficult to converge,[204] especially for transition state structures. For some reaction steps, we assumed that the solvent does not substantially affect the geometries of the involved species and the molecular mechanism. In those cases where the solvent is suspected to be directly involved in the reaction, we introduced explicitly modeled water molecules into the gas phase geometry optimizations.

Tarade et al.[219] used a similar approach to study the chlorination mechanism of organic amines by HOCl. In that work, structures were optimized in gas phase, and explicit molecules of water were included in the calculations of the transition structures. Implicit solvent calculations were then carried out on the gas phase micro-solvated clusters. Free energies of activation were computed with the B2PLYPD model chemistry. Tarade et al. also compared geometry optimizations and frequencies performed with an implicit solvent model to those obtained in gas phase. Use of the implicit solvent model was found to lead to very small changes in the geometries of the reactants and transition state structures. Thus the Tarade et al. study supports the assumption that gas phase geometries of microsolvated clusters were sufficient to describe transition state structures of the chlorination of amines by HOCl.

A.1.3.7 Quantum chemical modeling of the activation free energy of reaction step g.

The reaction free energy of activation of step g was modeled with one explicit water molecule hydrogen-bonded to the electron-deficient proton of the *NHBr* fragment of *Br – DMS*. This explicit solvent cluster arrangement is justified as follows. According to NPA charge analysis, the transition state structure of reaction step g is characterized by two negatively-charged nitrogen atoms and a net neutral SO_2 leaving group. In this reaction mechanism, a bond between the two geminal nitrogen atoms can be formed by cleaving the SO_2 fragment. The extrusion of SO_2 group can only take place if the SO_2 group would gain electron density from the molecule. Thus, by associating one explicit molecule of water that can donate electron density to the proton of the *NHBr* fragment, the overall transition state structure is stabilized. We expect that specific interactions with the solvent would further stabilize the transition state only by way of increased transfer of electron density that would help to liberate the electron-deficient SO_2 group. However, aside from the proton of the *NHBr* fragment, no other hydrogen-bond donor groups are available on the molecule to accept electron density from solvent. Thus, the addition of more explicit water molecules is considered unlikely to influence substantially the reaction barrier.

A.1.3.8 Reaction Steps a, b, c, and d in the Presence of HOCl. Chlorination Rates of DMS versus DMS^- and Speciation Equilibria of $Cl – DMS/Cl – DMS^-$. Previous experimental work demonstrated that *N,N*-dimethylsulfide forms NDMA in the presence of HOCl and O_3 , absent bromide.[288] This suggests that a rapid chlorination of *N,N*-dimethylsulfamide takes place, forming $Cl-DMS/Cl-DM^-$ (Figure 4.1, reactions *a-d*), analogous to the mechanism involving HOBr discussed in the main text. We did not conduct

stopped-flow kinetic experiments with HOCl. Rate constants for halogenation by HOBr typically exceed those of HOCl by 2 to 3 orders of magnitude, for organic compounds.[4] By analogy to our results with HOBr, chlorination of DMS^- by HOCl (reaction pathway *c*) is expected to predominate over pathway *b*. The resulting Cl–DMS anion would become partly protonated at neutral pH, since the conjugate acid Cl–DMS has an estimated pK_a of 7.9 based on quantum chemical computations (main text). Based on these considerations, the expected predominating pathway for chlorination of *N,N*-dimethylsulfamide (steps *a*, *c*) parallels that of the bromination pathway.

A.1.3.9 Reactions of Intermediates B, C, D, and F in the $\text{O}_3 + \text{HOCl}$ System. When substituted with chlorine ($X = \text{Cl}$) instead of bromine, structure B undergoes a similar reaction branching, according to quantum chemical calculations. Again using the elongated N-S bond as a reaction coordinate, the chlorinated $B(\text{H}_2\text{O})_5$ complex is found to have a low activation free energy of $2.5 \text{ kcal mol}^{-1}$ for reaction step *o*, indicating that the corresponding reaction rate is very fast ($k_o \sim 10^{11 \pm 1.5} \text{ s}^{-1}$). However, unlike the situation with bromine, the chlorinated $B(\text{H}_2\text{O})_5$ complex also experiences an apparently low activation free energy of $3.6 \text{ kcal mol}^{-1}$ for the departure of the halide ion (reaction *m*) to produce intermediate F, corresponding to a near-thermally-controlled reaction rate ($k_m \sim 10^{10 \pm 2.5} \text{ s}^{-1}$). Intermediate F leads to the instantaneous formation of NDMA, as discussed below. Finally, based on relaxed scan calculations of the N-S-N angle, the chlorinated $B(\text{H}_2\text{O})_5$ complex encounters a low free energy of activation of $4.2 \text{ kcal mol}^{-1}$ for the intramolecular rearrangement reaction *k*, indicating a reaction of $k_k \sim 10^{10 \pm 2.5} \text{ s}^{-1}$. This leads immediately to formation of NDMA. Step *k* is analogous to *ClNO* reaction with dimethylamine, which produces NDMA.[428] Thus the three reaction steps *o*, *m*, and *k* all exhibit very low reaction activation free energies, corresponding to fast first order reaction rates. Analysis of reaction thermodynamics indicates that the three pathways (*o*, *m*, and *k*) are near-neutral or favorable. Reactions *o* and *m* are approximately neutral, with $\Delta G_{aq,rxn}^*$ values of -1.4 and $2.1 \text{ kcal mol}^{-1}$, respectively. Reaction *k* is thermodynamically favorable, with estimated $\Delta G_{aq,rxn}^* = -4.0 \text{ kcal mol}^{-1}$. However these decomposition reactions are interpreted as irreversible at the dilute concentrations of the products. Hence the back-reactions are considered unimportant. In summary, O_3 reacts very rapidly with $\text{Cl} - \text{DMS}^-$ to form chlorinated intermediate B, which can readily decompose either via pathways that forms NDMA (steps *m*, *k*) or a pathway that does not form NDMA (step *o*). Analogous to the bromine-containing system, we are unable to resolve the differences in the rates of these three reaction branches, within the accuracy of the methods applied here. Thus we remain unable to explain the differences in yield of NDMA from DMS that have been observed previously in the O_3 +bromide system versus the $\text{O}_3 + \text{HOCl}$ system. However our analysis demonstrates a fast pathway for NDMA formation from *N,N*-dimethylsulfamide in the presence of O_3 and HOCl, analogous to that in the O_3 +bromide system.

A.1.3.10 Intermediate F Leads to NDMA. Intermediate F, which is not a halogenated molecule, can rapidly form NDMA. Relaxed scan calculations were performed with the N-S-N angle as a reaction coordinate. IRC calculations confirmed that the transition state connected

the reactants and products. The resulting SO₂ extrusion activation free energy of 3.1 kcal mol⁻¹ (reaction *n*) leads to the formation of NDMA (Figure A.14). This corresponds to a very fast rate constant of $k_n \sim 10^{10 \pm 2.5} \text{ s}^{-1}$. According to calculations, the SO₂ extrusion step *n* is very fast, exothermic, thermodynamically favored ($\delta G_{aq,rxn} = -38.0 \text{ kcal mol}^{-1}$), and effectively irreversible.

A.1.3.11 Theoretical branching ratios for the decomposition of structures B and C.

Following the suggestion of a reviewer, we calculated the branching ratios for intermediates B and C, using the formula:

$$\beta_y^X = \frac{k_y}{\sum_{z=y}^n k_z} \quad (\text{A.33})$$

where β_y is the branching of reaction *y*, k_y is the rate constant of reaction *y* and $\sum_{z=y}^n k_z$ is the sum of all the other rate constants associated with the compound *X*. For structure B, the pathways *o*, *k*, and *l* were considered, whereas pathway *j* was excluded because it is irreversible. For structure C, we considered pathways *l*, *p*, and *k*.

The uncertainties of β_y were calculated as follows:

$$\beta_{y,upper\ bound}^X = \frac{k_y^{high}}{k_y^{high} + \sum_{z \neq y}^n k_z^{low}} \quad (\text{A.34})$$

$$\beta_{y,lower\ bound}^X = \frac{k_y^{low}}{k_y^{low} + \sum_{z \neq y}^n k_z^{high}} \quad (\text{A.35})$$

where k_y^{high} (k_y^{low}) is the rate constant calculated by adding (or subtracting) a factor of 3 kcal mol⁻¹ to the free energy of activation.

Table A.10 Theoretical branching ratios for the decomposition pathways of structures B and C.

Species	Reaction Step	β_y	$\beta_{y,upper\ bound}^X$	$\beta_{y,lower\ bound}^X$
B	o	0.71	0.99998	0.00009
	k	0.29	0.99990	0.00002
	m	10 ⁻⁷	0.004	10 ⁻¹¹
C	k	10 ⁻⁶	0.05	10 ⁻¹⁰
	l	1.00	0.99999996	0.04
	p	0.001	0.96	10 ⁻⁹

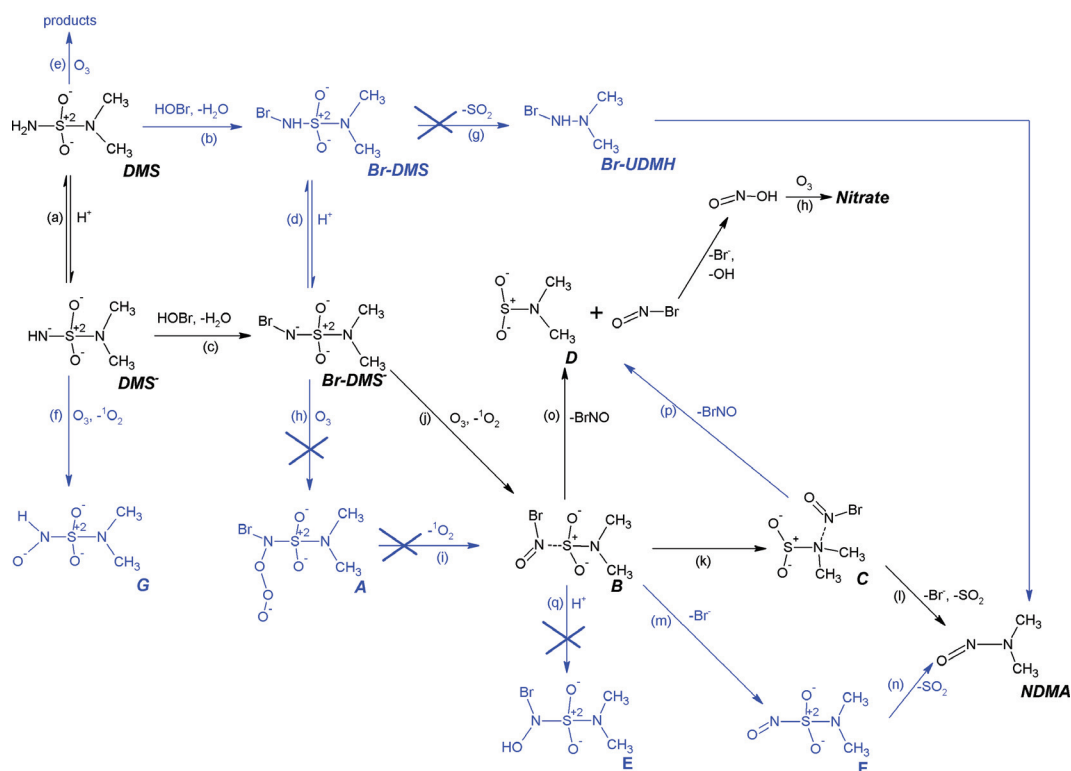


Fig. A.2 The previously proposed NDMA-formation pathway from N,N-dimethylsulfamide during ozonation of natural water.[288] The above figure is based on “Scheme 2” in that work. However for clarity we have re-labeled the elementary reaction steps and intermediate structures according to Figure 4.1 of the present study.

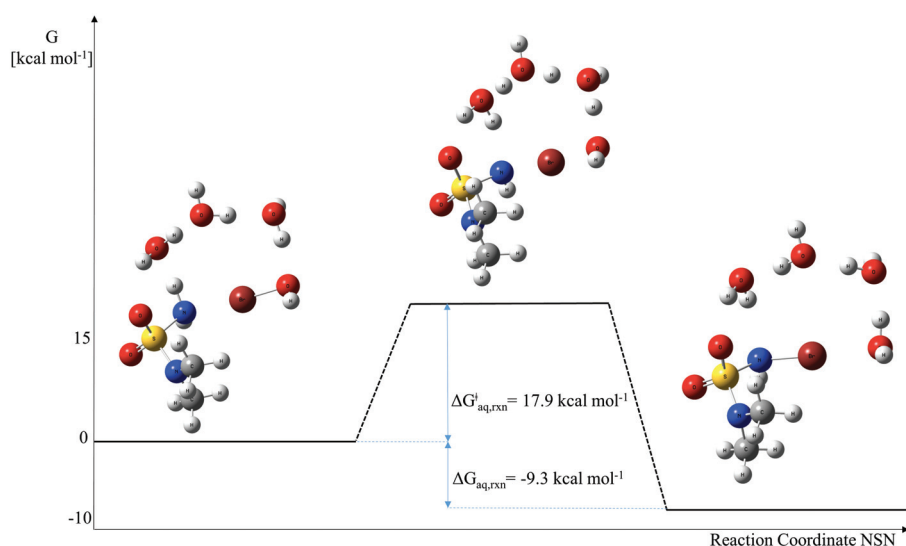


Fig. A.3 Bromination of neutral DMS by HOBr (reaction step *b*). According to quantum chemical calculations, the bromination reaction is facilitated by a proton shuttle involving three water molecules. Without the inclusion of explicit water molecules in the simulation, the computed reaction activation free energy is raised by $>40 \text{ kcal mol}^{-1}$, which would correspond to an unfeasible mechanism.

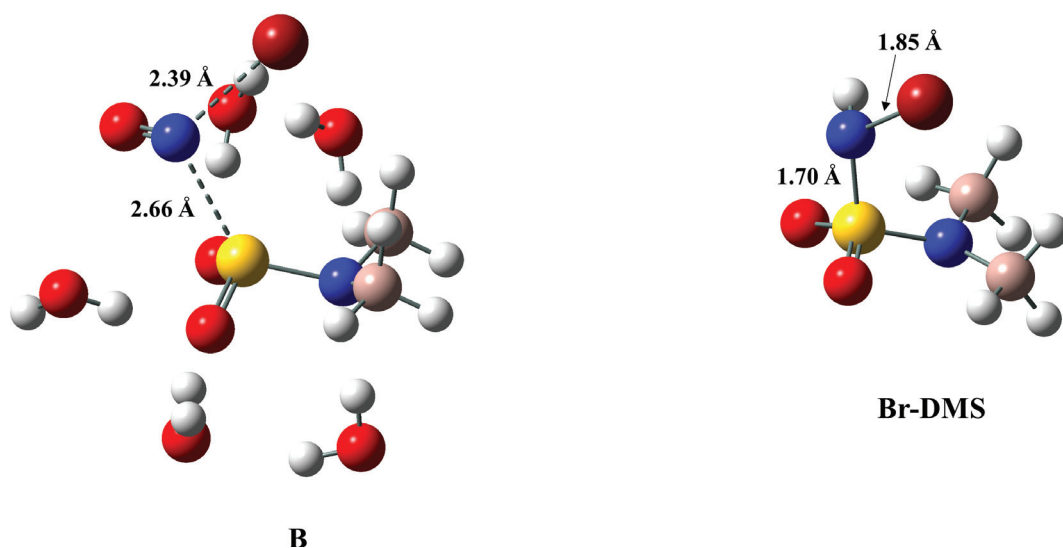


Fig. A.4 The anionic intermediate structure B (left) and Br-DMS (right), according to M05/aug-cc-pVTZ geometry optimizations in gas phase. The N-Br bond (2.39 Å) and N-S bond (2.66 Å) in structure B are both significantly elongated compared to the same bonds in Br-DMS, consistent with bond weakening. In the optimized $B(H_2O)_5$ cluster, explicit water molecules donate hydrogen-bonds to the two sulfonyl oxygen atoms, to the dimethyl-substituted N atom, and to the Br atom. This arrangement is intuitively reasonable: according to NPA calculations, these four atoms of structure B all bear substantial partial negative charge (Figure 4.2), indicative of excess electron density that is available to participate in hydrogen-bonding with the solvent.

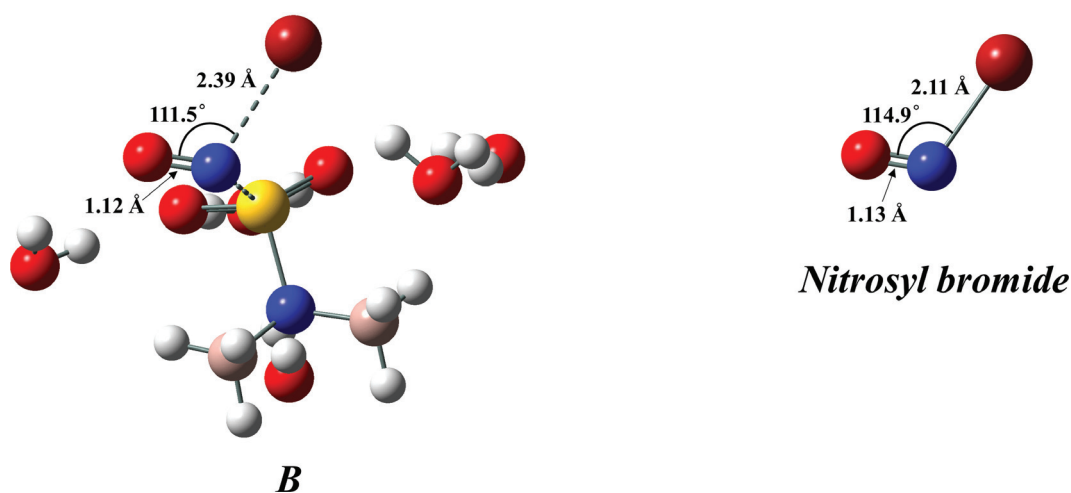


Fig. A.5 Geometric parameters of the BrNO fragment in intermediate structure B (left) are compared with those observed for nitrosyl bromide (right), based on M05/aVTZ geometry optimization in gas phase. The computed N=O bond length and Br-N=O angle in structure B are comparable to those of nitrosyl bromide. The N-Br bond of structure B is lengthened compared to nitrosyl bromide, consistent with bond weakening.

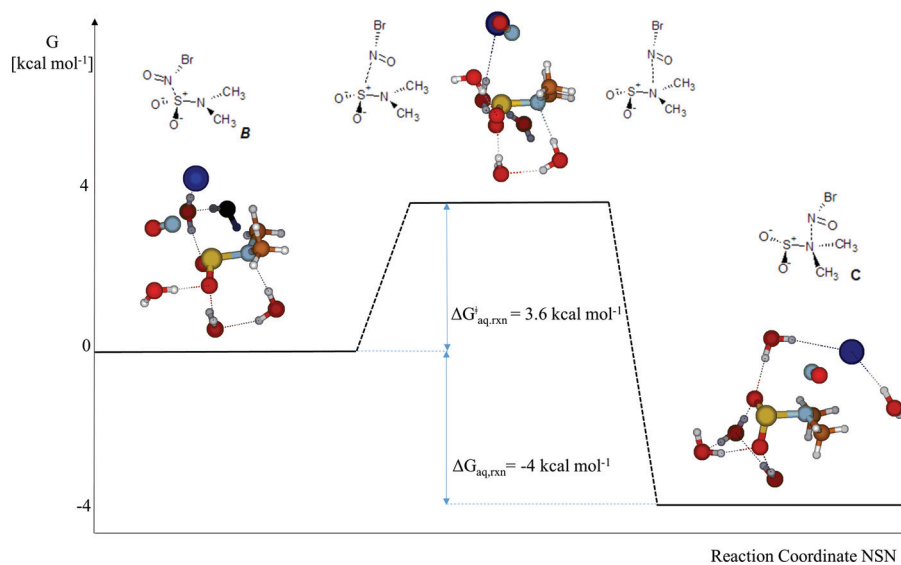


Fig. A.6 Schematic of reaction step k: the intermediate structure B (left), intermediate structure C (right), and the intervening activated structure (middle). Explicit water molecules included in the simulation are also shown. Lewis structures are proposed (top) based on NPA charge results.

Table A.11 Evaluation of M05, M06, B2PLYP, and B2PLYPD for the Error per bond in Total Atomization Energies (TAE) of O₃, NO, N₂O, HNO, SO₂, and Br₂, in kcal mol⁻¹.

Molecule	Benchmark		M05/aug-cc-pVTZ		M06/aug-cc-pVTZ		B2PLYP/aug-cc-pVTZ		B2PLYPD/aug-cc-pVTZ	
	W4 TAE ^a		TAE	Error per bond ^b	TAE	Error per bond ^b	TAE	Error per bond ^b	TAE	Error per bond ^b
O ₃	147.35		137.19	5.08	137.40	4.98	145.27	1.04	145.29	1.03
NO	152.30		149.35	2.95	148.92	3.38	153.42	-1.12	153.42	-1.12
N ₂ O	269.63		276.24	-3.30	273.87	-2.12	274.58	-2.48	274.62	-2.49
HNO	205.45		200.49	2.48	201.78	1.84	203.67	0.89	203.69	0.88
SO ₂	259.61		243.23	8.19	246.84	6.38	245.24	7.19	245.31	7.15
Br ₂	52.82		45.30	7.52	49.71	3.11	49.45	3.37	49.46	3.36
MUE per bond ^c				3.82		2.93		1.48		1.47

^aThe W4 benchmark estimate of the molecular Total Atomization Energy at 0 K was taken from Karton et al. 2006, excluding zero point vibrational energy, core-valence correlation correction, scalar relativistic correction, spin-orbit coupling, and diagonalized Born-Oppenheimer correction. ^bError per bond = $\frac{\text{Benchmark TAE} - \text{DFT TAE}}{\text{Total number of atoms} - 1}$.

^cThe mean unsigned error (MUE) is the average of the unsigned error per bond over the four molecules in the data set, in kcal mol⁻¹.

Appendix A

Table A.12 Complete List of Computed Gibbs Free Energies of Reaction ($\Delta G_{aq,rxn}$) for Elementary Steps of the NDMA Formation Pathway

Reaction ^a step ^a	Number of explicit waters included	Geometry Optimization Method ^b	$E_{gas,elec}$ Method ^c	$G_{gas,therm}$ Method ^d	ΔG_{SMD} Method ^e	Estimated Total $\Delta G_{aq,rxn}$ ($kcal\ mol^{-1}$) $X^f = Br$ $X^f = Cl$	
b	3	M05	M05	M05	SMD/M05	-0.8	-6.6
b	3	M05	B2PLYPD	M05	SMD/M05	-8.0	-11.2
b	0	B2PLYP	B2PLYP	M05	SMD/M05	-6.9	-10.0
b	0	B2PLYPD	B2PLYPD	M05	SMD/M05	-7.8	-10.6
b	0	MP2	MP2	M05	SMD/M05	-11.4	-13.9
b	0	MP2	CCSD(T)	M05	SMD/M05	-9.3	-10.7
b	0	M05	M05	M05	SMD/M05	-6.2	-12.0
b	0	M05	B2PLYPD	M05	SMD/M05	-7.8	-11.0
b	0	M06-L	M06-L	M06-L	SMD/M06-L	-7.1	-
b	0	M06-L	B2PLYPD	M06-L	SMD/M06-L	-8.6	-
c	0	M05	M05	M05	SMD/M05	-15.4	-22.3
c	0	M05	B2PLYPD	M05	SMD/M05	-17.9	-21.5
f	0	M05	M05	M05	SMD/M05	3.7	
f	0	M05	B2PLYPD	M05	SMD/M05	1.9	
g	1	M05	M05	M05	SMD/M05	-12.3	-
g	1	M05	B2PLYPD	M05	SMD/M05	-20.1	-
j	0	M05	M05	M05	SMD/M05	-27.4	-33.0
j	0	M05	B2PLYPD	M05	SMD/M05	-30.7	-34.2
k	5	M05	M05	M05	SMD/M05	0.3	0.0
k	5	M05	B2PLYPD	M05	SMD/M05	-4.0	-4.0
l	5	M05	M05	M05	SMD/M05	-36.0	-36.4
l	5	M05	B2PLYPD	M05	SMD/M05	-26.2	-31.3
m	5	M05	M05	M05	SMD/M05	-0.3	-3.7
m	5	M05	B2PLYPD	M05	SMD/M05	6.2	2.1
n	0	M05	M05	M05	SMD/M05	-34.3	
n	0	M05	B2PLYPD	M05	SMD/M05	-34.6	
o	5	M05	M05	M05	SMD/M05	-6.4	-4.0
o	5	M05	B2PLYPD	M05	SMD/M05	-2.8	-1.4
p	5	M05	M05	M05	SMD/M05	-6.6	-4.1
p	5	M05	B2PLYPD	M05	SMD/M05	1.2	2.6

^aElementary reaction step as depicted in Figure 4.1 (main text). ^bModel chemistry used to optimize the molecular geometries to energetic minima, for the purpose of computed $\Delta E_{gas,elec}$ estimates. The aug-cc-pVTZ basis set was used for all geometry optimizations. ^cModel chemistry employed to compute the electronic energy of the reaction, at fixed nuclear coordinates in gas phase. The aug-cc-pVTZ basis set was used for all computed $\Delta E_{gas,elec}$ estimates, except CCSD(T), for which an aug-cc-pV[D,T]Z basis set extrapolation was applied. ^dModel chemistry used to compute the gas phase thermal contributions (vibrations, rotations, and translation) to the Gibbs Free Energy of reaction, with a consistently optimized geometry. The aug-cc-pVTZ basis set was used for all $\Delta G_{gas,therm}$ computations. ^eSolvation model and model chemistry employed to compute the change in Gibbs Free Energy of aqueous solvation for the reaction. The aug-cc-pVTZ or cc-pVTZ basis set was used. ^fResults are shown for both the $O_3 +$ bromide-catalyzed pathway ($X = Br$) and the $O_3 + HOCl$ system pathway ($X = Cl$).

A.1. Supporting Information

Table A.13 Complete List of Computed Gibbs Free Energies of Reaction ($\Delta G_{aq,rxn}^\ddagger$) for Elementary Steps of the NDMA Formation Pathway

Reaction ^a step ^a	Number of explicit waters included	Geometry Optimization Method ^b	$\Delta E_{gas,elec}^\ddagger$ Method ^c	$\Delta G_{gas,therm}^\ddagger$ Method ^d	ΔG_{SMD}^\ddagger Method ^e	Estimated Total $\Delta G_{aq,rxn}^\ddagger$ ($kcal\ mol^{-1}$) $X^f = Br$ $X^f = Cl$	
b	3	M05	M05	M05	SMD/M05	15.6	-
b	3	M05	B2PLYPD	M05	SMD/M05	17.9	-
g	0	M05	M05	M05	SMD/M05	43.2	-
g	0	M05	B2PLYPD	M05	SMD/M05	36.4	-
g	1	M05	M05	M05	SMD/M05	39.4	-
g	1	M05	B2PLYPD	M05	SMD/M05	33.9	-
j	0	M05	M05	M05	SMD/M05	13.4	12.7
j	0	M05	B2PLYPD	M05	SMD/M05	10.6	10.5
k	5	M05	M05	-	SMD/M05	2.0	3.70
k	5	M05	B2PLYPD	-	SMD/M05	3.6	4.2
l	5	M05	M05	-	SMD/M05	<1.0	<1.0
m	5	M05	M05	-	SMD/M05	6.3	0.2
m	5	M05	B2PLYPD	-	SMD/M05	12.2	3.6
n	0	M05	M05	M05	SMD/M05	10.0	
n	0	M05	B2PLYPD	M05	SMD/M05	3.1	
o	5	M05	M05	-	SMD/M05	2.6	2.3
o	5	M05	B2PLYPD	-	SMD/M05	3.0	2.5
p	5	M05	M05	-	SMD/M05	1.4	5.4
p	5	M05	B2PLYPD	-	SMD/M05	5.1	11.4

^aElementary reaction step as depicted in Figure 4.1 (main text). ^bModel chemistry used to optimize the molecular geometries to energetic minima, for the purpose of computed $\Delta E_{gas,elec}^\ddagger$ estimates. The aug-cc-pVTZ basis set was used for all geometry optimizations. ^cModel chemistry employed to compute the electronic energy of the reaction, at fixed nuclear coordinates in gas phase. The aug-cc-pVTZ basis set was used for all computed $\Delta E_{gas,elec}^\ddagger$ estimates. ^dModel chemistry used to compute the gas phase thermal contributions (vibrations, rotations, and translation) to the Gibbs Free Energy of reaction, with a consistently optimized geometry. The aug-cc-pVTZ basis set was used for all $\Delta G_{gas,therm}^\ddagger$ computations. For some solvated clusters, the $\Delta G_{gas,therm}^\ddagger$ contribution was not computed, and these entries are left blank (see main text). ^eSolvation model and model chemistry employed to compute the change in Gibbs Free Energy of aqueous solvation for the reaction. The aug-cc-pVTZ or cc-pVTZ basis set was used. ^fResults are shown for both the $O_3 +$ bromide-catalyzed pathway ($X = Br$) and the $O_3 + HOCl$ system pathway ($X = Cl$).

Appendix A

Table A.14 Experimental pK_a Data For 4 Neutral Nitrogen Acids and Quantum Chemical LFER pK_a Estimates for DMS, BrDMS, CIDMS.

	Experimental pK _a value	Uncorrected ^a quantum chemical pK _a	Quantum chemical LFER pK _a estimate
Known pK_a data			
CF ₃ SO ₂ NH ₂ /NH ⁻	6.3[259]	8.59	5.0
H ₂ NSO ₂ NH ₂ /NH ⁻	10.4[260]	16.90	9.7
HN ₃ /N ₃ ⁻	4.72[259]	10.63	6.2
CH ₃ CONH ₂ /NH ⁻	15.1[259]	27.64	15.7
Experimental pK_a data			
DMS/DMS ⁻	10.4 ^b	18.04	10.3
BrDMS/BrDMS ⁻	-	15.63	9.0
CIDMS/CIDMS ⁻	-	13.76	7.9

^aComputed according to eq 4.7 in the main text. ^bBased on stopped-flow results and eq 4.8.

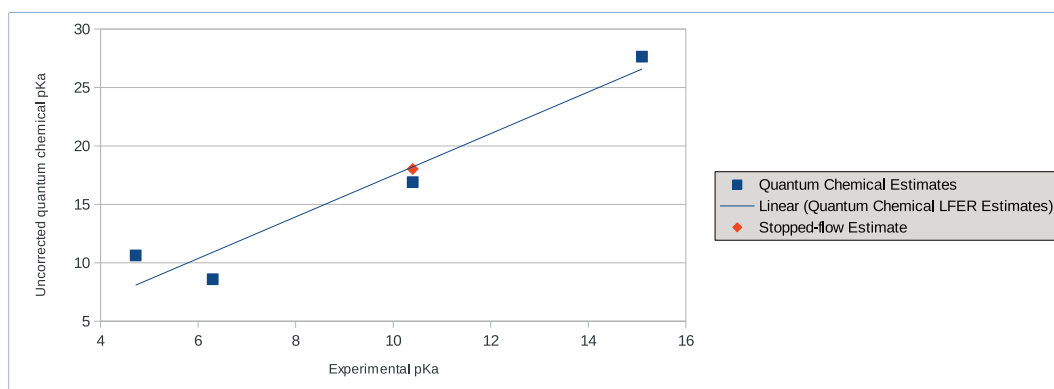


Fig. A.7 Graph showing the correlation between the experimental pK_a values and the uncorrected quantum chemical pK_a^{uncorr} results for hydrazoic acid, sulfamide, acetamide, and trifluoromethanesulfamide.

A.1.4 Mechanisms of OCS Formation in Seawater from DMS, Biogenic Thiols, and Polysulfides

- SUPPORTING INFORMATION

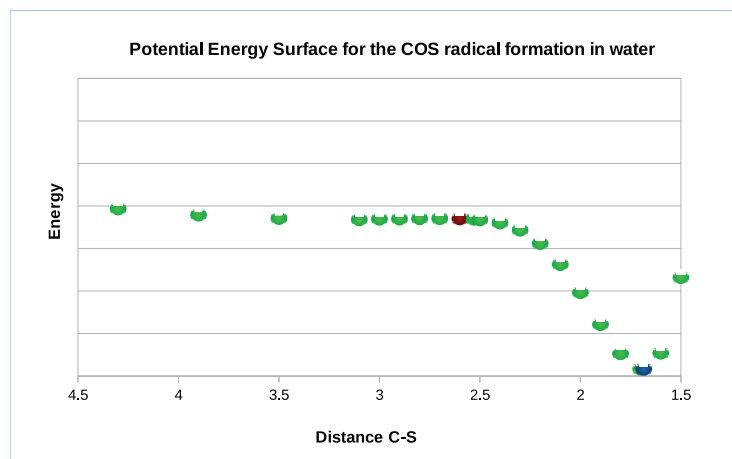


Fig. A.8 Potential energy surface for the attack of CO on S^{2-} . A relaxed scan computation was performed with the SMD/M06-2X/aug-cc-pVTZ model chemistry along the variable represented by the distance of the carbon atom of CO and the sulfur atom of S^{2-} . Further single point energy calculations with the model SMD/B2PLYPD/aug-cc-pVTZ have been carried out to obtain a more accurate electronic energy. Thermal contributions to the free energy are not included in the energy profile. The red point represents the transition state structure, whereas the blue point indicates the minimum energy structure (*i.e.* COS^{2-}).

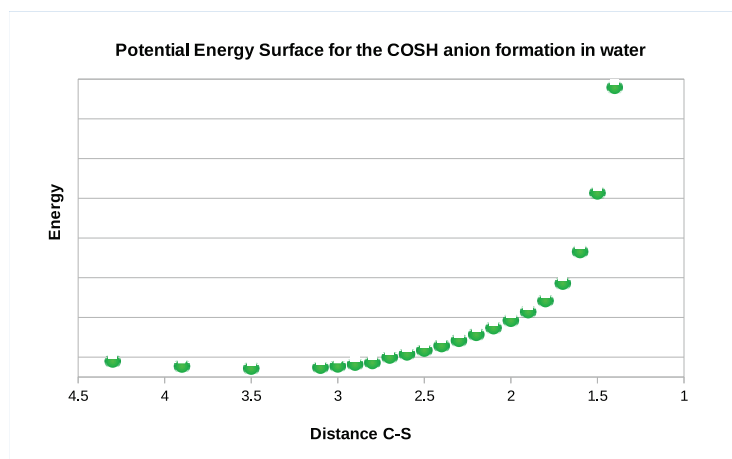


Fig. A.9 Potential energy surface for the attack of CO on SH^{-} . A relaxed scan computation was performed with the SMD/M06-2X/aug-cc-pVTZ model chemistry along the variable represented by the distance of the carbon atom of CO and the sulfur atom of SH^{-} . Further single point energy calculations with the model SMD/B2PLYPD/aug-cc-pVTZ have been carried out to obtain a more accurate electronic energy. Thermal contributions to the free energy are not included in the energy profile. The red point represents the transition state structure, whereas the blue point indicates the minimum energy structure (*i.e.* $COSH^{-}$).

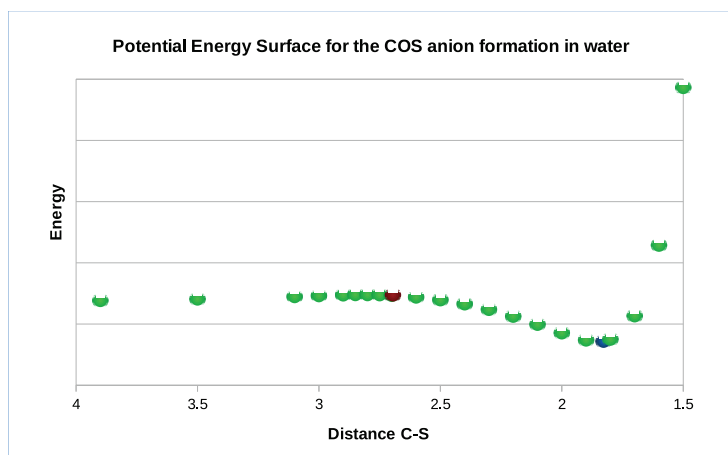


Fig. A.10 Potential energy surface for the attack of CO on S^{2-} . A relaxed scan computation was performed with the SMD/M06-2X/aug-cc-pVTZ model chemistry along the variable represented by the distance of the carbon atom of CO and the sulfur atom of S^{2-} . Further single point energy calculations with the model SMD/B2PLYPD/aug-cc-pVTZ have been carried out to obtain a more accurate electronic energy. Thermal contributions to the free energy are not included in the energy profile. The red point represents the transition state structure, whereas the blue point indicates the minimum energy structure (*i.e.* COS²⁻).

Table A.15 Aqueous free energies of reactions and aqueous free energies of activation for polysulfide reactions with CO leading to OCS: SMD/M06-2X computational estimates. Values are in kJ mol^{-1}

Reactions	$\Delta G_{rxn,aq}^{*M06-2X}$	$\Delta G_{rxn,aq}^{\ddagger M06-2X}$
Radical Reactions		
$\text{HS}^\cdot + \text{CO} \rightleftharpoons \text{COSH}^\cdot$	18	27
$\text{HS}_2^\cdot + \text{CO} \rightleftharpoons \text{OCS} + \text{HS}^\cdot$	-1	80
$\text{HS}_3^\cdot + \text{CO} \rightleftharpoons \text{OCS} + \text{HS}_2^\cdot$	-55	85
$\text{HS}_4^\cdot + \text{CO} \rightleftharpoons \text{OCS} + \text{HS}_3^\cdot$	-56	85
$\text{HS}_5^\cdot + \text{CO} \rightleftharpoons \text{OCS} + \text{HS}_4^\cdot$	-59	83
$\text{HS}_6^\cdot + \text{CO} \rightleftharpoons \text{OCS} + \text{HS}_5^\cdot$	-60	83
$\text{HS}_7^\cdot + \text{CO} \rightleftharpoons \text{OCS} + \text{HS}_6^\cdot$	-56	89
$\text{S}^{\cdot-} + \text{CO} \rightleftharpoons \text{COS}^{\cdot-}$	-69	15
$\text{S}_2^{\cdot-} + \text{CO} \rightleftharpoons \text{OCS} + \text{S}^{\cdot-}$	43	78
$\text{S}_3^{\cdot-} + \text{CO} \rightleftharpoons \text{OCS} + \text{S}_2^{\cdot-}$	-12	112
$\text{S}_4^{\cdot-} + \text{CO} \rightleftharpoons \text{OCS} + \text{S}_3^{\cdot-}$	-82	95
$\text{S}_5^{\cdot-} + \text{CO} \rightleftharpoons \text{OCS} + \text{S}_4^{\cdot-}$	-71	88
$\text{S}_6^{\cdot-} + \text{CO} \rightleftharpoons \text{OCS} + \text{S}_5^{\cdot-}$	-82	71
$\text{S}_7^{\cdot-} + \text{CO} \rightleftharpoons \text{OCS} + \text{S}_6^{\cdot-}$	-37	86
Anionic Reactions		
$\text{HS}^- + \text{CO} \rightleftharpoons \text{COSH}^-$	N/A ^a	N/A ^a
$\text{HS}_2^- + \text{CO} \rightleftharpoons \text{OCS} + \text{HS}^-$	-63	75
$\text{HS}_3^- + \text{CO} \rightleftharpoons \text{OCS} + \text{HS}_2^-$	-39	93
$\text{HS}_4^- + \text{CO} \rightleftharpoons \text{OCS} + \text{HS}_3^-$	-51	94
$\text{HS}_5^- + \text{CO} \rightleftharpoons \text{OCS} + \text{HS}_4^-$	-55	89
$\text{HS}_6^- + \text{CO} \rightleftharpoons \text{OCS} + \text{HS}_5^-$	-57	90
$\text{HS}_7^- + \text{CO} \rightleftharpoons \text{OCS} + \text{HS}_6^-$	-55	92
$\text{S}^{2-} + \text{CO} \rightleftharpoons \text{COS}^{2-}$	-2	20
$\text{S}_2^{2-} + \text{CO} \rightleftharpoons \text{OCS} + \text{S}^{2-}$	20	66
$\text{S}_3^{2-} + \text{CO} \rightleftharpoons \text{OCS} + \text{S}_2^{2-}$	14	87
$\text{S}_4^{2-} + \text{CO} \rightleftharpoons \text{OCS} + \text{S}_3^{2-}$	-36	73
$\text{S}_5^{2-} + \text{CO} \rightleftharpoons \text{OCS} + \text{S}_4^{2-}$	-20	89
$\text{S}_6^{2-} + \text{CO} \rightleftharpoons \text{OCS} + \text{S}_5^{2-}$	-46	93
$\text{S}_7^{2-} + \text{CO} \rightleftharpoons \text{OCS} + \text{S}_6^{2-}$	-54	90

^aThe adduct COSH^- was not found in the potential energy surface described by the SMD/M06-2X electronic structure method.

Table A.16 NPA partial atomic charge distributions and spin densities computed for the transition state structures of the radical reactions involving polysulfides and CO. NPA partial charge values are in e^- .

Reaction 7			Reaction 8			Reaction 9			Reaction 10			Reaction 11			Reaction 12			Reaction 13		
TS ^a	NPA charge	Spin Density	TS	NPA charge	Spin Density	TS	NPA charge	Spin Density	TS	NPA charge	Spin Density	TS	NPA charge	Spin Density	TS	NPA charge	Spin Density	TS	NPA charge	Spin Density
O	0.1	0.6	O	-0.5	0.0	O	0.0	0.5	O	0.0	0.6	O	-0.5	0.1	O	-0.5	0.1	O	-0.6	0.0
C	0.8	0.4	C	0.4	0.1	C	0.6	0.5	C	0.6	0.4	C	0.5	0.4	C	0.7	0.5	C	0.2	0.1
S	-1.3	0.0	S	-0.3	0.4	S	-0.6	0.0	S	-0.5	0.1	S	0.0	0.3	S	-0.1	0.4	S	0.1	0.5
H	0.4	0.0	S	0.1	0.4	S	0.0	0.0	S	-0.2	0.0	S	0.0	0.1	S	0.0	0.0	S	0.1	0.2
			H	0.4	0.0	S	-0.3	0.0	S	0.1	0.0	S	0.0	0.0	S	0.0	0.0	S	0.1	0.1
						H	0.3	0.0	S	-0.2	0.0	S	0.0	0.0	S	0.0	0.0	S	0.0	0.0
									H	0.1	0.0	H	0.2	0.0	S	0.0	0.0	S	0.1	0.0
															S	-0.2	0.0	S	-0.1	0.0
															H	0.2	0.0	S	-0.3	0.0
															H	0.4	0.0	H	0.4	0.0

Reaction 14			Reaction 15			Reaction 16			Reaction 17			Reaction 18			Reaction 19			Reaction 20		
TS	NPA charge	Spin Density	TS	NPA charge	Spin Density	TS	NPA charge	Spin Density	TS	NPA charge	Spin Density	TS	NPA charge	Spin Density	TS	NPA charge	Spin Density	TS	NPA charge	Spin Density
O	0.1	0.7	O	-0.2	0.3	O	-0.7	0.0	O	-0.5	0.0	O	-0.6	0.0	O	-0.6	0.0	O	-0.6	0.0
C	0.7	0.3	C	0.7	0.5	C	0.3	0.5	C	0.6	0.1	C	0.3	0.1	C	0.5	0.0	C	0.5	0.0
S	-1.9	0.0	S	-0.7	0.1	S	0.2	0.4	S	-0.3	0.1	S	-0.2	0.5	S	-0.5	0.0	S	-0.5	0.0
			S	-0.8	0.0	S	-0.3	0.0	S	-0.4	0.1	S	0.2	0.3	S	-0.2	0.0	S	-0.3	0.0
						S	-0.6	0.0	S	0.2	0.4	S	0.0	0.1	S	0.1	0.1	S	0.0	0.0
									S	-0.6	0.2	S	0.0	0.0	S	0.1	0.2	S	0.0	0.1
												S	-0.8	0.0	S	0.2	0.5	S	0.2	0.4
															S	-0.6	0.2	S	-0.2	0.4

^aTS refers to the transition state structure of the reaction considered.

Table A.17 NPA partial atomic charge distributions computed for the transition state structures of the anionic reactions involving polysulfides and CO. NPA charge values are in e^- .

Reaction 22		Reaction 23		Reaction 24		Reaction 25		Reaction 26		Reaction 27	
TS ^a	NPA charge	TS	NPA charge	TS	NPA charge	TS	NPA charge	TS	NPA charge	TS	NPA charge
O	-0.7	O	-0.8	O	-0.3	O	-0.7	O	-0.6	O	-0.5
C	0.3	C	0.3	C	0.1	C	0.1	C	0.5	C	0.5
S	-0.3	S	-0.2	S	-0.3	S	-0.1	S	-0.3	S	-0.3
S	-0.7	S	-0.1	S	-0.4	S	0.1	S	-0.1	S	-0.5
H	0.4	S	-0.4	S	0.0	S	-0.2	S	-0.4	S	-0.2
		H	0.2	S	-0.4	S	0.0	S	-0.1	S	0.0
				H	0.4	S	-0.3	S	0.0	S	-0.1
						H	0.2	S	-0.3	S	0.0
								H	0.2	S	-0.3
										H	0.3

Reaction 28		Reaction 29		Reaction30		Reaction 31		Reaction 32		Reaction 33	
TS ^a	NPA charge	TS	NPA charge	TS	NPA charge	TS	NPA charge	TS	NPA charge	TS	NPA charge
O	-0.6	O	-0.7	O	-0.7	O	-0.4	O	-0.3	O	-0.4
C	0.3	C	0.3	C	0.3	C	0.4	C	0.4	C	0.4
S	-0.3	S	-0.3	S	-0.4	S	-0.3	S	-0.4	S	-0.5
S	-1.4	S	-0.5	S	-0.4	S	-0.2	S	0.0	S	-0.3
		S	-0.9	S	0.0	S	0.0	S	-0.2	S	-0.1
				S	-0.8	S	-0.9	S	-0.2	S	0.0
						S	-0.5	S	-0.7	S	-0.2
								S	-0.6	S	-0.1
										S	-0.7

^aTS refers to the transition state structure of the reaction considered.

Appendix A

Table A.18 Previously reported aqueous reactions involving sulfide and polysulfide species.

Reactions	k_{aq}
$HS^- + O_2 \longrightarrow SO_2^{2-} + H^+$	$5 \times 10^9 M^{-1} s^{-1}$ [410]
$HS^- + HS^- \longrightarrow H_2S_2$	$5.0 \pm 0.7 \times 10^9 M^{-1} s^{-1}$ [416]
$S^{2-} + S^{2-} \rightleftharpoons S_2^{2-}$	$9 \pm 2 \times 10^9 s^{-1}$ [416]
$S_2^{2-} + HS^- \rightleftharpoons S_2^{2-} + HS^-$	$9 \times 10^9 M^{-1} s^{-1}$ [410]
$S_x^{2-} + HS^- \rightleftharpoons S_x^{2-} + HS^-$	[410]
$2 S_x^{2-} \rightleftharpoons S_{2x}^{2-}$	[410]
$HS^- + H_2O_2 \longrightarrow HSOH + OH^-$	[357]
$HS^- + HOCl \longrightarrow HSCl + OH^-$	$4.8 \times 10^9 M^{-1} s^{-1}$ [429]
$HS^- + OH^- \longrightarrow H_2O + HS^-$	$1.5 \times 10^{10} M^{-1} s^{-1}$ [416]
$HS^- + HS^- \longrightarrow HSSH^{2-}$	$5.4 \times 10^9 M^{-1} s^{-1}$ [430]
	$5.3 \times 10^5 M^{-1} s^{-1}$ [431]
$HS^- + O_2 \longrightarrow SO_2^{2-} + H^+$	$5 \times 10^9 M^{-1} s^{-1}$
$HS^- \rightleftharpoons S^{2-} + H^+$	[416]
$HSSH^{2-} \rightleftharpoons HSS^{2-} + H^+$	[416]
$H_2S + H^- \longrightarrow H_2 + HS^-$	$10^{10} M^{-1} s^{-1}$ [432]
$HS^- + OH^- \longrightarrow \text{Products}$	$9 \times 10^8 M^{-1} s^{-1}$ [390]
$H_2S + e_{aq}^- \longrightarrow H^- + HS^-$	$9.2 \pm 1.4 \times 10^9 M^{-1} s^{-1}$ [416] ^a
$HS^- + S^{2-} \rightleftharpoons HS_2^{2-}$	$4.0 \pm 0.6 \times 10^9 M^{-1} s^{-1}$ [416] ^b
$HS_2^{2-} + O_2 \rightleftharpoons HS_2^- + O_2^{\cdot -}$	$4.0 \pm 0.6 \times 10^8 M^{-1} s^{-1}$ [416]
Redox reaction with aqueous inorganic oxidants	
$HS^- + SO_4^{2-} \longrightarrow HS^- + SO_4^{2-}$	$3.0 \pm 0.5 \times 10^9 M^{-1} s^{-1}$ [416]
$HS^- + CO_3^{2-} \longrightarrow HS^- + CO_3^{2-}$	$2.0 \pm 0.3 \times 10^8 M^{-1} s^{-1}$ [416]
$HS^- + I_2^- \longrightarrow HS^- + I_2^{2-}$	$4.6 \pm 0.6 \times 10^8 M^{-1} s^{-1}$ [416]
$HS^- + C_6H_5NH_2^- \longrightarrow HS^- + C_6H_5NH_2^{2-}$	$7.0 \pm 1.0 \times 10^8 M^{-1} s^{-1}$ [416]

^aThe reaction of the aqueous free electron with sulfide involves the addition followed by elimination of HS^- with a mechanism that is similar to the one that involves organic thiols.[416]

^bThe aqueous equilibrium constant is $8 \times 10^3 M^{-1}$. [416]

Bibliography

- 1 Werner R. Haag and Jurg Hoigné. Ozonation of Bromide-Containing Waters: Kinetics of Formation of Hypobromous Acid and Bromate. *Environ. Sci. Technol.*, 17(5):261–267, 1983.
- 2 Urs von Gunten and Jurg Hoigné. Bromate Formation during Ozonation of Bromide-Containing Waters: Interaction of Ozone and Hydroxyl Radical Reactions. *Environ. Sci. Technol.*, 28(7):1234–1242, 1994.
- 3 Marc-Olivier Buffle, Sonja Galli, and Urs von Gunten. Enhanced bromate control during ozonation: the chlorine-ammonia process. *Environ. Sci. Technol.*, 38(19):5187–95, October 2004.
- 4 Michèle B. Heeb, Justine Criquet, Saskia G. Zimmermann-Steffens, and Urs von Gunten. Oxidative treatment of bromide-containing waters: Formation of bromine and its reactions with inorganic and organic compounds - A critical review. *Water Res.*, 48:15–42, September 2014.
- 5 Yan Zhao, Oksana Tishchenko, Jeffrey R. Gour, Wei Li, Jesse J. Lutz, Piotr Piecuch, and Donald G. Truhlar. Thermochemical Kinetics for Multireference Systems: Addition Reactions of Ozone. *J. Phys. Chem. A*, 113(19):5786–99, May 2009.
- 6 Kirk A. Peterson, Benjamin C. Shepler, Detlev Figgen, and Hermann Stoll. On the spectroscopic and thermochemical properties of ClO, BrO, IO, and their anions. *J. Phys. Chem. A*, 110(51):13877–83, December 2006.
- 7 Christopher J. Cramer. *Essentials of Computational Chemistry Theories and Models*. John Wiley & Sons Inc., second edition, 2004.
- 8 Steven E. Wheeler, Daniel H. Ess, and K. N. Houk. Thinking Out of the Black Box: Accurate Barrier Heights of 1,3-Dipolar Cycloadditions of Ozone with Acetylene and Ethylene. *J. Phys. Chem. A*, 112(8):1798–807, February 2008.
- 9 Susan D. Richardson. Drinking Water Disinfection By-products. In R. A. Meyers, editor, *Encycl. Environ. Anal. Remediat. Vol. 3*, page 1398. Wiley, New York, NY, 1998.

Bibliography

- 10 Susan D. Richardson, Michael J. Plewa, Elizabeth D. Wagner, Rita Schoeny, and David M. Demarini. Occurrence, genotoxicity, and carcinogenicity of regulated and emerging disinfection by-products in drinking water: a review and roadmap for research. *Mutat. Res.*, 636(1-3):178–242, 2007.
- 11 Yuji Kurokawa, Shozo Takayama, Yoichi Konishi, Yoshio Hiasa, Shogo Asahina, Michihito Takahashi, Akihiko Maekawa, and Yuzo Hayashi. Long-term in vivo carcinogenicity tests of potassium bromate, sodium hypochlorite, and sodium chlorite conducted in Japan. *Environ. Health Perspect.*, 69:221–35, November 1986.
- 12 Anthony B. DeAngelo, Michael H. George, Steve R. Kilburn, Tanya M. Moore, and Douglas C. Wolf. Carcinogenicity of potassium bromate administered in the drinking water to male B6C3F1 mice and F344/N rats. *Toxicol. Pathol.*, (5):587–594, 1998.
- 13 Bernard Legube. Ozonation By-Products. *Handb. Environ. Chem.*, 5:95–116, 2003.
- 14 Simon F. Watts. The mass budgets of carbonyl sulfide, dimethyl sulfide, carbon disulfide and hydrogen sulfide. *Atmos. Environ.*, 34:761–779, 2000.
- 15 Gregory A. Cutter, Lynda S. Cutter, and Katherine C. Filippino. Sources and cycling of carbonyl sulfide in the Sargasso Sea. *Limnol. Oceanogr.*, 49(2):555–565, 2004.
- 16 Otmar R. Flöck and Meinrat O. Andreae. Photochemical and non-photochemical formation and destruction of carbonyl sulfide and methyl mercaptan in ocean waters. *Mar. Chem.*, 54:11–26, 1996.
- 17 Willer H. Pos, Daniel D. Riemer, and Rod G. Zika. Carbonyl sulfide (OCS) and carbon monoxide (CO) in natural waters: evidence of a coupled production pathway. *Mar. Chem.*, 62:89–101, 1998.
- 18 Otmar R. Flöck, Meinrat O. Andreae, and M. Drager. Environmentally relevant precursors of carbonyl sulfide in aquatic systems. *Mar. Chem.*, 59:71–85, 1997.
- 19 Richard G. Zepp and Meinrat O. Andreae. Factors affecting the photochemical production of carbonyl sulfide in seawater. *Geophys. Res. Lett.*, 21(25):2813–2816, 1994.
- 20 M. von Hobe, G. A. Cutter, A. James Kettle, and Meinrat O. Andreae. Dark production: A significant source of oceanic COS. *J. Geophys. Res.*, 106(c12), 2001.
- 21 M. von Hobe, R. G. Najjar, A. J. Kettle, and M. O. Andreae. Photochemical and physical modeling of carbonyl sulfide in the ocean. *J. Geophys. Res.*, 108(C7):3229, 2003.
- 22 Meinrat O. Andreae. Ocean-atmosphere interactions in the global biogeochemical sulfur cycle. *Mar. Chem.*, 30:1–29, January 1990.
- 23 Ian Faloona. Sulfur processing in the marine atmospheric boundary layer: A review and critical assessment of modeling uncertainties. *Atmos. Environ.*, 43(18):2841–2854, June 2009.

-
- 24 Robert J. Charlson, James E. Lovelock, Meinrat O. Andreae, and Stephen G. Warren. Oceanic phytoplankton, atmospheric sulphur, cloud albedo and climate. *Nature*, 326(6114):655–661, April 1987.
- 25 Greg P. Ayers and Jill M. Cainey. The CLAW hypothesis: a review of the major developments. *Environ. Chem.*, 4(6):366–374, 2007.
- 26 Christian E. Junge and James E. Manson. Stratospheric aerosol studies. *J. Geophys. Res.*, 66(7):2163–2182, July 1961.
- 27 Paul J. Crutzen. The possible importance of CSO for the sulfate layer of the stratosphere. *Geophys. Res. Lett.*, 3(2):73–76, February 1976.
- 28 Paul J. Crutzen and Uta Schmailzl. Chemical budgets of the stratosphere. *Planet. Space Sci.*, 31(9):1009–1032, September 1983.
- 29 Barbara J. Finlayson-Pitts and James N. Jr. Pitts. *Chemistry of the Upper and Lower Atmosphere. Theory, Experiments, and Applications*. Academic Press, 2000.
- 30 Mian Chin and D. D. Davis. Global Sources and Sinks of OCS and CS₂ and their distributions. *Global Biogeochem. Cycles*, 7(2):321–337, 1993.
- 31 R. E. Stickel, M. Chin, E. P. Daykin, A. J. Hynes, P. H. Wine, and T. J. Wallington. Mechanistic studies of the OH-initiated oxidation of CS₂ in the presence of O₂. *J. Phys. Chem.*, 97(51):13653–13661, 1993.
- 32 J. Gun, A. Goifman, I. Shkrob, A. Kamyshny, B. Ginzburg, O. Hadas, I. Dor, A.D. Modestov, and O. Lev. Formation of Polysulfides in an Oxygen Rich Freshwater Lake and Their Role in the Production of Volatile Sulfur Compounds in Aquatic Systems. *Environ. Sci. Technol.*, 34(22):4741–4746, November 2000.
- 33 Alexey Kamyshny, A. Goifman, D. Rizkov, and O. Lev. Formation of carbonyl sulfide by the reaction of carbon monoxide and inorganic polysulfides. *Environ. Sci. Technol.*, 37(9):1865–72, May 2003.
- 34 Cristina M. Villanueva and Laia Font-Ribera. Health impact of disinfection by-products in swimming pools. *Ann. Ist. Super Sanità*, 48(4):387–396, 2012.
- 35 X. L. Armesto, M. Canle L., M. V. García, and J. A. Santaballa. Aqueous chemistry of N-halo-compounds. *Chem. Soc. Rev.*, 27:453–460, 1998.
- 36 National Research Council. *Drinking Water and Health, Volume 2*. The National Academies Press, Washington, DC, 1980.
- 37 National Research Council. *Drinking Water and Health, Volume 7 Disinfectants and Disinfectants By-Products*. The National Academies Press, Washington, DC, 1987.

Bibliography

- 38 U.S. Environmental Protection Agency. Information about Chloramine in Drinking Water. Technical report, 2012.
- 39 J. Carrel Morris. The Acid Ionization Constant of HOCl from 5 to 35 °. *J. Phys. Chem.*, 70(12):3798–3805, 1966.
- 40 Ira Weil and J. Carrell Morris. Kinetic Studies on the Chloramines. I. The Rates of Formation of Monochloramines, N-Chlormethylamine and N-Chlordimethylamine. *J. Am. Chem. Soc.*, 71(3):1664–1671, 1949.
- 41 J. Carrell Morris. Kinetics of reactions between aqueous chlorine and nitrogen compounds. In Samuel D. Faust and Joseph Hunter, editors, *Princ. Appl. Water Chem.*, pages 23–53. 1967.
- 42 J. Carrell Morris and Russell A. Isaac. A critical review of kinetic and thermodynamic constants for the aqueous chlorine-ammonia system. In R. L. Jolley, W. A. Brungs, J. A. Cotruvo, R. B. Cumming, J. S. Mattice, and V. A. Jacobs, editors, *Water Chlorination Environ. Impact Heal. Eff.*, volume 4, chapter 2, pages 50–62. Ann Arbor Science, Ann Arbor, MI, 1981.
- 43 Dale W. Margerum and Edward T. Gray. Chlorination and the Formation of N-Chloro Compounds in Water Treatment. In *Organometals Organometalloids Occur. Fate Environ.*, chapter 17, pages 278–291. 1978.
- 44 Chad T. Jafvert and Richard L. Valentine. Reaction Scheme for the Chlorination of Ammoniacal Water. *Environ. Sci. Technol.*, 26(3):577–586, March 1992.
- 45 Roy L. Wolfe, N. Robert Ward, and Betty H. Olson. Inorganic Chloramines as Drinking Water Disinfectants: A Review. *J. AWWA*, 76(5):74–88, 1984.
- 46 P. J. Vikesland, K. Ozekin, and R. L. Valentine. Monochloramine decay in model and distribution system waters. *Water Res.*, 35(7):1766–76, May 2001.
- 47 Johannes Edmund Wajon and J. Carrell Morris. Bromamination Chemistry. In R. L. Jolley, W. A. Brungs, R. B. Cumming, and V. A. Jacobs, editors, *Water Chlorination Environ. Impact Heal. Eff. Vol. 3*, chapter 16, pages 171–181. Ann Arbor Science, Ann Arbor, MI, 1980.
- 48 J. Donald Jonhson and Ragnar Overby. Bromine and Bromamine Disinfection Chemistry. *J. Sanit. Eng. Div.*, 97(5):617–628, 1971.
- 49 Michael Gazda, Lindy E. Dejarne, Tarun K. Choudhury, R. Graham Cooks, and Dale W. Margerum. Mass Spectrometric Evidence for the Formation of Bromochloramine and N-Bromo-N-chloromethylamine in Aqueous Solution. *Environ. Sci. Technol.*, 27(3):557–561, 1993.
- 50 Michael Gazda and Dale W. Margerum. Reactions of Monochloramine with Br₂, Br₃⁻, HOBr, and OBr⁻: Formation of Bromochloramines. *Inorg. Chem.*, 33(1):118–123, 1994.

-
- 51 Guy W. Inman, Thomas F. LaPointe, and J. Donald Johnson. Kinetics of Nitrogen Tribromide Decomposition in Aqueous Solution. *Inorg. Chem.*, 15(12):3037–3042, 1976.
- 52 Guy W. Inman and J. Donald Johnson. Kinetics of Monobromamine Disproportionation-Dibromamine Formation in Aqueous Ammonia Solutions. *Environ. Sci. Technol.*, 8(6):219–224, 1984.
- 53 Hend Galal-Gorchev and J. Carrell Morris. Formation and Stability of Bromamide, Bromimide, and Nitrogen Tribromide in Aqueous Solution. *Inorg. Chem.*, 4(6):899–905, 1965.
- 54 B. Michel Soulard, Francois Bloc, and Andre Hatterer. Diagrams of Existence of Chloramines and Bromamines in Aqueous Solution. *J. Chem. Soc. - Dalt. Trans.*, (2300):2300–2310, 1981.
- 55 A. Bousher, Peter Brimblecombe, and D. Midgley. Kinetics of reactions in solutions containing monochloramine and bromide. *Water Res.*, 23(8):1049–1058, 1989.
- 56 Hongxia Lei, Benito J. Mariñas, and Roger A. Minear. Bromamine decomposition kinetics in aqueous solutions. *Environ. Sci. Technol.*, 38(7):2111–9, April 2004.
- 57 Jeanne Luh and Benito J. Mariñas. Kinetics of bromochloramine formation and decomposition. *Environ. Sci. Technol.*, 48(5):2843–52, March 2014.
- 58 Alicia C. Diehl, Gerald E. Speitel Jr., James M. Symons, Stuart W. Krasner, Cordelia J. Hwang, and Sylvia E. Barrett. DBP formation during chloramination. *J. AWWA*, 92(6):76–90, 2000.
- 59 Julien Le Roux, Hervé Gallard, and Jean-Philippe Croué. Formation of NDMA and Halogenated DBPs by Chloramination of Tertiary Amines: the Influence of Bromide Ion. *Environ. Sci. Technol.*, 46(3):1581–9, February 2012.
- 60 Hongxia Lei, Roger A. Minear, and Benito J. Mariñas. Cyanogen bromide formation from the reactions of monobromamine and dibromamine with cyanide ion. *Environ. Sci. Technol.*, 40(8):2559–64, April 2006.
- 61 Peter J. Vikesland and Richard L. Valentine. Effect of Natural Organic Matter on Monochloramine Decomposition: Pathway Elucidation through the Use of Mass and Redox Balances. *Environ. Sci. Technol.*, 32(10):1409–1416, 1998.
- 62 Martin P. Snyder and Dale W. Margerum. Kinetics of Chlorine Transfer from Chloramine to Amines, Amino Acids, and Peptides. *Inorg. Chem.*, 21:2545–2550, 1982.
- 63 Russell A. Isaac and J. Carrel Morris. Transfer of Active Chlorine from Chloramine to Nitrogenous Organic Compounds: 1. Kinetics. *Environ. Sci. Technol.*, 17(12):738–742, 1983.

Bibliography

- 64 Russell A. Isaac and J. Carrel Morris. Transfer of Active Chlorine from Chloramine to Nitrogenous Organic Compounds. 2. Mechanism. *Environ. Sci. Technol.*, 19(9):810–814, 1985.
- 65 Amisha D. Shah and William A. Mitch. Halonitroalkanes, Halonitriles, Haloamides, and N-Nitrosamines: A Critical Review of Nitrogenous Disinfection Byproduct Formation Pathways. *Environ. Sci. Technol.*, 46:119–131, 2012.
- 66 Stephen E. Durr and Richard L. Valentine. Modeling dichloroacetic acid formation from the reaction of monochloramine with natural organic matter. *Water Res.*, 40(14):2667–74, August 2006.
- 67 I. Marie Schreiber and William A. Mitch. Influence of the Order of Reagent Addition on NDMA Formation during Chloramination. *Environ. Sci. Technol.*, 39(10):3811–8, May 2005.
- 68 I. Marie Schreiber and William A. Mitch. Nitrosamine Formation Pathway Revisited: the Importance of Chloramine Speciation and Dissolved Oxygen. *Environ. Sci. Technol.*, 40(19):6007–14, October 2006.
- 69 Richard L. Valentine. Bromochloramine oxidation of N,N-diethyl-p-phenylenediamine in the presence of monochloramine. *Environ. Sci. Technol.*, 20(2):166–70, February 1986.
- 70 G. Holzwarth, R. G. Balmer, and L. Soni. The Fate of Chlorine and Chloramines in Cooling Towers. *Water Res.*, 18(11):1421–1427, 1984.
- 71 Nicolas Cimetiere and Joseph De Laat. Henry's law constant of N,N-dichloromethylamine: application to the contamination of the atmosphere of indoor swimming pools. *Chemosphere*, 77(4):465–70, October 2009.
- 72 Susan D. Richardson, David M. DeMarini, Manolis Kogevinas, Pilar Fernandez, Esther Marco, Carolina Lourencetti, Clara Ballesté, Dick Heederik, Kees Meliefste, A. Bruce McKague, Ricard Marcos, Laia Font-Ribera, Joan O. Grimalt, and Cristina M. Villanueva. What's in the pool? A comprehensive identification of disinfection by-products and assessment of mutagenicity of chlorinated and brominated swimming pool water. *Environ. Health Perspect.*, 118(11):1523–30, November 2010.
- 73 M. Hery, G. Hecht, J.M. Gerber, J.C. Gendreau, G. Hubert, and J. Rebuffaud. Exposure to Chloramines in the atmosphere of indoor swimming pools. *Ann. occup. Hyg.*, 39(4):427–439, 1995.
- 74 David I. Pattison and Michael J. Davies. Kinetic Analysis of the Reactions of Hypobromous Acid with Protein Components: Implications for Cellular Damage and Use of 3-Bromotyrosine as a Marker of Oxidative Stress. *Biochemistry*, 43(16):4799–4809, April 2004.

-
- 75 Edwin L. Thomas, Paula M. Bozeman, M. Margaret Jefferson, and Charles C. King. Oxidation of Bromide by the Human leukocyte Enzymes Myeloperoxidase and Eosinophil Peroxidase. *J. Biol. Chem.*, 270(7):2906–2913, 1995.
- 76 Stephen J. Weiss, Samuel T. Test, Carel M. Eckmann, Dirk Roos, and Sandra Regiani. Brominating Oxidants Generated by Human Eosinophils. *Science (80-.)*, 234(4773):200–203, 1986.
- 77 Martin D. Rees, Tane N. McNiven, and Michael J. Davies. Degradation of extracellular matrix and its components by hypobromous acid. *Biochem. J.*, 401(2):587–96, January 2007.
- 78 Anna L. P. Chapman, Ojia Skaff, Revathy Senthilmohan, Anthony J. Kettle, and Michael J. Davies. Hypobromous acid and bromamine production by neutrophils and modulation by superoxide. *Biochem. J.*, 417(3):773, February 2009.
- 79 Zheng Xue, Woo Hyoung Lee, Kimberly M Coburn, and Youngwoo Seo. Selective Reactivity of Monochloramine with Extracellular Matrix Components Affects the Disinfection of Biofilm and Detached Clusters. *Environ. Sci. Technol.*, 48:3832–3839, 2014.
- 80 David I. Pattison, Robert J. O'Reilly, Ojia Ska, Leo Radom, Robert F. Anderson, and Michael J. Davies. One-Electron Reduction of N -Chlorinated and N -Brominated Species Is a Source of Radicals and Bromine Atom Formation. *Chem. Res. Toxicol.*, 24:371–382, 2011.
- 81 Robert J. O'Reilly, Amir Karton, and Leo Radom. Effect of Substituents on the Preferred Modes of One-Electron Reductive Cleavage of N-Cl and N-Br Bonds. *J. Phys. Chem. A*, 117:460–472, 2013.
- 82 R. K. Milburn, C. F. Rodriquez, and A. C. Hopkinson. Theoretical Enthalpies of Formation of NHmCln: Neutral Molecules, Cations, and Anions. *J. Phys. Chem. B*, 5647(96):1837–1844, 1997.
- 83 C. Moeller and M.S. Plesset. Note on an Approximation Treatment for Many-Electron Systems. *Phys. Rev.*, 46:618–622, 1934.
- 84 R. Krishnan and J. A. Pople. Approximate Fourth-Order Perturbation Theory of the Electron Correlation Energy. *Int. J. Chem. Kinet.*, XIV:91–100, 1978.
- 85 R. Krishnan, M. J. Frisch, and J. A. Pople. Contribution of triple substitutions to the electron correlation energy in fourth order perturbation theory. *J. Chem. Phys.*, 72(7):4244, 1980.
- 86 H. Bernhard Schlegel. Moeller-Plesset Perturbation Theory with Spin Projection. *J. Phys. Chem.*, 92:3075–3078, 1988.

Bibliography

- 87 John A. Pople, Martin Head-Gordon, and Krishnan Raghavachari. Quadratic configuration interaction. A general technique for determining electron correlation energies. *J. Chem. Phys.*, 87(10):5968, 1987.
- 88 Sierra Rayne and Kaya Forest. Survey of main group compounds (HBr) at the Gaussian-4 level of theory: Adiabatic ionization energies and enthalpies of formation. *Comput. Theor. Chem.*, 974(1-3):163–179, November 2011.
- 89 Larry A. Curtiss, Paul C. Redfern, and Krishnan Raghavachari. Gaussian-4 theory. *J. Chem. Phys.*, 126(8):084108, February 2007.
- 90 Sierra Rayne and Kaya Forest. Thermodynamic properties of chloramine formation and related reactions during water treatment: A G4MP2, G4, and W1BD theoretical study. *J. Environ. Sci. Health. A. Tox. Hazard. Subst. Environ. Eng.*, 49(7):753–62, January 2014.
- 91 Larry A. Curtiss, Paul C. Redfern, and Krishnan Raghavachari. Gaussian-4 theory using reduced order perturbation theory. *J. Chem. Phys.*, 127(12):124105, September 2007.
- 92 Amir Karton, Shauli Daon, and Jan M.L. Martin. W4-11: A high-confidence benchmark dataset for computational thermochemistry derived from first-principles W4 data. *Chem. Phys. Lett.*, 510(4-6):165–178, July 2011.
- 93 Amir Karton, Elena Rabinovich, Jan M.L. Martin, and Branko Ruscic. W4 theory for computational thermochemistry: In pursuit of confident sub-kJ/mol predictions. *J. Chem. Phys.*, 125(14):144108, October 2006.
- 94 Amir Karton, Peter R. Taylor, and Jan M.L. Martin. Basis set convergence of post-CCSD contributions to molecular atomization energies. *J. Chem. Phys.*, 127(6):064104, August 2007.
- 95 David Feller, Kirk A. Peterson, and David A. Dixon. A survey of factors contributing to accurate theoretical predictions of atomization energies and molecular structures. *J. Chem. Phys.*, 129(20):204105, November 2008.
- 96 Kirk A. Peterson, David Feller, and David A. Dixon. Chemical accuracy in ab initio thermochemistry and spectroscopy: current strategies and future challenges. *Theor. Chem. Acc.*, 131:1079, January 2012.
- 97 Amir Karton, Srinivasan Parthiban, and Jan M.L. Martin. Post-CCSD(T) ab initio thermochemistry of halogen oxides and related hydrides XO_x, XO₂, HO_x, XO_n, and HXO_n (X = F, Cl), and evaluation of DFT methods for these systems. *J. Phys. Chem. A*, 113(16):4802–16, April 2009.
- 98 Amir Karton and Jan M.L. Martin. Basis set convergence of explicitly correlated double-hybrid density functional theory calculations. *J. Chem. Phys.*, 135(14):144119, October 2011.

-
- 99 Attila Tajti, Péter G. Szalay, Attila G. Császár, Mihály Kállay, Jürgen Gauss, Edward F. Valeev, Bradley A. Flowers, Juana Vázquez, and John F. Stanton. HEAT: High accuracy extrapolated ab initio thermochemistry. *J. Chem. Phys.*, 121(23):11599–613, December 2004.
- 100 Yannick J. Bomble, Juana Vázquez, Mihály Kállay, Christine Michauk, Péter G. Szalay, Attila G. Császár, Jürgen Gauss, and John F. Stanton. High-accuracy extrapolated ab initio thermochemistry. II. Minor improvements to the protocol and a vital simplification. *J. Chem. Phys.*, 125(6):64108, August 2006.
- 101 Michael E. Harding, Juana Vázquez, Branko Ruscic, Angela K. Wilson, Jürgen Gauss, and John F. Stanton. High-accuracy extrapolated ab initio thermochemistry. III. Additional improvements and overview. *J. Chem. Phys.*, 128(11):114111, March 2008.
- 102 Jan M. L. Martin and Glenisson de Oliveira. Towards standard methods for benchmark quality ab initio thermochemistry—W1 and W2 theory. *J. Chem. Phys.*, 111(5):1843, 1999.
- 103 A. Daniel Boese, Mikhal Oren, Onur Atasoylu, Jan M. L. Martin, Mihály Kállay, and Jürgen Gauss. W3 theory: robust computational thermochemistry in the kJ/mol accuracy range. *J. Chem. Phys.*, 120(9):4129–41, March 2004.
- 104 David Feller, Kirk A. Peterson, and Branko Ruscic. Improved accuracy benchmarks of small molecules using correlation consistent basis sets. *Theor. Chem. Acc.*, 133:1407, November 2013.
- 105 J. D. Cox, D. D. Wagman, and V. A. Medvedev. *CODATA Key Values for Thermodynamics*. Hemisphere Publishing Corp., New York, 1989.
- 106 Branko Ruscic, Reinhardt E. Pinzon, Melita L. Morton, Gregor von Laszewski, Sandra J. Bittner, Sandeep G. Nijssure, Kaizar A. Amin, Michael Minkoff, and Albert F. Wagner. Introduction to Active Thermochemical Tables: Several “Key” Enthalpies of Formation Revisited †. *J. Phys. Chem. A*, 108(45):9979–9997, November 2004.
- 107 Branko Ruscic, Reinhardt E. Pinzon, Gregor von Laszewski, Deepti Kodeboyina, Alexander Burcat, David Leahy, David Montoy, and Albert F. Wagner. Active Thermochemical Tables: thermochemistry for the 21st century. *J. Phys. Conf. Ser.*, 16:561–570, January 2005.
- 108 Malcolm W. Chase. NIST-JANAF Thermochemical Tables, Forth Edition. *J. Phys. Chem. Ref. Data, Monogr.* 9, pages 1–1951, 1998.
- 109 Russell D. Johnson III, editor. *NIST Computational Chemistry Comparison and Benchmark Database, NIST Standard Reference Database Number 101 Release 16a*. 2013.
- 110 George D. Purvis and Rodney J. Bartlett. A full coupled-cluster singles and doubles model: The inclusion of disconnected triples. *J. Chem. Phys.*, 76(4):1910, 1982.
- 111 Krishnan Raghavachari, Gary W. Trucks, John A. Pople, and Martin Head-Gordon. A fifth-order perturbation comparison of electron correlation theories. *Chem. Phys. Lett.*, 157(6):479–483, 1989.

Bibliography

- 112 John F Stanton. Why CCSD (T) works: a different perspective. *Chem. Phys. Lett.*, 281:130–134, 1997.
- 113 P.G. Szalay J.F. Stanton, J. Gauss, M.E. Harding, A. V. Mitin with contributions from A.A. Auer, R.J. Bartlett, U. Benedikt, C. Berger, D.E. Bernholdt, Y.J. Bomble, L. Cheng, O. Christiansen, M. Heckert, O. Heun, C. Huber, T.-C. Jagau, D. Jonsson, J. Jusélius, K. Klein, W.J. Lauderdale, D.A. Matthews, T. Metzroth, L, and C. van Wüllen. CFOUR, Coupled-Cluster techniques for Computational Chemistry, a quantum-chemical program package with integral packages MOLECULE, PROPS, ABACUS and ECP routines, 2010.
- 114 Jozef Noga and Rodney J. Bartlett. The full CCSDT model for molecular electronic structure. *J. Chem. Phys.*, 86(12):7041, 1987.
- 115 Gustavo E. Scuseria and Henry F. Schaefer III. A new Implementation of the Full CCSDT model for molecular electronic structure. *Chem. Phys. Lett.*, 152(4):1–5, 1988.
- 116 John D. Watts and Rodney J. Bartlett. The coupled-cluster single, double, and triple excitation model for open-shell single reference functions. *J. Chem. Phys.*, 93(8):6104, 1990.
- 117 Yannick J. Bomble, John F Stanton, Mihály Kállay, and Jürgen Gauss. Coupled-cluster methods including noniterative corrections for quadruple excitations. *J. Chem. Phys.*, 123(5):054101, August 2005.
- 118 Stanislaw A. Kucharski and Rodney J. Bartlett. Recursive intermediate factorization and complete computational linearization of the coupled-cluster single, double, triple, and quadruple excitation equations. *Theor Chim Acta*, 80:387–405, 1991.
- 119 Nevin Oliphant and Ludwik Adamowicz. Coupled-cluster method truncated at quadruples. *J. Chem. Phys.*, 95(9):6645, 1991.
- 120 Stanislaw A. Kucharski and Rodney J. Bartlett. The coupled-cluster single, double, triple, and quadruple excitation method. *J. Chem. Phys.*, 97(6):4282, 1992.
- 121 Mihály Kállay and Péter R. Surján. Higher excitations in coupled-cluster theory. *J. Chem. Phys.*, 115:2945, 2001.
- 122 Stefan Grimme. Semiempirical hybrid density functional with perturbative second-order correlation. *J. Chem. Phys.*, 124(3):034108, January 2006.
- 123 Tobias Schwabe and Stefan Grimme. Double-hybrid density functionals with long-range dispersion corrections: higher accuracy and extended applicability. *Phys. Chem. Chem. Phys.*, 9(26):3397–3406, July 2007.
- 124 M. J. Frisch, G. W. Trucks, H. B. Schlegel, G. E. Scuseria, M. A. Robb, J. R. Cheeseman, G. Scalmani, V. Barone, B. Mennucci, G. A. Petersson, H. Nakatsuji, M. Caricato, X. Li, H. P. Hratchian, A. F. Izmaylov, J. Bloino, G. Zheng, J. L. Sonnenberg, M. Hada, M. Ehara,

- K. Toyota, R. Fukuda, J. Hasegawa, M. Ishida, T. Nakajima, Y. Honda, O. Kitao, H. Nakai, T. Vreven, J. A. Montgomery Jr., J. E. Peralta, F. Ogliaro, M. Bearpark, J. J. Heyd, E. Brothers, K. N. Kudin, V. N. Staroverov, R. Kobayashi, J. Normand, K. Raghavachari, A. Rendell, J. C. Burant, S. S. Iyengar, J. Tomasi, M. Cossi, N. Rega, M. J. Millam, M. Klene, J. E. Knox, J. B. Cross, V. Bakken, C. Adamo, J. Jaramillo, R. Gomperts, R. E. Stratmann, O. Yazyev, A. J. Austin, R. Cammi, C. Pomelli, J. W. Ochterski, R. L. Martin, K. Morokuma, V. G. Zakrzewski, G. A. Voth, P. Salvador, J. J. Dannenberg, S. Dapprich, A. D. Daniels, Ö. Farkas, J. B. Foresman, J. V. Ortiz, J. Cioslowski, and D. J. Fox. Gaussian 09 Revision D.01, 2009.
- 125 M. Valiev, E. J. Bylaska, N. Govind, K. Kowalski, T. P. Straatsma, H.J.J. Van Dam, D. Wang, J. Nieplocha, E. Apra, T. L. Windus, and W. A. de Jong. NWChem: A comprehensive and scalable open-source solution for large scale molecular simulations. *Comput. Phys. Commun.*, 181(9):1477–1489, September 2010.
- 126 Thom H. Dunning Jr. Gaussian basis sets for use in correlated molecular calculations. I. The atoms boron through neon and hydrogen. *J. Chem. Phys.*, 90:1007–1023, 1989.
- 127 R. A. Kendall, T. H. Dunning Jr., and R. J. Harrison. Electron affinities of the first-row atoms revisited. Systematic basis sets and wave functions. *J. Chem. Phys.*, 96:6796–6806, 1992.
- 128 Thom H. Dunning Jr., Kirk A. Peterson, and Angela K. Wilson. Gaussian basis sets for use in correlated molecular calculations. X. The atoms aluminum through argon revisited. *J. Chem. Phys.*, 114(21):9244, 2001.
- 129 W. A. de Jong, R. J. Harrison, and D. A. Dixon. Parallel Douglas–Kroll energy and gradients in NWChem: Estimating scalar relativistic effects using Douglas–Kroll contracted basis sets. *J. Chem. Phys.*, 114(1):48, 2001.
- 130 Kirk A. Peterson and Thom H. Dunning Jr. Accurate correlation consistent basis sets for molecular core–valence correlation effects: The second row atoms Al–Ar, and the first row atoms B–Ne revisited. *J. Chem. Phys.*, 117(23):10548, 2002.
- 131 John D. Watts, Jürgen Gauss, and Rodney J. Bartlett. Coupled-cluster methods with noniterative triple excitations for restricted open-shell Hartree–Fock and other general single determinant reference functions. Energies and analytical gradients. *J. Chem. Phys.*, 98(11):8718, 1993.
- 132 Vincenzo Barone. Anharmonic vibrational properties by a fully automated second-order perturbative approach. *J. Chem. Phys.*, 122(1):14108, January 2005.
- 133 Malgorzata Biczysko, Pawel Panek, Giovanni Scalmani, Julien Bloino, and Vincenzo Barone. Harmonic and Anharmonic Vibrational Frequency Calculations with the Double-Hybrid B2PLYP Method: analytic second Derivatives and benchmark Studies. *J. Chem. Theory Comput.*, 6:2115–2125, 2010.

Bibliography

- 134 Karl K. Irikura. Experimental Vibrational Zero-Point Energies: Diatomic Molecules. *J. Phys. Chem. Ref. Data*, 36(2):389, 2007.
- 135 P. J. Linstrom and W. G. Mallard, editors. *NIST Chemistry WebBook, NIST Standard Reference Database Number 69*. National Institute of Standards and Technology, Gaithersburg MD, 20899, <http://webbook.nist.gov>, (accessed September, 2012).
- 136 Gerhard Herzberg. *Molecular Spectra and Molecular Structure. Volume 1 - Spectra of Diatomic Molecules*. Krieger Publishing Company, Malabar, Florida, second edition, 1989.
- 137 Terrell L. Hill. *An Introduction to Statistical Thermodynamics*. Dover Publications, Inc., New York, 1986.
- 138 Stanislaw A. Kucharski and Rodney J. Bartlett. Coupled-Cluster Methods that include Connected quadruple excitations, T4: CCSDQ-1 and Q(CCSDT)*. *Chem. Phys. Lett.*, 158(6):550–555, 1989.
- 139 Wim Klopper. Highly accurate coupled-cluster singlet and triplet pair energies from explicitly correlated calculations in comparison with extrapolation techniques. *Mol. Phys.*, 99(6):481–507, 2001.
- 140 Amir Karton and Jan M. L. Martin. Comment on: “Estimating the Hartree–Fock limit from finite basis set calculations” [Jensen F (2005) *Theor Chem Acc* 113:267]. *Theor. Chem. Acc.*, 115(4):330–333, December 2005.
- 141 Frank Jensen. Estimating the Hartree–Fock limit from finite basis set calculations. *Theor. Chem. Acc.*, 113(5):267–273, June 2005.
- 142 Frank Jensen. On the accuracy of numerical Hartree-Fock energies. *Theor. Chem. Acc.*, 113(3):187–190, January 2005.
- 143 Wim Klopper, Jozef Noga, Henrik Koch, and Trygve Helgaker. Multiple basis sets in calculations of triples corrections in coupled-cluster theory. *Theor. Chem. Accounts Theory, Comput. Model. (Theoretica Chim. Acta)*, 97(1-4):164–176, October 1997.
- 144 Jan M. L. Martin and Peter R. Taylor. Benchmark quality total atomization energies of small polyatomic molecules. *J. Chem. Phys.*, 106(20):8620, 1997.
- 145 Asger Halkier, Trygve Helgaker, Poul Jørgensen, Wim Klopper, Henrik Koch, Jeppe Olsen, and Angela K. Wilson. Basis-set convergence in correlated calculations on Ne, N₂, and H₂O. *Chem. Phys. Lett.*, 286:243–252, 1998.
- 146 David Feller, Kirk A. Peterson, and T. Daniel Crawford. Sources of error in electronic structure calculations on small chemical systems. *J. Chem. Phys.*, 124(5):054107, February 2006.

-
- 147 Asger Halkier, Wim Klopper, Trygve Helgaker, Poul Jørgensen, and Peter R. Taylor. Basis set convergence of the interaction energy of hydrogen-bonded complexes. *J. Chem. Phys.*, 111(20):9157, 1999.
- 148 Keld L Bak, Poul Jørgensen, Jeppe Olsen, Trygve Helgaker, and Wim Klopper. Accuracy of atomization energies and reaction enthalpies in standard and extrapolated electronic wave function basis set calculations. *J. Chem. Phys.*, 112(21):9229–9242, 2000.
- 149 Markus Reiher. Douglas–Kroll–Hess Theory: a relativistic electrons-only theory for chemistry. *Theor. Chem. Acc.*, 116(1-3):241–252, January 2006.
- 150 M. Douglas and N. M. Kroll. Quantum electrodynamical corrections to fine-structure of helium. *Ann. Phys.*, 82:88–155, 1974.
- 151 B.A. Hess. Applicability of the no-pair equation with free-particle projection operators to atomic and molecular-structure calculations. *Phys. Rev. A*, 32:756–763, 1985.
- 152 B.A. Hess. Relativistic electronic-structure calculations employing a 2-component no-pair formalism with external-field projection operators. *Phys. Rev. A*, 33:3742–3748, 1986.
- 153 G. Jansen and B.A. Hess. Revision of the Douglas-Kroll transformation. *Phys. Rev. A*, 39:6016–6017, 1989.
- 154 L. Visscher and K.G. Dyall. Dirac-Fock atomic electronic structure calculations using different nuclear charge distributions. *At. Data Nucl. Data Tables*, 67:207–224, 1997.
- 155 C.E. Moore. *Atomic Energy Levels*, volume I and II. National Bureau of Standards, Washington, D.C., 1971.
- 156 David Feller, Kirk A. Peterson, Wibe A. de Jong, and David A. Dixon. Performance of coupled cluster theory in thermochemical calculations of small halogenated compounds. *J. Chem. Phys.*, 118(8):3510, 2003.
- 157 Chengteh Lee, Weitao Yang, and Robert G. Parr. Development of the Colle-Salvetti correlation-energy formula into a functional of the electron density. *Phys. Rev. B*, 37(2):785, 1988.
- 158 Axel D. Becke. A new mixing of Hartree–Fock and local density-functional theories. *J. Chem. Phys.*, 98(2):1372, 1993.
- 159 T.H. Dunning Jr. and P. J. Hay. Gaussian Basis Sets for Molecular Calculations. In Henry F. Schaefer III, editor, *Methods Electron. Struct. Theory*, Vol.3, page 462. 1977.
- 160 Luis R. Kahn, Paul Baybutt, and Donald G. Truhlar. Ab initio effective core potentials: Reduction of all-electron molecular structure calculations to calculations involving only valence electrons. *J. Chem. Phys.*, 65(10):3826, 1976.

Bibliography

- 161 Yoon S. Lee, Walter C. Ermler, and Kenneth S. Pitzer. Ab initio effective core potentials including relativistic effects. I. Formalism and applications to the Xe and Au atoms. *J. Chem. Phys.*, 67(12):5861, 1977.
- 162 Phillip A. Christiansen, Yoon S. Lee, and Kenneth S. Pitzer. Improved ab initio effective core potentials for molecular calculations. *J. Chem. Phys.*, 71(11):4445, 1979.
- 163 Luis Fernandez Pacios and P. A. Christiansen. Ab initio relativistic effective potentials with spin-orbit operators. I. Li through Ar. *J. Chem. Phys.*, 82(6):2664, 1985.
- 164 M. M. Hurley, Luis Fernandez Pacios, P. A. Christiansen, R. B. Ross, and W. C. Ermler. Ab initio relativistic effective potentials with spin-orbit operators. II. K through Kr. *J. Chem. Phys.*, 84(12):6840, 1986.
- 165 Jürgen Gauss, Attila Tajti, Mihály Kállay, John F. Stanton, and Péter G. Szalay. Analytic calculation of the diagonal Born-Oppenheimer correction within configuration-interaction and coupled-cluster theory. *J. Chem. Phys.*, 125(14):144111, October 2006.
- 166 Larry A. Curtiss, Krishnan Raghavachari, Paul C. Redfern, and John A. Pople. Assessment of Gaussian-2 and density functional theories for the computation of enthalpies of formation. *J. Chem. Phys.*, 106(3):1063, 1997.
- 167 Amir Karton, Alex Tarnopolsky, Jean-François Lamère, George C. Schatz, and Jan M.L. Martin. Highly accurate first-principles benchmark data sets for the parametrization and validation of density functional and other approximate methods. Derivation of a robust, generally applicable, double-hybrid functional for thermochemistry and thermochemical. *J. Phys. Chem. A*, 112(50):12868–86, December 2008.
- 168 Kirk A. Peterson, Sergei Skokov, and Joel M. Bowman. A theoretical study of the vibrational energy spectrum of the HOCl/HClO system on an accurate ab initio potential energy surface. *J. Chem. Phys.*, 111(16):7446, 1999.
- 169 Richard A. Ashby. The infrared spectrum of HOCl. *J. Mol. Spectrosc.*, 23(4):439–447, 1967.
- 170 Richard A. Ashby. On the infrared spectrum of HOCl. *J. Mol. Spectrosc.*, 40(3):639–640, December 1971.
- 171 Kenneth Hedberg and Richard M. Badger. The Infrared Spectra of HOCl and DOCl. *J. Chem. Phys.*, 19(4):508, December 1951.
- 172 Pablo A. Denis. Thermochemistry of the hypobromous and hypochlorous acids, HOBr and HOCl. *J. Phys. Chem. A*, 110(17):5887–92, May 2006.
- 173 Branko Ruscic, Reinhardt E. Pinzon, Melita L. Morton, Nanda K. Srinivasan, Meng-Chih Su, James W. Sutherland, and Joe V. Michael. Active Thermochemical Tables: accurate enthalpy of formation of hydroperoxyl radical, HO₂. *J. Phys. Chem. A*, 110(21):6592–601, June 2006.

-
- 174 Y. Koga, H. Takeo, S. Kondo, M. Sugie, C. Matsumura, G.A. McRae, and E.A. Cohen. The Rotational Spectra, Molecular Structure, Dipole Moment and Hyperfine Constants of HOBr and DOBr. *J. Mol. Spectrosc.*, 138:467–481, 1989.
- 175 G.A. McRae and E.A. Cohen. The ν_2 band of HOBr. *J. Mol. Spectrosc.*, 139(2):369, 1990.
- 176 I. Barnes, V. Bastian, K.H. Becker, R. Overath, and T. Zhu. Rate constants for the reactions of Br atoms with a series of alkanes, alkenes, and alkynes in the presence of O₂. *Int. J. Chem. Kinet.*, 21(7):499, 1989.
- 177 Matthew D. Liptak and George C. Shields. Thermodynamic Cycles Used for pKa Complete Basis Set and Gaussian- n Models Combined with CPCM Continuum Solvation Methods. *Int. J. Quantum Chem.*, 85:727–741, 2001.
- 178 Gregory V. Korshin. Chlorine Based Oxidants for Water Purification and Disinfection. In P. Tratnyek, T. Grundl, and S. Haderlein, editors, *Aquat. Redox Chem.*, chapter 11, pages 223–245. American Chemical Society: Washington, DC, 2012.
- 179 Vincent C. Hand and Dale W. Margerum. Kinetics and Mechanisms of Decomposition of Dichloramine in Aqueous Solution. *Inorg. Chem.*, 22(23):1449–1456, 1983.
- 180 Johannes Edmund Wajon and J. Carrell Morris. Rates of Formation of N-Bromo Amines in Aqueous Solution. *Inorg. Chem.*, 21(12):4258–4263, 1982.
- 181 Richard L. Valentine, Chad T. Jafvert, and Solomon W. Leung. Evaluation of Chloramine Decomposition Model Incorporating General-Acid Catalysis. *Water Res.*, 22(9):1147–1153, 1988.
- 182 John L. Cromer, Guy W. Inman, and J. Donald Johnson. Dibromamine Decomposition Kinetics. In A. J. Rubin, editor, *Chem. Wastewater Technol.*, chapter 14, pages 213–225. Ann Arbor Science, Ann Arbor, MI, 1980.
- 183 Jose Luis S. Saguinsin and J. Carrell Morris. The chemistry of aqueous nitrogen trichloride. In J.D. Johnson, editor, *Disinfect. - Water wastewater Treat.*, pages 277–299. Ann Arbor Science, Ann Arbor, MI, 1975.
- 184 Edward T. Gray, Dale W. Margerum, and Ronald P. Huffman. Chloramine Equilibria and the Kinetics of Disproportionation in aqueous solution. In F.E. Brechman and J.M. Bellama, editors, *Organometals Organometalloids Occur. Fate Environ.*, chapter 16, pages 264–277. 1978.
- 185 Richard L. Valentine and Chad T. Jafvert. General Acid Catalysis of Monochloramine Disproportionation. *Environ. Sci. Technol.*, 22(6):691–696, 1988.
- 186 Guy W. Inman and J. Donald Johnson. Kinetics of Monobromamine Disproportionation-Dibromamine formation in aqueous ammonia solutions. *Environ. Sci. Technol.*, 18(4):219–224, 1984.

Bibliography

- 187 Sebastien Allard, Jace Tan, Cynthia A. Joll, and Urs von Gunten. Mechanistic Study on the Formation of Cl-/Br-/I-Trihalomethanes during Chlorination/Chloramination Combined with a Theoretical Cytotoxicity Evaluation. *Environ. Sci. Technol.*, 49(18):11105–14, September 2015.
- 188 Guanghui Hua and David A. Reckhow. Comparison of disinfection byproduct formation from chlorine and alternative disinfectants. *Water Res.*, 41(8):1667–78, April 2007.
- 189 Hekap Kim, Jaeho Shim, and Soohyung Lee. Formation of disinfection by-products in chlorinated swimming pool water. *Chemosphere*, 46(1):123–130, January 2002.
- 190 Julien Le Roux, Hervé Gallard, and Jean-Philippe Croué. Chloramination of nitrogenous contaminants (pharmaceuticals and pesticides): NDMA and halogenated DBPs formation. *Water Res.*, 45(10):3164–74, May 2011.
- 191 Eleni Malliarou, Chris Collins, Nigel Graham, and Mark J. Nieuwenhuijsen. Haloacetic acids in drinking water in the United Kingdom. *Water Res.*, 39(12):2722–30, July 2005.
- 192 Xiangyu Bi, Bin Xu, Yi-Li Lin, Chen-Yan Hu, Tao Ye, and Cao Qin. Monochloramination of Oxytetracycline: Kinetics, Mechanisms, Pathways, and Disinfection By-Products Formation. *CLEAN - Soil, Air, Water*, 41(10):969–975, June 2013.
- 193 Hiroshi Sakai, Shunsuke Tokuhara, Michio Murakami, Koji Kosaka, Kumiko Oguma, and Satoshi Takizawa. Comparison of chlorination and chloramination in carbonaceous and nitrogenous disinfection byproduct formation potentials with prolonged contact time. *Water Res.*, 88:661–70, January 2016.
- 194 Fabian Soltermann, Silvio Canonica, and Urs von Gunten. Trichloramine reactions with nitrogenous and carbonaceous compounds: Kinetics, products and chloroform formation. *Water Res.*, 71:318–329, 2015.
- 195 Julien Le Roux, Maolida Nihemaiti, and Jean-Philippe Croué. The role of aromatic precursors in the formation of haloacetamides by chloramination of dissolved organic matter. *Water Res.*, 88:371–9, January 2016.
- 196 Chiheng Chu, Paul R. Erickson, Rachel A. Lundeen, Dimitrios Stamatelatos, Peter J. Alaimo, Douglas E. Latch, and Kristopher McNeill. Photochemical and Nonphotochemical Transformations of Cysteine with Dissolved Organic Matter. *Environ. Sci. Technol.*, 50(12):6363–6373, June 2016.
- 197 Yi-Hsueh Chuang and Hsin-Hsin Tung. Formation of trichloronitromethane and dichloroacetonitrile in natural waters: precursor characterization, kinetics and interpretation. *J. Hazard. Mater.*, 283:218–26, February 2015.
- 198 Meric Selbes, Daekyun Kim, Nuray Ates, and Tanju Karanfil. The roles of tertiary amine structure, background organic matter and chloramine species on NDMA formation. *Water Res.*, 47(2):945–53, February 2013.

-
- 199 Ina Kristiana, Jace Tan, Cynthia A. Joll, Anna Heitz, Urs von Gunten, and Jeffrey W. A. Charrois. Formation of N-nitrosamines from chlorination and chloramination of molecular weight fractions of natural organic matter. *Water Res.*, 47(2):535–546, 2013.
- 200 Junghoon Choi and Richard L. Valentine. Formation of N-nitrosodimethylamine (NDMA) from reaction of monochloramine: a new disinfection by-product. *Water Res.*, 36(4):817–24, February 2002.
- 201 Julien Le Roux, Jean-Philippe Croue, and Marie Deborde. NDMA Formation by Chloramination of Ranitidine: Kinetics and Mechanism. *Environ. Sci. Technol.*, 46:11095–11103, 2012.
- 202 Jeanne Luh and Benito J. Mariñas. Bromide ion effect on N-nitrosodimethylamine formation by monochloramine. *Environ. Sci. Technol.*, 46(9):5085–92, May 2012.
- 203 Zhuo Chen and Richard L. Valentine. Modeling the formation of N-nitrosodimethylamine (NDMA) from the reaction of natural organic matter (NOM) with monochloramine. *Environ. Sci. Technol.*, 40(23):7290–7, December 2006.
- 204 Yong Dong Liu, Meric Selbes, Chengchu Zeng, Rugang Zhong, and Tanju Karanfil. Formation Mechanism of NDMA from Ranitidine, Trimethylamine, and Other Tertiary Amines during Chloramination: A Computational Study. *Environ. Sci. Technol.*, 48(15):8653–63, July 2014.
- 205 Timothy W. Trofe, Guy W. Inman, and J. Donald Johnson. Kinetics of monochloramine decomposition in the presence of bromide. *Environ. Sci. Technol.*, 14(5):544–549, May 1980.
- 206 Thomas F. LaPointe, Guy W. Inman, and J. Donald Johnson. Kinetics of Tribromamine decomposition. In *Disinfect. Water wastewater Treat.*, chapter 15, pages 301–338. 1975.
- 207 Andrew Bousher, Peter Brimblecombe, and Derek Midgley. Rate of hypobromite formation in chlorinated seawater. *Water Res.*, 20(7):865–870, July 1986.
- 208 Krishan Kumar and Dale W. Margerum. Kinetics and Mechanism of General-Acid-Assisted Oxidation of Bromide by Hypochlorite and Hypochlorous Acid. *Inorg. Chem.*, 26(4):2706–2711, 1987.
- 209 Z. Chen, L. Yang, X. Zhai, S. Zhao, A. Li, and J. Shen. N-nitrosamine formation during chlorination/chloramination of bromide-containing water. *Water Sci. Technol. Water Supply -WSTWS*, 10(3):462–471, 2010.
- 210 Lilly Heller-Grossman, Anna Idin, Bracha Limoni-Relis, and Menahem Rebhun. Formation of Cyanogen Bromide and Other Volatile DBPs in the Disinfection of Bromide-Rich Lake Water. *Environ. Sci. Technol.*, 33(6):932–937, March 1999.

Bibliography

- 211 Clare L. Hawkins and Michael J. Davies. The role of reactive N-bromo species and radical intermediates in hypobromous acid-induced protein oxidation. *Free Radic. Biol. Med.*, 39(7):900–912, October 2005.
- 212 Krishan Kumar, Roger W. Shinness, and Dale W. Margerum. Kinetics and Mechanisms of the Base Decomposition of Nitrogen Trichloride in Aqueous Solution. *Inorg. Chem.*, 26:3430–3434, 1987.
- 213 Werner R. Haag and Milton H. Lietzke. A kinetic model for predicting the concentration of active halogen species in chlorinated saline cooling waters. In *Water Chlorination Environ. Impact Heal. Eff. Vol. 3*, pages 415–426. 1980.
- 214 Ron Hofmann and Robert C. Andrews. Ammoniacal bromamines: a review of their influence on bromate formation during ozonation. *Water Res.*, 35(3):599–604, 2001.
- 215 Richard Sugam and George R. Helz. Chlorine Speciation in seawater; a metastable equilibrium model for Cl and Br species. *Chemosphere*, 10:41–57, 1981.
- 216 Juan M. Antelo, Florencio Arce, Juan Crujeiras, Edward T. Gray, and Patricia Yebra. Kinetics and thermodynamics of the reaction of aliphatic N-bromamines with bromide ion in acid media, and the pKa of N-bromamines. *J. Chem. Soc. Perkin Trans. 2*, (3):651–656, January 1999.
- 217 J. Andrés, M. Canle L., M.V. García, L.F. Rodríguez Vázquez, and J.A. Santaballa. A B3LYP/6-31G** study on the chlorination of ammonia by hypochlorous acid. *Chem. Phys. Lett.*, 342(3-4):405–410, July 2001.
- 218 Mark S. Rayson, Mohammednoor Altarawneh, John C. Mackie, Eric M. Kennedy, and Bogdan Z. Dlugogorski. Theoretical Study of the Ammonia-Hypochlorous Acid Reaction Mechanism. *J. Phys. Chem. A*, 114(7):2597–606, February 2010.
- 219 Tena Tarade and Valerije Vrček. Reactivity of amines with hypochlorous acid: Computational study of steric, electronic, and medium effects. *Int. J. Quantum Chem.*, 113(7):881–890, April 2013.
- 220 Anwar G. Baboul, Larry A. Curtiss, Paul C. Redfern, and Krishnan Raghavachari. Gaussian-3 theory using density functional geometries and zero-point energies. *J. Chem. Phys.*, 110(16):7650, April 1999.
- 221 Daniela Trogolo and J. Samuel Arey. Benchmark Thermochemistry of Chloramines, Bromamines, and Bromochloramines: Halogen Oxidants Stabilized by Electron Correlation. *Phys. Chem. Chem. Phys.*, 17(5):3584–3598, 2015.
- 222 Daniela Trogolo and J. Samuel Arey. Correction to "Benchmark Thermochemistry of Chloramines, Bromamines, and Bromochloramines: Halogen Oxidants Stabilized by Electron Correlation". *Phys. Chem. Chem. Phys.*, 18:31337–31337, 2016.

-
- 223 Arie Ben-Naim. *Solvation Thermodynamics*. Plenum Press, New York, 1987.
- 224 Vyacheslav S. Bryantsev, Mamadou S. Diallo, and William A. Goddard III. Calculation of Solvation Free Energies of Charged Solutes Using Mixed Cluster/Continuum Models. *J. Phys. Chem. B*, 112(32):9709–19, August 2008.
- 225 David E. Woon and Thom H. Dunning. Gaussian basis sets for use in correlated molecular calculations. III. The atoms aluminum through argon. *J. Chem. Phys.*, 98(2):1358, January 1993.
- 226 Aleksandr V. Marenich, Christopher J. Cramer, and Donald G. Truhlar. Universal Solvation Model Based on Solute Electron Density and on a Continuum Model of the Solvent Defined by the Bulk Dielectric Constant and Atomic Surface Tensions. *J. Phys. Chem. B*, 113(18):6378–96, May 2009.
- 227 Vincenzo Barone and Maurizio Cossi. Quantum Calculation of Molecular Energies and Energy Gradients in Solution by a Conductor Solvent Model. *J. Phys. Chem. A*, 102(11):1995–2001, March 1998.
- 228 Maurizio Cossi, Nadia Rega, Giovanni Scalmani, and Vincenzo Barone. Energies, structures, and electronic properties of molecules in solution with the C-PCM solvation model. *J. Comput. Chem.*, 24(6):669–81, April 2003.
- 229 S. Miertuš, E. Scrocco, and J. Tomasi. Electrostatic interaction of a solute with a continuum. A direct utilization of ab initio molecular potentials for the prevision of solvent effects. *Chem. Phys.*, 55(1):117–129, February 1981.
- 230 Jacopo Tomasi, Benedetta Mennucci, and Roberto Cammi. Quantum mechanical continuum solvation models. *Chem. Rev.*, 105(8):2999–3093, August 2005.
- 231 Giovanni Scalmani and Michael J. Frisch. Continuous surface charge polarizable continuum models of solvation. I. General formalism. *J. Chem. Phys.*, 132(11):114110, March 2010.
- 232 A. Klamt and G. Schüürmann. COSMO: a new approach to dielectric screening in solvents with explicit expressions for the screening energy and its gradient. *J. Chem. Soc. Perkin Trans. 2*, (5):799, January 1993.
- 233 Darrin M. York and Martin Karplus. A Smooth Solvation Potential Based on the Conductor-Like Screening Model. *J. Phys. Chem. A*, 103(50):11060–11079, December 1999.
- 234 Daniela Trogolo, Brijesh Kumar Mishra, Michèle B. Heeb, Urs von Gunten, and J. Samuel Arey. Molecular Mechanism of NDMA Formation from N,N-Dimethylsulfamide During Ozonation: Quantum Chemical Insights into a Bromide-Catalyzed Pathway. *Environ. Sci. Technol.*, 49:4163–75, March 2015.

Bibliography

- 235 Lars Goerigk and Stefan Grimme. A General Database for Main Group Thermochemistry, Kinetics, and Noncovalent Interactions - Assessment of Common and Reparameterized (meta-) GGA Density Functionals. *J. Chem. Theory Comput.*, 6:107–126, 2010.
- 236 Martin Korth and Stefan Grimme. “Mindless” DFT Benchmarking. *J. Chem. Theory Comput.*, 5(4):993–1003, April 2009.
- 237 Roberto Improta, Vincenzo Barone, Giovanni Scalmani, and Michael J. Frisch. A state-specific polarizable continuum model time dependent density functional theory method for excited state calculations in solution. *J. Chem. Phys.*, 125(5):054103, August 2006.
- 238 Roberto Improta, Giovanni Scalmani, Michael J. Frisch, and Vincenzo Barone. Toward effective and reliable fluorescence energies in solution by a new state specific polarizable continuum model time dependent density functional theory approach. *J. Chem. Phys.*, 127(7):074504, August 2007.
- 239 Michèle B. Heeb. *The Role of Bromide in Oxidative Water Treatment*. PhD thesis, Ecole polytechnique Fédérale de Lausanne (EPFL), 2016.
- 240 Junming Ho and Michelle L. Coote. A universal approach for continuum solvent pKa calculations: are we there yet? *Theor. Chem. Acc.*, 125(1-2):3–21, November 2010.
- 241 Junming Ho. Are thermodynamic cycles necessary for continuum solvent calculation of pKas and reduction potentials? *Phys. Chem. Chem. Phys.*, 17(4):2859–68, January 2015.
- 242 Junming Ho and Mehmed Z Ertem. Calculating Free Energy Changes in Continuum Solvation Models. *J. Phys. Chem. B*, 120(7):1319–29, February 2016.
- 243 Shuming Zhang. A Reliable and Efficient First Principles-Based Method for Predicting pKa Values. 4. Organic Bases. *J. Comput. Chem.*, 33(31):2469–82, December 2012.
- 244 Peter R. Tentscher, Soren N. Eustis, Kristopher McNeill, and J. Samuel Arey. Aqueous Oxidation of Sulfonamide Antibiotics: Aromatic Nucleophilic Substitution of an Aniline Radical Cation. *Chem. - A Eur. J.*, 19(34):11216–23, August 2013.
- 245 Rodrigo Casasnovas, Joaquin Ortega-Castro, Juan Frau, Josefa Donoso, and Francisco Muñoz. Theoretical pKa calculations with continuum model solvents, alternative protocols to thermodynamic cycles. *Int. J. Quantum Chem.*, 114(20):1350–1363, October 2014.
- 246 J. A. Montgomery, M. J. Frisch, J. W. Ochterski, and G. A. Petersson. A complete basis set model chemistry. VI. Use of density functional geometries and frequencies. *J. Chem. Phys.*, 110(6):2822–27, 1999.
- 247 J. A. Montgomery Jr., M. J. Frisch, J. W. Ochterski, and G. A. Petersson. A complete basis set model chemistry. VII. Use of the minimum population localization method. *J. Chem. Phys.*, 112(15):6532–6542, 2000.

- 248 Matthew D. Liptak and George C. Shields. Accurate pKa Calculations for Carboxylic Acids Using Complete Basis Set and Gaussian-n Models Combined with CPCM Continuum Solvation Methods. *J. Am. Chem. Soc.*, 123(30):7314–9, August 2001.
- 249 Matthew D. Liptak, Kevin C. Gross, Paul G. Seybold, Steven Feldgus, and George C. Shields. Absolute pKa Determinations for Substituted Phenols. *J. Am. Chem. Soc.*, 124:6421–6427, 2002.
- 250 R. Casasnovas, J. Frau, J. Ortega-Castro, A. Salvà, J. Donoso, and F. Muñoz. Absolute and relative pKa calculations of mono and diprotic pyridines by quantum methods. *J. Mol. Struct. THEOCHEM*, 912:5–12, October 2009.
- 251 Yan Zhao, Nathan E. Schultz, and Donald G. Truhlar. Exchange-correlation functional with broad accuracy for metallic and nonmetallic compounds, kinetics, and noncovalent interactions. *J. Chem. Phys.*, 123(16):161103, October 2005.
- 252 D. H. Everett and B. R. W. Pinsent. The Dissociation Constants of Ethylene Diammonium and Hexamethylene Diammonium Ions from 0 degrees to 60 degrees C. *Proc. R. Soc. A Math. Phys. Eng. Sci.*, 215(1122):416–429, December 1952.
- 253 Norris F. Hall and Marshall R. Sprinkle. Relations between the structure and strength of certain organic bases in aqueous solution. *J. Am. Chem. Soc.*, 54(9):3469–3485, September 1932.
- 254 J. Hansson. Reaction between alkene oxides and amines. VII. Determination of dissociation constants for some mixed tertiary aliphatic amines. *Sven. Kem. Tidskr.*, 67:256–262, 1955.
- 255 H. C. Brown, D. H. McDaniel, O. Hafliger, and F. C. Nachod. Determination of Organic Structures by Physical Methods. In E.A. Braude and F.C. Nachod, editors, *Determ. Org. Struct. by Phys. Methods*, page 810. Academic Press, New York, 1955.
- 256 T. C. Bissot, R. W. Parry, and D. H. Campbell. The Physical and Chemical Properties of the Methylhydroxylamines I. *J. Am. Chem. Soc.*, 79(4):796–800, February 1957.
- 257 G. Schwarzenbach. Zur Berechnung intramolekularer Atomabstände aus den Dissoziationskonstanten zweibasischer Säuren II. Die Acidität einiger Dicarbonsäuren und Polymethylen-diammoniumionen in Wasser-Alkohol-Mischungen. *Helv. Chim. Acta*, 16(1):522–528, 1933.
- 258 Charles D. Hodgman, editor. *Handbook of Chemistry and Physics*. Chemical Rubber Publishing Company, Cleveland, OH, 1951.
- 259 G. Bordwell. Equilibrium Acidities in Dimethyl Sulfoxide Solution. *Acc. Chem. Res*, 21:456–463, 1988.

Bibliography

- 260 Thomas J. Hannigan and William J. Spillane. Basicity of Nitrogen-Sulphur(VI) Compounds. Part 4.1 Ionization of Di- and Tri-substituted Sulphamides. *J. Chem. Soc. Perkin Trans. II*, (3):851–855, 1982.
- 261 Rolf Sander. Henry's Law Constants. In P. J. Linstrom and W. G. Mallard, editors, *NIST Chem. WebBook, NIST Stand. Ref. Database Number 69*. National Institute of Standards and Technology, Gaithersburg MD, 20899, 2011.
- 262 Aleksandr V. Marenich, Casey P. Kelly, Jason D. Thompson, Gregory D. Hawkins, Candee C. Chambers, David J. Giesen, Paul Winget, Christopher J. Cramer, and Donald G. Truhlar. Minnesota Solvation Database, 2012.
- 263 R. Sander. Compilation of Henry's law constants (version 4.0) for water as solvent. *Atmos. Chem. Phys.*, 15(8):4399–4981, April 2015.
- 264 Marvin Leroy Granstrom. *The Disproportionation of Monochloramine*. PhD thesis, Harvard University, 1954.
- 265 Werner Stumm and James J. Morgan. *Aquatic Chemistry: Chemical Equilibria and Rates in Natural Waters*. Wiley-Interscience, 3 edition, 1995.
- 266 Eric V. Anslyn and Dennis A. Dougherty. *Modern Physical Organic Chemistry*. University Science Books, 2006.
- 267 David L. Sedlak and Urs von Gunten. The Chlorine Dilemma. *Science*, 331(6013):42–3, January 2011.
- 268 William A. Mitch and David L. Sedlak. Formation of N-Nitrosodimethylamine (NDMA) from dimethylamine during chlorination. *Environ. Sci. Technol.*, 36(4):588–95, February 2002.
- 269 Ning Dai and William A. Mitch. Relative Importance of N-Nitrosodimethylamine Compared to Total N-Nitrosamines in Drinking Waters. *Environ. Sci. Technol.*, 47(8):3648–56, April 2013.
- 270 Andreas C. Gerecke and David L. Sedlak. Precursors of N-Nitrosodimethylamine in Natural Waters. *Environ. Sci. Technol.*, 37(7):1331–1336, 2003.
- 271 David L. Sedlak, Rula A. Deeb, Elisabeth L. Hawley, William A. Mitch, D. Timothy, Sam Mowbray, Steve Carr, A. Mitch, D. Durbin, and L. Hawley. Sources and Fate of Nitrosodimethylamine in Municipal its Precursors Treatment Wastewater Plants. *Water Environ. Res.*, 77(1):32–39, 2005.
- 272 Stuart W. Krasner, William A. Mitch, Daniel L. McCurry, David Hanigan, and Paul Westerhoff. Formation, precursors, control, and occurrence of nitrosamines in drinking water: a review. *Water Res.*, 47(13):4433–50, September 2013.

-
- 273 William A. Mitch and David L. Sedlak. Characterization and fate of N-nitrosodimethylamine precursors in municipal wastewater treatment plants. *Environ. Sci. Technol.*, 38(5):1445–54, March 2004.
- 274 William A. Mitch, Jonathan O. Sharp, R. Rhodes Trussell, Richard L. Valentine, Lisa Alvarez-cohen, and David L. Sedlak. N-Nitrosodimethylamine (NDMA) as a Drinking Water Contaminant: A Review. *Environ. Eng. Sci.*, 20(5), 2003.
- 275 Ruqiao Shen and Susan A. Andrews. Demonstration of 20 pharmaceuticals and personal care products (PPCPs) as nitrosamine precursors during chloramine disinfection. *Water Res.*, 45(2):944–52, January 2011.
- 276 Wei-Hsiang Chen and Thomas M. Young. NDMA formation during chlorination and chloramination of aqueous diuron solutions. *Environ. Sci. Technol.*, 42(4):1072–7, February 2008.
- 277 Bin Xu, Cao Qin, Chen-Yan Hu, Yi-Li Lin, Sheng-Ji Xia, Qian Xu, Seleli Andrew Mwakagenda, Xiang-Yu Bi, and Nai-Yun Gao. Degradation kinetics and N-Nitrosodimethylamine formation during monochloramination of chlortoluron. *Sci. Total Environ.*, 417-418:241–7, February 2012.
- 278 Sang-Hyuck Park, Shuting Wei, Boris Mizaikoff, Amelia E. Taylor, Cedrick Favero, and Ching-Hua Huang. Degradation of Amine-based Water Treatment Polymers during Chloramination as N-Nitrosodimethylamine (NDMA) Precursors. *Environ. Sci. Technol.*, 43(5):1360–6, March 2009.
- 279 Riley C. Flowers and Philip C. Singer. Anion Exchange Resins as a Source of Nitrosamines and Nitrosamine Precursors. *Environ. Sci. Technol.*, 47(13):7365–72, July 2013.
- 280 Zhuo Chen and Richard L. Valentine. The Influence of the Pre-Oxidation of Natural Organic Matter on the Formation of N-Nitrosodimethylamine (NDMA). *Environ. Sci. Technol.*, 42(14):5062–7, July 2008.
- 281 Changha Lee, Carsten K Schmidt, Jeyong Yoon, and Urs von Gunten. Oxidation of N-Nitrosodimethylamine (NDMA) Precursors with Ozone and Chlorine Dioxide: Kinetics and Effect on NDMA Formation Potential. *Environ. Sci. Technol.*, 41(6):2056–63, March 2007.
- 282 Urs von Gunten. Ozonation of drinking water: part II. Disinfection and by-product formation in presence of bromide, iodide or chlorine. *Water Res.*, 37(7):1469–87, April 2003.
- 283 Przemysław Andrzejewski, Barbara Kasprzyk-Hordern, and Jacek Nawrocki. N-nitrosodimethylamine (NDMA) formation during ozonation of dimethylamine-containing waters. *Water Res.*, 42(4-5):863–70, February 2008.

Bibliography

- 284 Carsten K. Schmidt and Heinz-Jürgen Brauch. N,N-Dimethylsulfamide as Precursor for N-Nitrosodimethylamine (NDMA) Formation upon Ozonation and its Fate during Drinking Water Treatment. *Environ. Sci. Technol.*, 42(17):6340–6, September 2008.
- 285 Koji Kosaka, Katsuhito Fukui, Yasuo Kayanuma, Mari Asami, and Michihiro Akiba. N-Nitrosodimethylamine Formation from Hydrazine Compounds on Ozonation. *Ozone Sci. Eng.*, 36(3):215–220, June 2014.
- 286 Koji Kosaka, Mari Asami, Yusuke Konno, Masami Oya, and Shoichi Kunikane. Identification of Antiyellowing Agents as Precursors of N-Nitrosodimethylamine Production on Ozonation From Sewage Treatment Plant Influent. *Environ. Sci. Technol.*, 43(14):5236–41, July 2009.
- 287 Massimiliano Sgroi, Paolo Roccaro, Gregg L. Oelker, and Shane A. Snyder. N-Nitrosodimethylamine Formation upon Ozonation and Identification of Precursors Source in a Municipal Wastewater Treatment Plant. *Environ. Sci. Technol.*, 48:10308–10315, 2014.
- 288 Urs von Gunten, Elisabeth Salhi, Carsten K. Schmidt, and William A. Arnold. Kinetics and Mechanisms of N-Nitrosodimethylamine Formation upon Ozonation of Waters: Bromide Catalysis. *Environ. Sci. Technol.*, 44(15):5762–5768, 2010.
- 289 Werner R. Haag, Jurg Hoigné, and Heinz Bader. Improved Ammonia Oxidation by Ozone in the presence of Bromide Ion during Water Treatment. *Water Res.*, 18(9):1125–1128, 1984.
- 290 Francesco Fracchia, Claudia Filippi, and Claudio Amovilli. Multi-level Quantum Monte Carlo Wave Functions for Complex Reactions: the Decomposition of α -Hydroxy-Dimethylnitrosamine. *J. Comput. Chem.*, 35(1):30–8, January 2014.
- 291 Roberto Peverati and Donald G. Truhlar. Quest for a universal density functional: the accuracy of density functionals across a broad spectrum of databases in chemistry and physics. *Philos. Trans. R. Soc. A*, 372, 2014.
- 292 Yan Zhao and Donald G. Truhlar. How well can new-generation density functionals describe the energetics of bond-dissociation reactions producing radicals? *J. Phys. Chem. A*, 112(6):1095–9, February 2008.
- 293 Stefan Grimme. Semiempirical GGA-type density functional constructed with a long-range dispersion correction. *J. Comput. Chem.*, 27(15):1787–1799, 2006.
- 294 Yan Zhao, Nathan E. Schultz, and Donald G. Truhlar. Design of Density Functionals by Combining the Method of Constraint Satisfaction with Parametrization for Thermochemistry, Thermochemical Kinetics, and Noncovalent Interactions. *J. Chem. Theory Comput.*, 2:364–382, 2006.

- 295 Yan Zhao and Donald G. Truhlar. A new local density functional for main-group thermochemistry, transition metal bonding, thermochemical kinetics, and noncovalent interactions. *J. Chem. Phys.*, 125(19):194101, 2006.
- 296 Jingjing Zheng, Yan Zhao, and Donald G Truhlar. Thermochemical Kinetics of Hydrogen-Atom Transfers between Methyl , Methane , Ethynyl , Ethyne , and Hydrogen. *J. Phys. Chem. A*, 111:4632–4642, 2007.
- 297 Ernest R. Davidson. Comment on "Comment on Dunning' s correlation-consistent basis sets". *Chem. Phys. Lett.*, 260:514–518, 1996.
- 298 Jeffrey I. Steinfeld, Joseph S. Francisco, and William L. Hase. *Chemical Kinetics and Dynamics*. Pearson, second edition, 1999.
- 299 Jingzhi Pu, Jiali Gao, and Donald G Truhlar. Multidimensional Tunneling, Recrossing, and the Transmission Coefficient for Enzymatic Reactions. *Chem. Rev.*, 106(8):3140–69, August 2006.
- 300 Patrick Brezonc and William Arnold. *Water Chemistry: An Introduction to the Chemistry of Natural and Engineered Aquatic Systems*. Oxford University Press, 2011.
- 301 Jingzhi Pu and Donald G. Truhlar. Validation of variational transition state theory with multidimensional tunneling contributions against accurate quantum mechanical dynamics for $\text{H}+\text{CH}_4\Rightarrow\text{H}_2+\text{CH}_3$ in an extended temperature interval. *J. Chem. Phys.*, 117(4):1479–1481, 2002.
- 302 J. P. Foster and F. Weinhold. Natural hybrid orbitals. *J. Am. Chem. Soc.*, 102:7211–7218, 1980.
- 303 A. E. Reed, R. B. Weinstock, and F. Weinhold. Natural-population analysis. *J. Chem. Phys.*, 83:735–746, 1985.
- 304 A. E. Reed and F. Weinhold. Natural bond orbital analysis of near-Hartree-Fock water dimer. *J. Chem. Phys.*, 78:4066–4073, 1983.
- 305 A. E. Reed and F. Weinhold. Natural Localized Molecular Orbitals. *J. Chem. Phys.*, 83:1736–1740, 1985.
- 306 J. E. Carpenter and F. Weinhold. Analysis of the geometry of the hydroxymethyl radical by the different spins natural bond orbital procedure. *J. Mol. Struct. THEOCHEM*, 46:41–62, 1988.
- 307 A. E. Reed, Larry A. Curtiss, and F. Weinhold. Intermolecular interactions from a natural bond orbital, donor-acceptor viewpoint. *Chem. Rev.*, 88:899–926, 1988.
- 308 Robert C. Troy and Dale W. Margerum. Non-Metal Redox Kinetics: Hypobromite and Hypobromous Acid Reactions with Iodide and with Sulfite and the Hydrolysis of Bromosulfate. *Inorg. Chem.*, 30:3538–3543, 1991.

Bibliography

- 309 Michèle B. Heeb and Urs von Gunten. In Preparation.
- 310 John D. Sivey, J. Samuel Arey, Peter R. Tentscher, and A. Lynn Roberts. Reactivity of BrCl, Br₂, BrOCl, Br₂O and HOBr Toward Dimethenamid in Solutions of Bromide + Aqueous Free Chlorine. *Environ. Sci. Technol.*, 47(47):1330–1338, August 2013.
- 311 John D. Sivey, Corey E. McCullough, and A. Lynn Roberts. Chlorine monoxide (Cl₂O) and molecular chlorine (Cl₂) as active chlorinating agents in reaction of dimethenamid with aqueous free chlorine. *Environ. Sci. Technol.*, 44(9):3357–62, May 2010.
- 312 L. Abia, X. L. Armesto, M. Canle L., M. V. Garcia, and J. A. Santaballa. Oxidation of Aliphatic Amines by Aqueous Chlorine. *Tetrahedron*, 54:521–530, 1998.
- 313 Chunyang Peng, Philippe Y. Ayala, H. Bernhard Schlegel, and Michael J. Frisch. Using Redundant Internal Coordinates to Optimize Equilibrium Geometries and Transition States. *J. Comput. Chem.*, 17(1):49–56, 1996.
- 314 Kenichi Fukui. The Path of Chemical Reactions - The IRC Approach. *Acc. Chem. Res.*, 14(12):363–368, 1981.
- 315 Clifford Dykstra, Gernot Frenking, Kwang Kim, and Gustavo Scuseria, editors. *Theory and Applications of Computational Chemistry. The First Forty Years*. Elsevier, Amsterdam, 2005.
- 316 Clemens von Sonntag and Urs von Gunten. *Chemistry of Ozone in Water and Wastewater Treatment: From Basic Principles to Applications*. IWA Publishing, 2012.
- 317 Albino Castro, J. Ramón Leis, and M. Elena Peña. The efficiency of Nitrosyl Bromide in Nitrosating Aliphatic Amines. *J. Chem. Res.*, pages 216–217, 1986.
- 318 Hervé Gallard and Urs von Gunten. Chlorination of Phenols: Kinetics and Formation of Chloroform. *Environ. Sci. Technol.*, 36(5):884–90, March 2002.
- 319 Juan L. Acero, Philippe Piriou, and Urs von Gunten. Kinetics and mechanisms of formation of bromophenols during drinking water chlorination: assessment of taste and odor development. *Water Res.*, 39(13):2979–93, August 2005.
- 320 T. Launois, S. Belviso, L. Bopp, C. G. Fichot, and P. Peylin. A new model for the global biogeochemical cycle of carbonyl sulfide – Part 1: Assessment of direct marine emissions with an oceanic general circulation and biogeochemistry model. *Atmos. Chem. Phys.*, 15(5):2295–2312, March 2015.
- 321 Joe Berry, Adam Wolf, J. Elliott Campbell, Ian Baker, Nicola Blake, Don Blake, A. Scott Denning, S. Randy Kawa, Stephen A. Montzka, Ulrike Seibt, Keren Stimler, Dan Yakir, and Zhengxin Zhu. A coupled model of the global cycles of carbonyl sulfide and CO₂ : A possible new window on the carbon cycle. *J. Geophys. Res. Biogeosciences*, 118(2):842–852, June 2013.

-
- 322 Meinrat O. Andreae and Ronald J. Ferek. Photochemical production of carbonyl sulfide in seawater and its emission to the atmosphere. *Global Biogeochem. Cycles*, 6(2):175–183, June 1992.
- 323 M.A.K. Khalil and R.A. Rasmussen. Global sources, lifetimes and mass balances of carbonyl sulfide (OCS) and carbon disulfide (CS₂) in the earth's atmosphere. *Atmos. Environ.*, 18(9):1805–1813, January 1984.
- 324 I. Barnes, K. H. Becker, and I. Patroescu. The tropospheric oxidation of dimethyl sulfide: A new source of carbonyl sulfide. *Geophys. Res. Lett.*, 21(22):2389–2392, November 1994.
- 325 Ian Barnes, Jens Hjorth, and Nikos Mihalopoulos. Dimethyl sulfide and dimethyl sulfoxide and their oxidation in the atmosphere. *Chem. Rev.*, 106(3):940–75, March 2006.
- 326 S. Kloster, J. Feichter, E. Maier-Reimer, K. D. Six, P. Stier, and P. Wetzol. Biogeosciences DMS cycle in the marine ocean-atmosphere system – a global model study. *Biogeosciences*, 3:29–51, 2006.
- 327 David J. Kieber and Kenneth Mopper. Photochemistry and the Cycling of Carbon, Sulfur, Nitrogen and Phosphorus. In *Biogeochem. Mar. Dissolved Org. Matter*, chapter 9. 2002.
- 328 M. von Hobe, A.J. Kettle, and Meinrat O. Andreae. Carbonyl sulphide in and over seawater: summer data from the northeast Atlantic Ocean. *Atmos. Environ.*, 33(21):3503–3514, September 1999.
- 329 A.J. Kettle, T. S. Rhee, M. von Hobe, A. Poulton, J. Aiken, and M. O. Andreae. Assessing the flux of different volatile sulfur gases from the ocean to the atmosphere. *J. Geophys. Res.*, 106(D11):12193–12209, June 2001.
- 330 T. Launois, P. Peylin, S. Belviso, and B. Poulter. A new model of the global biogeochemical cycle of carbonyl sulfide – Part 2: Use of carbonyl sulfide to constrain gross primary productivity in current vegetation models. *Atmos. Chem. Phys.*, 15(16):9285–9312, August 2015.
- 331 R. P. Turco, R. C. Whitten, O. B. Toon, J. B. Pollack, and P. Hamill. OCS, stratospheric aerosols and climate. *Nature*, 283(5744):283–285, January 1980.
- 332 C. Brühl, J. Lelieveld, P. J. Crutzen, and H. Tost. The role of carbonyl sulphide as a source of stratospheric sulphate aerosol and its impact on climate. *Atmos. Chem. Phys.*, 12(3):1239–1253, February 2012.
- 333 E. C. Y. Inn, J. F. Vedder, B. J. Tyson, and D. O'Hara. COS in the stratosphere. *Geophys. Res. Lett.*, 6(3):191–193, March 1979.
- 334 A. J. Kettle. Global budget of atmospheric carbonyl sulfide: Temporal and spatial variations of the dominant sources and sinks. *J. Geophys. Res.*, 107(D22):4658, 2002.

Bibliography

- 335 Parvadha Suntharalingam, A. J. Kettle, S. M. Montzka, and D. J. Jacob. Global 3-D model analysis of the seasonal cycle of atmospheric carbonyl sulfide: Implications for terrestrial vegetation uptake. *Geophys. Res. Lett.*, 35(19):L19801, October 2008.
- 336 S. A. Montzka, P. Calvert, B. D. Hall, J. W. Elkins, T. J. Conway, P. P. Tans, and C. Sweeney. On the global distribution, seasonality, and budget of atmospheric carbonyl sulfide (COS) and some similarities to CO₂. *J. Geophys. Res.*, 112(D9):D09302, May 2007.
- 337 R. J. Ferek and M. O. Andreae. Photochemical production of carbonyl sulphide in marine surface waters. *Nature*, 307(5947):148–150, January 1984.
- 338 Veit S. Ulshöfer, Gunther Uher, and Meinrat O. Andreae. Evidence for a winter sink of atmospheric carbonyl sulfide in the northeast Atlantic Ocean. *Geophys. Res. Lett.*, 22(16):2601–2604, 1995.
- 339 Julia M. Diaz, Colleen M. Hansel, Bettina M. Voelker, Chantal M. Mendes, Peter F. Andeer, and Tong Zhang. Widespread production of extracellular superoxide by heterotrophic bacteria. *Science*, 340(6137):1223–6, June 2013.
- 340 Li Zhang, R. S. Walsh, and G. A. Cutter. Estuarine cycling of carbonyl sulfide: production and sea-air flux. *Mar. Chem.*, 61(3-4):127–142, 1998.
- 341 Gunther Uher and Meinrat O. Andreae. Photochemical production of carbonyl sulfide in North Sea water: A process study. *Limnol. Oceanogr.*, 42(3):432–442, 1997.
- 342 Peter S. Weiss, Steven S. Andrews, James E. Johnson, and Oliver C. Zafiriou. Photoproduction of carbonyl sulfide in South Pacific Ocean waters as a function of irradiation wavelength. *Geophys. Res. Lett.*, 22(3):215–218, February 1995.
- 343 Richard G. Zepp and Meinrat O. Andreae. Photosensitized formation of carbonyl sulfide in sea water. In *Eff. Sol. Ultrav. Radiat. Biogeochem. Dyn. Aquat. Environ.* 1990.
- 344 Joël Radford-Knoery and Gregory A. Cutter. Biogeochemistry of dissolved hydrogen sulfide species and carbonyl sulfide in the western North Atlantic Ocean. *Geochim. Cosmochim. Acta*, 58(24):5421–5431, 1994.
- 345 Peter S. Weiss, James E. Johnson, Richard H. Gammon, and Timothy S. Bates. Reevaluation of the open ocean source of carbonyl sulfide to the atmosphere. *J. Geophys. Res.*, 100(D11):23083, 1995.
- 346 N. Mihalopoulos, J. P. Putaud, B. C. Nguyen, and S. Belviso. Annual variation of atmospheric carbonyl sulfide in the marine atmosphere in the Southern Indian Ocean. *J. Atmos. Chem.*, 13(1):73–82, July 1991.
- 347 V.S. Ulshöfer, O.R. Flock, G. Uher, and M.O. Andreae. Photochemical production and air-sea exchange of carbonyl sulfide in the eastern Mediterranean Sea. *Mar. Chem.*, 53(1):25–39, 1996.

- 348 Simon F. Watts. The biogeochemistry of CS₂ and OCS in the sunlit ocean and precipitation. Technical report, GR9/65 Natural Environmental Research Council, Swindon, UK, 1991.
- 349 V.S. Ulshöfer and M.O. Andreae. Carbonyl Sulfide (COS) in the Surface Ocean and the Atmospheric COS Budget. *Aquat. Geochemistry*, 3(4):283–303, 1997.
- 350 Scott Elliott, Eric Lu, and F. Sherwood Rowland. Carbonyl sulfide hydrolysis as a source of hydrogen sulfide in open ocean seawater. *Geophys. Res. Lett.*, 14(2):131–134, February 1987.
- 351 Scott Elliott, Eric Lu, and F. Sherwood Rowland. Rates and mechanisms for the hydrolysis of carbonyl sulfide in natural waters. *Environ. Sci. Technol.*, 23(4):458–461, April 1989.
- 352 Degui Tang, Kent W Warnken, and Peter H Santschi. The distribution of biogenic thiols in surface waters of Galveston. *Limnol. Oceanogr.*, 45(6):1289–1297, 2013.
- 353 R. Al-Farawati and C. M. Van Den Berg. Thiols in coastal waters of the western North Sea and English Channel. *Environ. Sci. Technol.*, 35(10):1902–11, May 2001.
- 354 Haiying Hu, Steven E. Mylon, and Gaboury Benoit. Distribution of the thiols glutathione and 3-mercaptopropionic acid in Connecticut lakes. *Limnol. Oceanogr.*, 51(6):2763–2774, 2013.
- 355 Christopher L. Dupont, James. W. Moffett, Robert R. Bidigare, and Beth A. Ahner. Distributions of dissolved and particulate biogenic thiols in the subarctic Pacific Ocean. *Deep Sea Res. Part I Oceanogr. Res. Pap.*, 53(12):1961–1974, December 2006.
- 356 Anne Christine Le Gall and Constant M.G. Van Den Berg. Folic acid and glutathione in the water column of the North East Atlantic. *Deep Sea Res. Part I Oceanogr. Res. Pap.*, 45(11):1903–1918, November 1998.
- 357 Michael R. Hoffmann. Kinetics and mechanism of oxidation of hydrogen sulfide by hydrogen peroxide in acidic solution. *Environ. Sci. Technol.*, 11(1):61–66, January 1977.
- 358 Ira N. Levine. *Physical chemistry*. 2008.
- 359 A Ohno and S Oae. Thiols. In S. Oae, editor, *Org. Chem. Sulfur*, chapter 4, page 713. Plenum Press, New York, New York, NY, 1977.
- 360 P. S. Leung and M. R. Hoffmann. Kinetics and mechanism of autoxidation of 2-mercaptoethanol catalyzed by cobalt(II)-4,4',4'',4'''-tetrasulfophthalocyanine in aqueous solution. *Environ. Sci. Technol.*, 22(3):275–82, March 1988.
- 361 Klaus-Dieter Asmus. Sulfur-centered free radicals. *Methods Enzymol.*, 186, 1990.
- 362 Bruce C. Gilbert, Hugh A. H. Laue, Richard O. C. Norman, and Roger C. Sealy. Electron spin resonance studies. Part XLVI. Oxidation of thiols and disulphides in aqueous solution: formation of RS^{*}, RSO^{*}, RSO^{2*}, RSSR[•], and carbon radicals. *J. Chem. Soc., Perkin Trans. 2*, (9):892–900, January 1975.

Bibliography

- 363 Gábor Merényi, Johan Lind, and Lars Engman. The Dimethylhydroxysulfuranyl Radical. *J. Phys. Chem.*, 100(21):8875–8881, 1996.
- 364 David A. Armstrong, Robert E. Huie, Sergei Lyman, Willem H. Koppenol, Gabor Merényi, Pedatsur Neta, David M. Stanbury, Sten Steenken, and Peter Wardman. Standard electrode potentials involving radicals in aqueous solution: inorganic radicals. *Bioinorg. React. Mech.*, 9(1-4):59–61, January 2013.
- 365 Edyta Madej and Peter Wardman. The oxidizing power of the glutathione thiyl radical as measured by its electrode potential at physiological pH. *Arch. Biochem. Biophys.*, 462(1):94–102, 2007.
- 366 Silvio Canonica, Bruno Hellrung, and Jakob Wirz. Oxidation of Phenols by Triplet Aromatic Ketones in Aqueous Solution. *J. Phys. Chem. A*, 104(6):1226–1232, February 2000.
- 367 Silvio Canonica. Oxidation of Aquatic Organic Contaminants Induced by Excited Triplet States. *Chimia (Aarau)*, 61(10):641–644, 2007.
- 368 P. Neta, Robert E. Huie, and Alberta B. Ross. Rate constants for reaction of inorganic radicals in aqueous solution. *J. Phys. Chem. Ref. Data*, 17(3):1027–1284, 1988.
- 369 Kimberly M Parker and William A Mitch. Halogen radicals contribute to photooxidation in coastal and estuarine waters. *Proc. Natl. Acad. Sci. U. S. A.*, 113(21):5868–73, May 2016.
- 370 G. E. Adams, J. E. Aldrich, R. H. Bisby, R. B. Cundall, J. L. Redpath, and R. L. Willson. Selective Free Radical Reactions with Proteins and Enzymes: Reactions of Inorganic Radical Anions with Amino Acids. *Radiat. Res.*, 49(2):278, February 1972.
- 371 Christian Schoeneich, Ahmed Aced, and Klaus Dieter Asmus. Mechanism of oxidation of aliphatic thioethers to sulfoxides by hydroxyl radicals. The importance of molecular oxygen. *J. Am. Chem. Soc.*, 115(24):11376–11383, December 1993.
- 372 Schoen-nan Chen and Morton Z. Hoffman. Rate Constants for the Reaction of the Carbonate Radical with Compounds of Biochemical Interest in Neutral Aqueous Solution. *Radiat. Res.*, 56(1):40, October 1973.
- 373 T. David Waite, Donald T. Sawyer, and Oliver C. Zafriou. Panel 1: Oceanic reactive chemical transients. *Appl. Geochemistry*, 3(1):9–17, January 1988.
- 374 René-Christian Bouillon and William L. Miller. Photodegradation of dimethyl sulfide (DMS) in natural waters: laboratory assessment of the nitrate-photolysis-induced DMS oxidation. *Environ. Sci. Technol.*, 39(24):9471–7, December 2005.
- 375 Xianliang Zhou and Kenneth Mopper. Determination of photochemically produced hydroxyl radicals in seawater and freshwater. *Mar. Chem.*, 30:71–88, January 1990.

- 376 W. A. Prütz, J. Butler, E. J. Land, and A. J. Swallow. Unpaired electron migration between aromatic and sulfur peptide units. *Free Radic. Res. Commun.*, 2(1-2):69–75, 1986.
- 377 Peter Wardman. Reduction Potentials of One-Electron Couples Involving Free Radicals in Aqueous Solution. *J. Phys. Chem. Ref. Data*, 18(4):1637–1755, 1989.
- 378 Jeffrey J. Warren, Tristan A. Tronic, and James M. Mayer. Thermochemistry of proton-coupled electron transfer reagents and its implications. *Chem. Rev.*, 110(12):6961–7001, December 2010.
- 379 Parminder S. Surdhar and David A. Armstrong. Redox Potentials of Some Sulfur-Containing Radicals. *J. Phys. Chem.*, 2(15):5915–5917, 1986.
- 380 Werner R. Haag and Theodore Mill. Survey of Sunlight-Produced Transient Reactants in Surface Waters. In N. V. Blought and R. G. Zepp, editors, *Eff. Sol. Ultrav. Radiat. Biogeochem. Dyn. Aquat. Environ.*, pages 82–88. 1990.
- 381 Janel E. Grebel, Joseph J. Pignatello, Weihua Song, William J. Cooper, and William A. Mitch. Impact of halides on the photobleaching of dissolved organic matter. *Mar. Chem.*, 115(1-2):134–144, June 2009.
- 382 Andrew L. Rose, Eric A. Webb, T. David Waite, and James W. Moffett. Measurement and implications of nonphotochemically generated superoxide in the equatorial Pacific Ocean. *Environ. Sci. Technol.*, 42(7):2387–93, April 2008.
- 383 Marcello Brigante, Marco Minella, Gilles Mailhot, Valter Maurino, Claudio Minero, and Davide Vione. Formation and reactivity of the dichloride radical (Cl₂⁻) in surface waters: A modelling approach. *Chemosphere*, 95:464–469, October 2014.
- 384 Chun-Ying Liu, Min Zhao, Chun-Yan Ren, Gui-Peng Yang, Pei-Feng Li, and Yang Han. Direct Measurement of Nitric Oxide in Seawater Medium by Fluorometric Method. *Chinese J. Anal. Chem.*, 37(10):1463–1467, October 2009.
- 385 Emmanuel F. Olasehinde, Kazuhiko Takeda, and Hiroshi Sakugawa. Photochemical production and consumption mechanisms of nitric oxide in seawater. *Environ. Sci. Technol.*, 44(22):8403–8, November 2010.
- 386 Yan Zhao and Donald G. Truhlar. The M06 suite of density functionals for main group thermochemistry, thermochemical kinetics, noncovalent interactions, excited states, and transition elements: two new functionals and systematic testing of four M06-class functionals and 12 other function. *Theor. Chem. Acc.*, 120(1-3):215–241, July 2008.
- 387 Peter R. Tentscher and J. Samuel Arey. Geometries and Vibrational Frequencies of Small Radicals: Performance of Coupled Cluster and More Approximate Methods. *J. Chem. Theory Comput.*, 8:2165–2179, 2012.

Bibliography

- 388 Peter R. Tentscher and J. Samuel Arey. Binding in Radical-Solvent Binary Complexes: Benchmark Energies and Performance of Approximate Methods. *J. Chem. Theory Comput.*, 9(3):1568–1579, March 2013.
- 389 Richard J. Fehir, Jr. and James K. McCusker. Differential Polarization of Spin and Charge Density in Substituted Phenoxy Radicals. *J. Phys. Chem. A*, 113(32):9249–9260, August 2009.
- 390 George V. Buxton, Clive L. Greenstock, W. Phillip Helman, and Alberta B. Ross. Critical Review of Rate Constants for Reactions of Hydrated Electrons, Hydrogen Atoms and Hydroxyl Radicals ($\cdot\text{OH}/\cdot\text{O}\cdot$) in Aqueous Solution. *J Phys Chem Ref Data*, 17:513–886, 1988.
- 391 Francis Wilkinson and James G. Brummer. Rate constants for the decay and reactions of the lowest electronically excited singlet state of molecular oxygen in solution. *J. Phys. Chem. Ref. Data*, 10(4):809, 1981.
- 392 Kimberly M. Parker and William A. Mitch. Halogen radicals contribute to photooxidation in coastal and estuarine waters. *Proc. Natl. Acad. Sci.*, 113(21):5868–5873, May 2016.
- 393 Elisa De Laurentiis, Marco Minella, Valter Maurino, Claudio Minero, Gilles Mailhot, Mohamed Sarakha, Marcello Brigante, and Davide Vione. Assessing the occurrence of the dibromide radical ($\text{Br}_2\cdot$) in natural waters: Measures of triplet-sensitised formation, reactivity, and modelling. *Sci. Total Environ.*, 439:299–306, 2012.
- 394 Dov Zehavi and Joseph Rabani. Oxidation of aqueous bromide ions by hydroxyl radicals. Pulse radiolytic investigation. *J. Phys. Chem.*, 76(3):312–319, February 1972.
- 395 Marco Bodrato and Davide Vione. APEX (Aqueous Photochemistry of Environmentally occurring Xenobiotics): a free software tool to predict the kinetics of photochemical processes in surface waters. *Environ. Sci. Process. Impacts*, 16(4):732–740, 2014.
- 396 Fadi al Housari, Davide Vione, Serge Chiron, and Stéphane Barbat. Reactive photoinduced species in estuarine waters. Characterization of hydroxyl radical, singlet oxygen and dissolved organic matter triplet state in natural oxidation processes. *Photochem. Photobiol. Sci.*, 9(1):78–86, 2010.
- 397 Davide Vione, Marco Minella, Valter Maurino, and Claudio Minero. Indirect Photochemistry in Sunlit Surface Waters: Photoinduced Production of Reactive Transient Species. *Chem. - A Eur. J.*, 20(34):10590–10606, August 2014.
- 398 G. E. Adams, J. W. Boag, and B. D. Michael. Reactions of the hydroxyl radical. Part 2.—Determination of absolute rate constants. *Trans. Faraday Soc.*, 61(0):1417–1424, 1965.
- 399 Ai Sakamoto, Yutaka W. Watanabe, Masato Osawa, Kazuo Kido, and Shinichiro Noriki. Time series of carbonate system variables off Otaru coast in Hokkaido, Japan. *Estuar. Coast. Shelf Sci.*, 79(3):377–386, 2008.

- 400 Florian Weigend and Reinhart Ahlrichs. Balanced basis sets of split valence, triple zeta valence and quadruple zeta valence quality for H to Rn: Design and assessment of accuracy. *Phys. Chem. Chem. Phys.*, 7(18):3297–305, September 2005.
- 401 T. Chai and R. R. Draxler. Root mean square error (RMSE) or mean absolute error (MAE)? – Arguments against avoiding RMSE in the literature. *Geosci. Model Dev.*, 7(3):1247–1250, June 2014.
- 402 Morton Hoffman and E. Hayon. Pulse Radiolysis study of Sulfhydryl compounds in aqueous solution. *J. Phys. Chem.*, 77(8):990–996, 1973.
- 403 Daniel O. Martire, Janina A. Rosso, Sonia Bertolotti, and Carrillo Galo Le Roux. Kinetic Study of the Reactions of Chlorine Atoms and $\text{Cl}_2^{\bullet-}$ Radical Anions in Aqueous Solutions. II. Toluene, Benzoic Acid, and Chlorobenzene †. *J. Phys. Chem.*, 105:5385–5392, 2001.
- 404 Richard G. Zepp, Andre M. Braun, Juerg. Hoigne, and Jerry A. Leenheer. Photoproduction of hydrated electrons from natural organic solutes in aquatic environments. *Environ. Sci. Technol.*, 21(5):485–490, May 1987.
- 405 J. M. Nicovich, K. D. Kreutter, C. A. Van Dijk, and P. H. Wine. Temperature-dependent kinetics studies of the reactions bromine atom(2P_{3/2}) + hydrogen sulfide .tautm. mercapto + hydrogen bromide and bromine atom(2P_{3/2}) + methanethiol .tautm. methylthiol + hydrogen bromide. Heats of formation of mercapto and methylthio. *J. Phys. Chem.*, 96(6):2518–2528, March 1992.
- 406 Sidney W. Benson. Thermochemistry and kinetics of sulfur-containing molecules and radicals. *Chem. Rev.*, 78(1):23–35, February 1978.
- 407 Stephen J. Blanksby and G. Barney Ellison. Bond dissociation energies of organic molecules. *Acc. Chem. Res.*, 36(4):255–63, April 2003.
- 408 Joseph Berkowitz, G. Barney Ellison, and David Gutman. Three methods to measure RH bond energies. *J. Phys. Chem.*, 98(11):2744–2765, March 1994.
- 409 Marija Bonifačić and Klaus-Dieter Asmus. Stabilization of oxidized sulphur centres by halide ions. Formation and properties of R₂S-X radicals in aqueous solutions. *J. Chem. Soc., Perkin Trans. 2*, (5):758–762, 1980.
- 410 Rudolf Wedmann, Sarah Bertlein, Igor Macinkovic, Sebastian Böltz, Jan Lj. Miljkovic, Luis E. Muñoz, Martin Herrmann, and Milos R. Filipovic. Working with "H₂S": facts and apparent artifacts. *Nitric Oxide*, 41:85–96, September 2014.
- 411 Jacques Boulègue and Gil Michard. Constantes de formation des ions polysulfures S⁻² 6 , S⁻² 5 et S⁻² 4 en phase aqueuse. *J. français d'hydrologie*, 9(1):27–33, November 1978.
- 412 Alexey Kamyshny, M. Zilberbrand, I. Ekelchik, T. Voitsekovski, J. Gun, and O. Lev. Speciation of Polysulfides and Zerovalent Sulfur in Sulfide-rich Water Wells in Southern and Central Israel. *Aquat. Geochemistry*, 14(2):171–192, April 2008.

Bibliography

- 413 B. Y. W. Giggenbach. Optical Spectra and Equilibrium Distribution of Polysulfide Ions in Aqueous at 20'. *Inorg. Chem.*, 1333(6):1201–1207, 1972.
- 414 G. Schwarzenbach and A. Fisher. Die Acidität der Sulfane und die Zusammensetzung wässriger Polysulfidlösungen. *Helv. Chim. Acta*, 43:1365–1390, 1960.
- 415 Gregory A. Cutter and Christain F. Krahforst. Sulfide in Surface Waters of the Western Atlantic Ocean. *Geophys. Res. Lett.*, 15(12):1393–1396, 1988.
- 416 T. N. Das, R. E. Huie, P. Neta, and S. Padmaja. Reduction Potential of the Sulfhydryl Radical: Pulse Radiolysis and Laser Flash Photolysis Studies of the Formation and Reactions of $\cdot\text{SH}$ and $\text{HSSH}\cdot$ - in Aqueous Solutions. *J. Phys. Chem. A*, 103(27):5221–5226, July 1999.
- 417 Peter Nagy. Perspective of Hydrogen Sulfide Signaling. In Enrique Cadenas and Lester Packer, editors, *Methods Enzymol. Hydrog. sulfide redox Biol. Vol. 554 Part A*, chapter 1, page 344. Academic Press, 1st edition, 2015.
- 418 Philip M. Lessner, Frank R. McLarnon, Jack Winnick, and Elton J. Cairns. The Dependence of Aqueous Sulfur-Polysulfide Redox Potential on Electrolyte Composition and Temperature. *J. Electrochem. Soc.*, 140(7):1847, 1993.
- 419 M. Pettine, L. Patrolecco, M. Manganelli, S. Capri, and M.G. Farrace. Seasonal variations of dissolved organic matter in the northern Adriatic Sea. *Mar. Chem.*, 64(3):153–169, 1999.
- 420 D.M.DeR. Channer, C.E.J. de Ronde, and E.T.C. Spooner. The Cl-Br-I- composition of ~3.23 Ga modified seawater: implications for the geological evolution of ocean halide chemistry. *Earth Planet. Sci. Lett.*, 150(3-4):325–335, August 1997.
- 421 Jiping Huang and Scott A. Mabury. Steady-state concentrations of carbonate radicals in field waters. *Environ. Toxicol. Chem.*, 19(9):2181–2188, September 2000.
- 422 Silvio Canonica, Tamar Kohn, Marek Mac, Francisco J Real, Jakob Wirz, and Urs von Gunten. Photosensitizer method to determine rate constants for the reaction of carbonate radical with organic compounds. *Environ. Sci. Technol.*, 39(23):9182–8, December 2005.
- 423 Steven A. Loiselle, Luca Bracchini, Arduino M. Dattilo, Maso Ricci, Antonio Tognazzi, Andres Cózar, and Claudio Rossi. The optical characterization of chromophoric dissolved organic matter using wavelength distribution of absorption spectral slopes. *Limnol. Oceanogr.*, 54(2):590–597, March 2009.
- 424 G. Najjar, J. Erickson, and Sasha Madronich. Modeling the air-sea fluxes of gases formed from the decomposition of dissolved organic matter: Carbonyl sulfide and carbon monoxide. In Richard G. Zepp and C. Sonnyag, editors, *Role Nonliving Org. Matter Earth's Carbon Cycle*, pages 107–132. John Wiley & Sons Inc., 1995.
- 425 Abdirisak A. Isse and Armando Gennaro. Absolute Potential of the Standard Hydrogen Electrode and the Problem of Interconversion of Potentials in Different Solvents. *J. Phys. Chem. B*, 114(23):7894–9, June 2010.

-
- 426 Casey P. Kelly, Christopher J. Cramer, and Donald G. Truhlar. SM6: A Density Functional Theory Continuum Solvation Model for Calculating Aqueous Solvation Free Energies of Neutrals, Ions, and Solute - Water Clusters. *J. Chem. Theory Comput.*, 1:1133–1152, 2005.
- 427 Mary Beth Day, Karl N. Kirschner, and George C. Shields. Global Search for Minimum Energy (H₂O)_n Clusters, n = 3-5. *J. Phys. Chem. A*, 109(30):6773–8, August 2005.
- 428 A. L. Fridman, F. M. Mukhametshin, and S. S. Novikov. Advances in the Chemistry of Aliphatic N-Nitrosamines. *Russ. Chem. Rev.*, 40(1):34–50, 1971.
- 429 Péter Nagy and Christine C. Winterbourn. Rapid reaction of hydrogen sulfide with the neutrophil oxidant hypochlorous acid to generate polysulfides. *Chem. Res. Toxicol.*, 23(10):1541–3, October 2010.
- 430 W. Karmann, G. Meissner, and A. Henglein. Pulse radiolysis of hydrogen sulfide in an aqueous solution. *Zeitschrift fuer Naturforsch.*, 22(3):273–82, 1967.
- 431 G. Mills, K. H. Schmidt, M. S. Matheson, and D. Meisel. Thermal and photochemical reactions of sulfhydryl radicals. Implications for colloid photocorrosion. *J. Phys. Chem.*, 91(6):1590–1596, March 1987.
- 432 Harold A. Schwarz. Absolute Rate Constants for Some Hydrogen Atom Reactions in Aqueous Solution. *J. Phys. Chem.*, 67(12):2827–2830, December 1963.

Daniela Trogolo

Born July 20th, 1988 Susa, Italy
daniela.trogolo@gmail.com

EDUCATION

- 2012 – present **Swiss Federal Institute of Technology at Lausanne (EPFL), Switzerland**
Ph.D. in Computational Chemistry
(expected December 2016)
- 2007– 2012 **University of Torino, Italy**
M.Sc. in Chemistry, Summa Cum Laude
B.Sc. in Chemistry

CORE EXPERIENCE

Ph.D. Thesis: “Quantum Chemical Studies of Reactive Species in Water”

- + Formation of highly toxic disinfection byproducts in drinking water
- + Quantum chemical modeling of organic and inorganic molecules in gas phase and in water
- + Treatment, analysis, and interpretation of big data
- + 3 publications in high-impact factor peer-review journals and 1 in preparation

M.Sc. Thesis: “Formation of Cyclic Hydrocarbons in Combustion Conditions: Quantum Mechanical Study of the Reactions of Vinylacetylene and 1,3-butadiene with Propargyl Radical”

- + Reactivity of organic radical species (more than 300 transition state structures) during combustion
- + Quantum chemical modeling of kinetics and thermodynamic properties in gas phase
- + 2 publications in high-impact factor peer-review journals

ADDITIONAL EXPERIENCE

Teaching Assistant at the EPFL (2012-2016)

- + Bachelor courses (in French): Analysis, Linear Algebra, General Physics
- + Master course (in English): Fate and Behavior of Organic Pollutants

Other teaching activities (2004-2010)

- + Latin and Ancient Greek to high school students

B.Sc. Internship (2009)

- + Two-months internship at the Medical Analytic Laboratory at the Hospital of Susa, Italy

TECHNICAL SKILLS

Text and image editing and formatting tools

- + Latex, Office
- + Inkscape, Adobe Illustrator

IT competencies

- + Proficiency in Linux (Debian, Fedora, Ubuntu)
- + Proficiency in Shell/BASH and intermediate knowledge of Python scripting

Chemical modeling tools

- + Gaussian09, Molpro, CFOUR, QChem, NWChem, Multiwell, Amber

LANGUAGES

- + **English:** Fluent spoken and written (C1)
- + **French:** Fluent spoken (C1) and Intermediate written (B2)
- + **German:** Elementary spoken and written (A1-A2)
- + **Italian:** Native speaker

AWARDS

- + Special prize for teaching General Physics, EPFL, 2015
- + EPFL ENAC IIE Green Days, Best Poster Award, 2013
- + Master Thesis Award for Best Thesis with an Environmental Topic, Camera di Commercio, Torino, 2013

EXTRACURRICULAR ACTIVITIES

Continuing Education:

- + CTI Business Concept Course (EPFL, Spring 2016)
- + Communication for Research Engineers (EPFL, Fall 2015)
- + Scientific Writing (EPFL, Spring 2015)

Activities:

- + Savate – French Boxing (4 years)
- + EPFL First Aid team, First responder (2015 - Present)

